Modelling Cold Spray Splat Morphologies Using Smoothed Particle Hydrodynamics

Luke Stephen Mason

Submitted for the degree of

Doctor of Philosophy

Heriot-Watt University

Institute of Mechanical, Process and Energy Engineering

Engineering and Physical Sciences

July 28, 2015

Abstract

The small scale, short duration and hostile environment for instrumentation presented by cold spray coating makes experimental observations challenging, and therefore requires computational models capable of capturing the splat formation process. Current coating models are dominated by the Finite Element Method (FEM); whilst this has lead to significant improvements in understanding, the method is limited due to the reliance on a mesh coupled with the significant strains and strain rates involved. Eulerian methods have also been applied but retrieval of material histories and accurate interface tracking remains challenging. The Smoothed Particle Hydrodynamics (SPH) method is a meshless method that combines the advantages of FEM and Eulerian approaches. The current work extends the work of applying SPH to solid mechanics with heat conduction, improved tensile stability corrections and a novel zero impedance boundary. Solver performance is increased with the application of the multi-threading capabilities of the C++ 11 standard. The development of the SPH solver is described, validated and benchmarked against known analytical and experimental test cases. An in-depth investigation of parameters affecting splat morphologies is performed. Finally, a model of a coating formation process involoving multiple feedstock impact events is described and analysed in order to demonstrate the capabilities of the newly developed solver.

For Becky and Puff.

Acknowledgements

I would like to thank my supervisor Dr Yeaw Chu Lee for his help and support over the years as well as the members of our research group Alasdair Mckean, Odin Du'Plessis, Noel Ehigiamusoe and Samat Maxutov. I would also like to thank Dr Richard Fu for his supervision in the initial stages of the project and for his assistance with proof reading. This project was sponsored by AWE plc and I would like to thank Dr Robin Williams, David Youngs and Chris Batha who provided advice and invaluble feedback at our project review meetings. Finally I would like to thank my family and friends for their patience and support but most importantly my fiancée Rebecca without whom I would not have made it this far.

ACADEMIC REGISTRY
Research Thesis Submission

Name:			
School/PGI:			
Version: *(i.e. First, Resubmission, Final)*		Degree Sought (Award **and** Subject area)	

Declaration

In accordance with the appropriate regulations I hereby submit my thesis and I declare that:

1) the thesis embodies the results of my own work and has been composed by myself
2) where appropriate, I have made acknowledgement of the work of others and have made reference to work carried out in collaboration with other persons
3) the thesis is the correct version of the thesis for submission and is the same version as any electronic versions submitted*.
4) my thesis for the award referred to, deposited in the Heriot-Watt University Library, should be made available for loan or photocopying and be available via the Institutional Repository, subject to such conditions as the Librarian may require
5) I understand that as a student of the University I am required to abide by the Regulations of the University and to conform to its discipline.

* *Please note that it is the responsibility of the candidate to ensure that the correct version of the thesis is submitted.*

Signature of Candidate:		Date:	

Submission

Submitted By *(name in capitals):*	
Signature of Individual Submitting:	
Date Submitted:	

For Completion in the Student Service Centre (SSC)

Received in the SSC by *(name in capitals):*			
Method of Submission *(Handed in to SSC; posted through internal/external mail):*			
E-thesis Submitted ***(mandatory for final theses)***			
Signature:		Date:	

Please note this form should bound into the submitted thesis.

Updated February 2008, November 2008, February 2009, January 2011

Contents

List of Tables

List of Figures

Chapter 1

Literature Review

Before starting the literature review it is best to clarify some of the terminology used in the following text. Both the fields of cold spray coating and smoothed particle hydrodynamics (SPH) use the term particles when talking about very different objects or concepts. In spray coating the term particle is used to describe the individual powder grains that make up a feedstock whilst in SPH it is the name given to the Lagrangian points at which the governing equations are calculated. In general the specific meaning of "particle" is clear from context. Where the discussion becomes more complex involving both grains of feedstock and SPH integration points, the term "particle" will be reserved for SPH points and we will simply refer to "feedstock" instead of feedstock particle.

1.1 Cold Spray

Thermal spray coating methods are widely used to modify surface features and characteristics of components by application of a layer of material with beneficial properties. A coating is formed by accelerating and heating feedstock material using a carrier gas or plasma onto the substrate. Upon impact, the individual feedstock particles cool, bonding with one another and the adjacent substrate to form a coating layer. These coatings share common features of porosity, material oxidation and feedstock micro-structural changes, where the degree to which a coating exhibits these features depends on spray parameters that are broadly defined by the thermal spray method used. The majority of thermal spray methods include plasma spray, high velocity oxy-fuel (HVOF) and cold spray, with

some typical spray parameters given in Table 1.1; exact temperatures and velocities vary depending on the material being sprayed.

Method	Feedstock Velocity (m/s)	Gas Temperature (K)
Plasma	240	5773
HVOF	400 - 800	3373
Cold	500 - 1200	320

Table 1.1: Typical coating method parameters [1, 2, 3].

The key differences between the above thermal spray methods are how feedstock materials are propelled onto the substrate and whether the temperature is sufficient to cause melting. In plasma sprays for example, the feedstock powder is both melted by a jet of plasma. In HVOF, feedstock can also be melted or softened by the spray jet. Cold spray in contrast uses kinetic energy rather than thermal energy for bonding of feedstock onto the substrate. Feedstock particles are propelled by a high velocity carrier gas whilst experiencing only minor heating; it remains classified as a thermal spray process because the carrier gas is heated to increase flow velocity but the gas temperatures are well below the melting temperature of the material being sprayed. Consequently, the feedstock needs to be sprayed above a minimum velocity to produce plastic deformation before coating formation is possible [4]. This is referred to as the critical velocity and depends on feedstock material properties, size and temperature [3, 5, 6, 7, 8, 9]. There also exists a velocity above which feedstock will be eroded off the substrate which acts as an upper limit for gas velocity [10].

Cold spray was patented in 1994 [11] and has received increasing attention in recent years because it allows coating of heat sensitive components with decreasing residual stresses, levels of oxidation and porosity within the coating itself. Some example applications of cold spray coatings include lightning proofing of aircraft [12], manufacture of heat exchangers [13, 14], thermal barrier coatings [15], consolidation of thermite [16], and corrosion protection of components [17, 18]. The following sections will describe the key characteristics of cold sprayed coatings and how they are influenced by material properties and spray parameters.

Characteristics of Cold Sprayed Splats

A coating is formed from many individual feedstock impact events where its characteristics are dependent on the properties of the feedstock and substrate materials and the quality of bonds between feedstock/substrate and feedstock/feedstock interfaces, therefore the understanding of a single feedstock impact and its resulting morphology is vital to shed light on the parameters effecting bulk coating properties. In order to facilitate the following discussions of feedstock impacts several distinct regions within the splat will be defined: splat body, interface flanks and top and bottom centre, as shown in Figure 1.1.

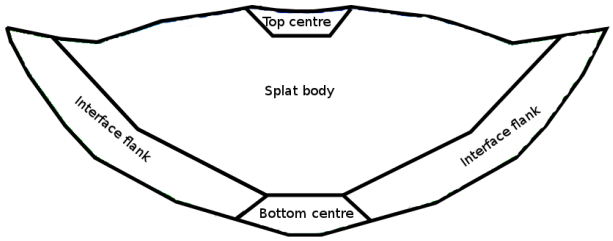

Figure 1.1: Schematic of splat regions.

The evolution of a typical splat impact is shown in Figure 1.2, where the direction of travel is towards the bottom of the page and the substrate has been omitted to maintain the focus on the feedstock deformation. Starting at the left of the figure the splat can be seen to be flattening at the bottom edge where it has ecountered the substrate. This flattening continues in the centre image where formation of the material jet can also be seen in the interface flank regions, at this time the impact is part way through and the particle retains some of it's initial velocity. The final image on the right of the figure shows a particle at steady state, a high degree of flattening is visible along with significant jetting.

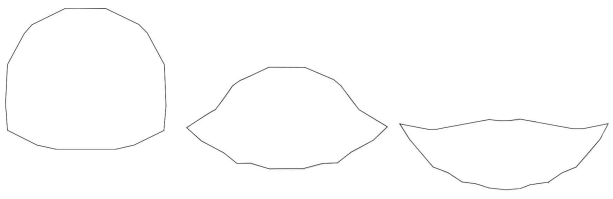

Figure 1.2: Evolution of a typical splat impact.

A key characteristic of cold spray splats is the non-uniform deformation that is highly

localised at the interface regions, which results in the formation of a material jet, creating the typical splat geometry shown in Figure 1.3. Here a significantly flattened copper splat is seen bonded to a steel substrate, the material jet can be seen as the distinct lip of material overhanging the edges of the crater.

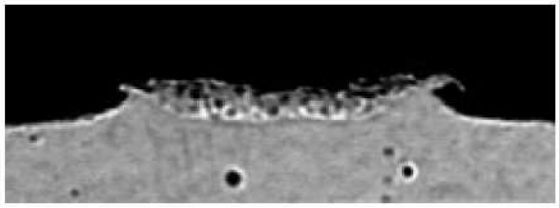

Figure 1.3: Cross section of a copper particle bonded to a stainless steel substrate. Particle velocity was 700 m/s [19].

The formation of this material jet occurs above a critical velocity for coating formation. Above this velocity threshold, there is a localisation of strain and heating at the interface region which results in a feedback loop of strain localisation and material softening, thus further weakening the material. This feedback loop of material weakening and straining is called a "shear band" instability. Although the critical velocity is normally used as the criterion for the formation of the shear instability and subsequent bonding, the shear instability is in fact initiated by the total energy from both kinetic and thermal energies of the feedstock particle at impact [20]. Since bulk feedstock heating from the carrier gas at the onset of instability is low in cold spray, the thermal softening of the feedstock due to gas temperature is of minor influence and the critical velocity is used as a criterion for instability onset.

Upon impact with the substrate, the feedstock deforms significantly as the crater formation forces the flanks of the feedstock up and out, away from the substrate as the non-impacted regions of the feedstock (in the splat body region) cause the splat morphology to flatten. The ensuing splat typically shows significant flattening compared to the initial feedstock dimensions; the degree of flattening depends on the ratio between feedstock impact velocity and the feedstock critical velocity [21]. The flattening ratio is a convenient measure of the amount of strain experienced by a feedstock particle. Since coating properties approach those of the bulk material as porosity decreases and this in turn depends on the amount of plastic strain, the flattening ratio is a good

indicator of coating quality [21]. Whilst the flattening ratio can certainly be useful in assessing the quality of inter-splat bonds, more care should be taken when considering its adhesion to the substrate [22]. The strain experienced by an impacting feedstock particle depends on the relative yield strengths and shear modulii of the feedstock and the substrate [23] because these dictate the deformation of each material due to impact. A harder feedstock impacting on a softer substrate will undergo less deformation than the substrate and jetting is likely to be around the crater edges rather than in the feedstock. In more extreme cases, it is possible that the first splat layer deposited onto the substrate becomes partially encapsulated by substrate material [23, 24] forming strong mechanical bonds without much flattening of the feedstock.

Bonding Mechanisms and Coating Properties

Coating formation will not take place if the feedstock impact velocity is below the critical threshold, the feedstock simply rebounds due to insufficient adhesion to the substrate. This velocity also coincides with the shear instability formation that results in material jetting. It has been proposed by Assadi et al [3] that the instability can be considered a condition for bonding, and the impact velocity at which the instability forms can accurately predict critical velocities from modelling data. Although it appears bonding will not occur without shear instabilities, examination of rebounded feedstock has found jetting features which indicate shear instability was experienced [25]. It is unclear whether the rebounded feedstock failed to bond or was eroded by later impacts since other feedstock of similar dimensions was found bonded in the same coating process. It does show however that material jetting does not guarantee successful coating formation. The jetting behaviour clearly plays a role in the bond formation process and it is thought that high strain in this region serves to clean the impact interface of any surface oxidation allowing for contact of clean material surfaces where metallurgical bonds can form under high impact pressures and heating [26, 27, 28].

The presence of a layer of oxides on the outer surface of the feedstock is formed during production of the feedstock powder; this oxide inhibits bonding between the feedstock and substrate. A numerical investigation of oxide layer behaviour during splat formation has been carried out by Yin et al [29] using the Finite Element Method. The oxide

is modelled as a thin layer of oxide ceramic evenly covering the exterior of a feedstock particle. It was found that the initial impact cracks the oxide and the fragments are removed from the interface by the jetting process, as seen in Figure 1.4. Some residual oxide was left at the bottom centre of the particle whilst the flanks were almost completely clean.

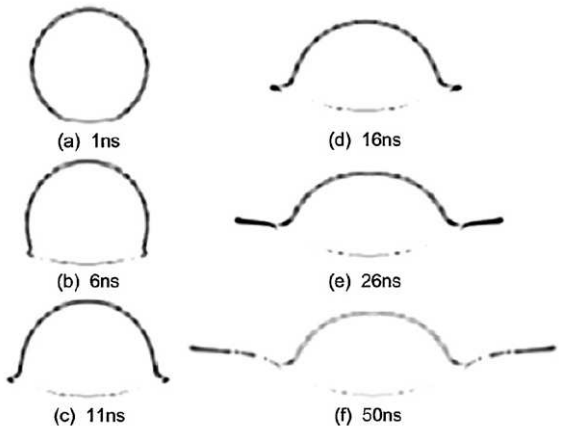

Figure 1.4: Oxide film (black lines) locations on an Al feedstock with an impact velocity of 700 m/s [29].

The residual oxide was not removed by increasing the impact velocity. Other authors have noted that feedstock bonding is most often present in these flank regions whilst there is a void at the bottom centre of single feedstock impact sites [23, 26, 30]. This is supported by Xiong et al [30] who found that jetting is stronger in these flank regions and a corresponding increase in temperature further improves the bond strength. Increasing the spray velocity has been shown to increase the amount of metallurgical bonds due to greater induced jetting cleaning interfaces and greater contact pressures [31].

In addition to the metallurgical bonds, there is evidence of mechanical interlocking between splats and the splats and the substrate [27, 32, 33, 34, 35]. The high rate of plastic strain in the interface region means the material can flow in a fluid like manner and so wave and vortex features may result in the interface mixing demonstrated in Figure 1.5 [27, 36, 37]. The degree of mixing will depend on the material properties since both materials need to experience high plastic strain rates, increased impact velocity and temperature. There has been evidence of material melt in the interface region for some combinations of feedstock and substrate and this also increases mixing and therefore me-

chanical bond strength whilst improving metallurgical bonds [5, 23, 38, 39, 40]. Mixing at the interface increases the contact area between the materials allowing a greater amount of metallurgical bonds to form, additionally the vortex and wave features mechanically lock the feedstock and substrate together. Grujicic et al [36] propose that the interfacial mixing shows some similarities to a Kelvin-Helmholtz instability. These instabilities form between layers of fluids of differing densities moving at different parallel velocities, where the instability causes slight disturbances such as waves to grow until turbulent mixing occurs at the interface. Metallurgical and mechanical bonding mechanisms are not mutually exclusive and both play a role in the bonding of splats [27]. The dominant mechanism in any coating will depend on the material properties of the substrate and feedstock as well as spray parameters.

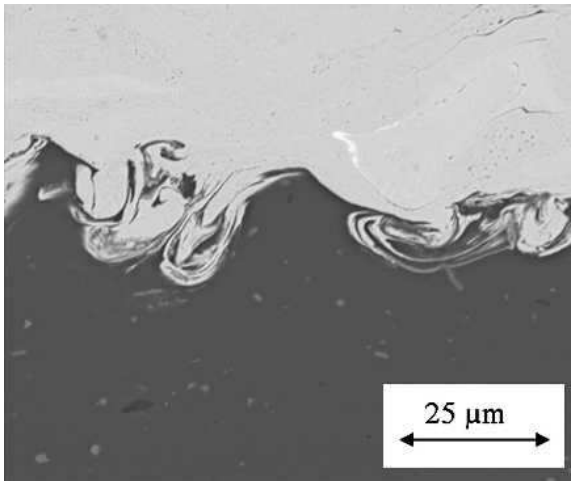

Figure 1.5: Interface mixing between a copper feedstock and aluminium substrate [27].

The nature of feedstock-substrate bonds and their adhesion strength is of particular interest since this largely defines the success of a coating/substrate combination. These bonds are more sensitive to the relative material properties. Substrate roughness has been shown to have a positive effect on adhesion [41, 42, 43, 44, 45, 46]; rough substrate surfaces increase the degree of interlocking as particles embed themselves in pits and become partially encapsulated or experience a greater concentration of stress and therefore plastic strains when impacting on a sharp surface feature. Heating the substrate has also been shown to improve adhesion either by thermally softening the material allowing for greater plastic strain or by evaporating contaminates such as oxide layers which are known to

inhibit bonding [41, 47].

Cold spray coatings typically have a very low level of porosity (2% or less) [20, 32, 48, 49, 50, 51] and form a tightly packed lamella structure with a density close to that of the initial feedstock [52]. A low level of porosity is important since the bulk properties of the coating depend on this characteristic [53]; some typical properties are shown in Table 1.2. The presence of voids decrease density, conductive properties and the contact area between splats from that of the bulk material. The lower contact area reduces the formation of bonds reducing tensile strength; it is also possible for the coating to crack along weak interface bonds, thus, reducing fatigue life [54]. In some cases, cracks initiated in the coating have propagated into the substrate lowering its fatigue resistance [55]. An etched cross section of a copper coating is shown in Figure 1.6 where individual splats and the low porosity is visible [56].

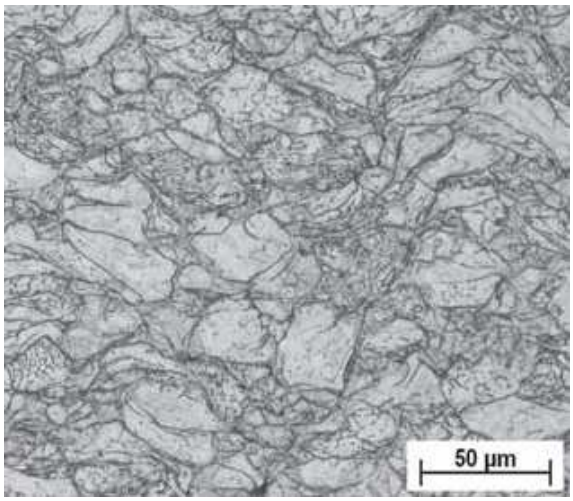

Figure 1.6: Etched copper coating showing splat interfaces.

The low level of porosity can be attributed to several factors. Firstly, high levels of deformation of the feedstock particles during impact leads to tightly conforming interfaces between feedstock particles and the feedstock and substrate [57]. The amount of deformation can be increased by increasing feedstock velocity and temperature with a corresponding decrease in porosity [8, 20, 58, 59, 60]. At higher temperatures the level of feedstock oxidation increases and these chemical changes alter the coating properties and impede the formation of bonds within the coating. Cold spray process parameters are selected to avoid this undesired oxidation and instead use higher velocities to supply

greater kinetic energy to the feedstock.

The successive impact of new feedstock particles onto the already formed coating layer serves to compress the feedstock particles into a tighter structure further eliminating porosity. Experiments have shown that the porosity of coatings does in fact increase in the top region of the coating furthest from the substrate compared to the deeper coating regions closer to the substrate [61]. This tamping effect has been exploited by the addition of hard ceramic powders to the feedstocks [43,62,63,64,65,66] to produce a denser coating. The ceramic particles have a much higher critical velocity than the feedstocks they are mixed with and so most of them rebound and are not present in the final coating [62], the craters left after the rebound roughen the substrate and promote mechanical bonding in subsequent impacting particles. The hard particles also clean surface oxides before impact with the substrate by colliding with feedstock whilst entrained in the gas jet [67].

Property	Percentage of bulk value (%)
Electrical Conductivity	77 [41]
Young's Modulus	32 [55] to 95 [52]

Table 1.2: Typical coating properties.

Coatings have higher values of hardness than the bulk feedstock [33, 41, 49, 68, 69, 70, 71, 72, 73] due to the amount of strain hardening during impact, whilst the heating and consequential thermal softening is localised and therefore has minimal effect on coating hardness. Coating hardness can be enhanced by increasing spray velocities [68, 74] or by addition of harder materials to the feedstock [66, 75].

Dynamics of Carrier Gas Jet

The carrier gas in a cold spray system is typically accelerated by a De Laval type nozzle into which the feedstock is injected as shown in Figure 1.7. The pressurised and heated main gas is fed into the pre-chamber where feedstock is introduced, the gas/feedstock mix is then forced out through the nozzle by the difference between pre-chamber and ambient or nozzle exit pressures. Gas velocity increases as the nozzle diameter decreases towards the throat diameter until it reaches Mach 1 at the throat and becomes a choked flow. At

this point the nozzle diameter expands and the gas accelerates into the lower pressure nozzle exit region. Gas pressures at the exit of the nozzle in cold spray systems are generally lower than the ambient (atmospheric) pressure to maximise gas velocity [76].

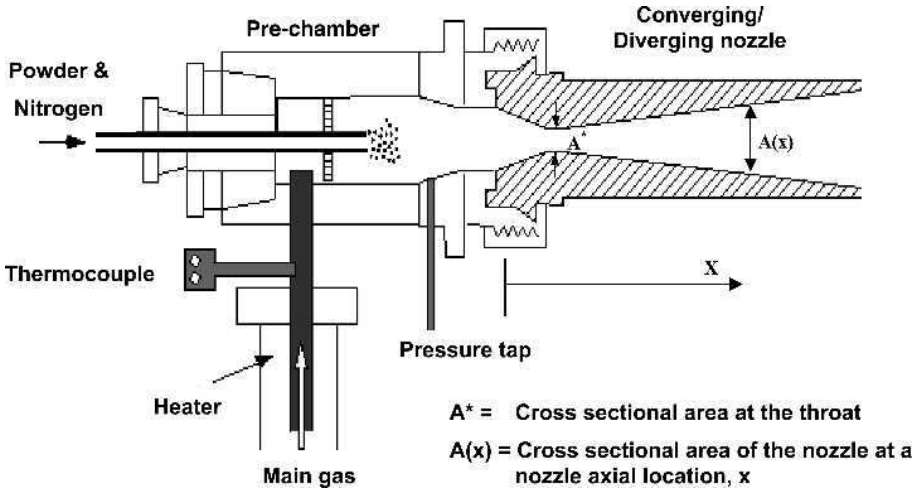

Figure 1.7: Schematic of cold spray nozzle [77].

The gas flow within the jet is complex and features oblique shocks, radial flow across the substrate and a bow shock where the jet impinges on the substrate. The highest gas velocity is along the centre axis of the nozzle where edge effect from the nozzle and interaction with the ambient atmosphere are minimised.

Feedstock is accelerated by drag forces [76] and is influenced by the feedstock particle size and density [78, 79]. Katanoda et al [78] propose two parameters (p_1, p_2) which can be used to accurately predict the feedstock velocity and temperature. These parameters are calculated from:

$$p_1 = d_f \rho_f \tag{1.1}$$

$$p_2 = {d_f}^2 \rho_f {c^v}_f \tag{1.2}$$

where d_f is the feedstock diameter, ρ_f is the feedstock density and ${c^v}_f$ is the feedstock specific heat. The inflight interactions between feedstock and carrier gas have been modelled and plotted against these parameters [78]. Models utilising the same carrier gases show close agreement between temperature and impact velocity for a variety of feedstock. The impact temperature and velocity of a particular feedstock can then be estimated by

consulting pre-calculated graphs rather than modelling the complex gas dynamics or performing experimental tests. Determining this relationship requires modelling of the in flight interactions for any given gas and gas velocity; this limits the applicability of these parameters for accurate predictions, although they can provide an estimate of a good feedstock powder size to obtain a required impact velocity and temperature. In general, the calculated results show an increase in impact velocity as feedstock size increases until a critical size is reached and velocity drops again. Impact temperature shows the opposite relationship with temperature declining as feedstock size increases before increasing past a critical size. The differences in the temperature plots are due to entrainment time in the carrier gas. As particle size and therefore, velocity increases the feedstock spends less time in the warm gas and so the total temperatures drop.

Smaller particles are more affected by the dynamics of the jet due to their lower inertia and so experience greater acceleration than larger feedstock particles [76,79,80,81]. Despite experiencing large initial accelerations, small feedstock can find it hard to cross the bow shock that forms as the gas jet interacts with the substrate, due to their lower inertia. As feedstock encounters this region it decelerates and can be pushed away from the substrate [76] or have its velocity reduced below the critical velocity [81]. Large feedstocks on the other hand have sufficient inertia to preserve their velocity as they cross the bow shock and so are more likely to successfully bond [77]. This bow shock feature therefore needs consideration to maximise coating efficiency and minimise waste. The shock forms as fast moving gas is bought abruptly to a halt by the substrate and is associated with the radial flow of gas over the substrate surface. The strength of the shock is related to the stand off distance from the nozzle and geometry of the substrate [81] since this dictates the degree of deceleration the gas has already experienced and the degree of further deceleration caused by encountering the substrate. Greater stand off distances reduce this effect but because the gas decelerates as soon as it leaves the nozzle, stand off distances have to be limited to ensure feedstock retains critical velocity on impact. Typical stand off distances are in the range of a few tens of millimetres and an optimum distance of ten millimetres has been calculated from CFD models and reported in the literature [81].

The gas is typically heated to increase flow velocity and so heat conduction into the feedstock and substrate need to be considered. Feedstock is introduced into the warm low

velocity gas in the pre-chamber where it is heated. The warm pressurised gas accelerates towards the nozzle exit and converts its thermal energy into kinetic energy. However, at the point of impact the gas has not converted all of its thermal energy into kinetic energy, so there is a net heating of the gas [76]. The gas jet has a heating effect on the substrate and its exact distribution depends on the spray angle [82] due to the change in gas flow across the substrate, see Figure 1.8. Assuming a flat substrate and with spray alignments normal to the substrate, the bow shock region and radial jets are evenly distributed. This produces a zone of peak heating along the nozzle centre axis from which the temperature decreases as the gas jet radius increases.

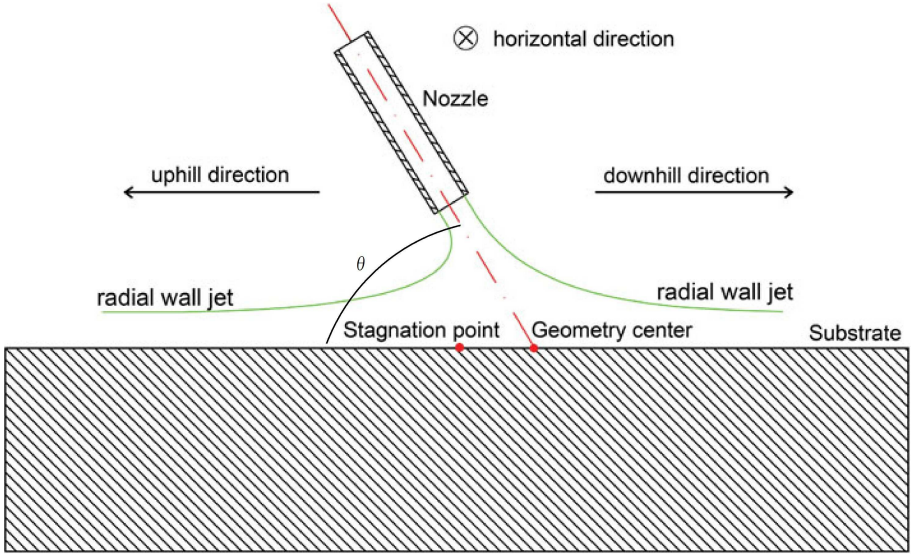

Figure 1.8: Schematic of cold spray nozzle alginment [82].

As the spray angle decreases towards the horizontal the temperature distribution is skewed towards the trailing edge of the substrate (see Figure 1.8) as the radial jetting has a strong bias in that direction. The magnitude of substrate heating will depend on the gas pre-heat temperature, thermal properties of the substrate and the duration of spray. A recent study by McDonald et al [83] has shown that substrate heating only become significant after a period of seconds of spraying depending on the gas temperature; substrates were exposed to a gas jets of varying temperatures typical of cold spray processes (373, 473, 573 and 673 K) for long durations. The substrates reached a peak temperature around half that of the gas temperatures after spray durations of tens of seconds. This peak heating was limited to the centre of the impinging gas jet and shows

a sharp drop off towards the edge of the gas jet. The experiments and models used only considered the gas jet and did not include feedstock particles, it is proposed that inclusion of the feedstock will alter the extent of heating as conduction of heat from the feedstock particles may play a larger role than the gas jet.

Modelling Cold Spray Coating Deposition

The experimentally obtained data describing the cold spray process and its coatings all indicate that the deformation of individual feedstock splats dictate the properties and quality of the coating. The deformations experienced by the particle influences porosity, mechanical interlock bonding, and the extent of jetting and subsequent oxide removal from contact faces. Investigating the physics of splat formation experimentally is challenging due to the short impact time and small scale involved. A greater understanding of the formation process can be obtained from a suitable model capable of capturing the high strain, strain rate, shear instability, work hardening and thermal softening involved in coating formation.

Dykhuizen et al [19] performed early modelling of splat formation using the Sandia National Laboratory's CTH solver. This is based on a Eulerian method designed for high velocity impact modelling. The results were verified against experimentally obtained splats and showed that increasing impact velocity increased crater depth but had little effect on flattening ratio once the splats became fully flattened. These early results also captured the material jetting at the feedstock-substrate interface and demonstrated the potential of numerical methods to further the understanding of splat formation and bonding mechanisms.

The vast majority of modelling to this date has used the Finite Element Method (FEM) and neglects the carrier gas. Initial work performed by Assadi et al [3] showed that modelling the splat formation process enable the critical velocities of feedstock/substrate combinations to be predicted and provided insight into the jet formation process. When calculating critical velocities some assumption as to when effective bonding occurs has to be made. Assadi et al used the formation of the shear instability as the bonding criteria which provided a resonably accurate estimate of the experimentally determined critical velocity. An adiabatic system was assumed to simplify the model, however Schimdt et

al [10] and Yokoyama et al [84], both demonstrated that heat conduction does play a role in splat formation. Schmidt et al found that copper feedstock with a diameter of $5\mu m$ does not experience jetting, since heat is conducted throughout the whole particle, therefore, there are less pronounced thermal gradients which prevents the formation of shear instabilities. As particle diameter increases, heat can no longer conduct through the entire particle over the short duration of the impact and so is confined to a narrow interface region. Once this region has started to soften it experiences more strain and further increases in temperature, forming a feedback loop of heating and softening that serves to further localise the strain and this leads to the jet behaviour central to cold spray bonding. Yokoyama et al also found that the peak temperature was lower when considering heat conduction. Clearly heat conduction needs to be included when modelling cold spray processes and when included particle size becomes a factor in determining feedstock critical velocity. Wang et al [85] found that the inclusion of heat conduction has little effect on the deformation and final morphology of the feedstocks. Arabgol et al [86] used FEM to show that the thermal loading of the coating and substrate can cause distortion of thin components. Xiong et al [30] studied the impact of dissimilar materials and found that jetting produced in FEM models occurs in the weaker material. Bond strength was found to increase on softer substrates for a given feedstock material, where greater deformation of the substrate increases the surface area of the contact zone between the feedstock and substrate which increases the extent of bonding.

FEM has been shown to successfully model splat formation. However, modelling high strains with FEM can present problems because the mesh is tied to the material being modelled. Accuracy decreases as the mesh becomes highly distorted and in worst case scenarios the calculation will fail. The high strains and strain rates involved in splat formation present problems for FEM which can be reduced by using a re-meshing algorithm such as arbitrary Lagrangian-Eulerian re-meshing. This maps the existing distorted FEM model onto an Eulerian grid and then recalculates a new undistorted Lagrangian mesh and maps the Eulerian description onto it, which can lead to errors and violate conservation laws. Assadi et al [3] limited these errors by re-meshing as infrequently as possible. It would obviously be better to use a method that can naturally handle the high strains to improve accuracy and remove the overhead required to re-mesh the problem.

An analysis of the numerical method used to model cold spray has been carried out by Yin et al [87]. Two- and three-dimensional FEM was compared against two-dimensional finite volume (FV) and simple three-dimensional Smoothed Particle Hydrodynamics (SPH) methods. The results confirm the mesh distortion problem in FEM, particularly as the mesh size used decreases. This means the mesh distortion becomes greater as the resolution increases which limits the obtainable accuracy. Better results were produced using FV but Yin reports problems with tracking the interface between substrate and feedstock precisely due to the limitations of defining interface locations within one Eulerian element. The whole computational domain has to be meshed when using an FV method and this could make the method less efficient than FEM and SPH. Material histories are much harder to track because only material flux between cells are calculated naturally unlike in the Lagrangian FEM and SPH models where the element is tied to the material.

SPH is a mesh-free Lagrangian method and so shares some of the advantages of both FEM and FV methods. Having no mesh to be distorted means high strains are not a problem and being Lagrangian also avoids meshing the entire domain whilst providing material histories naturally. The three-dimensional SPH solver used by Yin et al [87] is relatively simple and does not capture the complete physics of elastic-plastic solid materials, instead a fluid material model was used. Despite this, the results presented show the potential of a properly developed SPH solver to improve cold spray modelling and Yin recommends further development of the SPH cold spray model.

1.2 Smoothed Particle Hydrodynamics

SPH is a Lagrangian mesh free particle method first described by Gingold and Monaghan [88] and Lucy [89] for application to astrophysical problems. The application area of these early works meant boundary condition treatments were of low importance and a simple summation density method was used despite introducing a density drop off at the edges of material bodies; this density error was later corrected by Monaghan [90] (discussed in more detail in Section 1.2.2).

A fundamental part of implementing the SPH method is the efficient identification of sets of neighbouring particles. This problem is also seen in molecular dynamics (MD), and

similar methods of determining neighbour sets are used. The simplest way to do this is a brute force search across the whole domain which is obviously prohibitively expensive for large particle counts, this is the method used in the early work of Gingold [88] and Lucy [89]. Monaghan and Lattanzio [91] introduced a linked list or cell search algorithm that divides the total domain into sub-domains or cells. A particle then limits its search over a range of neighbouring cells such that it searches the full width of it's support domain. This is a robust algorithm which can be extended to facilitate reflective and periodic boundary conditions, variable smoothing lengths and differing domain dimensionality with ease. An alternative is the K-D tree as proposed by Hernquist and Katz [92], where particles are sorted into the tree depending on their relative positions and the tree can then be searched to identify neighbouring particles.

Calculating the first derivative of functions is reasonably straight forward in SPH, the calculation of second derivatives is more challenging however due to an increased sensitivity to particle disorder in kernel second derivatives, which reduces the accuracy of the calculation. Flebbe et al [93] and Watkins et al [94] used a nested set of first derivative estimates to calculate a second derivative; this approach is costly and introduces additional error from the multiple SPH estimates required. Brookshaw [95] first directly calculated second derivatives for one dimensional heat conduction by combining the SPH estimate to a function derivative with a Taylor estimate of the first derivative of a function. The method was extended to two-dimensions by Cleary et al [96, 97] and a similar technique was used by Morris et al [98] to model viscous fluids. Espanol et al [99] proved the extension to three-dimensions and Violeau [100] provides a good summary of the differing derivations.

The following sections will described in more detail key aspects of the SPH methodology before reviewing the specific application of SPH to modelling the cold spray process. The description of the exact implementation of the methodology used in the current work will be given in Chapter 2

1.2.1 Kernel Functions

The particles in a SPH model are treated as integration points for the system governing equations with the interconnectivity of the particles described by the particle kernel

function. The size of the kernel support domain controls the sphere of influence and amount of neighbours for a particle. The size of the support domain is controlled by the smoothing length, h, which is proportional to the initial particle spacing and a coefficient, k, which is a property of the desired kernel. Using these two parameters the size of the support domain is determined as kh. Although in theory it is possible to use a kernel of infinite width, for computaional efficiency reasons functions with a compact support are more commonly used. In order to be applicable as a kernel a function has to meet several criteria (Fulk [101]):

1. As the width of the kernel approaches zero it must approach the Dirac-delta.

$$\lim_{h \to 0} \left(w \left(x - x', h \right) \right) = \delta \left(x - x' \right) \tag{1.3}$$

2. The kernel must integrate to one across its support domain. This is the normalisation criterion.

$$\int \left(w \left(x - x', h \right) \right) dx' = 1 \tag{1.4}$$

3. The kernel should be a symmetric function.

$$\int \left(x - x' \right) \left(w \left(x - x', h \right) \right) dx' = 0 \tag{1.5}$$

4. Kernel values should monotonically decrease from the kernel centre.

5. The kernel must be sufficiently smooth and continuous.

6. When used to model a physical system the chosen kernel function must remain positive across its support domain to avoid non-physical negative properties.

A bell shaped kernel was used by Lucy [89], where the function benefits from the simplicity of being a single equation rather than the more complex piecewise kernels that are currently more common. This kernel is not as sharply peaked as later kernels and so does not approximate a Dirac-delta as well as newer kernels. Increasing the smoothing length with this kernel would therefore have a proportionally larger effect on results than with sharper functions. Gingold and Monaghan [88] used a Gaussian kernel which better approximates a delta function and is very smooth. The function is theoretically infinite but kernel values become negligible rapidly enough for the kernel to be considered

practically compact (within $4h$). This support domain is still quite wide and increases the neighbour count and therefore makes using this kernel quite expensive compared to narrower kernels. In order to reduce this additional work whilst approximating the Gaussian kernel Monaghan and Lattanzio [91] described the cubic spline kernel which has a support domain half the width of the Gaussian. The reduction in support domain came at the cost of smoothness with only the first derivative remaining continuous. Despite this, the cubic spline has become the most common kernel currently in use. Smoother kernels have been been proposed by Wendland [102] and Morris [98]; these kernels have higher continuous derivatives hoping to improve the stability and accuracy of the SPH calculations but take longer to compute than simpler kernels such as the cubic spline.

An analysis of a number of kernels was performed by Fulk [101]. A measurement of the error produced when replicating a series of functions using each kernel was compared for both ordered and disordered particles. Fulk concludes that no one kernel performs better than any other, with the cubic spline showing good levels of accuracy for both the ordered and disordered particle distributions. This lack of significant accuracy increase when using higher order kernels has also been noted by Monaghan [103]. Both Fulk and Monaghan propose that this is due to the discretisation into the particle form of the equations for practical application of the method, when this is done the errors caused by particle size and disorder are greater than those caused by the differences between the kernels and so higher order kernels only become useful as $h \to 0$.

1.2.2 Domain Boundaries and Boundary Conditions

Kernel Correction for Truncated and Non-symmetric Kernel Summations

The general formulation of the SPH method (see Table 2.2) suffers from kernel truncation in boundary regions which prevents the normalisation criterion being met. A related problem is that of particle disorder where the kernel sum can become unbalanced and violate the symmetric condition. In early SPH work, the density of a material was calculated using:

$$\rho_i = \sum_{j=0}^{j=n} m_j w\left(x_i - x_j, h\right) \tag{1.6}$$

which lead to an non-physical drop in density around material boundaries. Monaghan [90] introduced a new form of the density approximation as shown in:

$$\frac{d\rho_i}{dt} = \sum_{j=0}^{j=n} m_j \vec{v_{ij}} \cdot \nabla w \left(x_i - x_j, h\right) \tag{1.7}$$

where $\vec{v_{ij}}$ is the relative velocity between particle i and j. The kernel truncation effect is avoided due to particle density being dependant on the divergence rather than particle positions. SPH is mostly used to model the Navier-Stokes equations which are largely dependant on density because energy is calculated from the expansion and contraction of a material and pressure is calculated from the density and energy. This means that use of the continuum density equation will solve a vast majority of the boundary truncation errors. Johnson et al [104] developed a kernel gradient normalisation method that removes the effect of a truncated or non-symmetric kernel summation. The normalisation was tested by modelling the impact of metal bars (Taylor bar tests) and comparing it to a standard non-normalised SPH scheme and FEA results. Two different types of artificial viscosity were also considered, a nodal viscosity similar to artificial viscositys used in FEM and the SPH artificial viscosity of Monaghan and Gingold [105]. The non-normalised results display voids opening up in the bars but generally show greater agreement with the FEM results than the normalised kernels when Monaghan and Gingolds viscosity is used, although the normalised kernel results show greater agreement if the FEM viscosity is used. The void formation could be due to the SPH tensile instability and the results show that the instability has been reduced when using normalised kernel gradients. Randles et al [106] extended the kernel gradient normalisation to any tensor field. Bonet et al [107] included an adaptation of the kernel normalisation of Liu et al [108] developed for the reproducing kernel particle method in addition to the gradient normalisation of Johnson et al [104] with good results, but state that the method is computationally expensive and is not recommended for explicit solvers. Chen et al [109] extended and generalised the normalisation techniques to higher order derivatives. Liu et al [110] carried out an investigation into SPH shock wave modelling and compared standard non-normalised SPH with the normalisation method of Chen et al [109] and with a new discontinuous SPH formulation. The shock tube results show a significant error when the normalised kernel methods are used whilst the standard and discontinuous SPH show good agreement with

each other and exact solutions. The normalisations act to damp variations in particle position and restore a symmetric kernel summation, essentially assuming and attempting to enforce a smooth incompressible laminar flow which has a detrimental effect on shock driven processes. The proposed discontinuous formulation showed a slight improvement over standard SPH but at the cost of additional computational effort; so for weak shocks the standard SPH method seems acceptable. The shock tube modelled by Liu et al [110] has a Mach number of 1.48 calculated using:

$$M_n = \frac{|\vec{v}|}{c} \tag{1.8}$$

The Taylor bars of Johnson et al [104] have an impact velocity of 305 m/s and a material sound speed of 3600 m/s giving a Mach number of 0.08472. An approximation for a cold spray process can be made by using an impact velocity of 700 m/s and the sound speed of copper 3940 m/s to obtain a Mach number of 0.18. With the close agreement between standard and discontinuous SPH at a stronger shock than those estimated in cold spray the extra computational effort required for discontinuous calculations is unnecessary.

Boundary Conditions

The early work with SPH was focused on astrophysical problems such as large gas clouds and toy stars. There was no need for flow near rigid boundaries and little interest in flows requiring more complex boundaries such as periodic conditions. This changed when interest in applying SPH to more standard engineering CFD problems increased. Monaghan [111] proposed a repulsive force boundary that used a Leonard-Jones force acting between SPH fluid particles and fixed boundary points which acts to repel fluid particles. This is a simple and robust way to model a rigid boundary but it does have some drawbacks, firstly it can not be used to apply a Dirichlet boundary condition to the fluid. Secondly there exists a problem due to boundary roughness, the repulsive force is calculated between boundary points and the fluid particles and each point can be thought of as having a zone of influence. A particle moving parallel to the boundary will see peaks and troughs in the repulsive force as it moves between boundary points. One solution is to use boundary points with a much lower separation than the typical separation of fluid particles but this can get increasingly costly and does not completely remove the

problem. Monaghan et al [112] proposed a new repulsive force calculation that removes the roughness by calculating the repulsive force along the inward pointing normal to the boundary. This is suitable for a large range of boundary shapes but experiences problems when the inward normals cross and it becomes hard to select an appropriate direction. To further generalise the boundary force, Monaghan et al [113] proposed a radial force that is summed over a series of neighbouring boundary particles. This boundary remains reasonably smooth whilst avoiding the ambiguous direction problem.

An alternative to repulsive force boundaries is to use ghost particles as introduced by Libersky et al [114], this is a versatile approach that enables the application of various boundary conditions. As particles near the defined boundary their reflections are created across the boundary and the reflections treated as normal SPH particles with the exception of being deleted rather than included in the time integration. The effective boundary condition is set by choosing how to reflect the properties of the particles. Inverting the velocity normal to the boundary mimics the repulsive force conditions of Monaghan [111, 112, 113] whilst allowing slip parallel to the boundary. If the parallel velocity components are inverted then non-slip conditions are obtained. Ghost particles are effective when the boundary is simple, such as a straight line. For arbitrary shaped boundaries it can be challenging to correctly determine the location of reflected particles and exactly which particle should be reflected. Liu et al [115] used a boundary consisting of a combination of repulsive force and ghost particles when modelling underwater explosions because under the extreme accelerations the ghost particles alone could not contain the fluid in the domain.

Morris et al [98] used SPH particles that were not allowed to accelerate to model boundaries for low Reynolds number incompressible flows, these boundaries are refered to as dynamic boundaries. The particles are treated in all respects as normal SPH particles and repel approaching fluid particles through the acceleration equations and the density and therefore pressure increase caused by the approach of a fluid particle. The interpretation of what these boundary particles represent can lead to some ambiguity about their slip or non-slip nature and further leads to difficulties of selecting the initial properties to assign. Morris et al [98] used the particles to describe rigid boundaries enclosing Couette and Poiseuille flows and the particles were not considered to be flow particles although they were given the material properties of the flow. This has lead to

the addition of a relative velocity correction to enforce non-slip conditions between the boundary particles and the flow particles. Since the particles are given the properties of the flow and Liu et al [116] have shown that a boundary only a single particle deep is needed to model Couette and Poiseuille flows if a continuum density is used. Alternatively it could be argued that this boundary particle represents the first fluid particle attached to a rigid boundary. In this case the fixed velocity of the boundary particle represents the non-slip condition between that particle and the rigid boundary. The selection of material properties for these boundaries can be somewhat problematic if there are several different materials in the flow, particularly if they are of significantly different densities. Nevertheless these boundaries are quite robust and if used carefully can be used to constrain a flow within a domain and by fixing boundary properties apply Dirichlet boundary conditions on the flow.

Neumann boundary conditions were implemented to produce isothermal boundaries by Cleary and Monaghan [97]. They applied a sink term to a dynamic boundary to allow heat flux out of the boundary. These boundaries suffer from the same problems as standard dynamic boundaries but have the same benefits of simplicity. Ryan et al [117] fixed the sensitivity to particle disorder by applying the Neumann boundary condition over a more diffuse volume rather than a sharp boundary and provide a method to calculate the width of this zone.

1.2.3 Elastic-Plastic Materials

The ability of SPH to handle high deformations without costly re-meshing methods makes it an attractive method to model the plastic deformation of solid materials. The pioneering work was performed by Libersky et al [118] in 1991 and was formulated for three-dimensions shortly afterwards [114]. A radial return plasticity model using a fixed flow stress was used along with artificial viscosity as described by Monaghan [91] to capture shocks, a Mie-Grunisen equation of state (applicable to shock compressed solids) and a frame indifferent Jaumann rate of shear stress is employed. No instability correction was included in their work because it pre-dates Swegle's analysis [119] and later proposed corrections in the literature (see Section 1.2.4 for more details). Taylor bar and hyper-velocity impacts were calculated and shown to agree well with experiment al-

though convergence was not performed due to limited resources. A Grady-Kipp fracture model [120] was added by Benz and Asphaug [121] and used to model asteroid impacts. Although successful the authors note that the fracture model tends to under estimate the strength of a material because it is a statistical method better suited to highly cracked materials. Randles and Libersky [106] added a Johnson-Cook flow stress model and summarised developments applicable to elastic-plastic materials such as boundary handling and instability correction. They also presented results for a number of applications including bomb casing detonation and various high velocity impacts. Libersky et al [122] incorporated conservative smoothing and kernel re-normalisation to remove the tensile instability (see Section 1.2.4) and apply a contact algorithm to correct errors in interpolation around interfaces between materials of significantly different densities. Particles from particular materials only interact through the SPH equations with other particles in that material and interactions between materials are carried out by applying a boundary condition. Hoover et al [123] highlighted a problem with conservation of angular momentum and demonstrate significant errors when modelling a free rotating solid disc. Angular momentum conservation is broken by errors in the calculation of spatial velocity gradients using the SPH particle formulations. Hoover et al [123] applied a strong velocity smoothing correction following Monaghan [124] along with rescaling the velocity gradients to reduce the effect. Cleary et al [125] applied SPH to forging and casting processes. A viscous fluid model was used to investigate how liquid metals fill a mold and an elastic-plastic model including the weakly compressible equation of state and a Jaumann rate of stress was applied to problems of forging and extrusion, however, no tensile correction was described. Liu et al [126] used anisotropic kernels to better match the high flattening ratios experienced during high velocity impacts. Non-symmetric kernels were first proposed by Fulbright et al [127] where the particle smoothing length is allowed to independantly vary along each axis, these were applied to collisions of stars with extreme levels of flattening. Cleary [128] modelled lower velocity flyer/wall impacts. The velocities considered were sufficent to induce plastic flow in both the impacting solid and the target. Thin plates were used as the targets and these retained the plastic deformation caused after the impact, a Jaumann rate of stress was used along with the weakly compressible equation of state since material energies were not considered. Failure of shear panel dampers was modelled by Chen et al [129]. The method used a Jaumann rate

of stress, artificial viscosity and Monaghan's tensile correction; again material energies were not considered despite this the SPH method accurately modelled the failure of the dampers considered. There has been some early work applying SPH to cold spray splat formation and this is discussed in Section 1.2.5.

1.2.4 Stability

SPH is a very robust method and so numerical instabilities do not normally result in a failure of the model, instead the model will complete but produce physically incorrect results. Care must be taken to eliminate instabilities in order to ensure accuracy of a SPH calculation. The use of kernel functions in the SPH method introduces an instability in the equations that typically surfaces in regions of negative pressure. The instability was also encountered by Phillips and Monaghan [130] in magnetohydrodynamics problems. Early applications of SPH used equations of state that only produced positive pressures such as the ideal gas equation and so they did not suffer from the instability. It is more typical to use equations of state such as the weakly compressible or Mie-Grunisen that produce negative pressures when modelling solids, although the weakly compressible is also applied to fluids [98]. An analysis of the instability was performed by Swegle et al [119] which demonstrated that the heart of the instability is the sign change of the second derivative of the kernel and the resulting effect on the first derivative. Figure 1.9 plots the first and second derivatives of the quintic kernel (see Equation (2.32)).

Whilst the second derivative is positive the SPH method is stable in compression (positive pressure) because decreasing the distance between two particles increases the repulsive effect. Once a particle is pushed past the point where the second derivative has become negative, decreasing the distance between particles will actually reduce the repulsion which is clearly non-physical. The opposite is true for states of tension with the outer edges of the kernel producing unstable and non-physical behaviour since increasing the separation reduces the attractive force between the particles and decreasing the separation increases it, whilst the inner section (unstable for compression) is stable. The instability in a purely compressive stress model tends to be avoided due to the correct repulsion behaviour, using variable h and artificial viscosities further prevent particles entering the unstable region. The tensile case is much more prevalent because the standard

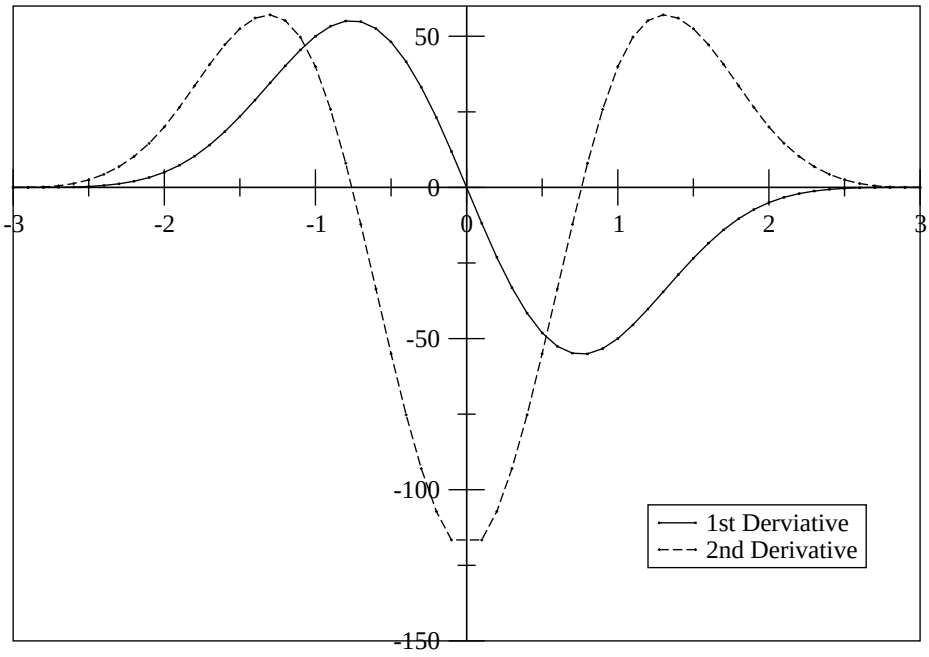

Figure 1.9: Quintic kernel derivatives.

particle separation lies in the unstable region. The instability manifests as non-physical particle clumping and can be triggered by a minor perturbation as demonstrated by Figures 1.10 and 1.11. In this example resembling that of Swegle [119], a two-dimensional copper block is deployed in tension and enclosed by a dynamic boundary, the centre particle is given a perturbation of magnitude 1×10^{-10} m/s. The particle clumping is clearly seen in Figure 3.17b.

Morris [131] suggests modifying the kernel to remove the instability, he notes however that the developed kernels tend to produce summation errors since the central particle no longer is guaranteed to have the largest weighting. In addition no general method to correct the instability is proposed, instead several different solutions are given dependant on the problem description. Randles et al [106] extended the conservative smoothing method of Wen et al [132] to multiple dimensions. Conservative smoothing effectively smooths out the velocity variations between neighbouring particles effectively increasing

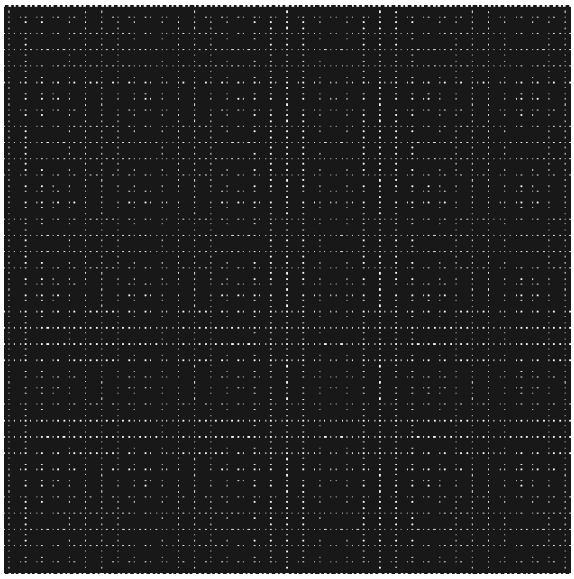

Figure 1.10: Tensile test initial condition.

dissipation. Hoover et al [123] later used Monaghan's [124] XSPH velocity smoothing to stabilise SPH calculations in a similar way. Johnson et al [104] proposed a quadratic kernel without the sign change of the second derivative, the second derivative is in fact constant. Although this serves to cure the tensile instability, the lack of higher derivatives reduces the applicability. Monaghan [133] seeking a general solution described a repulsive force acting between particles and based on the kernel itself:

$$R_{ij} f_{ij}^n \tag{1.9}$$

$$f_{ij} = \frac{w\left(\vec{r}_{ij}, h\right)}{w\left(\Delta x, h\right)} \tag{1.10}$$

which is introduced to the governing equations as an artificial pressure. The pressure acts between all particles and increases as particle separation decreases following equation 1.10 where Δx is the average initial particle spacing and n is a user selected constant that controls the strength of the force. The exact form of R_{ij} varies depending on the form chosen for the pressure terms in the energy and acceleration equations following Monaghan [133] R_{ij} is defined as:

$$R_{ij} = R_i + R_j \tag{1.11}$$

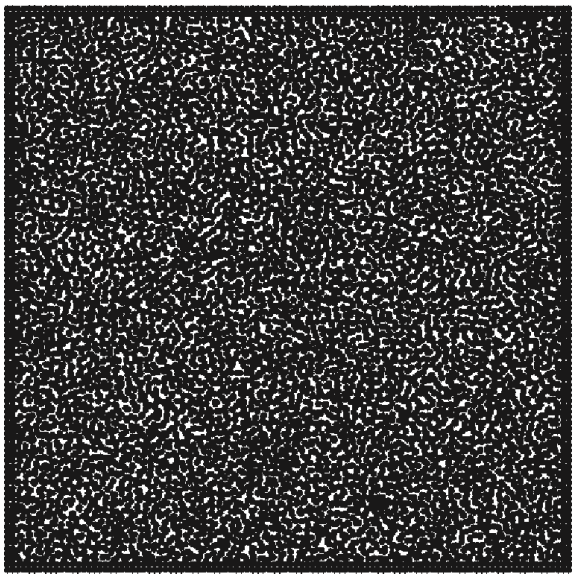

Figure 1.11: Tensile test without correction at t = 0.001716 s.

$$R_i = \frac{\epsilon p_i}{{\rho_i}^2} \tag{1.12}$$

where p_i is the pressure of particle i and ϵ is a user defined constant. R_{ij} is taken as zero unless the particle pressure is negative (a state of tension), this ensures that the force only operates in zones of instability. This correction is simple to calculate and effective at removing the instability (see Chapter 3). In addition, it can be used for a large variety of kernels and its affect is limited to areas of instability. An extension of this correction was made by Gray et al [134] where the correction was applied to the principle stresses and a XSPH velocity is used with good results.

1.2.5 SPH Application to Cold Spray

As discussed in Section 1.1, SPH has the potential to improve the models of splat formation, however, to date little work has been done in this area. Yin et al [87] performed a preliminary analysis using a three-dimensional SPH formulation, unfortunately few details were given on the equation set used and the details that are provided indicate the solid impact has instead been modelled as a viscous fluid. In addition there is no mention made of an artificial viscosity or an instability correction which puts the accuracy of the results in question. Despite these points the results show some good agreement when

compared to FEM and FV methods. This work was expanded upon by Li et al [135] and whilst this paper offers a more in-depth analysis of the cold spray process the SPH formulation appears the same as that used by Yin et al [87]. Li et al [135] state that no tensile correction was used due to the compressive nature of the impact process again there was no mention of the inclusion of an artificial viscosity. The SPH instability is not only present for tensile stresses and if the particles are allowed to approach too close to each other the compressive state becomes unstable, artificial viscosities prevent this close approach in regions experiencing strong shocks. Manap et al [136, 137] used a two-dimensional SPH formulation with the introduction of a cohesive zone model to model adhesion between the feedstock and substrate. In the general SPH formulation all particles can form pair interactions with all other particles in the problem regardless of material type. This results in material boundaries becoming undefined once particles from different materials have started interacting. This leads to problems modelling contact of separate material bodies because as soon as they are in contact the solver regards them as one material. Manap et al [136] state that they do not use a special solution for this contact condition and instead allow particles to interact via the governing equations. With this consideration it seems unnecessary to include an additional adhesive term such as the cohesive zone when material 'bonding' is already assumed by use of the general SPH formulation. SPH particles always interact if they are within the kernel support domain and so are considered one material which may have discontinuous properties. The cohesive zone model appears to suppress some features of the splat around the lip of the crater and the jet region because of the additional inter-surface traction.

1.3 Summary

The formation of a cold sprayed coating is a complex process, involving high levels of strain, plastic deformation, intense local heating and multiple successive feedstock impacts. The small scale and short duration of the impact events further complicate attempts to experimentally monitor the splat formations involved in the generation of a coating and so modelling represents the best method to increase understanding in this area. Currently the finite element method is most commonly used, despite being poorly suited to strains of the magnitude experienced during coating formation. The smoothed

particle hydrodynamics method can cope with these strains with ease whilst retaining the benefits of a Lagrangian method, and early work has shown its promise for enhancing the understanding of cold spray processes. The current work will extend the existing SPH models of cold spray by improving on solution stability and effciency in three-dimensions. Heat conduction terms will be added and a proper investigation into the effects of applied boundary conditions will be conducted. A new zero impedance boundary is described for efficiently modelling infinite domains. A novel method of predicting coating adhesion from modelling results alone is proposed and the potential for modelling entire coating formations is discussed and demonstrated.

1.4 Aims and Objectives

The current work aims to improve capabilities for modelling cold spray splat and coating formation, in order to enable greater control of the final coating properties from controllable spray parameters such as velocity and temperature. The key objectives of this study are listed below:

1. A multi-thread capable Smoothed Particle Hydrodynamics solver is to be developed.

2. The solver must be capable of modelling gases, viscous fluids and elastic-plastic solids in three-dimensions.

3. Additional models of heat conduction are to be included along with work hardening and thermal softening of elastic-plastic materials.

4. The accuracy of the developed solver is to be validated and its performance benchmarked before a study of the cold spray process is undertaken.

5. Boundary conditions for modelling infinite domains are to be tested for applicability to models of single splat morphology.

6. The effects of varying initial feedstock velocity, size and temperature are to be investigated.

7. Both adiabatic and heat conductive splat models are to be compared and the most applicable model selected.

8. Multiple simultaneous feedstock impacts will be considered to demonstrate the developed solver capabilties.

Chapter 2

Methodology

2.1 General Formulation

The particles in a SPH model are used as interpolation points field variable values. Where the governing equations are formulated over a discrete set of particles using a kernel function to weight the particle interactions. In a continuous space a function, f, is described in SPH as:

$$f(x) = \int_v f(x') \, \delta(x - x') \, dx' \tag{2.1}$$

where δ is the Dirac delta:

$$\delta(x - x') = \begin{cases} \infty & x = x' \\ 0 & x \neq x' \end{cases} \tag{2.2}$$

Since the Dirac delta has point support Equation (2.1) provides the exact value of $f(x)$ but is of limited use because it requires the evaluation of $f(x)$. In order to approximate the function using neighbouring particle data the Dirac delta is replaced by a bell shaped kernel function, w:

$$f(x) = \int_v f(x') \, w(x - x', h) \, dx' \tag{2.3}$$

where h is the smoothing length used to control the width of the kernel. In contrast to the Dirac delta these kernel functions are compactly supported with a width of kh, where k is a property of the kernel that depends on the piecewise function used to describe it, for

example, the cubic spline (Equation (2.30) consists of two piecewse equations and $k = 2$. The kernel support domain is set to encompass a number of surrounding particles and so changes the exact value of f obatained from Equation (2.1) to an estimate utilising local field variable values.

Similarly, the spatial gradient of a function, $\nabla f(x)$, can be estimated using the kernel via:

$$\nabla_x f(x) = \int_v \nabla_{x'} f(x') w(x - x', h) dx' \tag{2.4}$$

It would be helpful to be able to approximate $\nabla f(x')$ without needing specific information about the function gradient. This can be performed by applying the product rule:

$$\nabla(\psi\phi) = \phi\nabla\psi + \psi\nabla\phi \tag{2.5}$$

where $\psi = f(x')$ and $\phi = w(x - x', h)$ to give:

$$\int_v \nabla_{x'} f(x') w(x - x', h) dx' = \int_v \nabla_{x'} [f(x') w(x - x', h)] dx' - \int_v f(x') \nabla_{x'} w(x - x', h) dx' \tag{2.6}$$

Applying Gauss' theorem to the first integral on the left hand side of Equation (2.6) to convert the volume integral into a flux across the surface of the considered volume:

$$\int_v \nabla_{x'} f(x') w(x - x', h) dx' = \int_s [f(x') w(x - x', h)] \cdot \vec{n} dx' - \int_v f(x') \nabla_{x'} w(x - x', h) dx' \tag{2.7}$$

the compact kernel support requires the kernel to equate to zero on this surface further reducing Equation (2.7) to:

$$\int_v \nabla_{x'} f(x') w(x - x', h) dx' = -\int_v f(x') \nabla_{x'} w(x - x', h) dx' \tag{2.8}$$

The kernel gradient in Equation (2.8) is taken with respect to the neighbour particle, to maintain consistancy with the function approximation (see Equation (2.3)) where kernel weights are calculated with respect to the centre particle this gradient should be taken

wih respect to the centre particle as well. This is done by exploiting kernel symmetry such that:

$$\nabla_x w\left(x-x',h\right)=-\nabla_{x'} w\left(x-x',h\right) \tag{2.9}$$

$$\nabla_x f\left(x\right)=\int_v f\left(x'\right)\nabla_x w\left(x-x',h\right)dx' \tag{2.10}$$

However, this form of the SPH derivative will not always return a zero gradient for a constant field in cases of disordered particle arrangments. There are various forms of this derivative that correctly capture a constant field and each can be obtained by selecting a different value of ϕ as described by Monghan [103] which is a rearrangement of the product rule, given by:

$$\nabla f\left(x\right)=\frac{1}{\phi}\left\{\nabla\left[f\left(x\right)\phi\right]-f\left(x\right)\nabla\phi\right\} \tag{2.11}$$

In integral form this becomes

$$\nabla f\left(x\right)=\frac{1}{\phi}\int_v f\left(x'\right)\phi\nabla w\left(x-x',h\right)dx'-\frac{f\left(x\right)}{\phi}\int_v \phi\nabla w\left(x-x',h\right)dx' \tag{2.12}$$

With $\phi=1$, the SPH derivative becomes:

$$\nabla f\left(x\right)=-\int_v\left[f\left(x\right)-f\left(x'\right)\right]\nabla w\left(x-x',h\right)dx' \tag{2.13}$$

For a constant field the $f\left(x\right)$ and $f\left(x'\right)$ terms cancel ensuring a zero gradient. Although other values of ϕ can be chosen Equation (2.13) will be used for the rest of this section to keep the derivations tidy.

To model physical processes such as viscous drag or heat conduction, second derivatives are also required. Equation (2.10) suggests it is possible to use the second derivative of the kernel to approximate these, however, the results are highly sensitive to particle positions and can be quite unstable (see Section 1.2.4). Several alternative solutions to obtaining second derivatives have been used in the literature. Flebbe et al [93] and Watkins et al [94] used a nested set of first derivative estimates as shown:

$$\int_v \left[\nabla^2 f(x')\right] w(x-x',h)\,dx' =$$

$$-\int_v \left\{ \int_v \left[f(x)-f(x')\right]\cdot\nabla w(x-x',h)\,dx' \right\} \nabla w(x-x',h)\,dx' \quad (2.14)$$

This is very costly because an additional calculation over the kernel support domain is required, the double approximation also reduces the overall accuracy. An alternative approach is to directly approximate the second derivative by recognising that $\nabla^2 f(x) = \nabla\cdot[\nabla f(x)]$. Equation (2.12) can then to used to calculate the gradient of $\nabla f(x)$ but the repeated summation seen in Equation (2.14) is avoided by application of a Taylor expansion to estimate the first derivative. This process is now demonstrated by taking $\phi = 1$ in Equation (2.12) for simplicity:

$$\nabla\cdot[\nabla f(x)] = -\int_v [\nabla f(x)-\nabla f(x')]\cdot\nabla w(x-x',h)\,dx' \quad (2.15)$$

In order to avoid a costly second integration, estimates of $\nabla f(x)$ and $\nabla f(x')$ are required. First the substitution:

$$\nabla w(x-x',h) = \nabla w(|x-x'|,h)\cdot\vec{e}_{x,x'} \quad (2.16)$$

where

$$\vec{e}_{x,x'} = \frac{x-x'}{|x-x'|} \quad (2.17)$$

is made which after rearrangement produces:

$$\nabla\cdot[\nabla f(x)] = \int_v [\nabla f(x)\cdot\vec{e}_{x,x'} - \nabla f(x')\cdot\vec{e}_{x,x'}]\nabla w(|x-x'|,h)\,dx' \quad (2.18)$$

$\nabla f(x)$ and $\nabla f(x')$ can be estimated using Taylor expansions and multiplied by $\vec{e}_{x,x'}$ to produce:

$$\nabla f(x)\cdot\vec{e}_{x,x'} = \frac{f(x)-f(x')}{|x-x'|} \quad (2.19)$$

$$-\nabla f\left(x'\right)\cdot\vec{e}_{x,x'}=\frac{f\left(x\right)-f\left(x'\right)}{\left|x-x'\right|} \tag{2.20}$$

When Equations (2.19) and (2.20) are substituted into Equation (2.18) the second derivative approximation of a function is obtained:

$$\nabla\cdot\left(\nabla f\left(x\right)\right)=-2\int_{v}\frac{\left[f\left(x\right)-f\left(x'\right)\right]}{\left|x-x'\right|}\nabla w\left(\left|x-x'\right|,h\right)dx' \tag{2.21}$$

The continuous equations for approximating a function and its first two derivatives are summarised in Table 2.1

	SPH continuous approximation
$f\left(x\right)$	$\int_{v} f\left(x'\right)w\left(x-x',h\right)dx'$
$\nabla f\left(x\right)$	$-\int_{v}\left[f\left(x\right)-f\left(x'\right)\right]\nabla w\left(x-x',h\right)dx'$
$\nabla^{2}f\left(x\right)$	$-2\int_{v}\frac{\left[f(x)-f(x')\right]}{\left\|x-x'\right\|}\nabla w\left(\left\|x-x'\right\|,h\right)dx'$

Table 2.1: Summary of continuous SPH approximations.

The continuous SPH approximations formulated for calculation over a set of discrete particles are shown in Table 2.2, where m is particle mass and ρ is particle density, the particle volume $\frac{m}{\rho}$ replaces the infinitesimal volume dx in the continuous integral from. Calculations are performed for each particle over a set of neighbouring particles which is determined by the kernel support domain. In the following equations subscripts will be used to differentiate the particles in a calculation, i will denote the particle the calculation is being performed for, j indicates a neighbouring particle to i and n is the number of neighbours. It is important to note that a particle is considered to neighbour itself. The determination of neighbour sets is discussed in Section 2.3.2.

This form of the SPH equations suffers some additional error over the continuous form because the normalisation criterion is no longer exactly met due to the summation forming a numerical estimate to the exact integral. This can be thought of in terms of the rectangle or trapezium method of estimating an integral. As the number of rectangles used decreases the accuracy of the approximation decreases, this is the same effect as using less particles in the summation. If the SPH particles are disordered then it is also

	SPH discrete approximation
$f(x_i)$	$\sum_{j=0}^{j=n}\left(\frac{m_j}{\rho_j}\right) f(x_j)\, w(x_i - x_j, h)$
$\nabla f(x_i)$	$-\sum_{j=0}^{j=n}\left(\frac{m_j}{\rho_j}\right) [f(x_i) - f(x_j)]\, \nabla w(x_i - x_j, h)$
$\nabla^2 f(x_i)$	$-2\sum_{j=0}^{j=n}\left(\frac{m_j}{\rho_j}\right) \frac{[f(x_i)-f(x_j)]}{\lvert x_i - x_j\rvert} \nabla w(\lvert x_i - x_j\rvert, h)$

Table 2.2: Summary of discrete SPH approximations.

possible for the symmetric condition to be broken. The methods used to correct kernel truncation errors can also be used to enforce normalisation even for non truncated kernels (see Section 1.2.2).

2.1.1 Errors in the SPH interpolation

Assesment of the errors inherent in the SPH method is complex there are two influencing factors that produce competing requirements for accuracy. The continuous space description of the method states that exact solutions are gained if the Dirac delta function is used, use of kernel functions with larger support domains degrades this accuraccy as they depart further from the delta function however. A taylor expansion of $f(x')$ around x in the continuous space approximation of a function (see Equation (2.3)) up to second order produces:

$$\begin{aligned} f(x) = f(x) \int_v w(x - x', h)\, dx' \\ + \nabla f(x) \int_v (x - x')\, w(x - x', h)\, dx' \\ + \nabla^2 f(x) \int_v (x - x')^2 w(x - x', h)\, dx' \end{aligned} \tag{2.22}$$

Applying the identities

$$\int_v w(x - x', h)\, dx' = 1 \tag{2.23}$$

and

$$\int_v (x - x') \, w \, (x - x', h) \, dx' = 0 \tag{2.24}$$

results in:

$$f \, (x) = f \, (x) + \nabla^2 f \, (x) \int_v (x - x')^2 w \, (x - x', h) \, dx' \tag{2.25}$$

More terms could be included in the Taylor expansions without affecting the conclusions because all odd power terms equate to zero leaving only even terms of which the second order terms are the most significant. The errors in the continuous space approximation are therefore:

$$f \, (x) = f \, (x) + O(h^2) \tag{2.26}$$

This prediction of error applies only in continous space or as $h \to 0$ in the discrete formulation. The errors in the discrete formulation are hard to determine analytically because they depend strongly on the extent of particle disorder. In general SPH particles niether conform to an ordered grid nor do they assume completely random distributions, instead their arrangment is closely tied to the dynamics of the problem considered. Monaghan [103] states that the best way to assess errors is to perform carefully selected verification tests and compare the results with known solutions. The discrete errors can be understood as similar to those present in rectangle method approximations to integrals. The accuraccy of these approximations increases with the addition of more intervals, corrosponding to including more SPH particles in the summations. The number of particles involved in the summation is increased by increasing the smoothing length, h. This conflicts with the error estimate given in Equation (2.26) which states that errors increase as h increases, further complicating the error analysis and reinforcing the need for careful model verification.

2.1.2 Kernels

The criteria a kernel function has to meet have been described in Section 1.2.1 There are many kernels in use across the literature some of which will be described here. Lucy [89] used the narrow kernel function:

$$\vec{W}_{ij} = \alpha_c \begin{cases} \left[1 + 3\left(\frac{|\vec{r}_{ij}|}{h_{ij}}\right)\right]\left[1 - \left(\frac{|\vec{r}_{ij}|}{h_{ij}}\right)\right]^3 & : 0 \leq \frac{|\vec{r}_{ij}|}{h_{ij}} \leq 1 \\ 0 & : 1 < \frac{|\vec{r}_{ij}|}{h_{ij}} \end{cases} \tag{2.27}$$

the normalisation factors for which are given by:

$$\alpha_l = \begin{cases} \frac{5}{4h} & : \text{one-dimensional} \\ \frac{5}{\pi h^2} & : \text{two-dimensional} \\ \frac{105}{16\pi h^3} & : \text{three-dimensional} \end{cases} \tag{2.28}$$

the normalisation factors are chosen to enforce the normalisation criterion for the corresponding dimensionality. This kernel function has a small support domain which reduces the number of nearest neighbours and therefore the accuracy of any calculations using it. Typical values of h are taken over the range of $1.1\Delta x$ to $1.3\Delta x$ so this kernel effectively samples one particle separation in any coordinate direction.

In contrast Gingold, and Monaghan [88] used the Gaussian kernel:

$$w\left(x - x', h\right) = \left(\frac{1}{\pi h^2}\right)^{\frac{3}{2}} \exp\left(\frac{-(x - x')^2}{h^2}\right) \tag{2.29}$$

which is not compactly supported although the values become negligible, resulting in an accurate but inefficient approximation. The cubic spline introduced by Monaghan and Lattanzio [91] is the most widely used:

$$\vec{W}_{ij} = \alpha_c \begin{cases} \frac{2}{3} - \left(\frac{|\vec{r}_{ij}|}{h_{ij}}\right)^2 + \frac{1}{2}\left(\frac{|\vec{r}_{ij}|}{h_{ij}}\right)^3 & : 0 \leq \frac{|\vec{r}_{ij}|}{h_{ij}} < 1 \\ \frac{1}{6}\left(2 - \left(\frac{|\vec{r}_{ij}|}{h_{ij}}\right)\right)^3 & : 1 \leq \frac{|\vec{r}_{ij}|}{h_{ij}} < 2 \\ 0 & : 2 \leq \frac{|\vec{r}_{ij}|}{h_{ij}} \end{cases} \tag{2.30}$$

where

$$\alpha_c = \begin{cases} \frac{1}{h} & : \text{one-dimensional} \\ \frac{15}{7\pi h^2} & : \text{two-dimensional} \\ \frac{3}{2\pi h^3} & : \text{three-dimensional} \end{cases} \tag{2.31}$$

It balances efficiency and accuracy whilst giving a continuous second derivative, support domain of $2h$ and remains positive throughout its support domain. The quintic spline:

$$\vec{W}_{ij} = \alpha_q \begin{cases} \left(3 - \frac{|\vec{r}_{ij}|}{h_{ij}}\right)^5 - 6\left(2 - \frac{|\vec{r}_{ij}|}{h_{ij}}\right)^5 + 15\left(1 - \frac{|\vec{r}_{ij}|}{h_{ij}}\right)^5 & : 0 \leq \frac{|\vec{r}_{ij}|}{h_{ij}} < 1 \\ \left(3 - \frac{|\vec{r}_{ij}|}{h_{ij}}\right)^5 - 6\left(2 - \frac{|\vec{r}_{ij}|}{h_{ij}}\right)^5 & : 1 \leq \frac{|\vec{r}_{ij}|}{h_{ij}} < 2 \\ \left(3 - \frac{|\vec{r}_{ij}|}{h_{ij}}\right)^5 & : 2 \leq \frac{|\vec{r}_{ij}|}{h_{ij}} < 3 \\ 0 & : 3 \leq \frac{|\vec{r}_{ij}|}{h_{ij}} \end{cases} \tag{2.32}$$

$$\alpha_q = \begin{cases} \frac{120}{h} & : \text{one-dimensional} \\ \frac{7}{478\pi h^2} & : \text{two-dimensional} \\ \frac{3}{359\pi h^3} & : \text{three-dimensional} \end{cases} \tag{2.33}$$

is a smoother kernel and is therefore less sensitive to particle disorder but the extended support domain of $3h$ increases the number of nearest neighbours and significantly increases computational time over the cubic spline. Some authors have attempted to correct the instability (see Section 1.2.4) by altering the kernel itself. Johnson et al [104] proposed a quadratic kernel:

$$\vec{W}_{ij} = \begin{cases} \frac{1}{\pi {h_{ij}}^2}\left[\frac{3}{8}\left(\frac{|\vec{r}_{ij}|}{h_{ij}}\right)^2 - \frac{3}{2}\left(\frac{|\vec{r}_{ij}|}{h_{ij}}\right) + \frac{3}{2}\right] & : 1 \leq \frac{|\vec{r}_{ij}|}{h_{ij}} \leq 2 \\ 0 & : 2 < \frac{|\vec{r}_{ij}|}{h_{ij}} \end{cases} \tag{2.34}$$

for two-dimensions that removes the compressive instability but does not solve the tensile instability, further the kernel lacks a useful second derivative.

2.2 Governing Equations

2.2.1 Equations of Motion

The Cauchy equation of motion is used to calculate the material flow. Momentum excluding external forces is given by the Lagrangian derivative:

$$\frac{d\vec{v}}{dt} = \frac{1}{\rho}\frac{d\sigma}{d\vec{x}} \tag{2.35}$$

where $\vec{v}$ is velocity, t is time, ρ is mass density and the Cauchy stress tensor, σ is given by:

$$\sigma^{\alpha\beta} = -p\delta^{\alpha\beta} + \tau^{\alpha\beta} \tag{2.36}$$

where p is the pressure and δ is the identity matrix, α and β indicate the tensor dimensions, the exact formulation of the stress tensor depends on whether a solid or fluid is being modelled (see Section 2.2.3).

The continuity equation is obtained from the material derivative and mass conservation law, given by:

$$\frac{d\rho}{dt} = -\rho\nabla \cdot \vec{v} \tag{2.37}$$

The thermodynamic energy per unit mass (this will simply be referred to as energy), inclusive of conductive terms is given by:

$$\frac{d\vec{E}}{dt} = \frac{\sigma^{\alpha\beta}}{\rho}\frac{d\vec{v}^{\alpha}}{d\vec{x}^{\beta}} + \frac{1}{\rho}\nabla \cdot (k\nabla T) \tag{2.38}$$

where k is the thermal conductivity and T is the temperature in Kelvin.

These equations need to be cast in the discrete SPH form, this is performed by application of Equation (2.11). In the previous discussion ϕ was taken as 1 to simplify to following derivations, at this point it is necessary to examine the exact value this constant should take. To do this, the derivation of the Cauchy equation of motion (see Equation (2.35)) in SPH form is considered. For simplicity, only the pressure terms:

$$\frac{d\vec{v_p}}{dt} = \frac{1}{\rho}\frac{d\,(-p)}{d\vec{x}} \tag{2.39}$$

are considered, the derivation of the full viscous equation is treated later. Taking $\phi = 1$ produces the SPH gradient approximation shown in Equation (2.13). Applying this to the pressure gradient in Equation (2.39) and converting to the discrete formulation gives:

$$\frac{dp}{d\vec{x}} = -\sum_{j=0}^{j=n}\left(\frac{m_j}{\rho_j}\right)(p_i - p_j)\,\nabla w\,(x_i - x_j, h) \tag{2.40}$$

This equation does not conserve momentum correctly however because for an interaction between two particles:

$$\frac{m_j}{\rho_j} = \frac{m_i}{\rho_i} \tag{2.41}$$

is not always satisfied, particles could have different masses or densities and therefore calculate different rates from the same interaction, breaking conservation. A symmetric

momentum equation is therefore required to ensure momentum conservation. If $\phi = \frac{1}{\rho}$ the integral approximation of a function gradient is:

$$\nabla f(x) = \rho(x) \left\{ \int_V \frac{f(x')}{\rho(x')} \left[\nabla w(x - x', h)\right] dx' - f(x) \int_v \frac{1}{\rho(x')} \left[\nabla w(x - x', h)\right] dx' \right\} \tag{2.42}$$

which can be cast in discrete form and used to approximate $\frac{d(-p)}{d\vec{x}}$ to produce:

$$\frac{d(-p)}{d\vec{x}} = \rho_i \left\{ -\sum_{j=0}^{j=n} \left[\frac{p_j}{{\rho_j}^2} m_j \nabla w(x_i - x_j, h) \right] + p_i \sum_{j=0}^{j=n} \left[\frac{m_j}{{\rho_j}^2} \nabla w(x_i - x_j, h) \right] \right\} \tag{2.43}$$

By inspection, it can be seen that a symmetric equation will not be obtained when the summations are combined becuase the mass and density only of the interacting particles is taken into consideration. Alternatively, the second integral on the RHS of Equation (2.42) is an approximation of:

$$\nabla \left(\frac{1}{\rho} \right) \tag{2.44}$$

Applying the reciprocal rule to Equation (2.44), converting to the SPH integral representation and substituting the result back into Equation (2.42) yields the following derivative:

$$\nabla f(x) = \rho(x) \left\{ \int_V \frac{f(x')}{\rho(x')} \left[\nabla w(x - x', h)\right] dx' + \frac{f(x)}{{\rho(x)}^2} \int_v \rho(x') \left[\nabla w(x - x', h)\right] dx' \right\} \tag{2.45}$$

which can be used to estimate Equation (2.39) resulting in:

$$\frac{d\vec{v}}{dt} = \left\{ -\sum_{j=0}^{j=n} \left[\frac{p_j}{{\rho_j}^2} m_j \nabla w(x_i - x_j, h) \right] - \sum_{j=0}^{j=n} \left[\frac{p_i}{{\rho_i}^2} m_j \nabla w(x_i - x_j, h) \right] \right\} \tag{2.46}$$

The complete pressure equation is obtained by combining the summations to give:

$$\frac{d\vec{v}}{dt} = -\sum_{j=0}^{j=n} \left(\frac{p_i}{{\rho_i}^2} + \frac{p_j}{{\rho_j}^2} \right) m_j \nabla w(x_i - x_j, h) \tag{2.47}$$

Note that from Equation (2.46), this SPH approximation only conserves momentum if a single particle mass is used throughout a problem. With this constraint on the particle masses used in a problem the SPH derivative shown in Equation (2.45) results in correct conservation and so will be used in the current work. The viscous terms of the momentum equation (Equation 2.48) are derived as follows:

$$\frac{d\vec{v_v}}{dt} = \frac{1}{\rho}\frac{d\tau}{d\vec{x}} \tag{2.48}$$

Applying Equation (2.42) to the shear stress gradient in Equation (2.48) and converting to the discrete form produces:

$$\frac{d\tau}{d\vec{x}} = \rho_i \left\{ \sum_{j=0}^{j=n} \left[m_j \nabla w \left(x_i - x_j, h \right) \frac{\tau_j}{{\rho_j}^2} \right] + \sum_{j=0}^{j=n} \left[m_j \nabla w \left(x_i - x_j, h \right) \frac{\tau_i}{{\rho_i}^2} \right] \right\} \tag{2.49}$$

Substituting Equation (2.49) into Equation (2.48) gives the rate of change of momentum due to viscous forces:

$$\frac{1}{\rho_i}\frac{d\tau}{d\vec{x}} = \sum_{j=0}^{j=n} m_j \nabla w \left(x_i - x_j, h \right) \left(\frac{\tau_j}{{\rho_j}^2} + \frac{\tau_i}{{\rho_i}^2} \right) \tag{2.50}$$

Finally, Equations (2.47) and (2.50) are combined to complete the momentum equation, yielding:

$$\frac{d\vec{v_i}}{dt} = -\sum_{j=0}^{j=n} \left(\frac{p_i}{{\rho_i}^2} + \frac{p_j}{{\rho_j}^2} \right) m_j \nabla w \left(x_i - x_j, h \right) + \sum_{j=0}^{j=n} m_j \nabla w \left(x_i - x_j, h \right) \left(\frac{\tau_j}{{\rho_j}^2} + \frac{\tau_i}{{\rho_i}^2} \right) \tag{2.51}$$

The SPH form of the energy equation is derived in a similar fashion as used for the momentum equation. The volumetric and deviatoric components of the stress tensor (see Equation (2.36)) will be treated separately before being combined into the final energy equation. The volumetric or pressure terms that result from tension and compression of the material (the trace of the strain rate tensor) are derived in SPH form from:

$$\frac{dE_p}{dt} = \frac{-p\delta^{\alpha\beta}}{\rho}\frac{d\vec{v}^{\alpha}}{d\vec{x}^{\beta}} \tag{2.52}$$

Seeking a similar form to the the momentum equation, the product rule is applied to the RHS of Equation (2.52) to give:

$$\frac{-p}{\rho}\frac{d\vec{v}}{d\vec{x}} = \vec{v}\frac{d\frac{-p}{\rho}}{d\vec{x}} - \frac{d\frac{-p\vec{v}}{\rho}}{d\vec{x}} \tag{2.53}$$

Applying Equation (2.10) to each of the gradients in Equation (2.53) and converting them to the discrete form yields:

$$\frac{dE_p}{dt} = \sum_{j=0}^{j=n} \frac{p_j}{{\rho_j}^2} m_j \left(\vec{v_i} - \vec{v_j}\right) \cdot \nabla w \left(x_i - x_j, h\right) \tag{2.54}$$

This is clearly not symmetric for a particle pair interaction and so energy will not be conserved. Following Monaghan [90] conservation is enforced by averaging the energy equation across the interaction pair. This produces the pressure terms of the SPH energy equation:

$$\frac{dE_{p,i}}{dt} = 0.5 \sum_{j=0}^{j=n} \left(\frac{p_i}{{\rho_i}^2} + \frac{p_j}{{\rho_j}^2}\right) m_j \left(\vec{v_i} - \vec{v_j}\right) \cdot \nabla w \left(x_i - x_j, h\right) \tag{2.55}$$

The deviatoric or viscous terms of the energy equation are:

$$\frac{dE_v}{dt} = \frac{\tau^{\alpha\beta}}{\rho}\dot{\epsilon}^{\alpha\beta} \tag{2.56}$$

where $\dot{\epsilon}^{\alpha\beta}$ is the traceless strain rate given by

$$\dot{\epsilon}^{\alpha\beta} = 0.5\left(\nabla_\beta \vec{v}^\alpha + \nabla_\alpha \vec{v}^\beta\right) - \frac{1}{3}\delta^{\alpha\beta}\nabla \cdot \left(\vec{v}\right) \tag{2.57}$$

The exact form of τ depends on whether a solid or fluid is modelled and is discussed in detail in Section 2.2.3. The viscous energy contribution is thus:

$$\frac{dE_{v,i}}{dt} = \frac{{\tau^{\alpha\beta}}_i : \dot{\epsilon}_i^{\alpha\beta}}{\rho_i} \tag{2.58}$$

The conductive energy terms (see Equation (2.38) require a modification of the SPH second derivative identity Equation (2.21) to include thermal conductivity, k. This is performed by applying the following identity:

$$\nabla \cdot (\phi \nabla \psi) = \phi \nabla^2 \psi + \nabla \phi \cdot \nabla \psi \tag{2.59}$$

to the conductive terms in Equation (2.38) to produce:

$$\frac{1}{\rho}\left[\nabla\cdot(k\nabla T)\right]=\frac{1}{\rho}\left(k\nabla^2 T+\nabla k\cdot\nabla T\right) \tag{2.60}$$

The SPH formulation for a second derivative can be applied to the $k\nabla^2 T$ terms above. However in order to maintain consistency with the other governing equations and ensure conservation, the second derivative will be reformulated by taking $\phi=\frac{1}{\rho}$ in Equation (2.12), which results in:

$$\nabla\cdot(\nabla f_i(x))=\rho_i\sum_{j=0}^{j=n}\left[\frac{f_{ij}(x)}{{\rho_i}^2}+\frac{f_{ij}(x)}{{\rho_j}^2}\right]m_j\left[\frac{|\nabla w(x_i-x_j,h)|}{|\vec{x}_{ij}|}\right] \tag{2.61}$$

where

$$f_{ij}(x)=f_i(x)-f_j(x) \tag{2.62}$$

and $f_i(x)$ and $f_j(x)$ are the evalutaion of the function $f(x)$ at particles i and j. In the current work, the kernel function does not return the magnitude of the kernel gradient. It is therefore desirable to express the bracket containing the kernel magnitude in terms of the gradient components as follows:

$$\nabla\cdot(\nabla f_i(x))=\rho_i\sum_{j=0}^{j=n}\left[\frac{f_{ij}(x)}{{\rho_i}^2}+\frac{f_{ij}(x)}{{\rho_j}^2}\right]m_j\left[\frac{\nabla w(x_i-x_j,h)\cdot\vec{x}_{ij}}{\vec{x_{ij}}\cdot\vec{x}_{ij}}\right] \tag{2.63}$$

Applying Equation (2.63) to the second derivative term in Equation (2.60) and Equation (2.45) to the first derivatives produces the SPH heat conduction equation:

$$\begin{aligned}\frac{1}{\rho}\left(k\nabla^2 T+\nabla k\cdot\nabla T\right)=&k_i\sum_{j=0}^{j=n}\left(\frac{T_{ij}}{{\rho_i}^2}+\frac{T_{ij}}{{\rho_j}^2}\right)m_j\left[\frac{\nabla w(x_i-x_j,h)\cdot\vec{x}_{ij}}{\vec{x_{ij}}\cdot\vec{x}_{ij}}\right]\\&+\sum_{j=0}^{j=n}m_j\left(\frac{k_j}{{\rho_j}^2}+\frac{k_i}{{\rho_i}^2}\right)\nabla w(x_i-x_j,h)\\&\cdot\sum_{j=0}^{j=n}m_j\left(\frac{T_j}{{\rho_j}^2}+\frac{T_i}{{\rho_i}^2}\right)\nabla w(x_i-x_j,h)\end{aligned} \tag{2.64}$$

The full energy rate equation is obtained by combining equations (2.55), (2.58) and (2.64).

The temperature of a given particle is calculated from its energy per unit mass using:

$$T_i = T_{0,i} + \left(\frac{E_i - E_{0,i}}{C_{v,i}} \right) \tag{2.65}$$

where C_v is the specific heat, E_0 is initial energy and T_0 is initial temperature. The density rate is derived from Equation (2.37). To maintain consistency in the governing equations the density is placed inside the gradient terms by application of the product rule

$$-\rho \nabla \vec{v} = \nabla \left(-\rho \vec{v} \right) - \vec{v} \nabla - \rho \tag{2.66}$$

and are converted to the discrete SPH from and the summations combined to produce the particle density rate:

$$\frac{d\rho_i}{dt} = \sum_{j=0}^{j=n} \left(\vec{v}_i - \vec{v}_j \right) m_j \nabla w \left(x_i - x_j, h \right) \tag{2.67}$$

The constraint of constant particle mass throughout a problem is used and so this form of continuum density conserves SPH particle volume and density.

The full equation set for momentum, energy and mass conservation is summarised below:

Momentum

$$\frac{d\vec{v_i}}{dt} = -\sum_{j=0}^{j=n} \left(\frac{p_i}{{\rho_i}^2} + \frac{p_j}{{\rho_j}^2} \right) m_j \nabla w \left(x_i - x_j, h \right) + \sum_{j=0}^{j=n} m_j \nabla w \left(x_i - x_j, h \right) \left(\frac{\tau_j}{{\rho_j}^2} + \frac{\tau_i}{{\rho_i}^2} \right) \tag{2.68}$$

Energy

$$\begin{aligned} \frac{dE}{dt} = 0.5 \sum_{j=0}^{j=n} \left(\frac{p_i}{{\rho_i}^2} + \frac{p_j}{{\rho_j}^2} \right) m_j \left(\vec{v_i} - \vec{v_j} \right) \cdot \nabla w \left(x_i - x_j, h \right) \\ + k_i \sum_{j=0}^{j=n} \left(\frac{T_{ij}}{{\rho_i}^2} + \frac{T_{ij}}{{\rho_j}^2} \right) m_j \left(\frac{\nabla w \left(x_i - x_j, h \right) \cdot \vec{x}_{ij}}{\vec{x_{ij}} \cdot \vec{x}_{ij}} \right) \\ + \sum_{j=0}^{j=n} m_j \left(\frac{k_j}{{\rho_j}^2} + \frac{k_i}{{\rho_i}^2} \right) \nabla w \left(x_i - x_j, h \right) \cdot \sum_{j=0}^{j=n} m_j \left(\frac{T_j}{{\rho_j}^2} + \frac{T_i}{{\rho_i}^2} \right) \nabla w \left(x_i - x_j, h \right) \end{aligned} \tag{2.69}$$

Mass Conservation

$$\frac{d\rho_i}{dt} = \sum_{j=0}^{j=n} \left(\vec{v}_i - \vec{v}_j \right) m_j \nabla w \left(x_i - x_j, h \right) \tag{2.70}$$

2.2.2 Artificial Corrections

The SPH equations developed in Section 2.2.1 represent the Navier-Stokes equations and is used to model material flow. There are however some numerical considerations required when utilising SPH to model cold spray splat formation. The instability described in Section 1.2.4 is foremost of these since the current work is concerned with solid mechanics and uses equations of state that produce negative pressures. The correction proposed by Monaghan [133] is used and the artificial stresses are included in both the energy and momentum equations in areas of tension. The weakly compressible equation of state was used by Monaghan [133] and Gray [134] and so they only applied the artificial stress to the momentum equation as this equation of state depends only on particle densities and sound speeds. The Mie-Grunisen equation of state is used in the current work however and this depends on the particles energy in addition to the state of compression. This requires that the tensile correction is added to the pressure terms of the energy equation; to ensure momentum and energy evolve with respect to the same state of stress. With the instability correction included, the momentum equation becomes:

$$\frac{d\hat{\vec{v}_i}}{dt} = \frac{d\vec{v_i}}{dt} + \sum_{j=0}^{j=n} \zeta f_{ij} \left(\frac{P_i}{\rho_i^2} + \frac{P_j}{\rho_j^2} \right) m_j \nabla \vec{W}_{ij} - \sum_{j=0}^{j=n} \zeta f_{ij} \left(\frac{\tau_j}{\rho_j^2} + \frac{\tau_i}{\tau_i^2} \right) m_j \nabla \vec{W}_{ij} \tag{2.71}$$

where

$$f_{ij} = \left(\frac{\vec{w}_{ij}(\vec{r}_{ij})}{\vec{w}_{ij}(\vec{r}_0)} \right)^n \tag{2.72}$$

and describes a repulsive force that increases as particles approach each other. The artificial stress is also included in the energy evolution in a similar manner to the momentum equation:

$$\frac{d\hat{E}_i}{dt} = \frac{dE_i}{dt} + \sum_{j=0}^{j=n} -\zeta f_{ij} \left(\frac{P_i}{\rho_i^2} + \frac{P_j}{\rho_j^2} \right) M_j \vec{v}_{ij} \cdot \nabla \vec{W}_{ij} - \frac{1}{\rho_i} f_{ij} \zeta \dot{\epsilon} \cdot \tau \tag{2.73}$$

where ζ and n are user defined constants whose value depends on the selected kernel. The current work uses the cubic spline kernel and so the coefficients are taken from Monaghan [133] as $\zeta = 0.3$ and $n = 4$. As discussed in Section 1.2.2, splat formation due to cold spray can experience weak shocks due to the impact of the feedstock onto the substrate.

In order to ensure that particles do not become too compressed and suffer from the compressive side of the instability, an artificial viscosity is included following Monaghan and Lattanzio [91]. This viscosity also serves to spread the effect of the narrow shock feature so that it can be resolved without a prohibitively high resolution requirement. The artificial viscosity is calculated as shown and only in regions of compression, given by:

$$\Pi_{ij} = \begin{cases} \frac{-\alpha \bar{C}_{ij} \psi_{ij} + \beta \psi_{ij}^2}{\bar{\rho}_{ij}} & : \vec{v}_{ij} \cdot \vec{x}_{ij} < 0 \\ 0 & : \vec{v}_{ij} \cdot \vec{x}_{ij} \geq 0 \end{cases} \tag{2.74}$$

$$\psi_{ij} = \frac{h \vec{v}_{ij} \cdot \vec{x}_{ij}}{\vec{x}_{ij}^2} \tag{2.75}$$

The artificial viscosity is added to the artificial stress corrected momentum and energy equations as shown:

$$\frac{d\breve{\vec{v}}_i}{dt} = \frac{d\hat{\vec{v}}_i}{dt} + \sum_{j=0}^{j=n} \Pi m_j \nabla w \left(x_i - x_j, h \right) \tag{2.76}$$

$$\frac{d\breve{E}_i}{dt} = \frac{d\hat{E}_i}{dt} + \sum_{j=0}^{j=n} \Pi m_j \vec{v}_{ij} \cdot \nabla w \left(x_i - x_j, h \right) \tag{2.77}$$

2.2.3 Constituitive Models

Equations of State

The pressures in the preceeding governing equations are calculated using a suitable equation of state. The exact equation of state used depends on the phase of material being modelled, either gas, liquid or solid. The ideal gas equation of state is used for problems concerning gas dynamics:

$$p = \left(\gamma - 1 \right) \rho E \tag{2.78}$$

where γ is the ratio of specific heats. The weakly compressible equation is used for problems involving incompressible fluids:

$$P = C^2 \left(\rho - \rho_0 \right) \tag{2.79}$$

Here the sound speed C is used to limit compressibility and is tuned to reduce the density fluctuations to less than the desired level in any particular model. An initial approximate value of this sound speed is taken as being fifty times the peak expected velocity in the model and is increased after low resolution model runs if the desired level of incompressibility has not been reached. The initial material density is included as ρ_0.

The Mie-Grüneisen equation is used for the elastic-plastic materials included in the current work following Libersky [114], given by:

$$p = (1 - 0.5\Gamma\eta)\, p_h + \Gamma\rho E \tag{2.80}$$

where Γ denotes the Gruneisen parameter at the material reference state, $\eta = \rho/\rho_0 - 1$ and p_h is the pressure defined on the Hugoniot curve, given by:

$$p_h = \begin{cases} a_0\eta + b_0\eta^2 + C_0\eta^3 & : \eta > 0 \\ a_0\eta & : \eta < 0 \end{cases} \tag{2.81}$$

The coefficients used to describe the Hugoniot curve are described below where s is an experimentally determined parameter [114].

$$a_0 = \rho_0 C^2 \tag{2.82}$$

$$b_0 = a_0\left[1 + 2\left(s - 1\right)\right] \tag{2.83}$$

$$c_0 = a_0\left[2\left(s - 1\right) + 3\left(s - 1\right)^2\right] \tag{2.84}$$

This equation of state is applicable for shock compressed solids and so is suitable for the high velocity impact experienced in cold spray spray coating formation.

Viscosity and Shear stresses

The calculation of shear stresses, τ, depends on whether the material is fluid or solid which is specified at problem set-up.

Viscous Fluids Since fluids do not sustain shear stresses the instantaneous effect of the viscosity is calculated from the traceless strain rate (Equation (2.57)) using:

$$\tau = 2\mu\left(\dot{\epsilon}^{\alpha\beta} - \frac{1}{3}\delta^{\alpha\beta}\dot{\epsilon}^{\gamma\gamma}\right) \tag{2.85}$$

where μ is the viscosity. The calculated shear stress is then used in the momentum and energy governing equations (Equations (2.68) and (2.69)). This formulation for viscous fluids is used in the current work to allow verification of the governing equations against Poiseuille and Couette flows whilst enabling the use of alternative constitutive models without changes to the main governing equations. The implemented elastic-plastic model is described below and is used to calculate the shear stress, τ.

Elasticity The state of stress within a body does not physically vary due to rigid body rotation, this is not the case for the Cauchy stress tensor however when it is calculated from it's rate. The stress tensor itself is invariant with rigid body rotations (see Equation (2.86) but the rate is not as shown in Equation (2.88).

$$\sigma = Q\sigma Q^{-1} \tag{2.86}$$

where Q defines a rigid body rotation such that

$$QQ^{-1} = 1 \tag{2.87}$$

$$\frac{Q\sigma Q^{-1}}{dt} = \dot{Q}\sigma Q^{-1} + Q\dot{\sigma}Q^{-1} + Q\sigma\dot{Q^{-1}} \neq Q\dot{\sigma}Q^{-1} \tag{2.88}$$

To illustrate this, consider a beam which is initially subjected to a small longitudinal strain before undergoing rigid body rotation as shown in Figure 2.1.
The strained beam is subject to stress along its length which is aligned with the x-axis before the rigid rotation is applied, the rotation causes no additional strain on the beam, and therefore the strain rate is zero. In order for the state of Cauchy stress to remain unchanged it must be aligned with the y-axis at the end of the rotation, but the calculated stress rate of zero means no changes will occur. Compare this to the case where a measure of stress such as the Piola-Kirchhoff 2 (PK2) is used. This describes stress in the undeformed body (reference configuration) and so rotations of the body have no effect on the stress description. The stress description relative to the deformed body (Cauchy tensor) is of greater practical value than the stresses relative to the undeformed body and so will be used in the current work. This does mean however that the stress

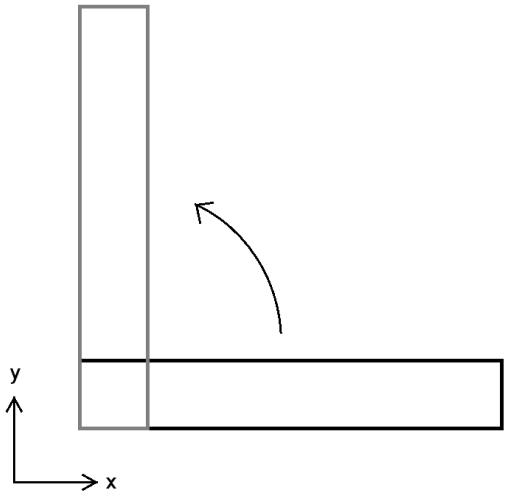

Figure 2.1: Schematic of rigid body rotation.

rate requires special treatment to account for rotations. The Jaumann rate of the Cauchy stress is such a rate and is simple to calculate as follows

$$\frac{d\tau}{dt} = G\left(\dot{\epsilon}^{\alpha\beta} - \frac{1}{3}\delta^{\alpha\beta}\dot{\epsilon}^{\gamma\gamma}\right) + \tau^{\alpha\gamma}\Omega^{\beta\gamma} - \Omega^{\alpha\gamma}\tau^{\gamma\beta} \tag{2.89}$$

where G is the material shear modulus and

$$\Omega^{\alpha\beta} = 0.5\left(\frac{d\vec{v}^{\alpha}}{d\vec{x}^{\beta}} - \frac{d\vec{v}^{\beta}}{d\vec{x}^{\alpha}}\right) \tag{2.90}$$

The Jaumann rate is a simplification of the Green-Naghdi rate which is itself a simplification of the Truesdell rate. These rates convert the Cauchy stress (current configuration) to the PK2 stress (reference configuration) before calculating the stress rate and then converting back to the Cauchy stress.

Plasticity

Radial Return When material shear stresses exceed the yield strength, the radial return plasticity method [138] is used to return the stresses to the yield surface. This is given by:

$$\sigma_{vm} = \sqrt{\frac{3}{2}\tau^{\alpha\beta}\tau^{\alpha\beta}} \tag{2.91}$$

if

$$\sigma_{vm} \geq Y_t \tag{2.92}$$

$$\tau^{\alpha\beta} = \tau^{\alpha\beta}\left(\frac{Y_t}{\sigma_{vm}}\right) \tag{2.93}$$

where Y_t is the current material yield strength.

Johnson-Cook Flow Stress The effects of strain hardening, strain rate hardening and thermal softening on the material yield strength are modelled using the Johnson-Cook method [139] following Randles & Libersky [106]. A new flow stress is calculated for each SPH particle at every time step according to:

$$Y_t = \left[Y_0 + B\epsilon_p^n\right]\left[1 + Cln\left(\dot{\epsilon_p}^*\right)\right]\left[1 - (T^*)^m\right] \tag{2.94}$$

where ϵ_p is plastic strain and $\dot{\epsilon}_{p0}$ is the reference plastic strain rate. Y_0, B, c, n and m are empirically derived material properties and a normalised temperature (T^*) is used

$$T^* = \frac{T - T_0}{T_m - T_0} \tag{2.95}$$

where T_m is the material melt temperature, T_0 is a reference temperature and T is the current material temperature as calculated from Equation 2.65.

$$\dot{\epsilon_p}^* = \frac{\dot{\epsilon}_p}{\dot{\epsilon}_{p0}} \tag{2.96}$$

where $\dot{\epsilon}_p$ is the plastic strain rate and $\dot{\epsilon}_{p0}$ is the reference strain rate at which the empical constants where obtained.

2.3 Numerical Methodology

2.3.1 Variable smoothing

A variable smoothing length approach is adopted to minimise the smearing effects that result from particle neighbour inconsistencies while making optimum use of the Lagrangian nature of SPH to allow variations in h as a function of change in density. Following Monaghan [90], the smoothing length of a particle is determined by:

$$\frac{dh}{dt} = -\frac{h}{\nu\rho}\frac{d\rho}{dt}, \tag{2.97}$$

where ν is the dimensionality of the domain.

2.3.2 Neighbour Search

The neighbour search is a fundamental but computationally expensive part of the SPH methodology. A robust method of reducing the computational effort required is to decompose the whole domain into a series of smaller cells that contain particles and limiting the neighbour search for a particular particle to those cells that are most likely to contain neighbour particles.

Fixed Smoothing Length Algorithm

In the standard cell search algorithm cells are as wide as the kernel function (kh) and neighbour searches are performed over a one cell radius from the centre cell as shown in Figure 2.2. This cell width is initialised at the start of computation and does not change. The standard cell width therefore has to be determined from the largest smoothing length in the problem, resulting in a potentially large number of checks against particles that are unlikely to be neighbours.

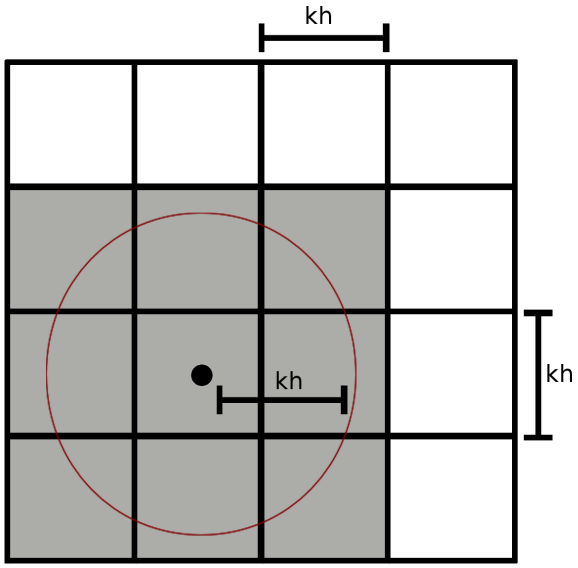

Figure 2.2: Schematic of standard cell search.

Variable Smoothing Length Algorithm

In contrast, the current work uses the smallest initial smoothing length present in the problem to set a single cell width, ω, and adjacent cells that encompass the support domain of a particle are determined using the following search range:

$$s = k\left(\frac{h}{\omega}\right)_{\text{round up}} \tag{2.98}$$

A schematic of this process is shown in Figure 2.3 where the particle for which the search is being performed is centred with its support domain denoted by the red circle, the adjacent cell array is also shown with the searched cells shaded. The approach facilitates the use of smaller cell sizes reducing the computational cost. The smaller cells hold less particles and represent a smaller proportion of the domain, therefore when the increase in h requires the addition of an extra cell there will be less unlikely neighbours to be checked. This reduction in unneeded work enhances the performance of the cell search algorithm.

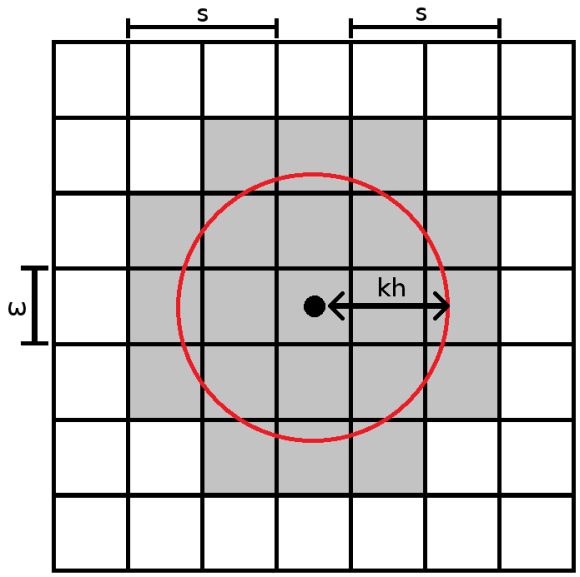

Figure 2.3: Schematic of cell search with variable smoothing length.

2.3.3 Interaction Pairs

Once every particle in the problem has identified its neighbours the system governing equations can be calculated. The most straight forward method of doing this is to have each particle calculate properties such as kernel gradient, relative velocities and its interaction with neighbours in order, since neighbouring is mutual (that is, if particle j is a neighbour of particle i then i is a neighbour of j) this results in the relative properties of a neighbour pair being calculated twice To avoid this, the current work takes a view point based on an interaction pair rather than treating each particle seperately, this is a common approach taken from molecular dynamics. Once a unique neighbour pair is identified by the cell search algorithm the identity of the neighbours are added to the neighbour lists of the particles involved, preventing the formation of a replica pair. All relative properties are then calculated for the interaction pair, assuming one of the particles is the particle of interest. The relative properties are inverted when necessary to allow calculation of the governing equations for the other particle thus saving repeated work.

2.3.4 Time Integration

Time integration of the SPH equations is performed using a second order accurate and explicit Verlet integration scheme for density, energy, shear stress, velocity, position and smoothing length, given by:

$$\rho^{n+1} = \rho^{n-1} + 2\frac{d\rho^n}{dt}\delta t \tag{2.99}$$

$$E^{n+1} = E^{n-1} + 2\frac{dE^n}{dt}\delta t \tag{2.100}$$

$$\tau^{n+1} = \tau^{n-1} + 2\frac{d\tau^n}{dt}\delta t \tag{2.101}$$

$$\vec{v}^{n+1} = \vec{v}^{n-1} + 2\frac{d\vec{v}^n}{dt}\delta t \tag{2.102}$$

$$\vec{x}^{n+1} = \vec{x}^n + \vec{v}^n\delta t + 0.5\frac{d\vec{v}^n}{dt}\left(\delta t^2\right) \tag{2.103}$$

$$h^{n+1} = h^{n-1} - 2\left(\frac{h^n}{D\rho^n}\right)\left(\frac{d\rho^n}{dt}\delta t\right) \tag{2.104}$$

and is coupled by the Euler scheme:

$$\rho^{n+1} = \rho^n + \frac{d\rho^n}{dt}\delta t \tag{2.105}$$

$$E^{n+1} = E^n + \frac{dE^n}{dt}\delta t \tag{2.106}$$

$$\tau^{n+1} = \tau^n + \frac{d\tau^n}{dt}\delta t \tag{2.107}$$

$$\vec{v}^{n+1} = \vec{v}^n + \frac{d\vec{v}^n}{dt}\delta t \tag{2.108}$$

$$\vec{x}^{n+1} = \vec{x}^n + \vec{v}^n\delta t + 0.5\frac{d\vec{v}^n}{dt}\left(\delta t^2\right) \tag{2.109}$$

$$h^{n+1} = h^n - \left(\frac{h^n}{D\rho^n}\right)\left(\frac{d\rho^n}{dt}\delta t\right) \tag{2.110}$$

every fifty iterations to suppress non-physical oscillations in steady flows that can be caused by the use of a historical property with a calculated zero rate; this typically occurs when a SPH particle no longer has any neighbours and so is a rare occurrence.

The size of time step, δt, is calculated by selecting the minimum of the following conditions which ensures the Courant-Friedrichs-Lewy (CFL) condition is met. Following Monaghan [90], the effects of the artificial viscosity, δt_{cv}, and particle accelerations, δt_f, are considered:

$$\delta t_{cv} = \iota\left[\frac{h}{c + 0.6\left(\alpha c + \beta\psi_{max}\right)}\right] \tag{2.111}$$

$$\delta t_f = \kappa\left(\sqrt{\frac{h}{\left|\dot{\vec{v}}\right|}}\right) \tag{2.112}$$

where $\dot{\vec{v}}$ is the SPH particle acceleration. With the incorporation of heat conduction a further constraint on δt is used following Cleary & Monaghan [97]

$$\delta t_t = \lambda \left(\frac{\rho c_v h^2}{k} \right) \tag{2.113}$$

ι, κ and λ are selected to maintain the accuracy of solution. The values of these coefficients have been refined during verification testing and unless stated otherwise $\iota = 0.3$, $\kappa = 0.09$ and $\lambda = 0.1$ are used.

2.3.5 Boundary Conditions

In the current work, dynamic, periodic and zero impedance boundaries are used and their implementations are discussed here.

Dynamic Boundaries

As described in Section 1.2.2 dynamic boundary particles are treated as standard SPH particles but have a constant velocity, they are included in interaction pairs in the same way as normal particles. The non-slip correction of Morris et al [98] is included, its use is optional and is selected at problem initialisation.

Periodic Boundaries

Periodic boundaries are used to model a semi-infinite domain. In the current work, the cell data structure is exploited to implement these boundaries. When an attempt to search a cell address that lies outside of the domain is made in a periodic problem the periodic search algorithm is used instead. This wraps the search across the upper and lower domain limits and subtracts the domain width from position calculations. The periodic search is illustrated in Figure 2.4 where the domain consists of a 2×2 square of cells. The black cell indicates a search that lies outside of the domain, when periodic conditions are used the cell to be searched is altered a valid cell on the opposite side of the domain. The new cell to be searched is coloured grey in Figure 2.4.

When a possible neighbour particle is identified in a corrected search cell the relative particle positions are calculated from:

$$x_{ij} = \begin{cases} x_{\min} - (x_{\max} - x_i) - x_j & : x_i > x_j \\ (x_{\max} + x_i) - x_j & : x_i < x_j \end{cases} \tag{2.114}$$

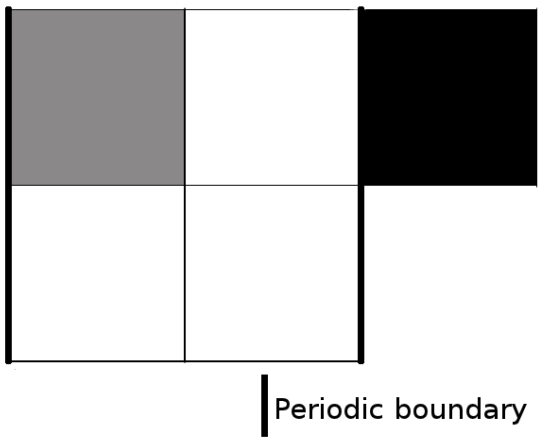

Figure 2.4: Schematic of periodic cell search.

where $x_{\min}$ and $x_{\max}$ are the coordinates of the lower and upper domain boundary along the corresponding axis respectively. The equation describes the position modification across a single flat plane boundary parallel to one of the global coordinate planes, and so represents a modification to a single component of the relative position. The modification needs to be applied separately to each required relative position coordinate. Other than this, relative position correction pair interactions across the periodic boundaries are unaffected. Particles moving off of the domain are wrapped so they re-enter at the opposite domain boundary; their reinsertion position is calculated from:

$$x_{new} = \begin{cases} x_{\min} + (x_{\text{out}} - x_{\max}) & : x_{\text{out}} > x_{\max} \\ x_{\max} - |x_{\min} - x_{\text{out}}| & : x_{\text{out}} < x_{\max} \end{cases} \tag{2.115}$$

where x_{out} is the position of a particle that has left the domain boundaries. As with the relative position corrections, this reinsertion routine needs performing on every axis separately.

Zero Impedance Boundaries

A shock damping or zero impedance boundary is implemented to allow for shock propagation and conduction out of the domain, thus enabling an isolated single splat formation to be modelled without requiring a large section of substrate to be considered. Ghost particles are created by replicating particles across the boundary and preserving the sign of all properties. This approximates an infinite substrate without wrapping the domain

such as is done in periodic domains and therefore corresponds more accurately to splat formation on an infinite substrate. A zero impedance condition uses the local properties of a material to predict the material state across the boundary. In this instance as a real particle approaches the boundary, its ghost should retreat from the boundary the same distance as the real particle approached. To obtain this relative position behaviour, ghost particle positions are calculated from the real particle positions following:

$$x_{ij} = \begin{cases} \vec{x}_i - \left[\vec{x}_{\max} + \left(\vec{x}_{\max} - \vec{x}_{j,0}\right) + \left(\vec{x}_{j,0} - \vec{x}_j\right)\right] & : c > c_{\max} \\ \vec{x}_i + \left(\vec{x}_{j,0} - \vec{x}_{\min}\right) + \left(\vec{x}_{j,0} - \vec{x}_j\right) & : c < c_{\min} \end{cases} \tag{2.116}$$

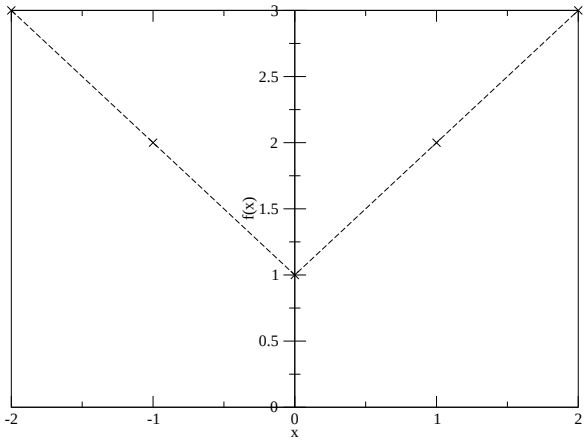

Figure 2.5: Representation of a function across a zero impedance boundary.

In order to demonstrate the characteristics of these boundaries, Figure 2.5 plots the behaviour of an arbitrary function across a zero impedance boundary, with the boundary at $x = 0$. For simplicity, a linear function is assumed but in practical models the relationship is likely to be more complex; additionally the exact choice of the exemplar function does not alter the general characteristics and boundary descriptions given. Material SPH particles are assumed at positions where $x \geq 0$, and ghost particles are created by reflecting these over the boundary at $x = 0$. It can also be seen that the function $f(x)$ is piecewise over the boundary and so can be described by two separate functions $G(x)$ and $T(x)$ following

$$f(x) = \begin{cases} G(x) & : x < 0 \\ T(x) & : x \geq 0 \end{cases} \tag{2.117}$$

and the SPH approximation across this boundary is given by

$$\nabla f(x) = \sum_{\text{material}} T(x_j) \frac{m_j}{\rho_j} \nabla w(x_i - x_j, h) + \sum_{\text{ghost}} G(x_j) \frac{m_j}{\rho_j} \nabla w(x_i - x_j, h) \tag{2.118}$$

Since $G(x)$ reflects $T(x)$ across the zero impedance boundary,

$$\sum_{\text{ghost}} G(x_j) \frac{m_j}{\rho_j} \nabla w(x_i - x_j, h) = - \sum_{\text{material}} T(x_j) \frac{m_j}{\rho_j} \nabla w(x_i - x_{j,b}, h) \tag{2.119}$$

where $x_{j,b}$ denotes the position of the ghost particle from the material particle j. Combining Equations (2.118) and (2.119) yields the following expression:

$$\nabla f(x) = \sum_{\text{material}} T(x_j) \frac{m_j}{\rho_j} \left[\nabla w(x_i - x_j, h) - \nabla w(x_i - x_{j,b}, h)\right] \tag{2.120}$$

From the above, the gradient sum of a particle on the boundary equates to zero. Since the number and location of ghost and real particles are balanced on both sides of the boundary, it results in no change in energy, velocity or density, thus eliminating undesired reflections. The zero impedance boundary affects the information transfer up to a distance of kh away and gradually damps out any function gradients near the boundary. Particles are allowed to move out of the domain because no repulsive effects are generated, and when this happens the particle is removed from the domain. Due to the above, small voids can form near zero impedance boundaries causing localised spurious accelerations. Therefore boundaries should be placed away from regions of high velocities and/or accelerations. In most cases, the above effect on a zero impedance boundary is negligible.

2.4 Solver Implementation

The solver has been designed for flexible and fast problem definition, with recompilation only required to switch dimensionality between two- and three-dimensions. A problem is

completely described in two .txt files, parameters.txt and particles.txt, allowing precise placement of particles and full control over all constitutive models, artificial corrections, threading, run-time and data output intervals. The parameter file is broken into several sections, first the computational domain is described followed by a description of each material included in the problem (see Table 2.4). An example of the domain description is given in Table 2.3 with comments describing each parameter. This is followed by an example description of a material body, in this case a copper cube of volume 1 m^3. Finally, the associated particle.txt file is given in Table 2.5.

2.4.1 Parameter Files

The file is split into several distinct sections, firstly the problem dimensionality, data output and run-time is described followed by computational domain descriptions including the location of upper and lower boundaries and their treatment and a series of toggles for activating various artificial corrections. Following this is the description of materials and dynamic boundaries, a dynamic boundary is treated exactly the same way as a material at problem setup. The boundary identifier simply serves to flag that these particles should not have their position or velocity updated by the solver. A material or boundary is described by its upper and lower boundaries, the type of material model to be used, which material from the solver's library is to be used, the total mass of the material, the initial velocity, external accelerations and initial temperature. Materials or boundaries described in the parameter file are associated with groupings of particles in the particles.txt file by their upper and lower boundaries.

2.4.2 Particle Files

The co-ordinates of a single particle occupy one line in the file with each co-ordinate separated by commas, a hash token separates groups of particles and so delineates different materials or boundaries. The file is searched at problem initialisation and the first particle of each grouping is checked against the material/boundary upper and lower boundaries described in the parameter file to determine which particle groups correspond to each material/boundary in the parameter file. For complex geometries where multiple particle sets may satisfy the criteria for a material, it is better to set the upper and

3	
dimensions	%The dimensionality of the problem
10	
threads	%Number of parallel thread employed
10	
endtime	%End time in seconds
0.1	
pv_interval	%Interval in seconds between .vtu file creation
0.65	
h	%Width of neighbour search cells
0	
sumden	%Toggle controlling the use of summation or continuum density
0	
xsph	%Toggle controlling the use of XSPH
0	
tc	%Toggle controlling the use of the tensile correction
0	
art_visc	%Toggle controlling the use of artificial viscosity
0	
plasticity	%Toggle controlling the use of the radial return plasticity model
0	
wtest	%Toggle controlling the use of the kernel weight and grad diagnostic functions
2	
k	%Parameter defining width of the kernel support domain
0	
gravity	%Toggle controlling the use of gravity along the y-axis
0	
morrisb	%Toggle controlling the use of Morris non-slip boundary condtion
0	
neumann	%Toggle controlling the use of neumann boundaries
1	
periodic	%Toggle controlling the use of periodic boundaries
1	
xperiod	%Activates x-axis periodic boundaries
1	
zperiod	%Activates z-axis periodic boundaries
0	
lx	%Domain lower x boundary
1	
ux	%Domain upper x boundary
0	
ly	%Domain lower y boundary
1	
uy	%Domain upper y boundary
0	
lz	%Domain lower z boundary
1	
uz	%Domain upper z boundary
1.4	
gamma	%ratio of specific heats
1	
alpha1	%Arftificial viscosity parameter
2	
beta	%Arftificial viscosity parameter

Table 2.3: Domain defintion section of parameters.txt.

0	
material	%Specifies a material region, dynamic boundaries are described with "boundary"
0	
copper	%Specifies material from solver internal library
0	
fluid	%Toggle controlling use of viscous fluid material model
0	
mlx	%Lower x-axis boundary
1	
mux	%Upper x-axis boundary
0	
mly	%Lower y-axis boundary
1	
muy	%Upper y-axis boundary
0	
mlz	%Lower z-axis boundary
1	
muz	%Upper z-axis boundary
0	
vx	%Initial x-axis velocity
0	
vy	%Initial y-axis velocity
0	
vz	%Initial z-axis velocity
0	
ax	%Body force applied as fixed acceleration to x-axis
0	
ay	%Body force applied as fixed acceleration to y-axis
0	
az	%Body force applied as fixed acceleration to z-axis
0.65	
h	%Smoothing length
0	
energy	%Initial energy
0	
shape	%Toggle for auto calculation of material mass (0 means use value provided in shapemass)
1000	
shapemass	%Mass of material
0	
temperature	%Initial temperature
0	
end	%End of material description

Table 2.4: Material defintion section of parameters.txt.

lower boundary ranges in the parameter file to only cover the first particle in the desired particle set.

2.4.3 Optimisations

Several optimisations have been made to the solver in order to reduce computation time. Firstly, particle interactions are calculated in a pairwise manner and secondly multi-thread computation is used where possible. Particle interactions are calculated from the view point of pairs of particles rather than individual particles in order to eliminate repeated work, for example all relative properties such as velocity, position and kernel weight are calculated only once for each pair rather than twice if a particle by particle view point is taken. The symmetry of the kernel is also exploited so that the kernel gradient is only calculated once and the required sign change is applied where appropriate. As well as the reduction in repeated work this pair view point also helps to reduce data access conflicts when operating in a multi-threaded mode since the pair type stores the relative properties and kernel data required for computation of the governing equations and so the variables stored in the relevant particle objects do not need to be accessed again.

The ability to split computation across multiple threads was added to C++ with the introduction of the C++ 11 standard and this functionality is utilised in the current work. Work is either divided by particle or pair objects over a number of threads specified by the user in the problem parameter file, a join operation pauses computation in the parent (main) thread until all child threads have completed their computation. Data access conflicts are resolved using the mutex class which restricts access to shared variables to a single thread at a time. A variable is shared if a read/write operation could be performed on it by multiple threads simultaneously. A thread will pause until it is able to get sole control of a shared variable by locking the associated mutex. Once locked, a mutex can not then be relocked until the owning thread issues an unlock. Care should be taken when developing functions for multi-threaded operation that mutex lock/unlock operations are not performed too often since this causes threads to pause whilst they await access more than is necessary and can force the code to become practically serial in operation. The concurrent vector class from the Threaded Building Blocks (TBB) library was used because the standard C++ vector class is not safe for multithread

operation. A flow chart showing the order of solution employed in the current work is shown in Figure 2.6 and a description of the function of each block in the diagram is given in Table 2.6, the threading type describes whether the work is split across threads on a particle by particle basis for by interaction pair.

0.25,0.25,0.25
0.25,0.75,0.25
0.75,0.25,0.25
0.75,0.75,0.25
0.25,0.25,0.75
0.25,0.75,0.75
0.75,0.25,0.75
0.75,0.75,0.75

Table 2.5: The particles.txt file associated with the example parameters.txt.

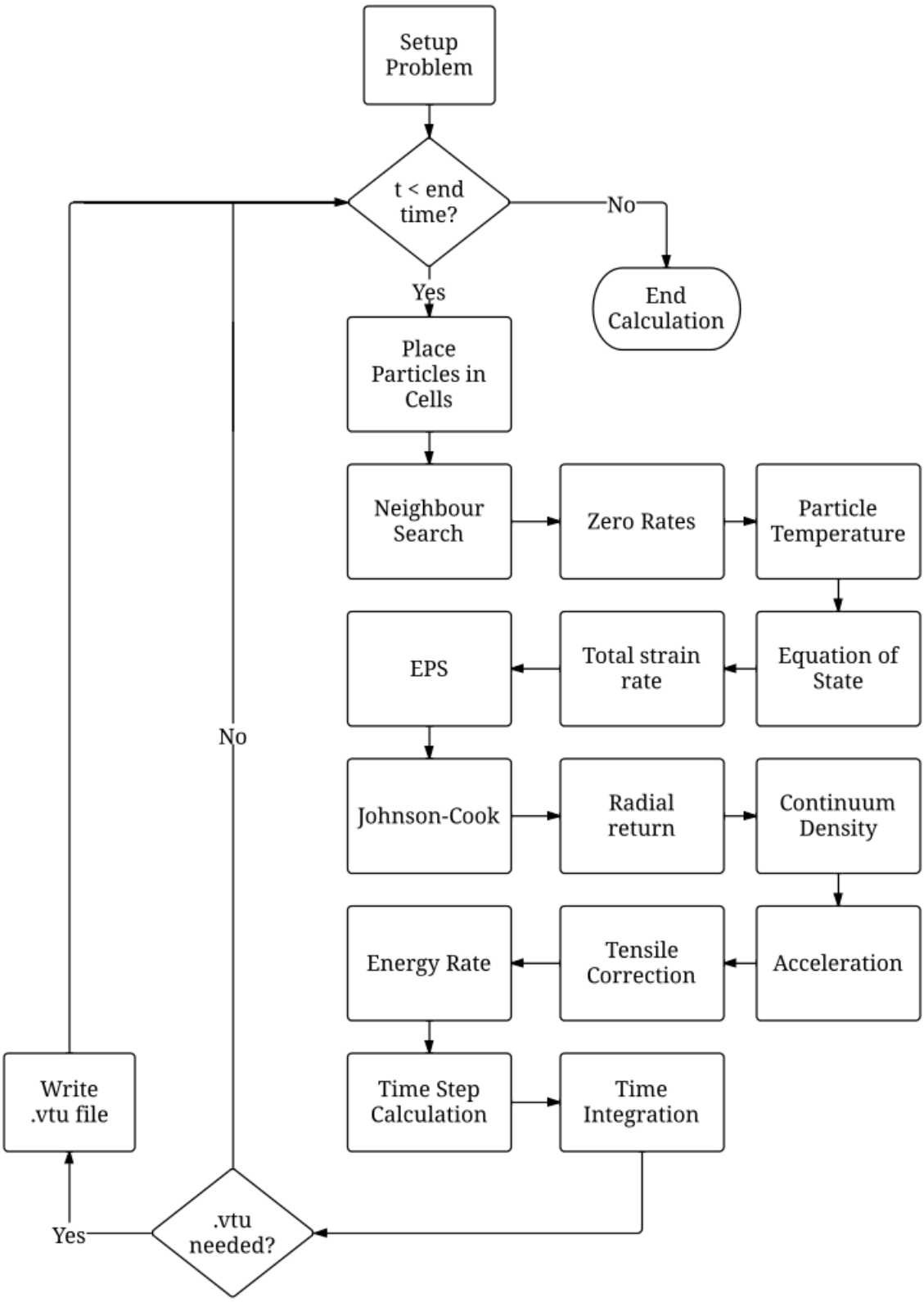

Figure 2.6: Solver functional flow chart.

Function	Description	Threaded
Setup problem	parameter.txt and particles.txt are read and the initial conditions of the problem are loaded into the solver	N/A
Place particles in cells	All particles are placed in a cell on the neighbour search grid corresponding to their co-ordinates.	Particle
Neighbour search	Unique pairs of neighbour particles are identified, a pair object is created and all relative properties of the pair are calculated	Particle
Zero rates	All rates of change (acceleration, density rate, etc) are set to zero before the calculation of new rates	Particle
Particle temperature	The temperature of all particles is calculated from their energy, density and specific heat	Particle
Equation of State	The pressure is calculated for each particle using the equation of state	Particle
Total strain rate	The traceless strain rate experienced by each particle is calculated	Pair
EPS	Plastic strain rates are calculated for each particle if the elastic-plastic material model is employed	Particle
Johnson-Cook	The flow stress is calculated for particles belonging to an elastic-plastic material	Particle
Radial return	Stresses are returned to the yield surface for plastically deforming particles	Particle
Continuum density	The density rate of all particles is calculated	Pair
Acceleration	The acceleration of all particles is calculated	Pair
Tensile correction	The tensile correction terms are calculated and added to the acceleration and energy equations if required	Pair
Energy rate	The time rate of change of energy is calculated for all particles	Pair
Time step	The time step size is calculated from the CFL conditions	N/A
Time integration	Time integration is performed for all particles	Particle
Write .vtu file	Particle data is written in xml format at exact time intervals specified in the parameter file	N/A

Table 2.6: Solver functional description.

Chapter 3

Verification Tests

The developed SPH solver has been rigorously tested to prove its accuracy, efficiency and scalability. Accuracy is obviously of paramount importance but computational time and resources need to be used efficiently to increase the applicability of the solver. In this chapter, these solver characteristics will be examined in depth, starting with accuracy and followed by performance benchmarks.

3.1 Verification Tests

The solver has been verified against a variety of standard tests, each testing one or more of the implemented equation sets relating to modelling cold spray splat morphologies. The tests are applied in a staged manner throughout development as complexity is increased. In this section, each of these tests will be described in detail and the results produced by the solver will be presented with a discussion of acceptable error and error sources.

3.1.1 Boundary Rebound

A single SPH material particle which is initially at rest is modelled falling under gravity and rebounding from a block of 6 SPH boundary particles using the weakly compressible equation of state (see Equation (2.79)) and the cubic kernel (see Equation (2.30)). The initial particle positions are shown in Figure 3.1 where the shaded circle represents the falling material particle and unshaded circles represent dynamic boundary particles. All particles are given the initial conditions and properties shown in Table 3.1, the only

exception being the material particle which has a constant acceleration of -9.81 m/s^2 along the y-axis applied throughout the entire test duration of 2 seconds. Particle spacing within the boundary is 0.1 m and a ratio of 1.3 is used to calculate initial smoothing lengths with the same smoothing length applied to the material particle. Data was printed every 1×10^{-3} seconds and the solver computed 2000 time steps. The sound speed was selected to limit the compressibility of the material, an estimate of the impact velocity was made and the sound speed was set to 50 times this value. Density fluctuations were successfully reduced to 2.17% as shown in Figure 3.2a.

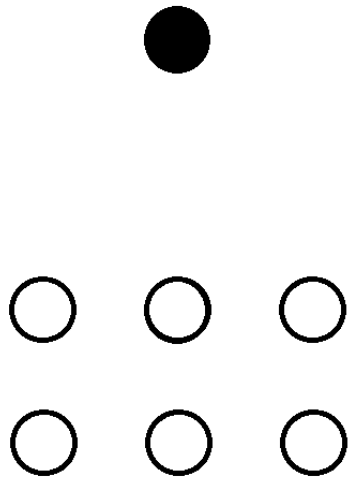

Figure 3.1: Schematic of initial particle postions.

This tests the invisicd momentum conservation, continuum density and smoothing length evolution equations. In this inviscid system, the material particle should bounce indefinitely, returning each time to its original position and retain its initial density and experiencing no net acceleration parallel to the boundary. The initial density is relevant because as previously discussed mass is invariant in SPH but density and therefore particle volume is not. This is similar to the normalised pressure term (NPT) test employed by Crespo et al [140] and the same analysis of the solver performance will be carried out.

Figure 3.2b plots the height of the material particle against time. It can be seen that there is no significant deviation between the maximum rebound height and the initial height with a peak error of 0.19% seen at the final return point. Figure 3.3a plots the y-axis velocity against time and it also shows a mostly regular bounce, with the notable exception around 1.5 seconds. The slight velocity oscillation seen here is caused by the

time integration algorithm. The integration uses a historic value and the current rate to calculate the next time step and this will cause the oscillation until the standard Euler algorithm is applied (every fifty time steps). This error only occurs when a particle leaves the support domain of all of its previous neighbours, indicating material fracture in a cold spray model. At the impact velocities and substrate thicknesses used in cold spraying, fracturing of the material is unlikely. Figure 3.3a also shows that the velocity returns to the expected profile once this period of oscillation is over, thus, making the error negligible. Figure 3.3b shows only negligible acceleration parallel to the dynamic particles with each perpendicular impact and subsequent rebound. The velocity of the material particle is plotted against height for the full two second duration in Figure 3.4. It can been seen that the velocity/height profile for each rebound is in close agreement with the other rebounds, demonstrating conservation of momentum.

Density, ρ	1000 kg/m^3
Mass, m	10 kg
Sound Speed, c	221.47 m/s
Smoothing length, h	0.13 m

Table 3.1: Boundary rebound initial conditions.

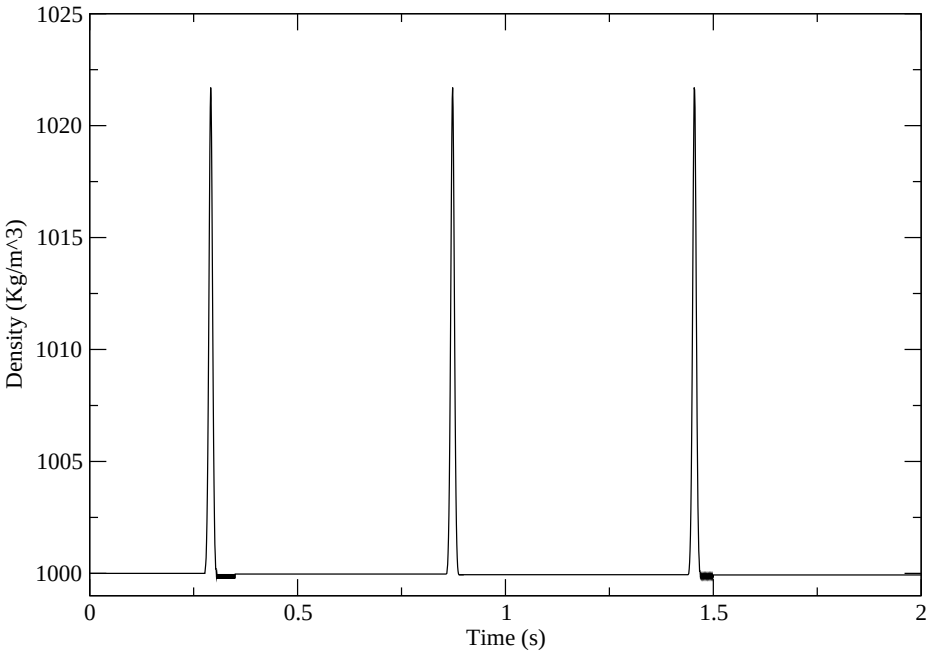

(a) Density fluctuation in the boundary rebound test.

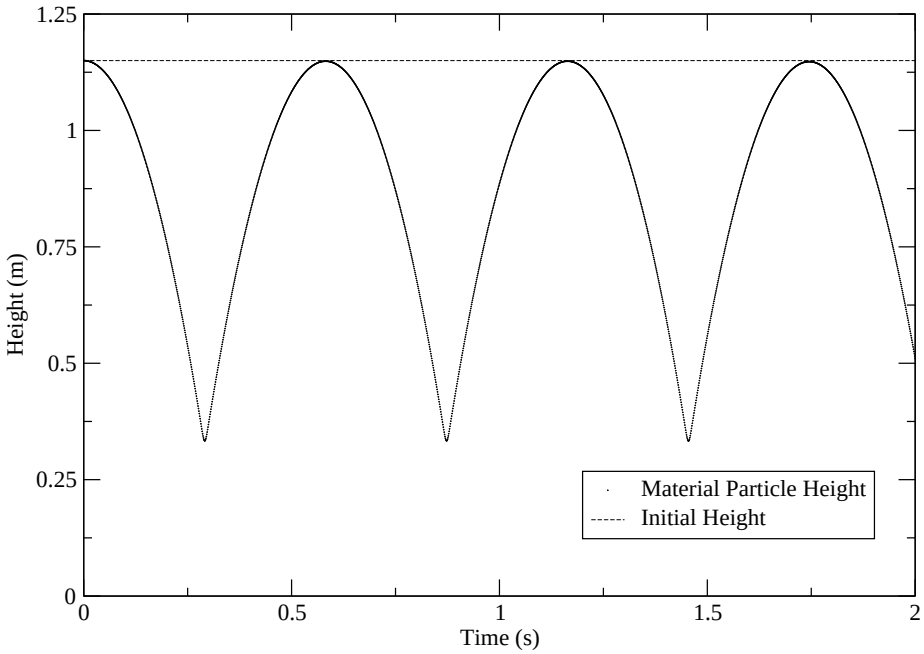

(b) Material particle rebound y-axis postions.

Figure 3.2: Rebound test density and height evolution.

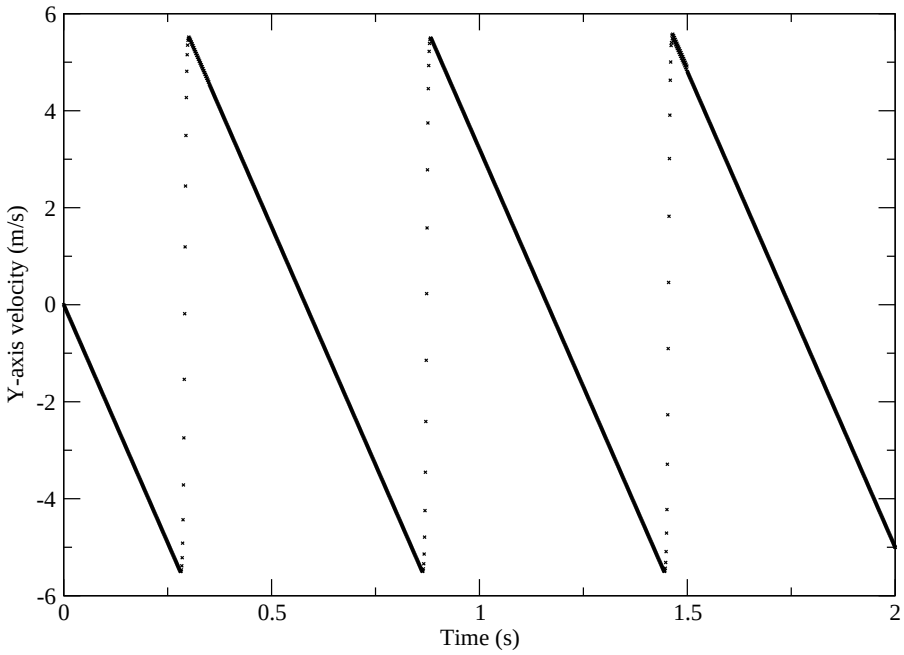

(a) Material particle rebound velocity against time data.

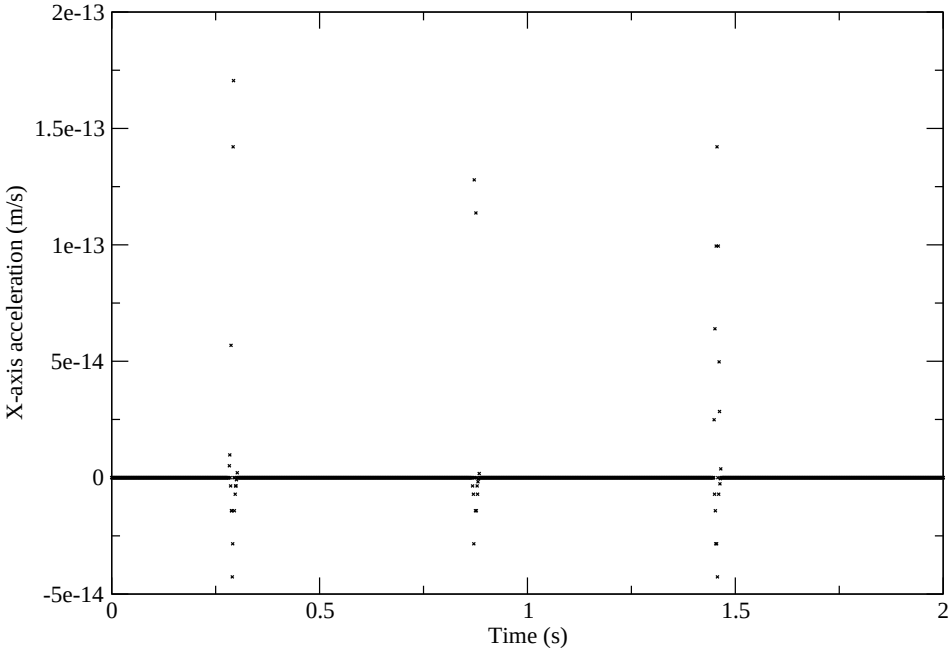

(b) Material particle rebound x-axis acceleration against time data.

Figure 3.3: Rebound test velocity and acceleration evolution.

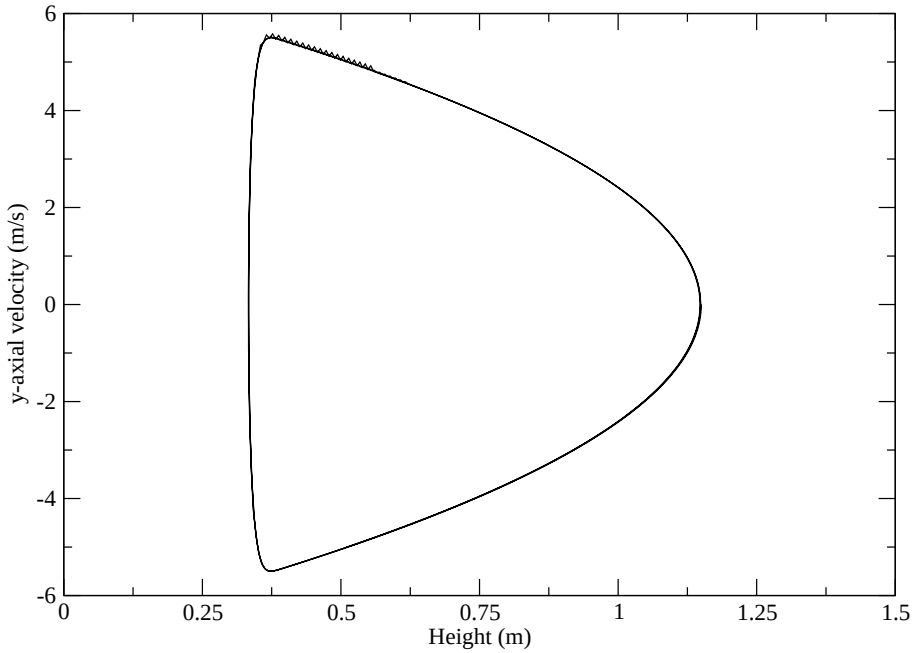

Figure 3.4: Material particle rebound y-axis velocity against particle height data.

3.1.2 Shock-Tube

The next test case employed is a two-dimensional shock-tube replicating conditions from Liu et al [141]. This tests shock handling capabilities in an inviscid ideal gas. Artificial viscosity and a cubic spline kernel are used with the ideal gas equation of state (see Equation(2.78)). A shock-tube of height 1.2 m and width 0.075 m is modelled and a zero impedance boundary condition is applied across all boundaries to obtain a semi infinite domain (see Figure 3.5).

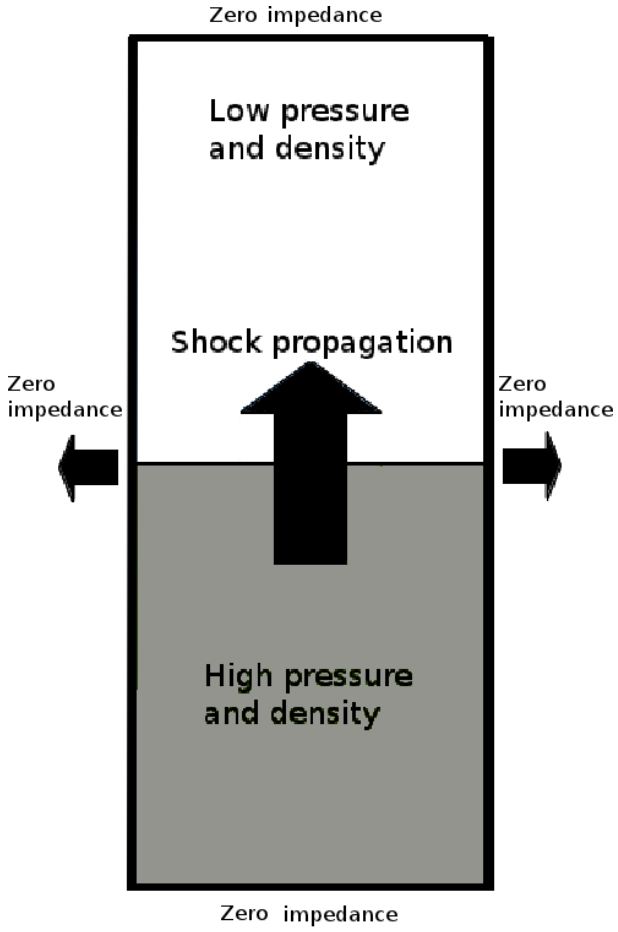

Figure 3.5: Shock-tube problem schematic.

The gases are initially at rest and are accelerated by a pressure and density discontinuity half way up the tube in the flow direction, the high pressure gas will expand rapidly into the low pressure region creating a shockwave travelling into the low pressure region and an expansion wave travelling backwards into the high pressure region. The initial conditions are described in Table 3.2. Sound speed is calculated from the initial

conditions following:

$$c = \sqrt{\frac{\gamma p}{\rho}} \tag{3.1}$$

where γ is the ratio of specific heats. A constant particle mass of 5.625×10^{-5} kg is used throughout the problem to ensure momentum, energy and mass conservation and particle volume is varied to correctly represent the gas densities.

	$y > 0.6$ (Zone 1)	$y < 0.6$ (Zone 4)
Mass (kg)	5.625×10^{-5}	5.625×10^{-5}
Density (kg/m^3)	0.25	1
Energy (J/kg)	1.795	2.5
Pressure (Pa)	0.1795	1
Sound Speed (m/s)	1.002597	1.18322
γ	1.4	1.4
Velocity (m/s)	0	0
Δx (m)	0.0075	0.00375
h (m)	0.00975	0.004875

Table 3.2: Shock-tube initial conditions.

To facilitate an accuracy assessment, an analytical result for the shock problem is calculated as follows. There are five distinct material property zones in a shock-tube as shown schematically in Figure 3.6, the relative sizes of these zones change over time as the compression and rarefaction waves propagate through the shock-tube.

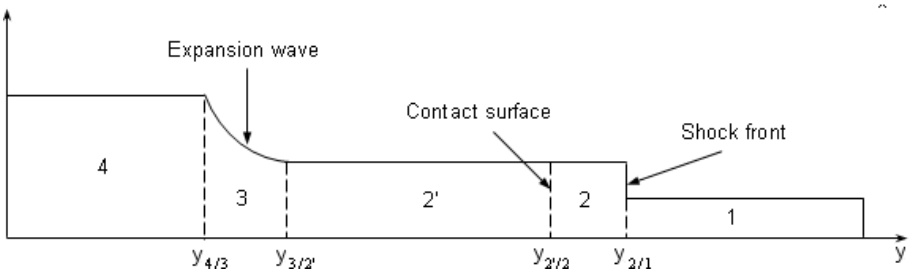

Figure 3.6: Shock-tube zones.

Zones 1 and 4 are the the initial gas conditions as described in Table 3.2. Zone 2 describes the post shock properties of the initially low pressure gas , zone 2′ describes the gas properties behind the contact discontinuity and zone 3 describes the properties with the rarefaction wave. The shock-front describes the location of the leading edge of the shockwave, the contact surface denotes the interface between the two gases and finally the expansion wave is seen moving into the high pressure region. To obtain the material properties within each region the following system of equations is solved:

Shock-tube Zone 2 Equations

$$\frac{p_4}{p_1} = \frac{p_2}{p_1}\left(1 - \frac{(\gamma-1)\left(\frac{c_1}{c_4}\right)\left(\frac{p_2}{p_1}-1\right)}{\sqrt{2\gamma\left(2\gamma+(\gamma+1)\left(\frac{p_2}{p_1}-1\right)\right)}}\right) \tag{3.2}$$

$$\vec{v}_{2,y} = \frac{c_1}{\gamma}\left(\frac{p_2}{p_1}-1\right)\sqrt{\frac{\frac{2\gamma}{\gamma+1}}{\frac{p_2}{p_1}+\frac{\gamma-1}{\gamma+1}}} \tag{3.3}$$

$$\rho_2 = \rho_1\left(\frac{\frac{p_2}{p_4}+\frac{\gamma-1}{\gamma+1}}{1+\frac{\gamma-1}{\gamma+1}\frac{p_2}{p_4}}\right) \tag{3.4}$$

Shock-Tube Zone 2′ Equations

$$p_{2'} = p_2 \tag{3.5}$$

$$\vec{v}_{2'} = \vec{v}_2 \tag{3.6}$$

$$\rho_{2'} = \rho_4\left(\frac{p_2}{p_4}\right)^{\frac{1}{\gamma}} \tag{3.7}$$

Shock-tube Zone 3 Equations

Property values are not constant with in the expansion zone and so the equations depend on a position varible y' which is defined as

$$y' = y - y_0 \tag{3.8}$$

where y is the current position being calculated and y_0 is the inital discontinuity position.

$$p_3 = p_4\left(1 - \frac{\gamma - 1}{2}\frac{\vec{v}_{3,y}}{c_4}\right)^{\frac{2\gamma}{\gamma-1}} \tag{3.9}$$

$$\vec{v}_3 = \frac{2}{\gamma + 1}\left(c_4 + \frac{y'}{t}\right) \tag{3.10}$$

$$\rho_3 = \rho_4\left(\frac{p_{3,y}}{p_4}\right)^{\frac{1}{1.4}} \tag{3.11}$$

For all points throughout the entire shocktube the energy is calculated from the density and pressure through the equation of state.

Shock-tube Zone Division Calculation

The exact location and length of the zones varies with time as the compression and rarefraction waves propagate. The exact positions are calculated with the following equations:

$$\vec{v}_s = c_1\sqrt{\left(\frac{\gamma + 1}{2\gamma}\right)\left(\frac{p_2}{p_1} - 1\right) + 1} \tag{3.12}$$

$$y_{1/2} = t\vec{v}_s + y_0 \tag{3.13}$$

$$y_{2'/2} = t\vec{v}_{2'} + y_0 \tag{3.14}$$

$$y_{3/2'} = t\left(\vec{v}_{2'} - c_{2'}\right) + y_0 \tag{3.15}$$

$$y_{4/3} = t\left(\vec{v}_{2'} - c_{2'}\right) + y_0 \tag{3.16}$$

$$c_{2'} = \sqrt{\frac{1.4p_{2'}}{\rho_{2'}}} \tag{3.17}$$

The shock conditions modelled represent a sharp discontinuity and so provide a rigorous test for shock handling. The density profile shown in Figure 3.7 shows a sharp discontinuity at 0.9 m where the leading edge of the shockwave is compressing the previously low pressure gas. There is a further jump in density at the interface between the

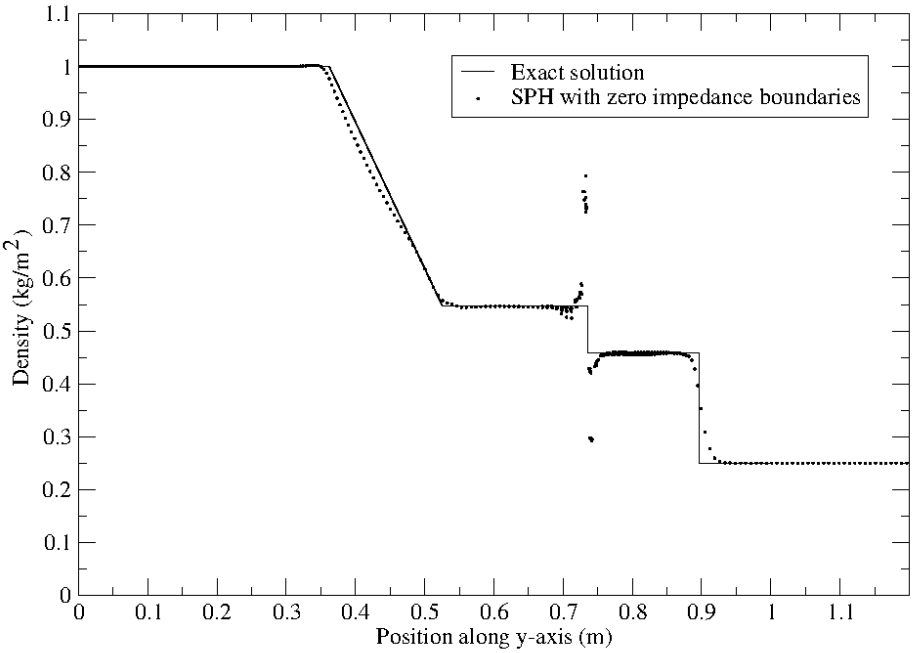

Figure 3.7: Shock-tube density profile at t = 0.2 s.

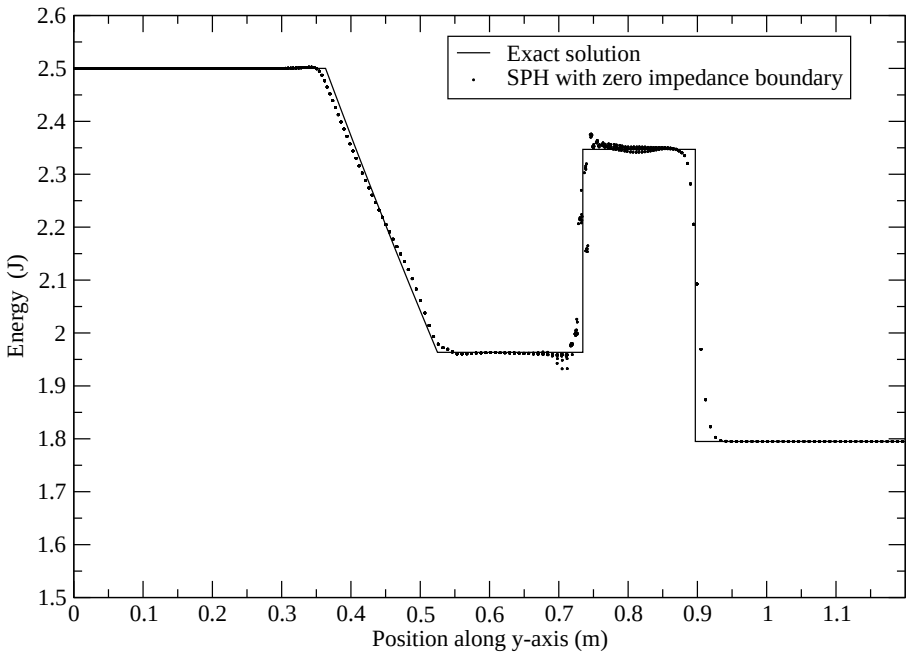

Figure 3.8: Shock-tube energy profile at t = 0.2 s.

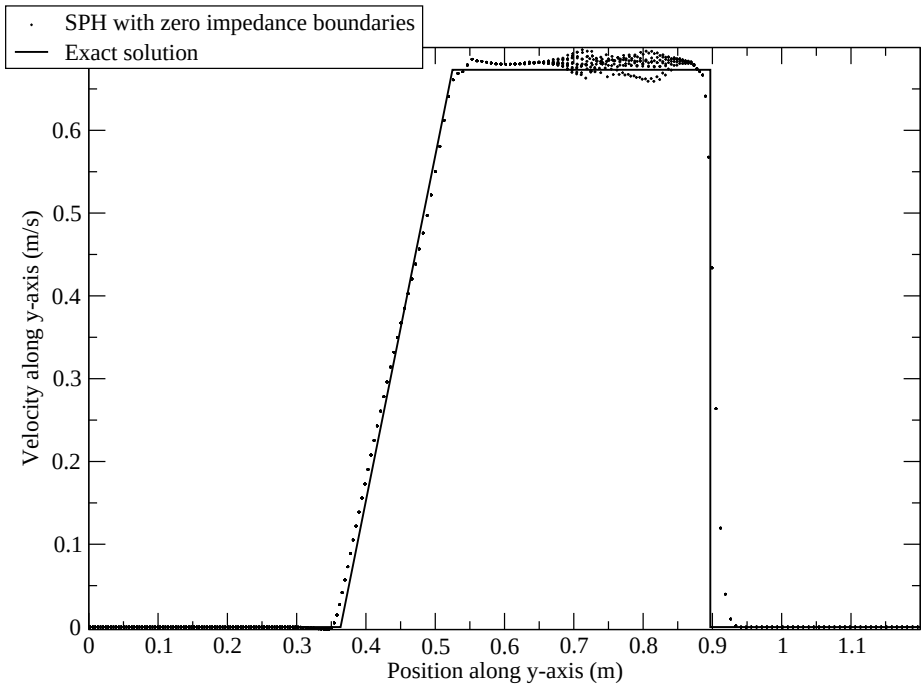

Figure 3.9: Shock-tube velocity profile at t = 0.2 s.

two gases where the expansion wave has not quite equalised the gas densities. Finally, the expansion wave can be seen moving in the opposite direction to the shockwave, causing a reduction in gas density. The highest errors are seen at the contact interface where the initial discontinuity was present, the pre- and post-interface densities return very quickly to the expected values however and the error is limited to a narrow band of witdht eqaul to the smoothing length, h, either side of the interface. The energy profile (see Figure 3.8) shows good agreement with the analytical solution, illustrating a sharp increase in energy at the shock front as the initially low pressure gas is compressed. This increased energy level can be seen stretching from the shock-front to the contact interface; the initially high pressure gas the other side of the interface has experienced a reduction in energy as it expands behind the shockwave. A sharp acceleration at the shock-front is seen in Figure 3.9 between the shock-front and expansion wave the gas shows a velocity oscillation across the width of the shocktude perpendicular to the shockwaves direction of travel, until the expansion creates a relatively smooth acceleration in the initially high pressure gas. Velocity osscillations were also seen in the one-dimension shocktube results published by Liu and Liu [141], these osscilations coincide with the location of the density errors seen at the contact interface. Despite these osscilations the pre- and post-shock velocities show good agreement with the analytical results. All three profiles show close agreement with the analytical solution with the largest errors present in the velocity profile, the pre- and post-shock gas properties show the expected values of density, energy and velocity however. Additionally, the shockwave travels at the correct speed through the gas despite these errors, proving them to be transisent errors introduced by the sharp discontinuity which have no effect on the steady state values.

The Mach number for this shock-tube is estimated to be 1.48 following:

$$M_n = \frac{|\vec{v}_s|}{c} \tag{3.18}$$

where $|\vec{v}_s|$ is the calculated shock velocity of 1.48 (from Equation (3.12)), and c as the sound speed of the gas experiencing the shock. The Mach number of a typical cold spray process for copper is estimated using an impact velocity of 700 m/s and a material sound speed of 3940 m/s this results in a Mach number of 0.18 which demostrates that shocks induced during cold spraying should be weaker than those modelled in the shock-tube

test and therefore the solver is capable of capturing the effects of any shockwaves present during coating formation.

3.1.3 Poiseuille Flow

A three-dimensional Poiseuille flow test case is used to examine viscous dissipation effects following Morris [98]. Periodic boundary conditions are employed to model a semi-infinite fluid bounded by two stationary parallel plates that are separated by a distance of 10^{-3} m. A three-dimensional schematic of the initial problem setup is shown in Figure 3.10.

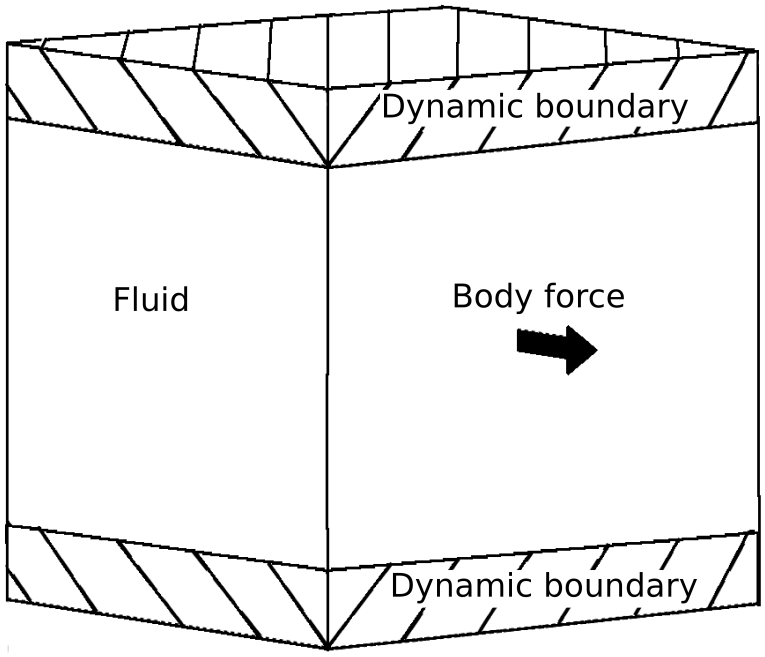

Figure 3.10: Schematic of Poiseuille flow test case.

The fluid is initially at rest and is driven by an acceleration of 10^{-4} m/s^{-2} parallel to the bounding plates. A quintic kernel (see Equation 2.32) is used to enable comparison with Morris [98], the weakly compressible equation of state (see Equation 2.79) and the viscous fluid constitutive model are used. The initial conditions are described in Table 3.3 and the driving acceleration is applied as a body force to the fluid particles. Dynamic boundaries are used to model the bounding plates with the additional application of the non-slip boundary condition described by Morris [98].

The exact analytical solution can be calculated using the following equation:

$$\vec{v} = y\,(H - y)\left(\frac{\dot{\vec{v}}\rho}{2\mu}\right) - \sum_{n=0}^{k}\left(\frac{4\dot{\vec{v}}\rho H^2}{\mu\pi^3}\right)\left(\frac{1}{n^3}\right)\sin\left(n\pi\frac{y}{H}\right)\exp\left(-n^2\pi^2\frac{\mu t}{\rho H^2}\right) \qquad (3.19)$$

where H is the height of the flow channel, y is the height in the flow channel of the current calculation point, ρ is the density, μ is dynamic viscosity, t is time, $\dot{\vec{v}}$ is the applied acceleration and k is used to control the number of terms in the summation.

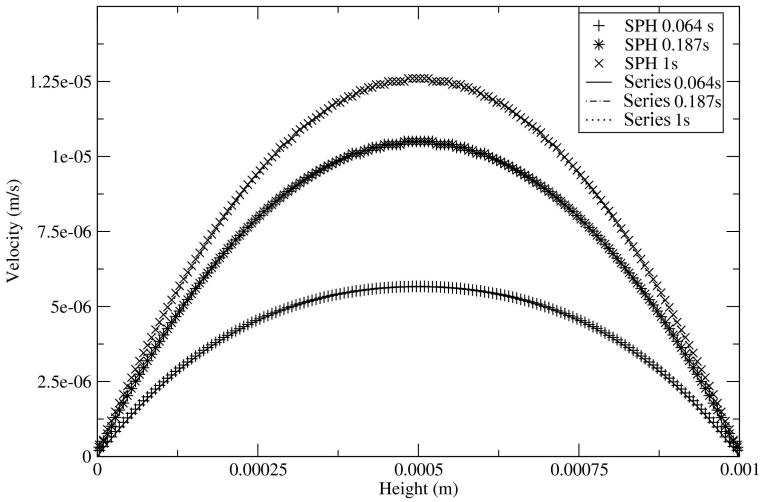

Figure 3.11: Evolution of Poiseuille flow velocity profiles.

The fluid particles are expected to undergo a continuous acceleration due to the applied body force. As the fluid velocity increases relative to the bounding plates the strength of the viscous drag or shear force increases until it reaches an equilibrium with the applied force. At this point the fluid velocity reaches steady-state and remains constant. The fluid can be seen to be accelerated as expected in Figure 3.11. The parabolic shape is created by the viscous drag between the bounding plates and the fluid particles and the applied non-slip boundary condition; these act to hold the initial layer of fluid at the bounding plate velocity. Particles see a diminishing drag effect and a greater subsequent acceleration further away from the bounding plate. The viscous drag terms in the momentum equation also act between fluid particles and so this velocity gradient produces the acceleration gradient that forms the parabolic profiles seen. The

flow profiles show that the non-slip condition applied is correctly limiting the fluid velocity to that of the bounding plate (in this case zero). The results show good agreement with predicted values with maximum error at steady-state of 0.56%.

Error is introduced by the roughness of the boundary caused by the discretisation of the SPH particles which introduces a small unphysical pressure effect on particles moving parallel to the boundary. The dynamic boundaries will only be used to contain SPH particles within the domain when modelling cold spray and will be well away from the impact site. For this reason the small effect of the boundary roughness can be considered negligible.

	Fluid	Lower boundary	Upper boundary
Dynamic viscosity, μ (Pa·s)	0.001	0.001	0.001
Density, ρ (kg/m^3)	1000	1000	1000
Energy, E (J/kg)	0	0	0
Pressure, p (Pa)	0	0	0
Velocity, $\vec{v}$ (m/s)	0	0	0
Acceleration, $\dot{\vec{v}}$ (m/s^2)	0.0001	0	0
Sound speed, c (m/s)	2.5×10^{-5}	2.5×10^{-5}	2.5×10^{-5}
Initial particle spacing, Δx (m)	6.25×10^{-6}	6.25×10^{-6}	6.25×10^{-6}
Smoothing length, h (m)	8.125×10^{-6}	8.125×10^{-6}	8.125×10^{-6}

Table 3.3: Poiseuille flow initial conditions.

3.1.4 Couette Flow

A three-dimensional Couette flow test case is modelled to provide further verification of the sheer stress terms of the momentum equation, a schematic of the problem is provided in Figure 3.12. Periodic boundary conditions are used to model a semi-infinite fluid bounded by two parallel plates that are separated by a distance of 10^{-3} m.

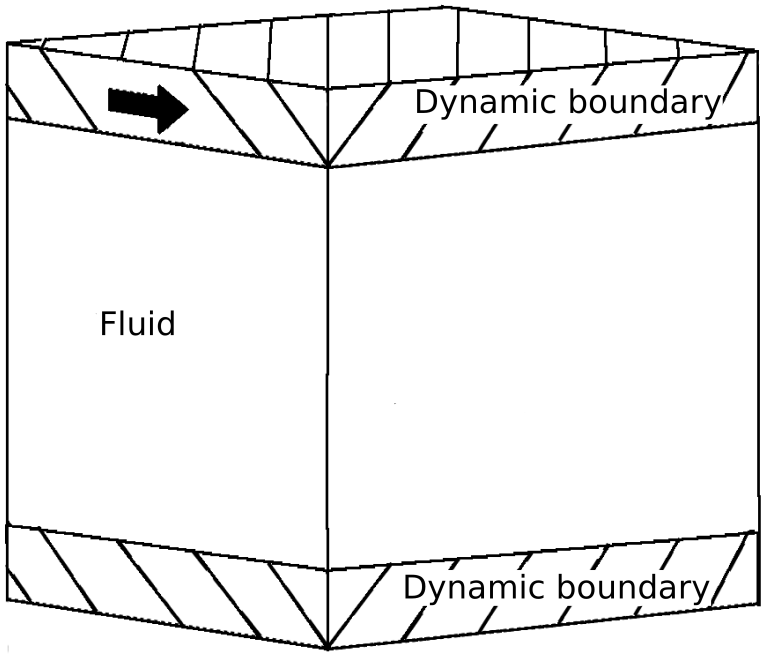

Figure 3.12: Schematic of Couette flow test case.

The fluid is initially at rest and is driven by the top plate which has a constant velocity of 12.5×10^{-6} m/s whilst the bottom plate is held stationary. The initial conditions match those used by Morris [98] and are summarised in Table 3.4. Particles are deployed 6.25×10^{-6} m apart with a smoothing length of $1.3\Delta x$ using a quintic kernel (see Equation (2.32)) and Morris' non-slip condition [98]. The initially stationary fluid will be accelerated by the viscous drag forces generated by the velocity difference between the moving top plate and the fluid. This acceleration is balanced against the drag between the non-stationary fluid and the stationary plate which acts to decelerate the fluid; these two competing viscous effects will eventually reach a steady state producing the non-uniform velocity evolution shown in Figure 3.13. The exact analytical solution can be calculated using the following equation:

$$\vec{v} = y\left(\frac{\vec{v}_0}{H}\right) + \sum_{n=0}^{k}\left(\frac{2\vec{v}_0}{n\pi}\right)(-1^n)\sin\left[\left(\frac{\mu\pi}{H}\right)y\right]\exp\left[-\mu t n^2\left(\frac{\pi^2}{H^2}\right)\right] \tag{3.20}$$

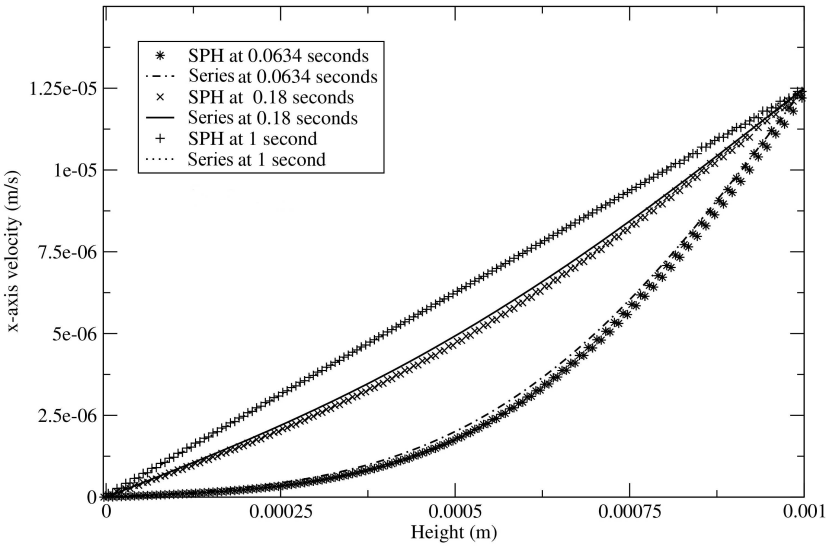

Figure 3.13: Evolution of Couette flow velocity profiles.

The steady state results show good agreement with expected values, with maximum error of 0.5% observed at the mid-point between the plates. The transient result errors are always in the centre of the flow because this is the point furthest from any driving forces or boundary conditions. The Poiseuille flow does not show this behaviour because a body force is applied to all fluid particles. These errors are increased by the use of the repeated sum method for obtaining the second derivative of the velocity field. When modelling cold spray, the elastic-plastic material model will be used which does not require the solution of the second derivative of the velocity field in the momentum equation. Therefore these errors will not effect the evolution of the splat morphology.

	Fluid	Lower boundary	Upper boundary
Dynamic viscosity, μ (Pa·s)	0.001	0.001	0.001
Density, ρ (kg/m^3)	1000	1000	1000
Energy, E (J/kg)	0	0	0
Pressure, p (Pa)	0	0	0
Velocity, $\vec{v}$ (m/s)	0	0	1.25×10^{-6}
Acceleration, $\dot{\vec{v}}$ (m/s^2)	0	0	0
Sound speed, c (m/s)	2.5×10^{-5}	2.5×10^{-5}	2.5×10^{-5}
Initial particle spacing, Δx (m)	6.25×10^{-6}	6.25×10^{-6}	6.25×10^{-6}
Smoothing length, h (m)	8.125×10^{-6}	8.125×10^{-6}	8.125×10^{-6}

Table 3.4: Couette flow initial conditions.

3.1.5 Heat Conduction in Slab

Heat conduction in a three-dimensional homogeneous slab is modelled to explore the effects of heat conduction. The slab has dimensions of 0.5 x 1 x 0.5 metres and is bounded by periodic boundaries in the x- and z-directions with a temperature discontinuity at y = 0.5 metres. A schematic of the problem setup is given in Figure 3.14. The weakly compressible equation of state (see Equation (2.79)) is used, along with a cubic kernel (see Equation (2.30)) and the viscous fluid material model (see Equation (2.85)). The exact material model used has no effect on the conduction test results because no material flow will occur and so the results of this test are applicable to all materials considered in the current work given correct material property descriptions.

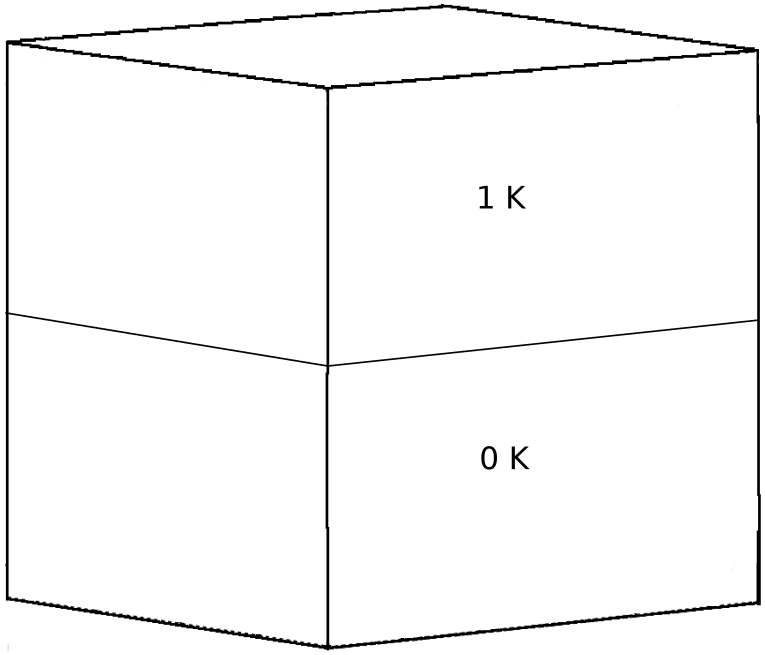

Figure 3.14: Schematic of heat conduction test case.

The exact analytical solution is calculated from the Gauss error functions following Carlsaw and Jaeger [142]. The heat conduction in the initially cold region is calculated using:

$$T = \frac{\sqrt{2}}{2\sqrt{2}} erfc\left(\frac{|x'|}{2\sqrt{x't}}\right) \tag{3.21}$$

whilst the conduction in the initially hot region is calculated using:

$$T = \frac{\sqrt{2}}{2\sqrt{2}} \left[1 + erf\left(\frac{|x'|}{2\sqrt{x't}} \right) \right] \tag{3.22}$$

The developed SPH solver is required to correctly calculate the rates of heating and cooling across the discontinuity utilising the energy condition terms described in Equation (2.64). The temperature of all SPH particles used is plotted along the y-axis and compared against the analytical solution at various time instances in Figure 3.15. The correct rates of heating and cooling across the initial temperature discontinuity can be seen with the numerical results showing good agreement with the analytical solution, the peak error at 20s is 0.5008%.

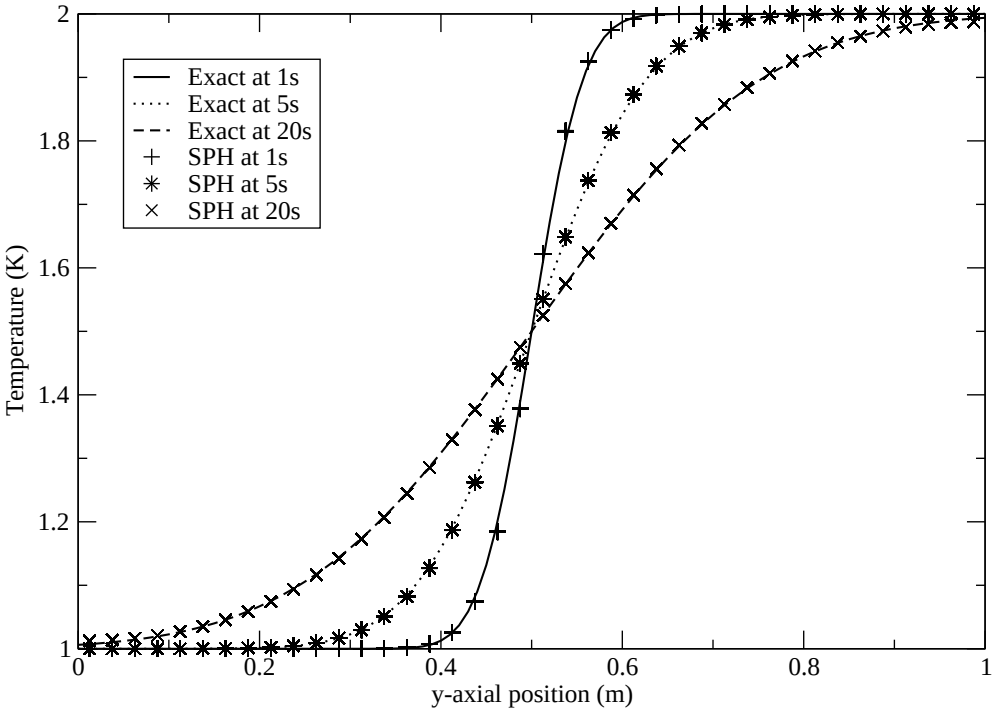

Figure 3.15: Evolution of temperature in heat conduction slab test.

	$y < 0.5$	$y > 0.5$
Dynamic viscosity (μ)	0.001	0.001
Density (ρ), kg/m^3	1000	1000
Energy (E), J/kg	0	0
Pressure (p), Pa	0	0
Velocity ($\vec{v}$), m/s	0	0
Acceleration $\left(\dot{\vec{v}}\right)$, m/s^2	0	0
Temperature (T), k	1	2
Sound speed (c), m/s	2.5×10^{-5}	2.5×10^{-5}
Initial particle spacing (Δx), m	0.01	0.01
Smoothing length (h), m	0.013	0.013

Table 3.5: Heat conduction initial conditions.

3.1.6 Instability Correction

An in depth discussion of the tensile instability is given in Section 1.2.4 which decribes the instability caused by the interaction between a negative pressure or tensile force acting between SPH particles and the kernel used in the calculation of SPH derivatives. The strength of interaction between two particles decreases as the particles move apart and this produces a non-physical reduction in the attractive force between the particles leading to the formation of clumps of particles and potentially the opening of voids in the material. When modelling the cold spray process; the described elastic-plastic material model with a Mie-Grunisen equation of state will be used and this has the potential to produce negative pressures, thus, making the the numerical solution susceptible to this instability. A similar test to that employed by Swegle [119] is used to verify the implemented corrections for this instability described in Equations (2.71) and (2.73). The corrections produce an artificial stress who magnitude is dependant on the kernel employed that acts to restore the correct increase in tensile force as the particles separate.

A 1×1 metre two-dimensional copper block being held under tension is modelled by specifying an initial density lower than the reference density to produce an initial pressure of -6.95461×10^7 Pa; the initial conditions are shown in Table 3.6. A particle near the centre of the block is then given a small perturbation of magnitude 1×10^{-10} m/s. The block is also constrained by a dynamic boundary that prevents the block increasing its volume. A cubic kernel is used for this test case along with the elastic-plastic material model and a Mie-Grunisen equation of state.

It can be seen from Figure 3.17b that the instability is present in the uncorrected solver, the formation of voids in the material is observed as the SPH particles form non-physical clumps. Repeating the same test but with the artificial corrections implemented removes the instability as shown in Figure 3.17c, where no voids or clumps are observed and the particles have remained close to their initial positions.

Mechanical Properties	
Reference Density, ρ_0 (kg/m^3)	9856
Density, ρ (kg/m^3)	8960
Young's Modulus, e (Pa)	124
Poisson's Ratio, ν	0.34
Shear Modulus, G (Pa)	46×10^9
Yield Strength, Y (Pa)	90×10^6
Particle Mass, m (kg)	0.776
Sound Speed, c (m/s)	3940
Initial particle spacing, Δx (m)	0.01
Smoothing length, h (m)	0.013
Mie-Grunisen	
S	1.49
Γ	2.02
Johnson-Cook	
A, (Pa)	90×10^6
B, (Pa)	292×10^6
C, (Pa)	0.025
N	0.31
M	1.09
Reference ϵ_p	1
Thermal Properties	
Specific heat, (C_v) (J/kgK)	383
Thermal conductivity, (k) (w/mK)	386
Melt temperature, (T_m) (K)	1356

Table 3.6: Instability correction test initial conditions.

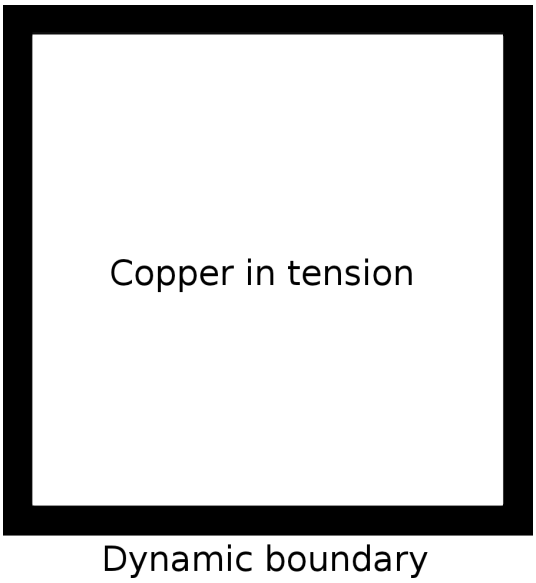

Figure 3.16: Tensile test initial condition schematic.

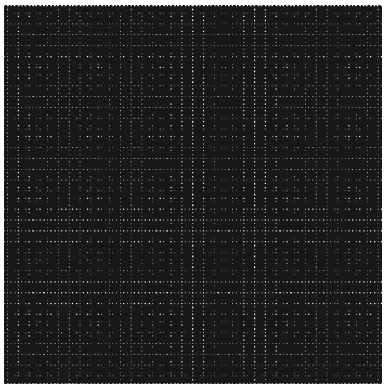

(a) Tensile test inital condition.

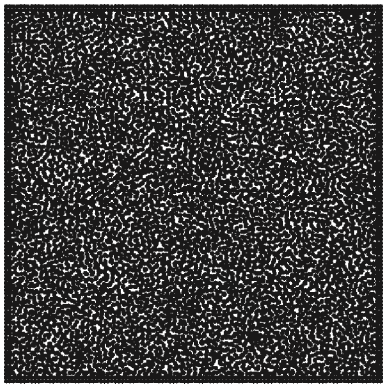

(b) Tensile test without correction at t = 0.0518 s.

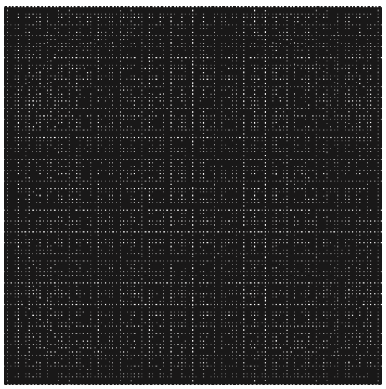

(c) Tensile test with correction at t = 0.0518 s.

3.1.7 Taylor Bar Impact

A Taylor-bar impact is considered to benchmark the accuracy of the developed methodology and will be compared against experimental results of Johnson et al [143] and numerical ones from Libersky et al [114]. In the current work the impact of two identical bars is modelled to examine the symmetry of the numerical scheme, ensuring that the feedstock and substrate responses to an impact are correct and not affected by the orientation of the model. This is equivalent to the reflective boundary setup employed by Libersky et al [114]. Material data from Johnson et al [143] is used with bars of mass 0.00909 kg each travelling at a velocity of 221 m/s; initial conditions and material properties are given in Table 3.7 and a schematic of the problem is illustrated in Figure 3.18. A cubic spline kernel is used along with the elastic-plastic material model and Mie-Grunisen equation of state.

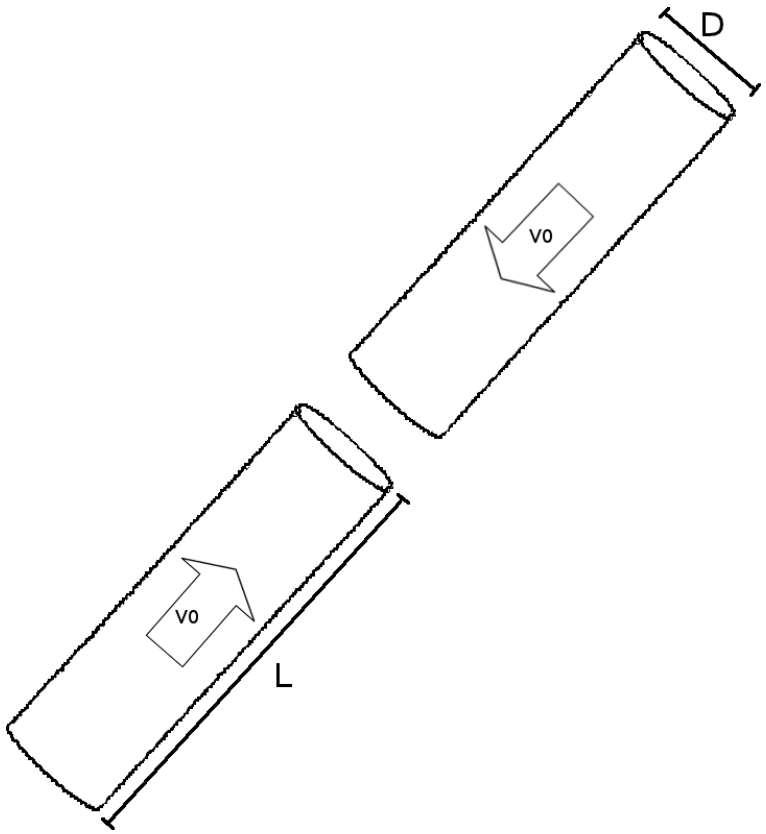

Figure 3.18: Taylor bar initial condition schematic.

The effect of SPH particle count on the resulting impact of the bars was initially investigated, by modelling the impact with increasing particle counts until a significant

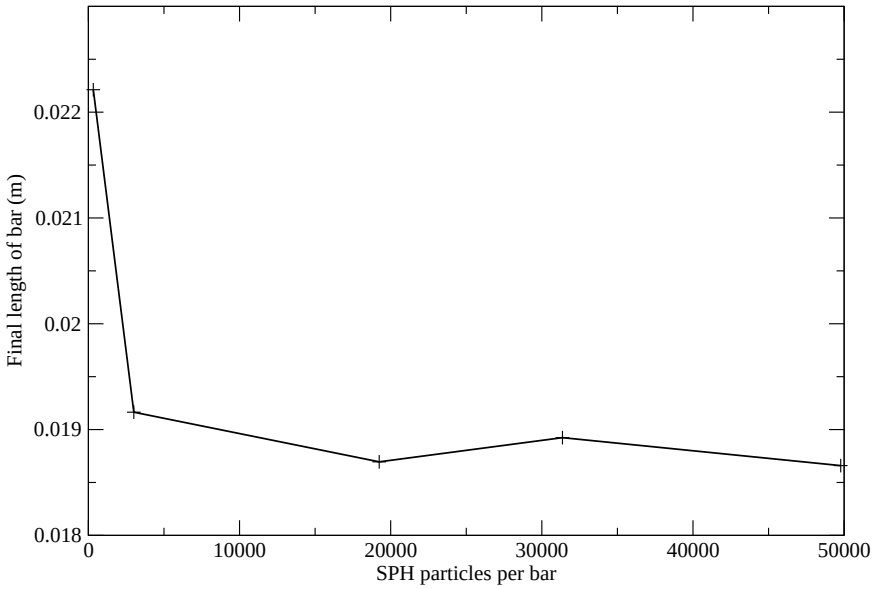

Figure 3.19: Taylor bar particle mass effects.

increase in particle count produces a change in final bar length of less than 2%. The results clearly show the effect of particle count on the modelled impact and can be seen in Figure 3.19. The variation in final length is negligible between the last two data points and so the model is considered converged when utilising 31363 SPH particles per bar.

Figure 3.20 shows a cross-section of the bar deformation during and after impact; the images are taken at 0, 30 and 60μs from left to right, respectively. At 30μs the foot of the bar can be seen to be widening, resulting in a reduction in bar height and plastic strains are limited to this foot region with the highest values in the bottom centre on the interface between the bars as seen in Figure 3.21. By 60 ns the foot has increased in diameter and started to bulge, at this point the initial impact velocity has been expended in heating and straining the bars and a phase of relieving elastic strains is entered. The distribution of Effective Plastic Strain (EPS) at 60 ns is plotted in Figure 3.22. It shows that a significant amount of plastic straining has occurred in the immediate vicinity of the interface with a decrease in plastic strain further up the bar.

Flattening ratio is calculated following Assadi et al [21] using:

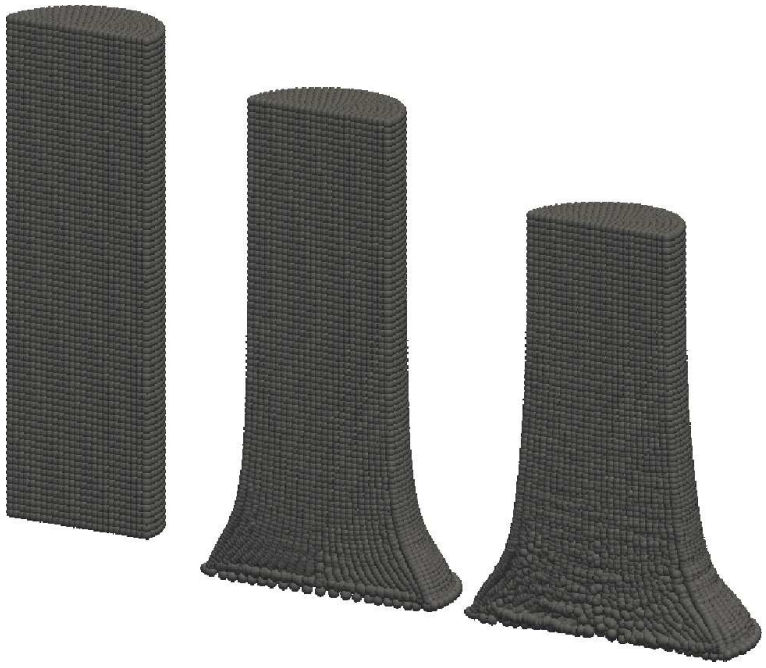

Figure 3.20: Taylor bar evolution.

$$\xi = 1 - \left(\frac{l_d}{l_0}\right) \tag{3.23}$$

where ξ is the flattening ratio, l_0 is the initial bar length and l_d is the current deformed length. Flattening ratio evolution for both bars is plotted against time in Figure 3.23 and is used to determine when the impact is completed. At 60 ns there is a 0.029% variation in flattening ratio and a continued decrease in this property is seen for the remainder of the runtime and so the final length is measured at this point. The oscillations seen in the flattening ratio plot are due to the bars ringing after the impact. The flattening ratios of the bars show close agreement throughout the entire impact and relief phase, demonstrating the symmetry of the impact. A comparison of final bar lengths is presented in Table 3.8.

Johnson et al [143] provided measurements of the experimental bar after impact and these have been used, while Libersky et al [114] did not and their final length is approximated from provided plots of particle positions. From the flattening ratio plot in Figure 3.23 it can be seen that both the top and bottom bars experience equivalent flattening throughout the impact demonstrating the symmetry of the methodology. Good agreement with experiment and previous numerical results was observed, with the final

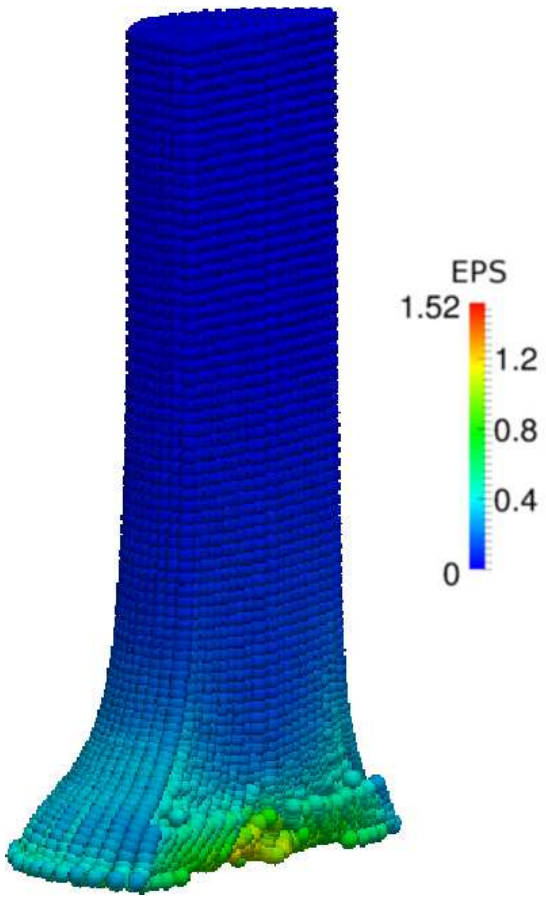

Figure 3.21: Taylor bar EPS cross section at 30×10^{-6} s.

length modelled in the current work exhibiting 4.43% error compared to the experimental bar impact. The current work shows a shorter predicted length than Libersky et al, where the difference in length is small at 0.92%. This shorter predicted length is likely due to the inclusion of thermal softening terms that were absent in the earlier work.

The described Talyor bar impact utilises the complete set of equations that will be used in the cold spray problems and so the good performance of the solver in this test case indicates the solver is capable of capturing the key physical processes involved in the splat formation accurately.

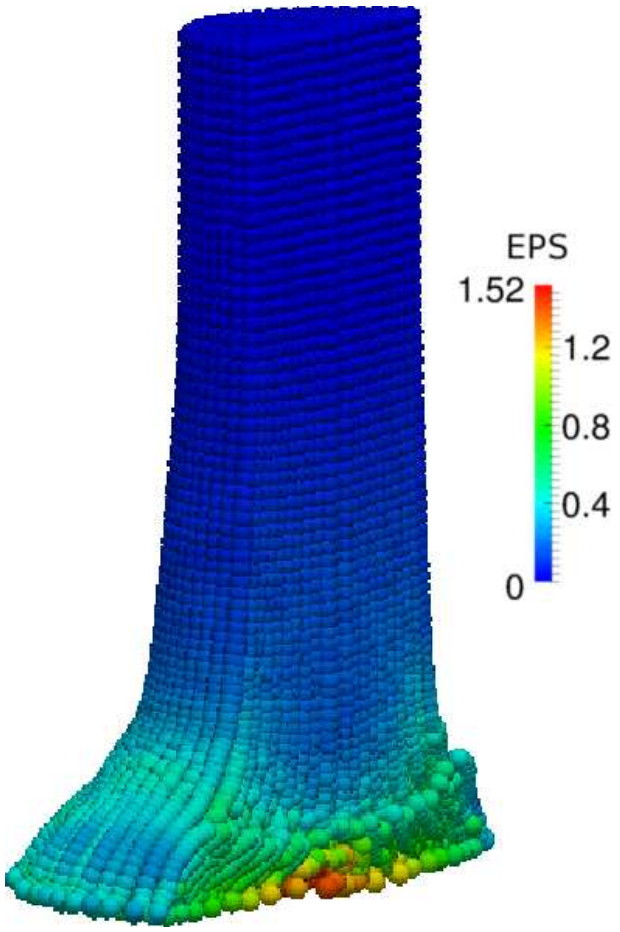

Figure 3.22: Taylor bar EPS cross section at 60×10^{-6} s.

Mechanical Properties	
Density, ρ (kg/m^3)	7890
Young's Modulus, e (pa)	200×10^9
Poisson's Ratio, ν	0.291
Shear Modulus, G (pa)	80×10^9
Yield Strength, Y (pa)	176×10^6
Particle Mass, m (kg)	0.193515×10^{-6}
Sound Speed, c (m/s)	3600
Particle initial spacing, Δx (m)	0.0002923
Smoothing length, h (m)	0.00038
velocity along impact axis, $\vec{v}$ (m/s)	221
Mie-Grunisen	
S	1.8
Γ	1.81
Johnson-Cook	
A (Pa)	175×10^6
B (Pa)	380×10^6
C (Pa)	0.06
N	0.32
M	0.55
Reference ϵ_p	1
Thermal Properties	
Specific heat, (C_v) (J/kgk)	452
Thermal conductivity, (k) (w/mk)	76.2
Melt temperature, (T_m) (k)	1811

Table 3.7: Taylor bar test initial conditions.

	Final Length (m)
Johnson et al [104]	19.8×10^{-3}
Libersky et al [114]	19.1×10^{-3}
Current work	18.9×10^{-3}

Table 3.8: Taylor bar comparison data.

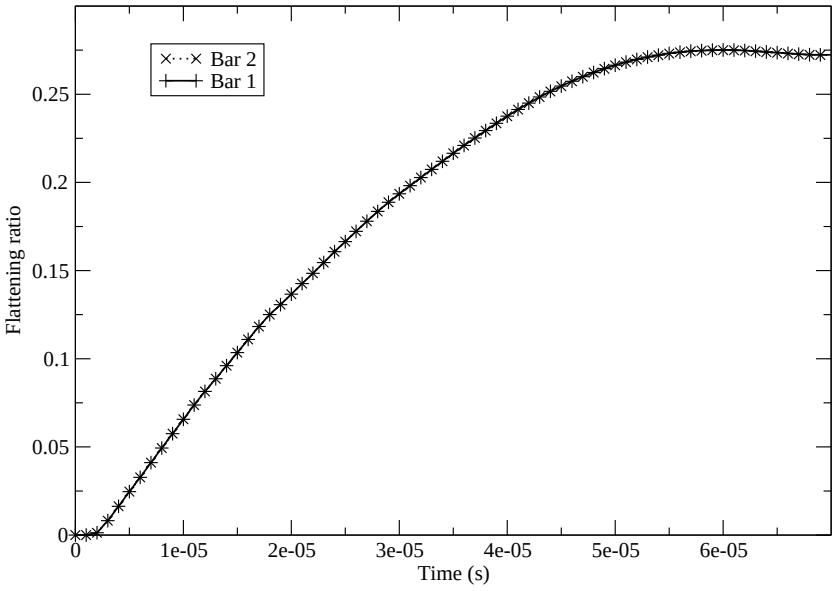

Figure 3.23: Taylor bar flattening ratio against time.

3.2 Scalability and Performance Benchmarks

Having explored the accuracy of the SPH solver, the efficiency of solution and speed up gained from parallelisation is examined. For these tests a stationary cube of copper with a volume of 1 m^3 is modelled using the elastic-plastic material model and a cubic kernel. The material is fully bounded by periodic boundaries, and the initial conditions are shown in Table 3.9.

SPH particle mass, spacing and smoothing length, h, are varied to produce differing particle pair interaction totals and the benchmark time is taken for a single time step. Benchmarks are performed on a 32 thread linux PC running at 3.1 GHz. Total pair interactions are listed for the benchmark because they better describe the computational cost of an SPH calculation than particle count. Using the same number of SPH particles but varying the smoothing length or changing to a kernel with a different support domain, kh, alters the total number of particle interactions present in the problem as more or less neighbour particles need consideration. This changes the amount of computational effort required to compute a problem for the same total particle count. The first benchmark is the time taken for a single thread to process a given number of pairs. The data is plotted in Figure 3.24. It shows that peak efficiency is reached at 39610000 pairs with a computational time of 6×10^{-6} seconds per pair.

With the single thread benchmark established, the effects of adding more threads to the calculation is now examined. A large test problem is used containing 116170769 pairs and the number of threads used is varied from 2 to 30. The total time taken to compute one timestep for one pair is plotted against the number of threads in Figure 3.25. There is an inital decrease in computational time to a peak performance of 1.94×10^{-6} seconds per pair utilising 10 threads, when the overheads of setting up the parallel computation are offset by the speed up gained. After this point no further perfomance gain is seen for the remaining thread counts considered of $18, 28, 30$; for the test problem specified these equate to $6453931, 4148956, 3872358$ pairs per thread, respectively. These pair per thread counts are below the value required for peak performance calculated in the single thread performance benchmark, indicating the problem size is not large enough to make best use of the available thread capacity, the use of larger test problems is restricted by the avaliable memory. It is also possible the problem is memory bound and the performance

Mechanical Properties	
Reference Density, ρ_0 (kg/m^3)	9856
Density, ρ (kg/m^3)	8960
Young's Modulus, e (Pa)	124
Poisson's Ratio, ν	0.34
Shear Modulus, G (Pa)	46×10^9
Yield Strength, Y (Pa)	90×10^6
Particle Mass, m (kg)	0.776
Sound Speed, c (m/s)	3940
Mie-Grunisen	
S	1.49
Γ	2.02
Johnson-Cook	
A, (Pa)	90×10^6
B, (Pa)	292×10^6
C, (Pa)	0.025
N	0.31
M	1.09
Reference ϵ_p	1
Thermal Properties	
Specific heat, (C_v) (J/kgK)	383
Thermal conductivity, (k) (w/mK)	386
Melt temperature, (T_m) (K)	1356

Table 3.9: Material data for scalability tests.

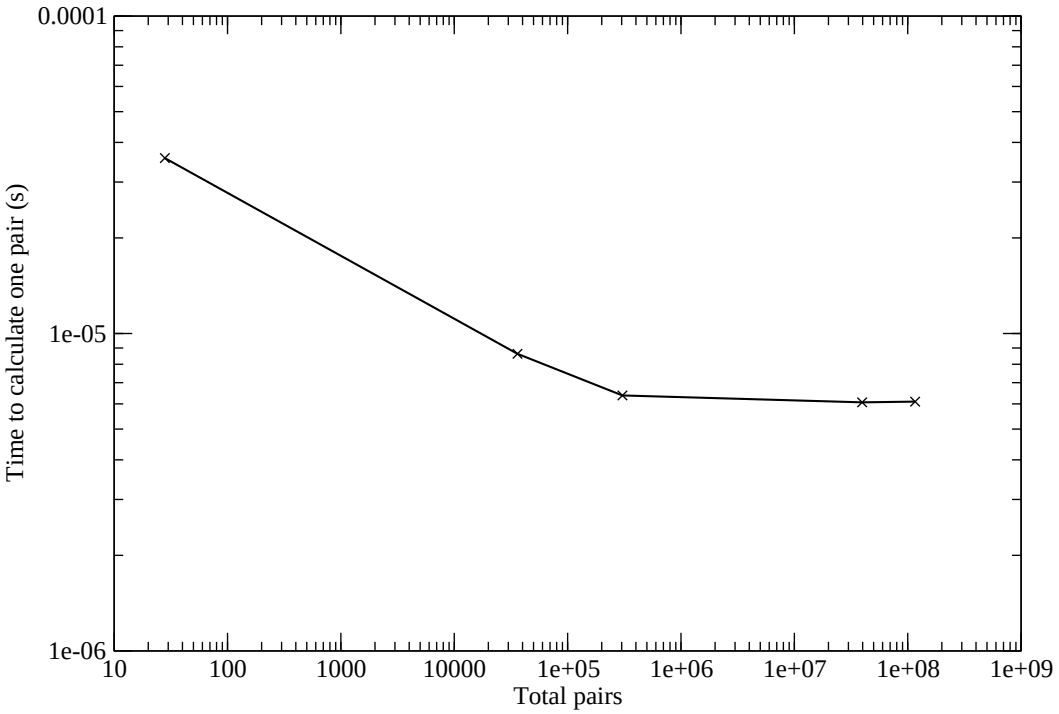

Figure 3.24: Single-thread benchmark.

is limited by memory bandwidth and full processor caches.

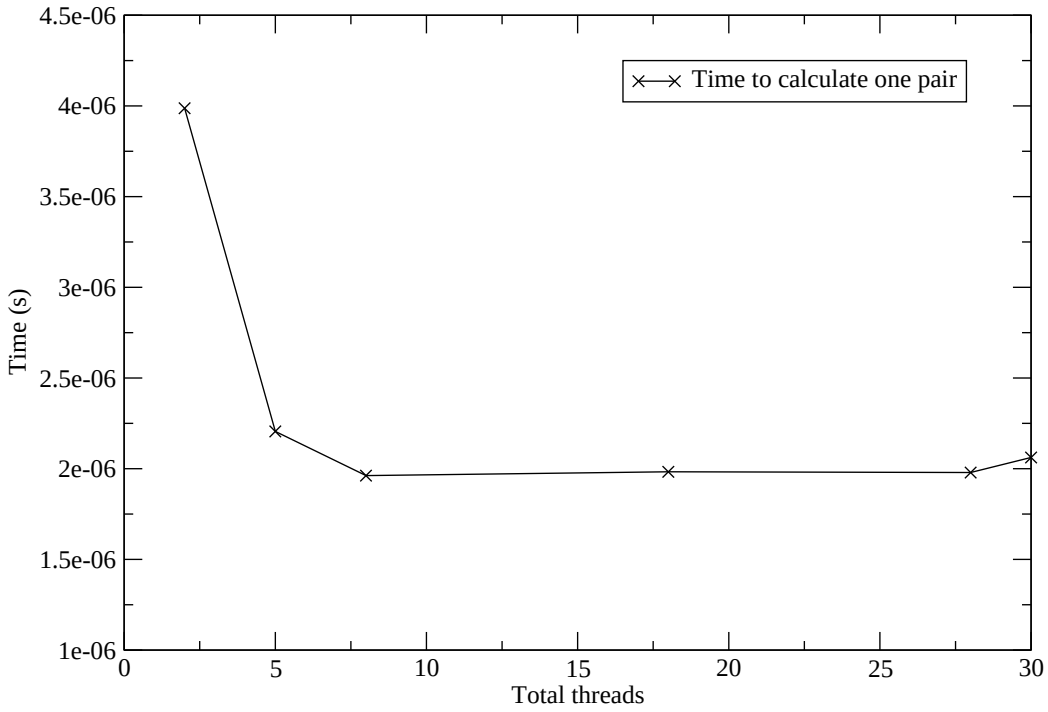

Figure 3.25: Multi-thread benchmarking.

The speed up (S) and efficency (E) of the parallel processing scheme can be calculated from:

$$S = \frac{t_1}{t_p} \tag{3.24}$$

$$E = \frac{t_1}{pt_p} \tag{3.25}$$

where t_1 is the time taken to solve the problem using a single thread, t_p is the time taken when using parallel processing and p is the number of threads. The time taken to calculate a single time step of the described test porblem using 116170769 SPH pairs is used to calculate the efficency. A single thread takes 774.2 seconds to compute a time step whilst 10 parallel threads complete the timestep in 225.9 seconds, resulting in

a speed up, S, of 3.427 with an efficency, E, of 0.342. This shows the parallel solver implemntation will reduce the time required to model cold spray splat formation by a third when compared to the same methodology in a serial implementation.

Chapter 4

Boundary Conditions for an Isolated Three-Dimensional Cold Spray Splat Morphology

Cold sprayed coatings are formed from the build up of many separate splat formation events, however, little is known about the physical processes involved in the formation of these separate splats, due to the difficulties in obtaining accurate qualitative and quantitive data from experiments. Progress has been made in recent years towards the development of suitable modelling methods, but none of the existing methods are entirely satisfactory (refer to Sections 1.1 and 1.2.5 for more detail). The current work aims to improve the understanding of the final coating properties and how they are related to initial feedstock properties and the parameters used in the spray process. Coating formation is a complex process, because at any given time during formation there will be many different splats at different points in their evolution within a small area of substrate. In addition to to the irregular impact intervals, no two feedstock particles will be exactly the same with variance in shape, size, exact material properties, heating and velocity, all of which affect the final splat morphologies and coating properties. Before considering this complex process a deeper understanding of the formation of a single splat is required.

Modelling a completely isolated three-dimensional feedstock impact is challenging if the models used are to remain efficient enough to be practical. The components coated are generally significantly larger than the average feedstock diameter of a few

tens of micro-metres and so modelling the whole substrate is undesirable. Instead, a section of the substrate is modelled and appropriate boundary conditions are used to approximate a relatively massive substrate. The application of unsuitable boundary conditions could introduce undesired physical effects to the modelled substrate such as shockwave reflections that would not occur in an infinite substrate. Consequently, it is important to understand the effects of potential boundary conditions and to select the most suitable treatment.

4.1 Problem Definition

A series of three-dimensional feedstock impacts have been considered utilising different boundary conditions; a basic domain with no special treatment, a periodic domain and a zero impedance domain. In each case, the modelled copper substrate will have dimensions of $60 \times 60 \times 60\mu$m and is impacted by a 10μm diameter copper feedstock travelling at 600 m/s; material properties of the copper used are given in Table 4.1.

A cubic spline kernel (see Equation (2.30)) is used along with the elastic-plastic material model, Mie-Grunisen equation of state and heat conduction terms. The artificial viscosity and instability corrections are also included.

Considering the properties of each of the boundary conditions, it is possible to form a hypothetical prediction of the suitability of each model. The basic domain model represents a finite substrate with the dimensions of the modelled material and so has the potential for stress reflections from the substrate edges which would not occur in an infinite substrate. Similarly, the periodic domain can be considered to model an infinite series of feedstock impacts along each axis perpendicular to the impact axis, although this accurately models a repeating infinite substrate it does not provide a truly isolated feedstock impact. The zero impedance boundary allows conduction and shock propagation from the domain meeting the requirement for an infinite domain and an isolated feedstock impact. In order to examine the effects of the boundary condition selection and to test the above hypothesis, results of models using these boundary conditions will be compared and examined. The three test cases will be examined in detail before comparisons are made. Finally, a suitable boundary condition setup will be chosen and used to model single feedstock impacts. A schematic of the test problem is given in Figure 4.1

Mechanical Properties	
Density, ρ (kg/m^3)	8960
Young's Modulus, e (Pa)	124
Poisson's Ratio, ν	0.34
Shear Modulus, G (Pa)	46×10^9
Yield Strength, Y (Pa)	90×10^6
Particle Mass, m (kg)	0.776
Sound Speed, c (m/s)	3940
Initial particle spacing, Δx (m)	0.01
Smoothing length, h (m)	0.013
Mie-Grunisen	
S	1.49
Γ	2.02
Johnson-Cook	
A, (Pa)	90×10^6
B, (Pa)	292×10^6
C, (Pa)	0.025
N	0.31
M	1.09
Reference ϵ_p	1
Thermal Properties	
Specific heat, (C_v) (J/kgK)	383
Thermal conductivity, (k) (w/mK)	386
Melt temperature, (T_m) (K)	1356

Table 4.1: Isolated splat formation boundary condition test material properties.

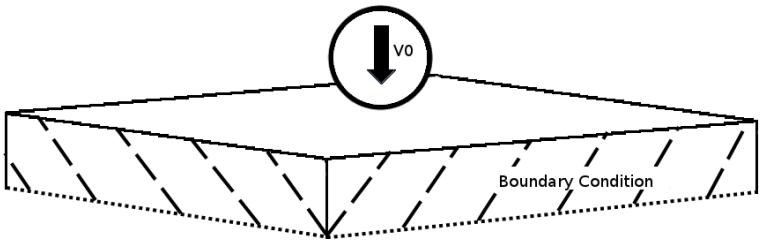

Figure 4.1: Schematic of initial conditions of feedstock and substrate.

Two cross sections will be taken through the substrate in order to examine the effects of the boundary condition, one parallel to the y-axis and another parallel to the x-axis as shown in Figures 4.2 and 4.3 respectively.

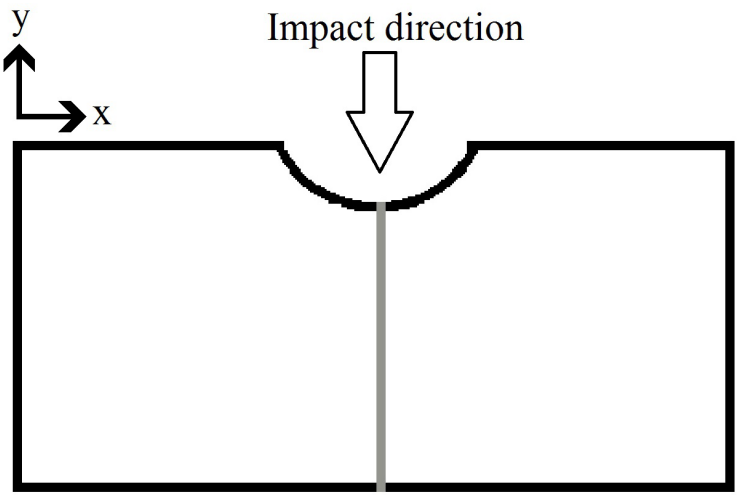

Figure 4.2: Schematic of y-axis cut section used for boundary condition suitability tests.

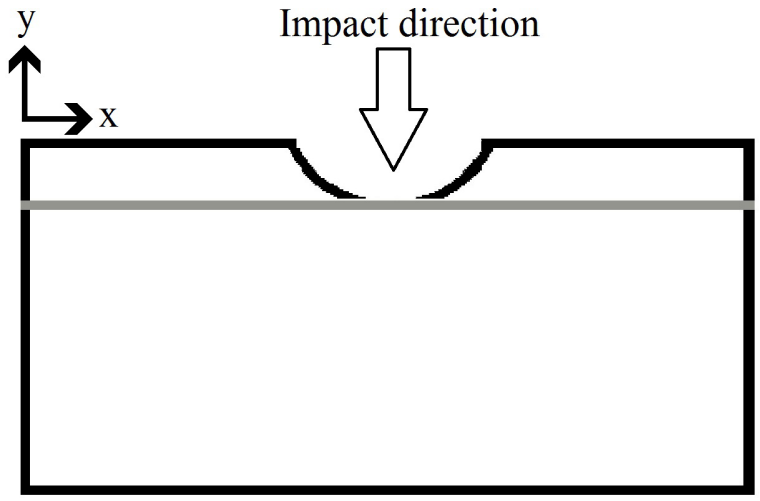

Figure 4.3: Schematic of x-axis cut section used for boundary condition suitability tests.

4.2 Particle Mass Independence

In order to ensure the solutions are independent of the SPH particle mass used, the zero impedance model is executed at steadily increasing resolutions and the peak pressure at the centre of the feedstock is been monitored. Resulting pressures are plotted against the total SPH particles in the feedstock in Figure 4.4 and shows a rapid decrease in calculated pressure with values gradually approaching a minimum pressure as the number of SPH particles is increased. A change in peak pressure of only 2.9% is seen between the 4225 and 8217 SPH particle count case, the model is therefore considered to have converged at 4225 particles in the feedstock. This number of SPH particles in the feedstock corresponds to a particle mass of 1.1×10^{-15} kg, resulting in a total particle count of 1444224 across the whole problem. This mass will be used for all of the boundary condition test cases in this chapter.

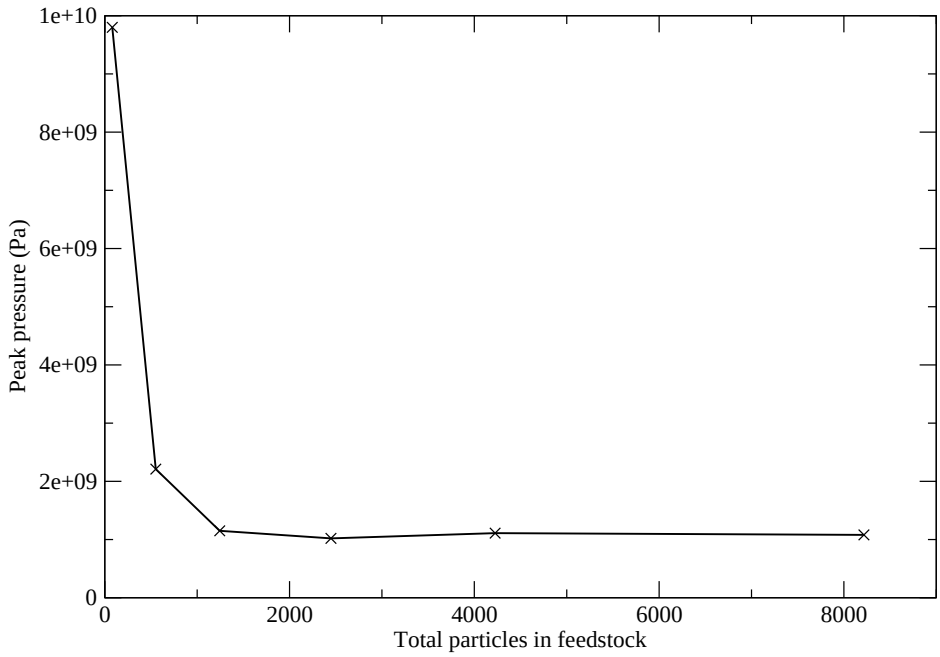

Figure 4.4: SPH particle mass independance.

4.3 Boundary Condition Selection

Three different boundary condition configurations and their effect on the substrate and feedstock properties have been investigated. A detailed disscusion of each set of results is given in Appendix A. This section compares the effects of these configurations to determine the one most suitable for approximating an isolated feedstock impact. A common feature of all of the configurations was the strong localisation of the energy, temperature and EPS profiles at the impact site. A comparison at 30 ns of these profiles along both the y-axis and x-axis cross-sections are shown in Figures 4.5 to 4.10; the close agreement of these profiles proves that the selection of boundary condition configuration has had no effect on the distribution or magnitude of these properties.

The most significant effects are seen in the distribution of Von Mises stress within the substrate as shown in Figures 4.11 and 4.12. In the y-axis direction (see Figure 4.11) stresses for all three combinations show some agreement at the feedstock/substrate interface but soon start to diverge from each other. All of the profiles exhibit a trough

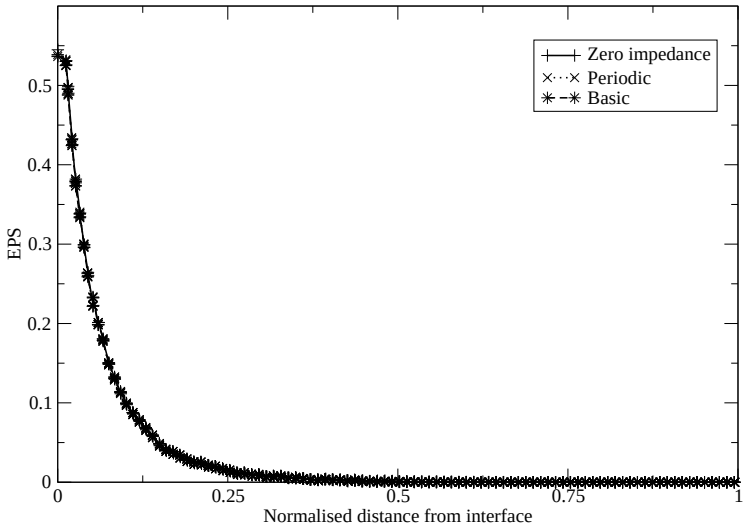

Figure 4.5: Comparison of EPS profile along the y-axis at 30 ns.

feature at a normalised distance of 0.125 from the interface. In this region there is greater agreement between the periodic and zero impedance models than the basic and zero impedance model. At distances between 0.2 and 0.7 this is no longer the case and instead there is best agreement between the basic and zero impedance domains. At distances greater than 0.7 only the zero impedance model shows the expected smooth decrease in stress whilst the periodic and no special treatment boundary condition models show oscillatory behaviour indicating shock reflections off the boundaries.

The x-axis profiles show greater differences between the boundary configurations because in this direction the domain boundaries are much closer to the impact site. The zero impedance model shows an increased level of Von Mises stress at the impact site and the boundary when compared to the other configurations. The zero impedance boundary condition in this case is allowing both the compression and relief waves to propagate out of the domain whilst the untreated domain reflects the waves back into the domain while the periodic configuration wraps the domain allowing a departing wave to re-enter the domain from the opposite side. The zero impedance model shows a more pronounced spike in stress at the flanks of the substrate crater. However, this feature appears to be eroded in the other configurations considered. The large differences in stress profiles is

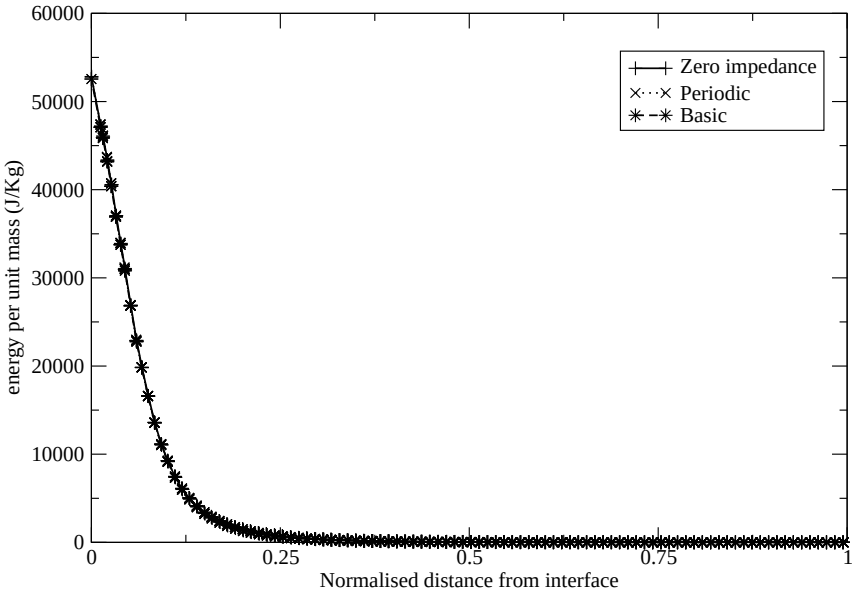

Figure 4.6: Comparison of energy profile along the y-axis at 30 ns.

seen closer to the interface and are caused by these stress reflections propagating back towards the feedstock and possibly affecting the splat morphology.

As well as considering the boundary effects on the substrate, the Von Mises stress distribution within the feedstock will also be investigated because this property demonstrated the greatest susceptibility to the boundary treatment. Peak stresses will be experienced in the initial phases of the impact when the impact velocity is at its peak and impact pressures are limited to a small region of the feedstock/substrate. The impact site is positioned far enough away from the enclosing substrate boundaries that peak stresses should remain unaffected by the selection of boundary treatment. The exact distribution of stress within the feedstock and substrate at any given time will vary however due to the reflection, reintroduction or damping of the stress waves caused by the selected boundary treatment. Von Mises stresses have been measured at $10, 20$ and 30 ns for each model and their maximum and minimum levels throughout the splat formation are presented in Table 4.2. As expected peak stresses are unaffected by the boundary condition whilst the zero impedance domain shows a 29% variance from the

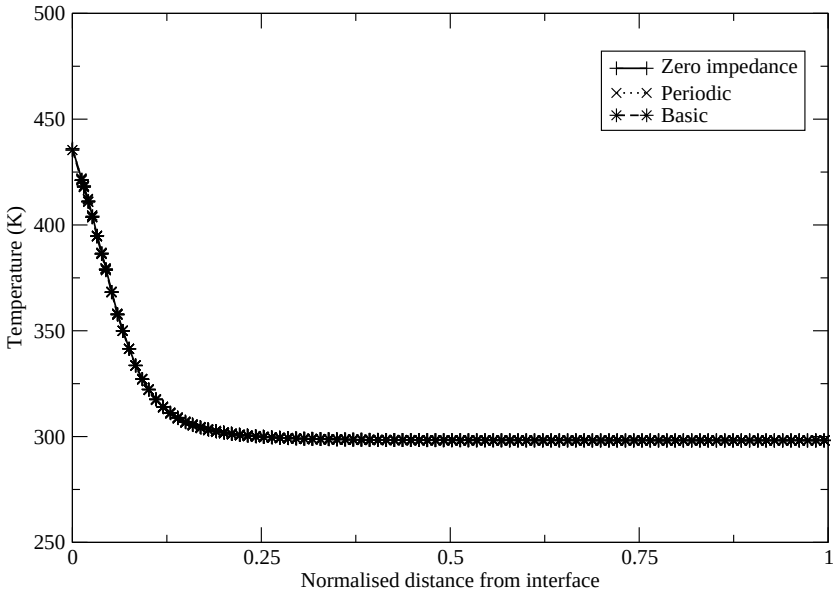

Figure 4.7: Comparison of temperature profile along the y-axis at 30 ns.

untreated domain and a 33% variance from the periodic domain minimum stress. In all cases the peak stress is observed at 20 ns and the lowest stresses at 30 ns. The pattern of stress waves in the untreated and periodic domains is complex and superposition of these waves is causing the observed changes in stress, and the resulting observed differences in minimum values.

Contours of Von Mises stresses in the feedstock at 30 ns are shown in Figure 4.13. All three of the splats exhibit the same general characteristics of stress distribution, the peak stresses are located around the feedstock/substrate interface and the lowest stresses from a band in the middle of the splat with an area of increased stress at the top centre of the splat.

The splat morphology at this time shows no significant differences between the boundary conditions, and the settling time to a constant flattening ratio shows negligible variation between boundary condition configurations. This is because the impact is domiated by the plastic deformation of the splat and EPS is highly localised at the impact interface away from the boundary.

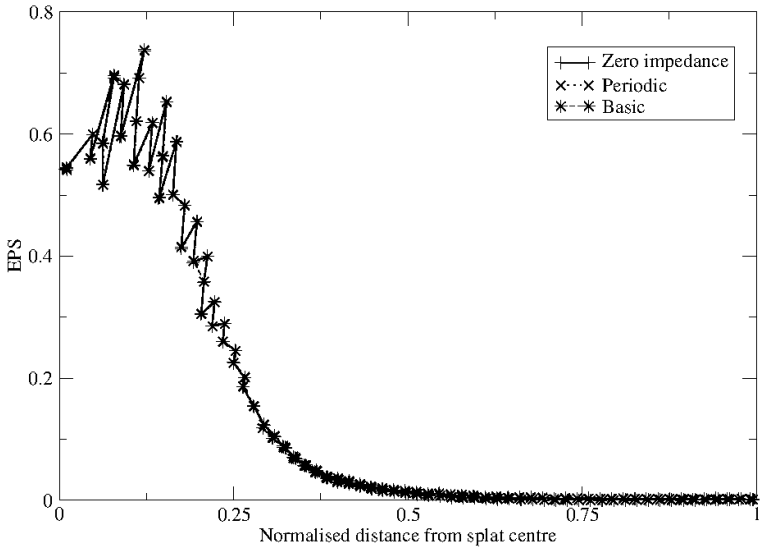

Figure 4.8: Comparison of x-axis EPS profiles at 30 ns.

For the cases considered the largest effect of varying the boundary conditions was found to be on the Von Mises stress profiles, with little to no variance in properties such as EPS, energy and temperature. Additionally, the flattening ratios, settling times and morphologies of the splats show close agreement between the boundary configurations examined. The splat formation process is dominated by plastic deformation and so these similarities in morphology and settling time are not surprising when the close agreement of the EPS, temperature and energy profiles are considered.

The periodic and untreated boundary condition domains do not allow for shockwave propagation out of the domain and so do not accurately approximate an isolated feedstock impact onto a relatively massive substrate. The zero impedance boundary does however allow this and been shown to introduce only slight oscillations in the Von Mises profiles which are restricted to within a narrow range of the boundary. For this reason the zero impedance boundary conditions will be used in the further analysis of isolated splat impacts.

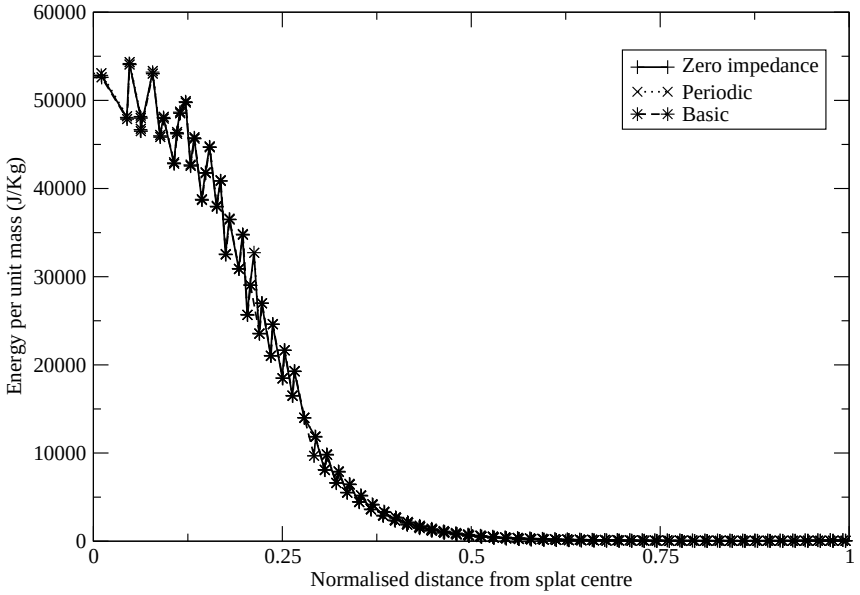

Figure 4.9: Comparison of energy profile along the x-axis at 30 ns.

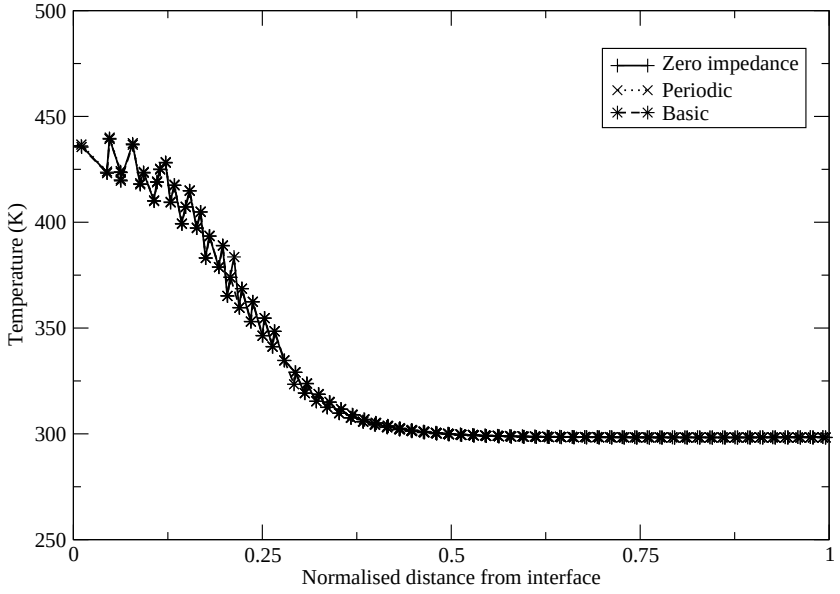

Figure 4.10: Comparison of temperature profile along the x-axis at 30 ns.

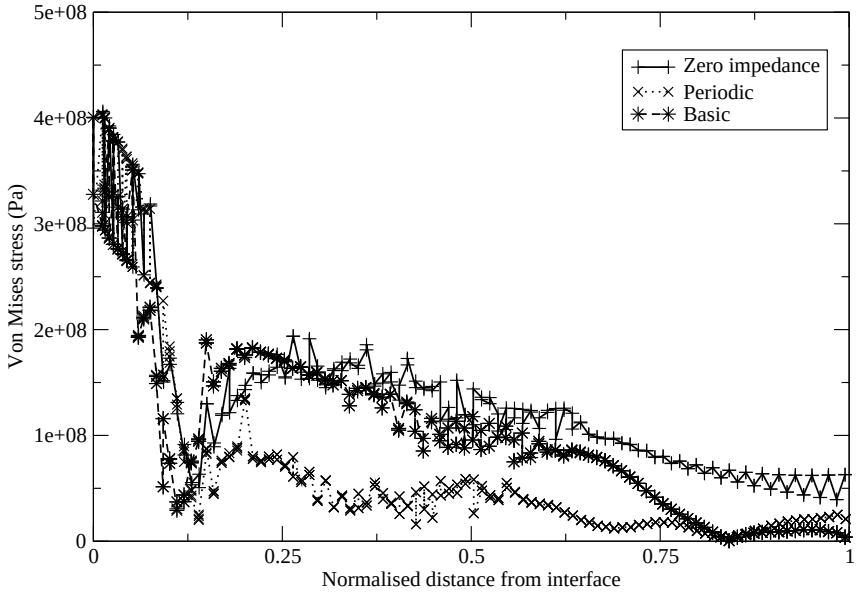

Figure 4.11: Comparison of y-axis Von Mises stress profiles at 30 ns.

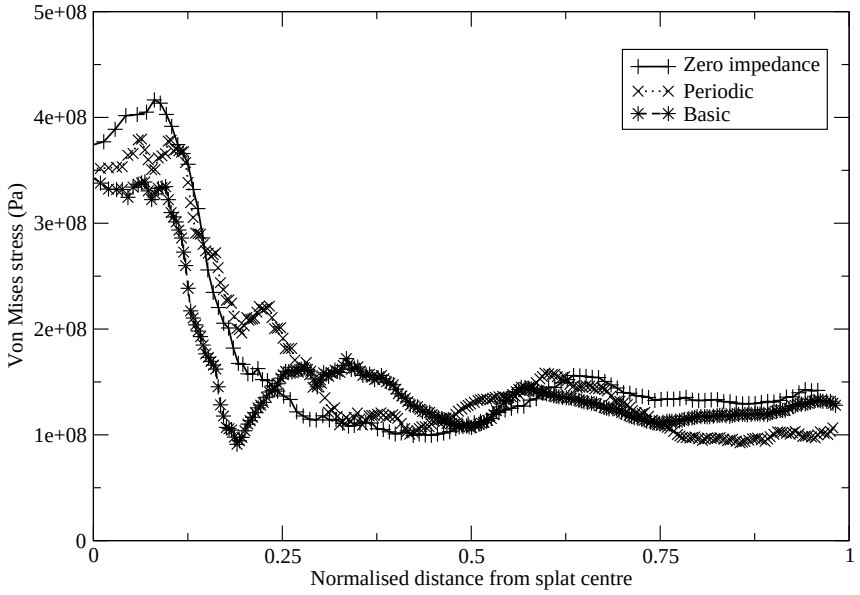

Figure 4.12: Comparison of x-axis Von Mises stress profiles at 30 ns.

Treatment	Minimum Von Mises (Pa)	Maximum Von Mises (Pa)
None	3.4×10^7	4.76×10^8
Periodic	3.3×10^7	4.76×10^8
Zero impedance	4.38×10^7	4.76×10^8

Table 4.2: Comparison of levels of Von Mises stress in the feedstock.

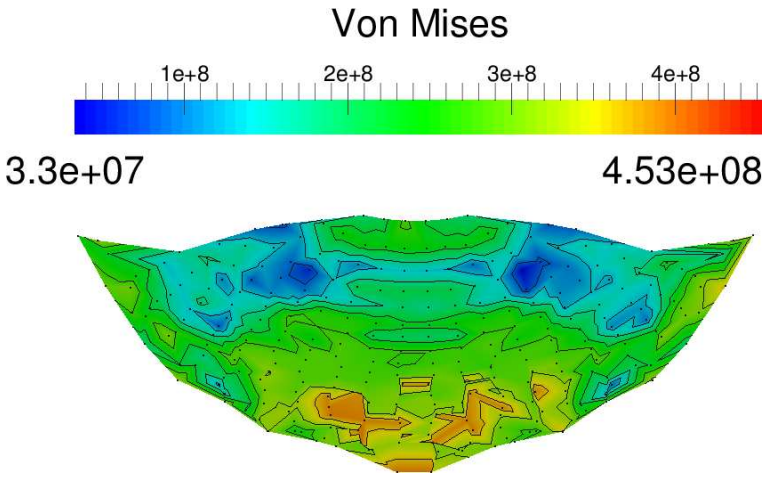

(a) Von Mises for the basic domain.

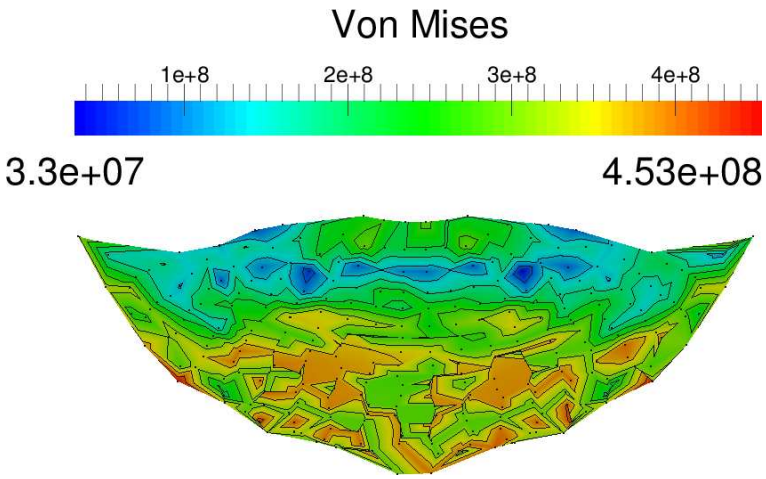

(b) Von Mises for the periodic domain.

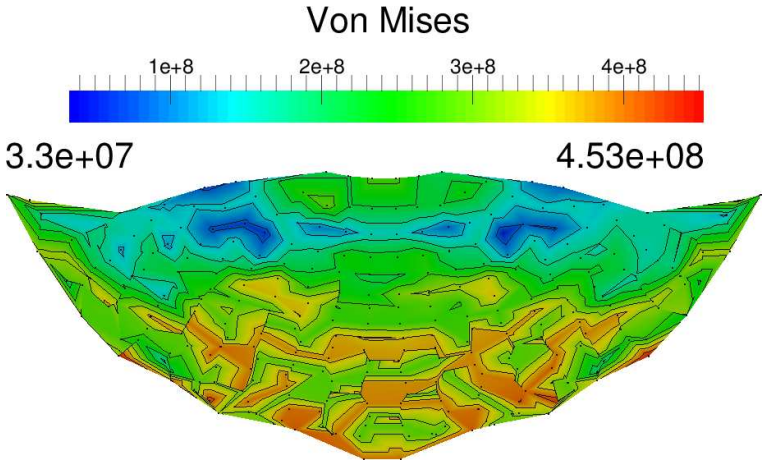

(c) Von Mises for the zero impedance domain.

Figure 4.13: Comparison of Von Mises stress in feedstock at 30 ns for different boundary conditions.

4.4 High Temperature Zero Impedance Domain

Previous studies of the effect of the boundary condition where performed using a room temperature feedstock (298.15 K) and concluded that a zero impedance domain best approximates a substrate that is relatively massive when compared to the feedstock. During this analysis the energy and temperature profiles showed no effect from the boundary. A typical gas jet temperature used for cold spraying copper is 593.15 K [3]. To test the boundary condition in an extreme case of particle heating, a feedstock particle with an initial temperature of 593.15 K is modelled impacting the substrate and the results analysed to ensure the suitability of the zero impedance boundary at this temperature. No heating of the substrate by the carrier gas jet is assumed and so the substrate initial temperature is 298.15 K.

The flattening ratio and splat height is shown in Figure 4.23. Due to the elevated feedstock temperature, the splat experiences greater flattening and the additional heat conducted into the substrate has also resulted in a deeper crater being formed than was seen for the room temperature impact (see Figure A.21). A steady-state morphology is also obtained 1 ns later than the low temperature model, these effects will be discussed in the next chapter due to them being a result of the temperature increase rather than a specific interaction with the boundary conditions.

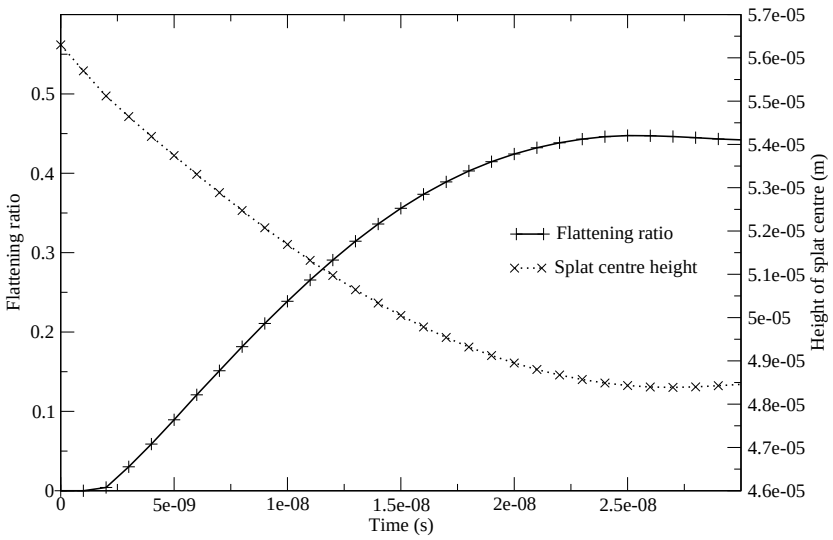

Figure 4.14: Flattening ratio and splat centre height for high temperature zero impedance boundary model.

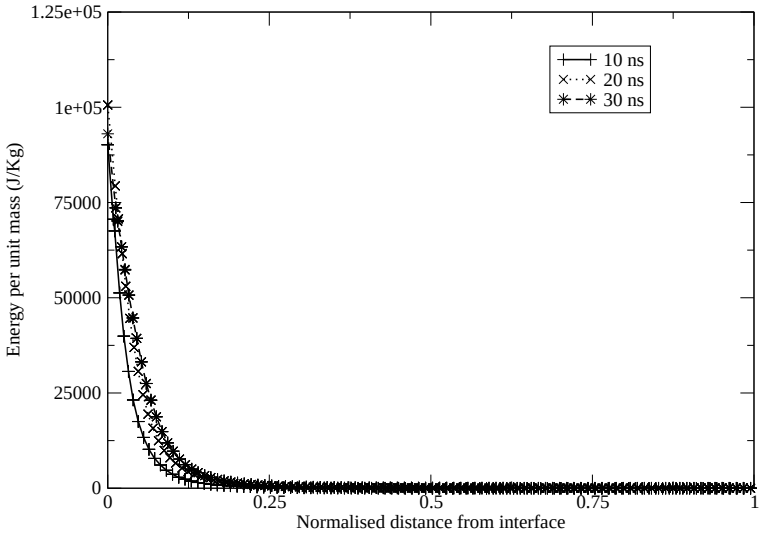

Figure 4.15: High temperature zero impedance domain energy profile along the y-axis.

The temperature, energy and EPS profiles show the expected localisation at the impact site with no contact with or effect from the boundary visible. The Von Mises profiles in Figure 4.16 indicate that the stress wave has come in contact with the boundary somewhere between 10 and 20 ns. There is evidence of a slight oscillatory stress feature near the boundary from 20 ns caused by the approximation of an infinite substrate. This feature is of relatively low amplitude and does not appear to propagate far into the substrate. The overall trend of the stress profiles in this noisy region is still that of a smooth reduction in stress without reflections off a material surface. When compared to the Von Mises profiles for the lower temperature splats the substrate shows the expected reduction in stress corresponding to an increased temperature caused by conduction from the hotter feedstock.

The profiles of energy, Von Mises stress, temperature and EPS along the x-axis cut section (see Figure 4.3) are plotted correspondingly in Figures 4.19 to 4.22.

The profiles of energy, temperature and EPS show strong localisation at the impact site and have not been affected by the boundary condition even at these elevated temperatures. The Von Mises stress profiles however show interaction with the boundary for all three time instances considered. In the immediate vicinity of the boundary there is

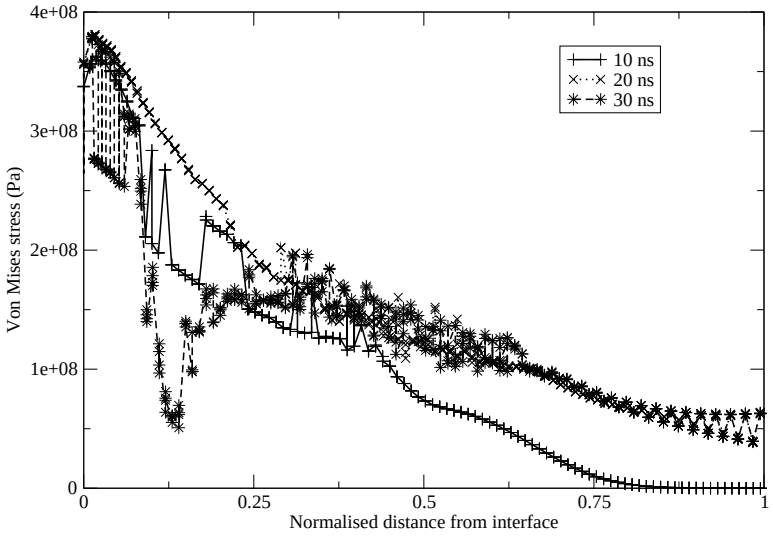

Figure 4.16: High temperature zero impedance domain y-axis Von Mises stress profile.

a slight oscillatory feature similar to that seen along the y-axis profile. The amplitude remains small and the propagation into the substrate is limited and so the effect on the dynamics of the splat formation is negligible. Contours of Von Mises stress within the feedstock are shown in Figure 4.23.

The higher temperature splat exhibits lower levels of Von Mises stress than those seen in the lower temperature zero impedance model (Figure A.30) due the higher initial temperature softening the feedstock even before the impact has started. In general terms the high temperature impact shows the same degree of interaction with the boundary treatment as the lower temperature impacts making the zero impedance boundaries a suitable treatment even at elevated impact temperature. This chapter is concerned with the specific effects of the boundary treatment rather than any particular initial impact conditions and so a deeper analysis of the temperature effects will be made in the next chapter.

4.5 Summary

The analysis presented in this chapter has been aimed at investigating the effects of

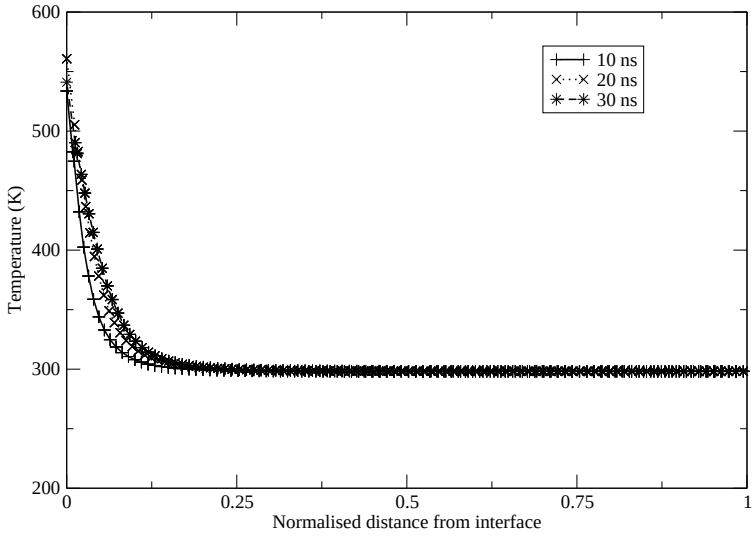

Figure 4.17: High temperature zero impedance domain temperature profile along the y-axis.

the boundary conditions on the splat formation event rather than being an in-depth investigation of the feedstock impact. The zero impedance boundary treatment was found to replicate an isolated splat impact most accurately. Additionally, the boundary was shown to produce only a small amount of deviation from expected results, this disturbance remains limited to the edges of the substrate and does not effect the splat itself. The boundary was tested at an elevated temperature and was shown to produce good results with the increased temperature having no effect on the boundary interaction. This zero impedance condition will be used in the following chapter to investigate the splat formation in greater depth.

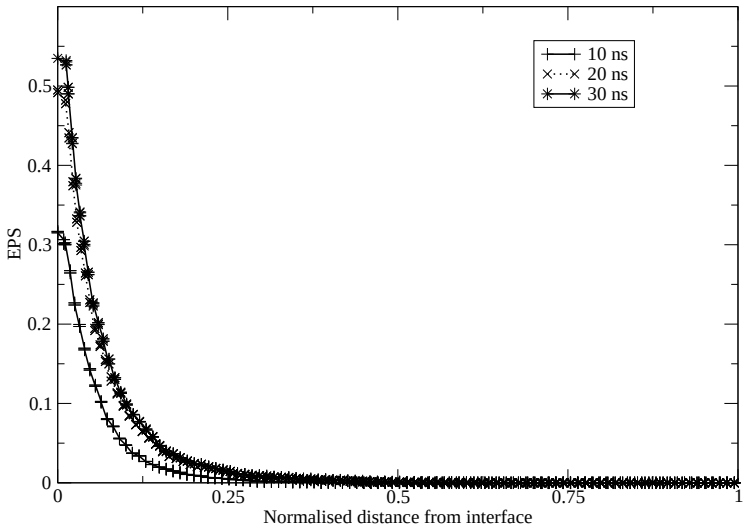

Figure 4.18: High temperature zero impedance domain EPS profile along the y-axis.

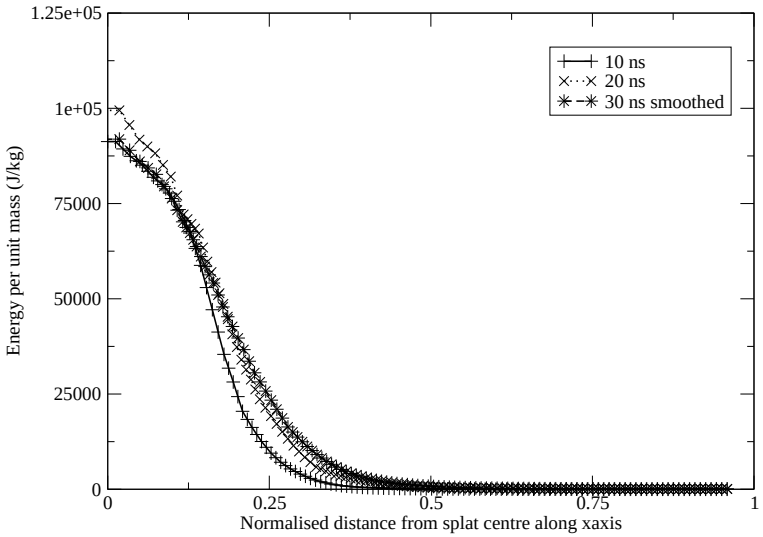

Figure 4.19: High temperature zero impedance domain energy profile along the x-axis.

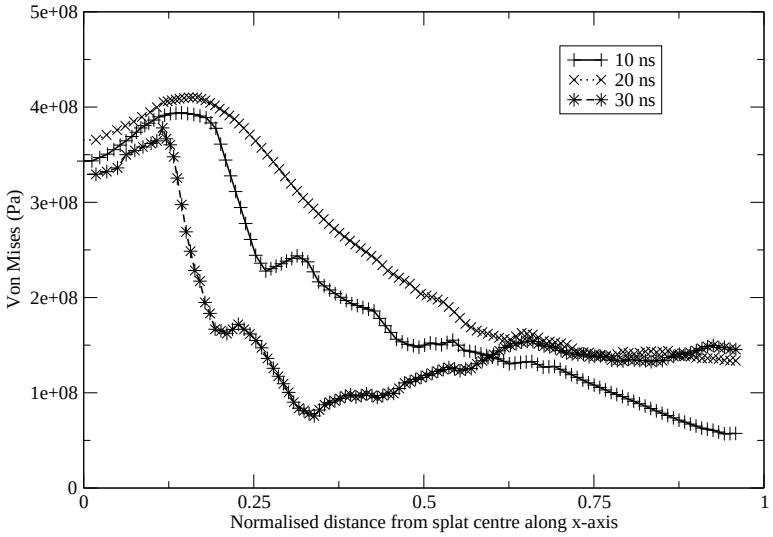

Figure 4.20: High temperature zero impedance domain Von Mises' stress profile along the x-axis.

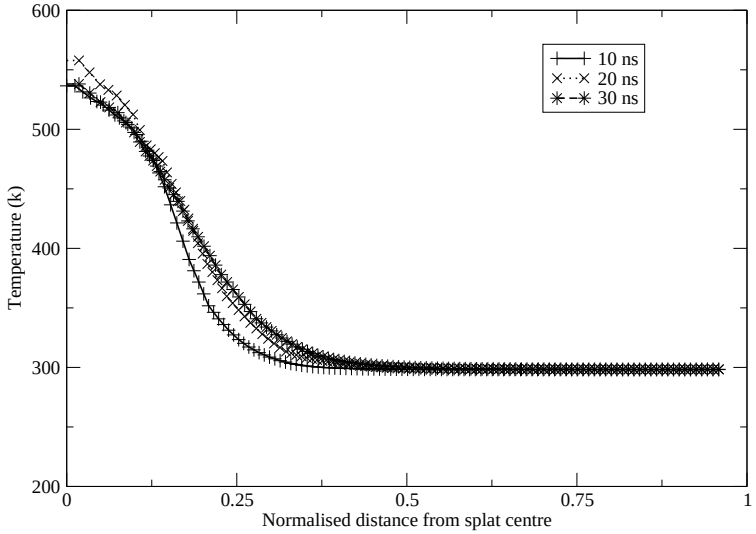

Figure 4.21: High temperature zero impedance domain temperature profile along the x-axis.

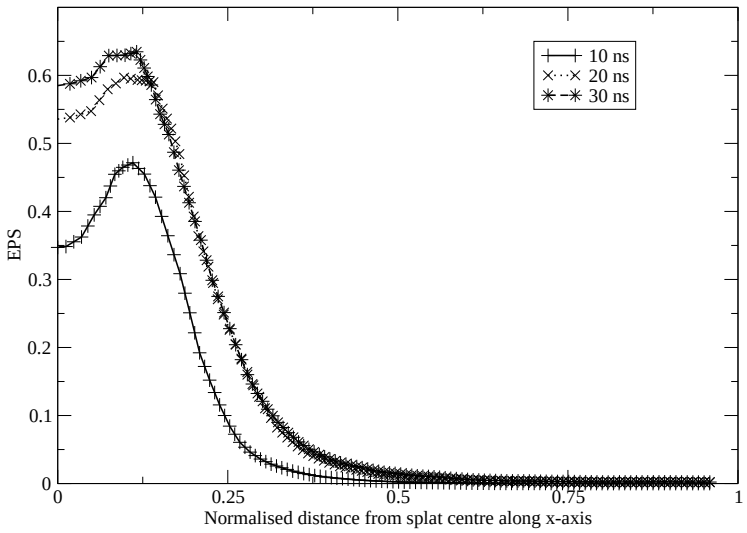

Figure 4.22: High temperature zero impedance domain x-axis EPS profile.

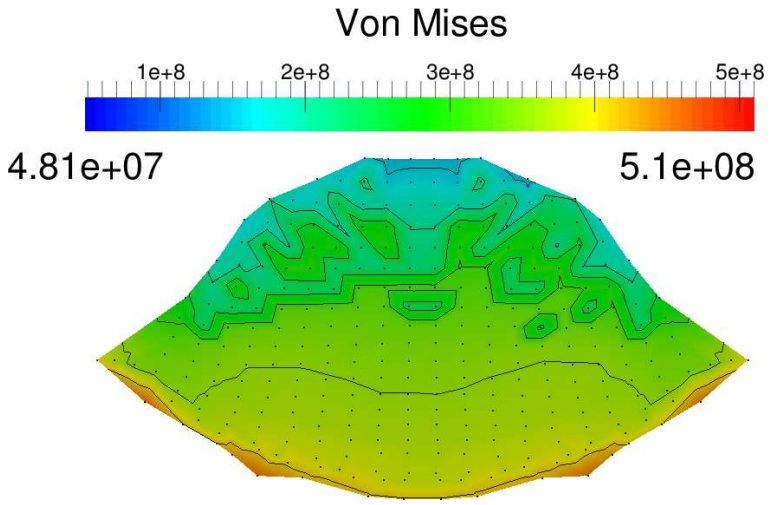

(a) Von Mises at 10 ns.

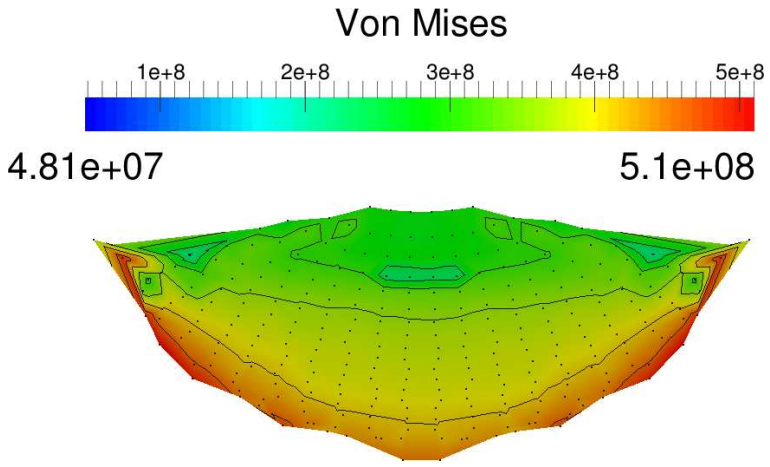

(b) Von Mises at 20 ns.

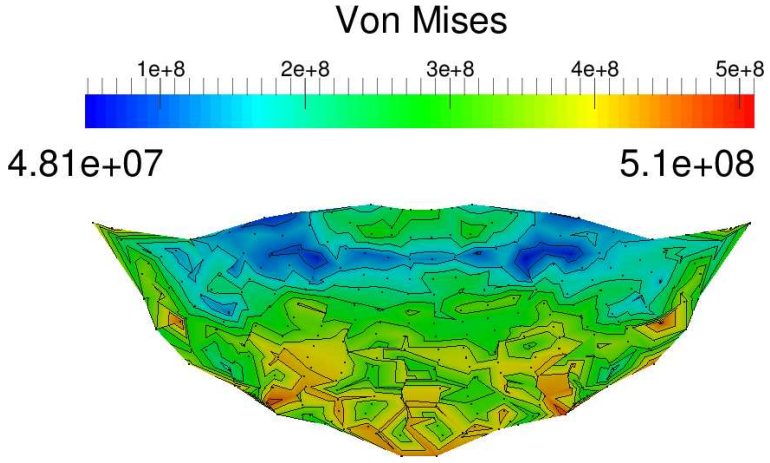

(c) Von Mises at 30 ns.

Figure 4.23: High temperature zero impedance domain contours of Von Mises stress in feedstock.

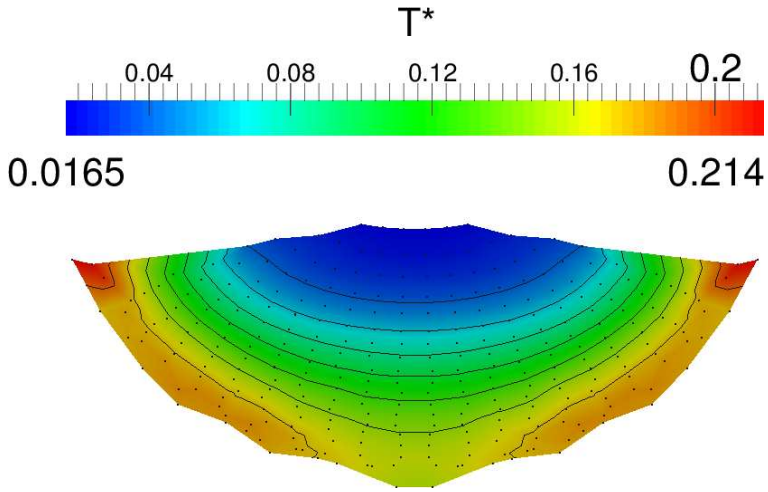

(a) Normalised temperature at 20 ns for 298.15 K initial temperature.

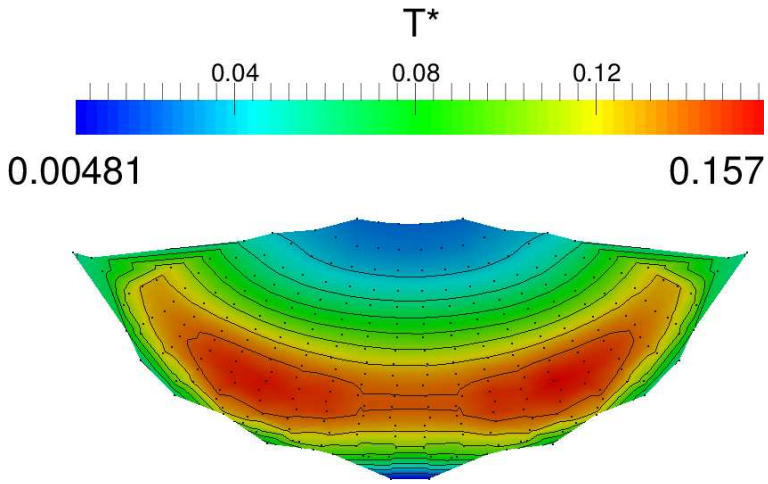

(b) Normalised temperature at 20 ns for 593.15 K initial temperature.

Figure 4.24: Comparison of normalised temperatures in feedstock at initial temperatures of 298.15 K and 593.15 K.

Chapter 5

Three-Dimensional Single Splat Formation

The aim of this chapter is to provide a detailed analysis of an isolated three-dimensional feedstock impact onto an infinite substrate. Factors such as initial temperatures, heat conduction, feedstock diameter and impact velocity will be considered and their effects on the splat morphologies detailed. A three-dimensional feedstock impact on an infinite substrate is modelled by application of suitable boundary conditions to the boundaries of a substrate with dimensions $6f_d \times 6f_d \times 6f_d$ where f_d is the diameter of the impacting feedstock. These dimensions where chosen to maintain stability at the zero impedance boundary. The shockwave produced from the impact is intially too strong for stable interaction with the boundary and so space has to be provided for the shock to be damped by the substrate before it can be safely propagated out of the domain. The selection of boundary conditions and a particle mass independence study for feedstock impacts of this type has been performed in Chapter 4, where a zero impedance boundary was found to best approximate the infinite substrate and mass independence was achieved at 4225 SPH particles per feedstock. The full range of initial parameters used in this study are presented in Table 5.1, velocities range from below the experimentally determined critical velocity for copper of 500 m/s [10] up to a high velocity impact at 800 m/s. The critical velocity is the minimum impact velocity required for bonding and so the selected velocities represent a case where no bonding is expected, where bonding has just been achieved and finally a case where bonding has definitely occured. Gas temperatures in cold sprays

are low compared to other thermal spray techniques and feedstock particles have a low entrainment time in the gas jet before deposition, resulting in little feedstock heating. For this reason a feedstock initial temperature of 298 K is used. This is compared to a case of much higher feedstock heating resulting in a feedstock initial temperature of 593 K to illustrate effects such as thermal softening. The effects of feedstock size will be examined by modelling feedstock with diameters of $2, 10$ and 20μm. Additionally the effects of heat conduction will be examined by comparison of adiabatic and conductive models. In the following sections each modelled splat morphology will be described before a detailed comparison of the effects of impact velocity, temperature, feedstock diameter and choice of heat conduction or adiabatic models is made.

Test case	Diameter $(1 \times 10^{-6}m)$	Temperature (K)	Velocity $(\frac{m}{s})$
A (adiabatic)	10	298.15	400
B (adiabatic)	10	298.15	600
C (adiabatic)	10	298.15	800
D (conduction)	10	298.15	400
E (conduction)	10	298.15	600
F (conduction)	10	298.15	800
G (conduction)	10	593.15	400
H (conduction)	10	593.15	600
I (conduction)	20	298.15	600
J (conduction)	20	593.15	600
K (conduction)	2	298.15	600
L (conduction)	2	593.15	600

Table 5.1: Modelled feedstock initial conditions for three-dimensional single splat formation.

There are several morphological characteristics shared by all cold sprayed splats regardless of their exact initial properties and/or morphology. The splats flatten as they impact the substrate forming a wider thinner splat, the edges of the splats show a pronounced lip of material which is extruded from the impact crater by the shear band

instability whilst the main body of the splat shows less strain than the splat edges. In the description of results and discussion of influencing factors on splat morphology that follow, several distinct regions of the splat will be referred to splat body, interface flanks and top and bottom centre, if required refer back to Figure 1.1 for a reminder of the locations of these zones. A detailed description of the results for test case B are inlcuded here in order to provide the reader which an understanding of the complex processes involoved in splat formation. An equally detailed description is given in Appendix B for the remaining test cases

5.0.1 Model B

The impact of a 10μm diameter adiabatic copper feedstock particle travelling at 600 m/s with an initial temperature of 298 K is considered in this section. In order to allow comparison of substrate penetration between different feedstock sizes a normalised penetration ratio:

$$P^* = \frac{(y_{\text{init}} - y_{\text{final}})}{f_d} \tag{5.1}$$

is defined, where y_{init} is the initial height of the splat centre, y_{final} is the final height of the splat centre and f_d is the initial feedstock diameter.

During the impact the splat flattens and broadens as expected as shown by the smooth increase of flattening ratio in Figure 5.1, from 22 ns the flattening ratio is 0.4 and variation in flattening ratio decreases to less than 1% and this variation continues to decrease from this point onwards. At this time, variation in splat centre height is less than 0.2% and this variation decreases in magnitude from this point onwards. The final values of flattening ratio, splat centre height and P^* are given in Table 5.2. The P^* value of 0.747 shows that the feedstock has created a significant crater in the substrate which increases the contact area between the materials which increases the chances of bonding being achieved. During the impact the feedstock has flattened by 40% of its initial diameter which shows significant deformation has occured and indicates a good quality coating can be formed from impacts at this velocity.

A pronounced lip feature can be seen forming from 10 ns onwards (see Figure 5.2) and this could be indicative of material jetting caused by a shear band instability. The

Flattening ratio	0.4
Splat centre height (μm)	48.8
P^*	0.747

Table 5.2: Model B flattening ratio, splat centre height and P^* data at 22 ns.

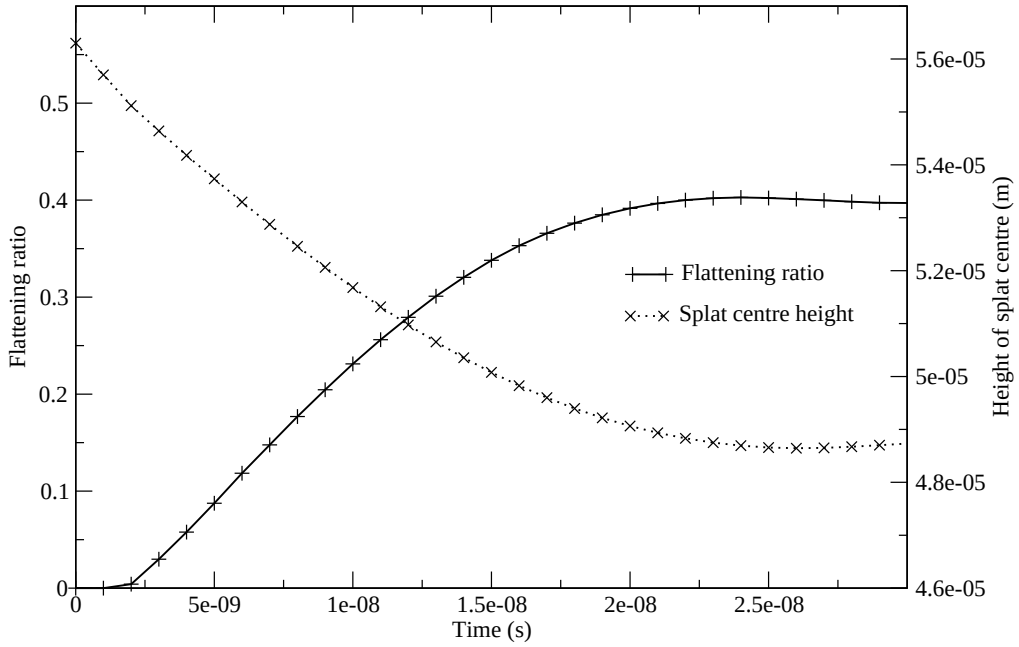

Figure 5.1: Flattening ratio plot for an adiabatic feedstock at 298 K and 600 m/s.

splat also shows considerable flattening caused by plastic deformation and therefore could indicate stronger material jetting (see Figure 5.2).

The distribution of heat within the splat at 10, 20 and 22 ns is shown in Figure 5.3 and shows strong temperature localisation to the flanks of the feedstock/substrate interface. Peak heating reaches 1480 K which is over the melt temperature of 1356 K; this extreme heating is found just below the tip of the lip feature on the interface between feedstock and substrate. The interface does not experience uniform heating. The flanks of the splat are significantly hotter than the splat bottom centre and the tips of the lip feature are also below the peak temperature. This indicates that the highest levels of mechanical

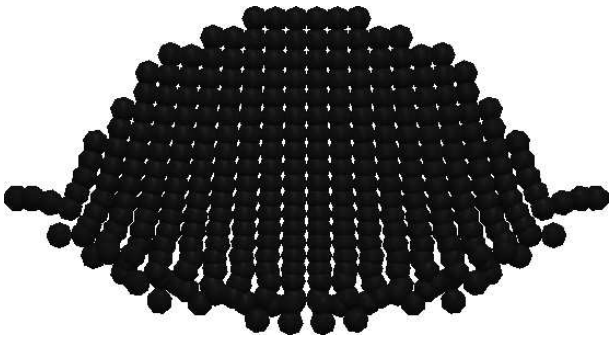

(a) 10 ns.

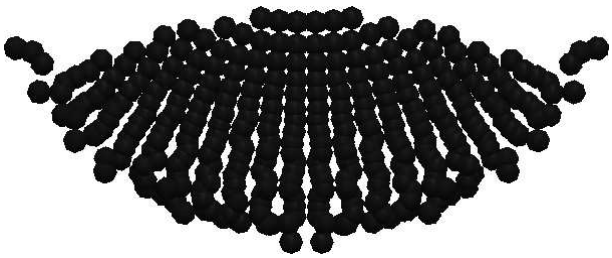

(b) 20 ns.

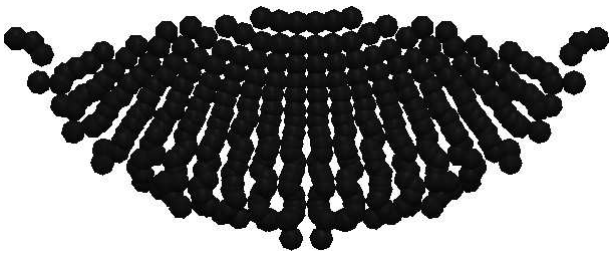

(c) 22 ns.

Figure 5.2: Model B, cross section through centre of 3-D splat morphology.

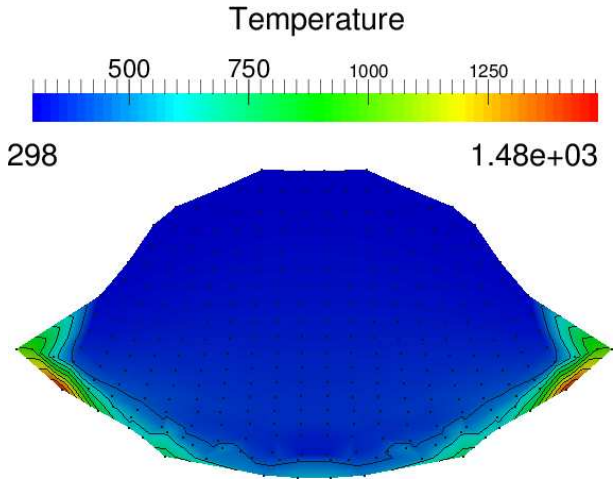

(a) 10 ns.

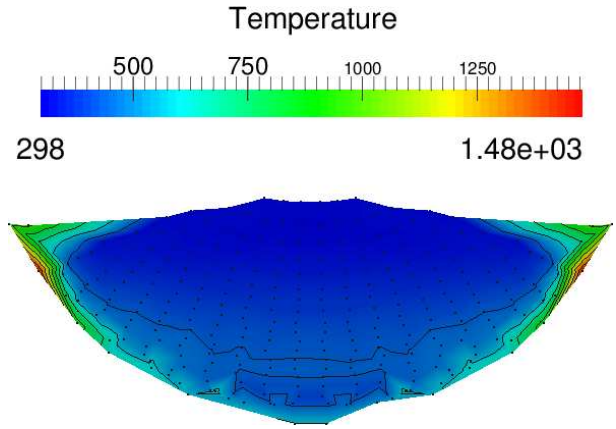

(b) 20 ns.

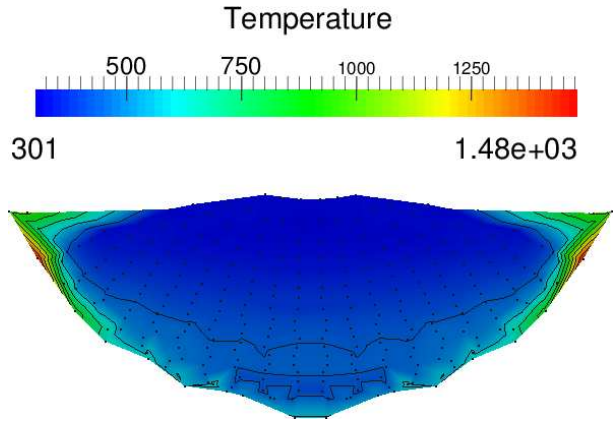

(c) 22 ns.

Figure 5.3: Model B, temperature cross section through centre of 3-D splat morphology.

strain are experienced at the splat flanks but not at the leading edge of the material jet.

EPS distributions are shown in Figure 5.4 and show less localisation than the temperature profiles although the location of the peak EPS value of 1.36 coincides with that of temperature. Also in agreement with the temperature contours there is an uneven distribution of EPS along the feedstock/substrate interface, the splat bottom centre shows less EPS than the flank regions and the tip of the lip feature shows slightly less EPS than the peak value. The splat top centre shows significantly less EPS than the interface regions although some degree of plastic strains have been induced.

The rate of EPS is plotted for the three time instances (10, 20 and 22 ns) considered in Figure 5.5. The peak value is reached early on in the impact event and quickly reduces, while the flanks of the feedstock/substrate interface experience the highest rate of EPS and two distinct lobes of increases strain rate can be seen radiating into the splat body from these regions. The splat bottom centre experiences significantly lower rates of strain than the interface flanks and the lowest rates are found at the splat top centre. The low rate of EPS is expected at the top centre as this is the area of the splat furthest from the impact interface and so experiences little strain.

Contour plots of the material yield strength as calculated by the Johnson-Cook model are shown in Figure 5.6. The regions of the feedstock/substrate interface that experience peak heating have a yield strength of zero corresponding to temperatures exceeding the material melt temperature. Away from these areas, the splat shows an overall dominance of material hardening over thermal softening with the most significant hardening found in the lower portion of the splat body.

The evolution of temperature in the jet region is plotted in Figure 5.7a. It shows a sharp rise at 2 ns to its peak value above the material melt temperature. For the time duration considered, there is no significant reduction in temperature. The EPS evolution in the jet (see Figure 5.7b) shows a smooth increase towards a peak value which is obtained at 22 ns.

Initially material hardening is dominant however yield strength in the jet region can be seen to decrease to zero at 6 ns (see Figure 5.8a) and this corresponds to the local temperature exceeding the melt temperature. Since there is no significant cooling throughout the time considered, the yield strength remains zero for the rest of the run. At the time thermal softening becomes dominant the jet region is undergoing a signifi-

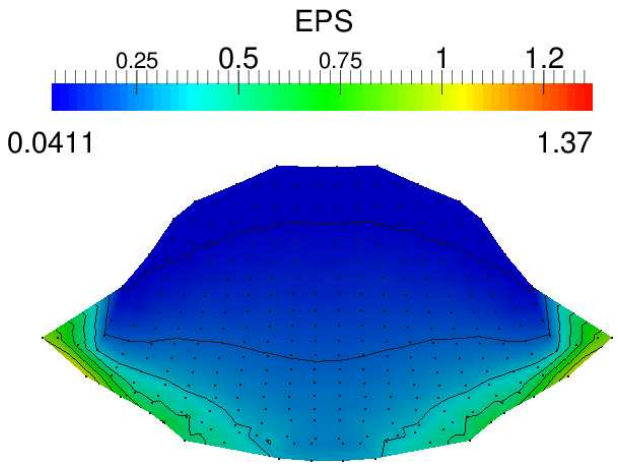

(a) 10 ns.

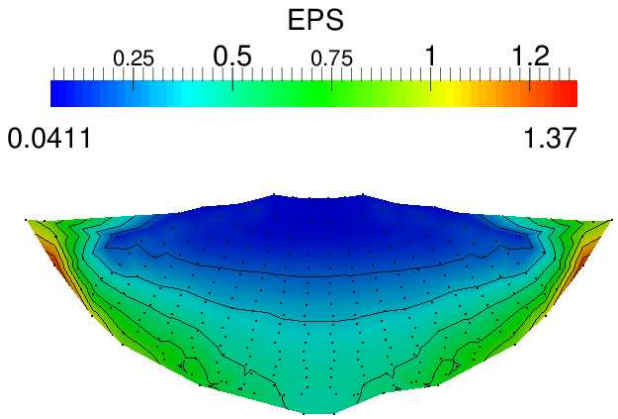

(b) 20 ns.

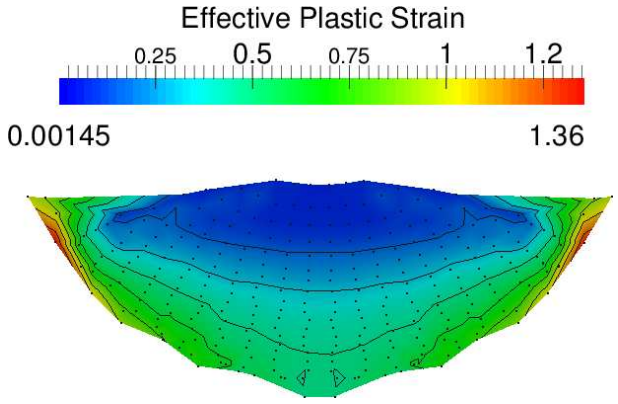

(c) 22 ns.

Figure 5.4: Model B, EPS cross section through centre of 3-D splat morphology.

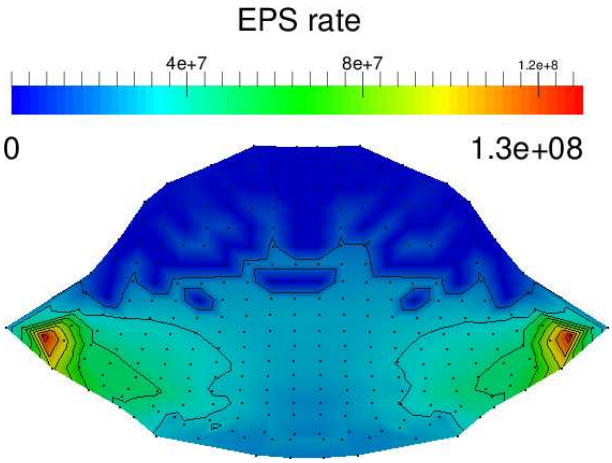

(a) 10 ns.

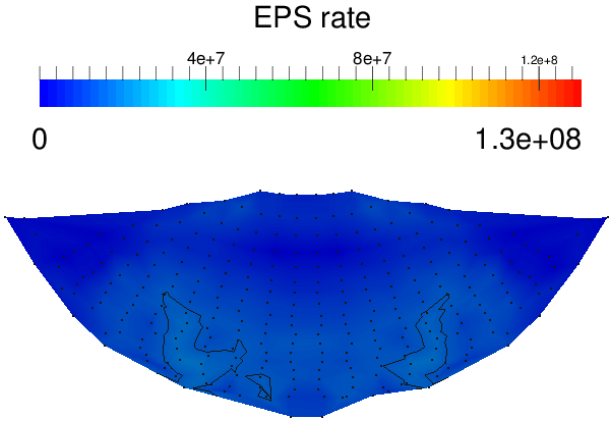

(b) 20 ns.

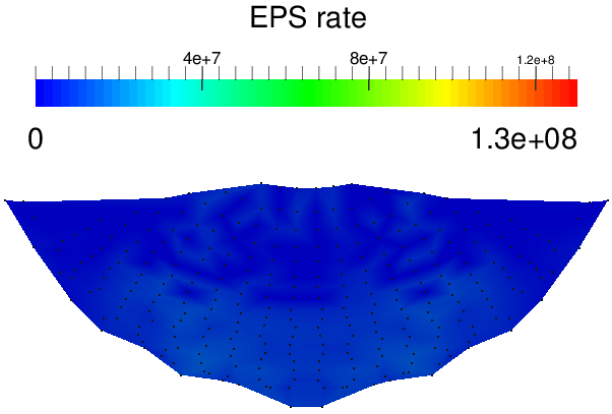

(c) 22 ns.

Figure 5.5: Model B, EPS rate cross section through centre of 3-D splat morphology.

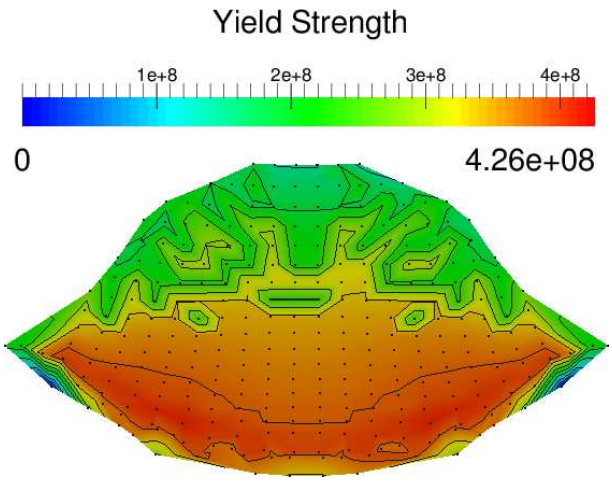

(a) 10 ns.

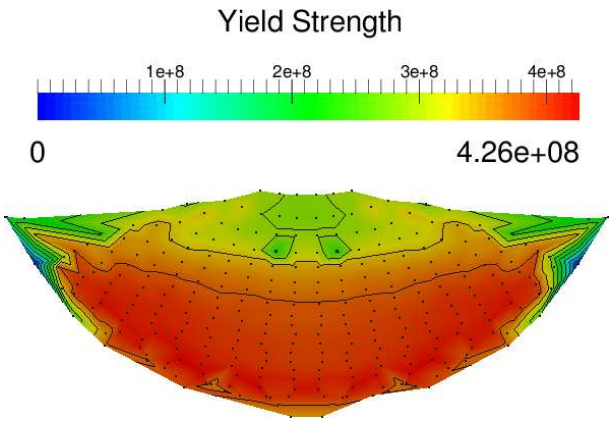

(b) 20 ns.

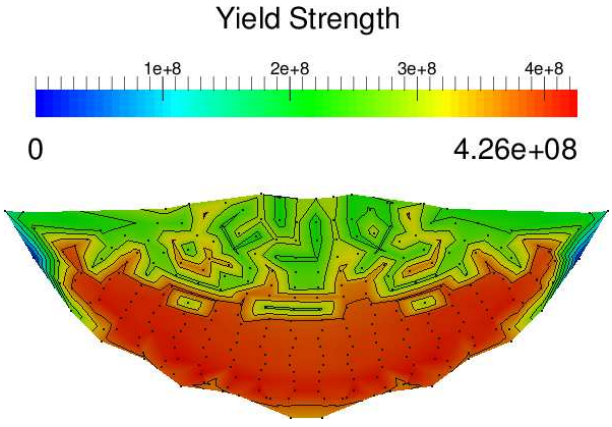

(c) 22 ns.

Figure 5.6: Model B, yield strength cross section through centre of 3-D splat morphology.

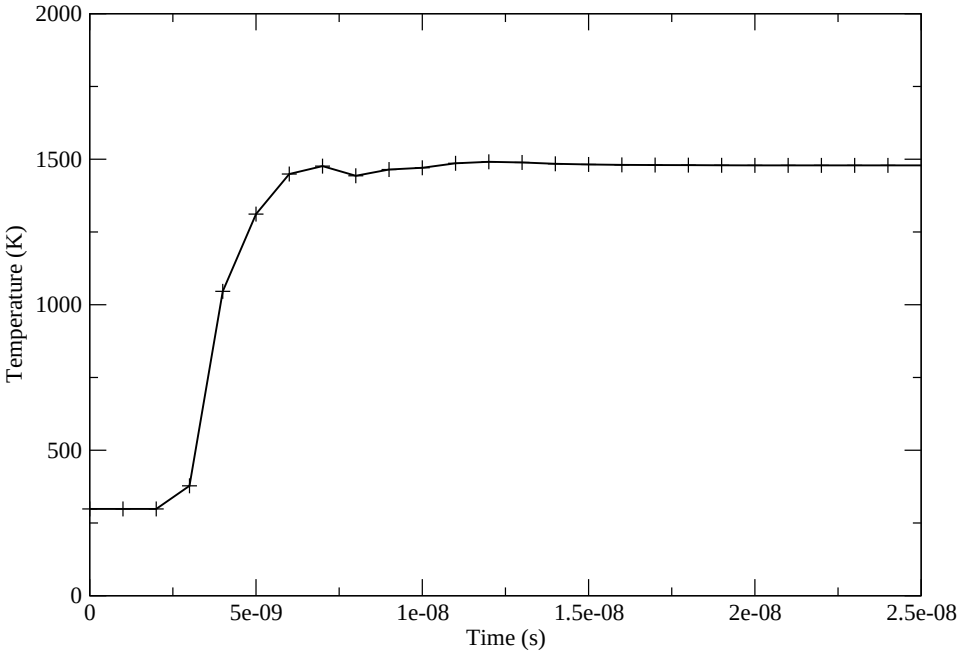

(a) Model B, temperature evolution in high EPS material jet region.

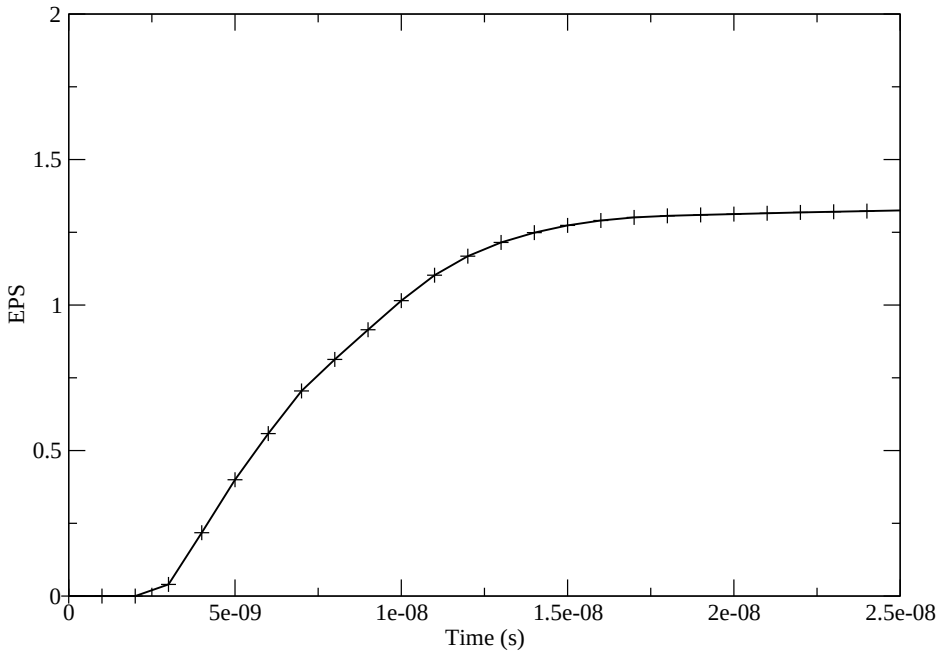

(b) Model B, EPS evolution in high EPS material jet region.

Figure 5.7: Model B, evolution of temperature and EPS in material jet.

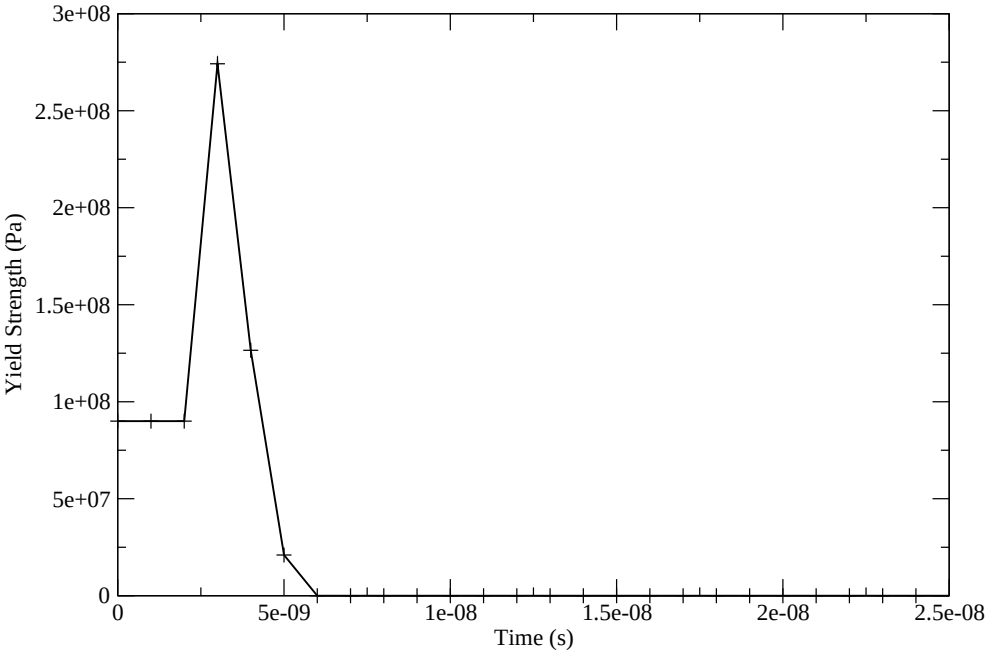

(a) Model B, yield strength evolution in high EPS material jet region.

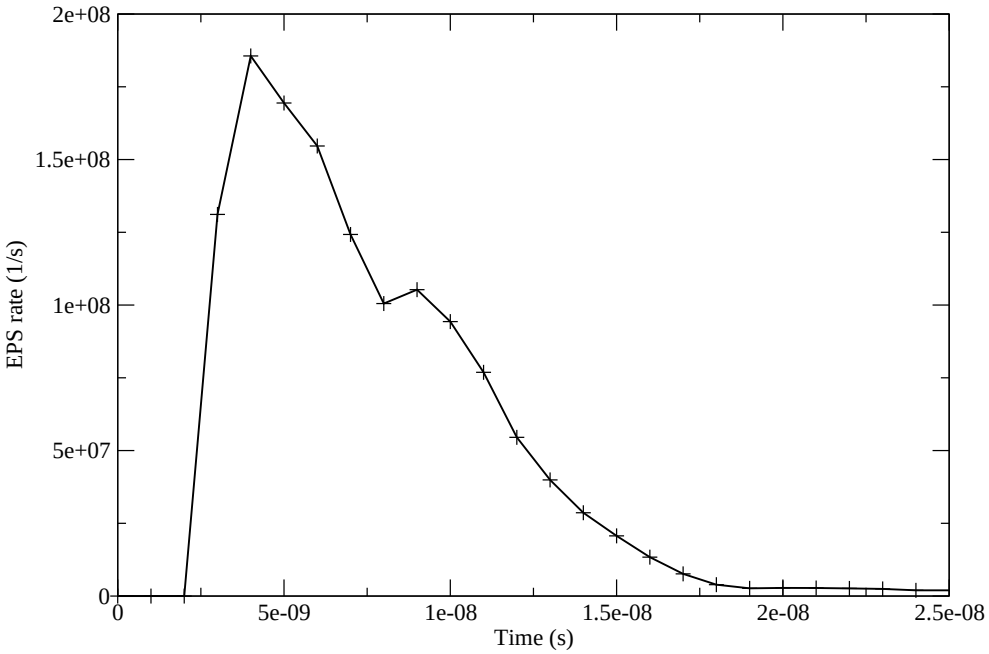

(b) Model B, EPS rate evolution in high EPS material jet region.

Figure 5.8: Model B, evolution of yield strength and EPS rate in material jet.

cant rate of EPS (see Figure 5.8b) and this could lead to the formation of a shear band instability on the flank of the feedstock/substrate interface. This is further supported by the distinct lip feature seen in the splat morphology and the high amount of EPS. The presence of this shear band instability and subsequent material jetting indicates that feedstock/substrate bonding has likely occurred; this corresponds to the initial velocity exceeding the experimentally derived critical velocity of 500 m/s.

5.1 Heat Conduction Effects on Splat Morphology and Properties

In order to examine the effects of heat conduction models on splat morphology and properties, the results of models A through F are compared. These models form pairs that share the same initial conditions with the only difference being the exclusion or inclusion of heat conduction; the pairs for comparison are given in Table 5.3. The impact of a 10μm copper feedstock with initial temperature of 298 K with a range of velocities are considered; the increasing impact velocities will produce progressively more heating in the feedstock and substrate and will enable the effect of the conduction models to be described over a range of heating intensities.

Pair ID	Adiabatic model	Conductive model	Initial velocity (m/s)
1	A	D	400
2	B	E	600
3	C	F	800

Table 5.3: Model pairing for comparison of adiabatic and conductive models.

5.1.1 Pair 1

Both models show nearly identical settling characteristics with a final flattening ratio of 0.306 reached at 24 ns in both cases. The biggest disparity is seen in the P^* values with the adiabatic model showing 12.6% more penetration into the substrate. The adiabatic

model shows more intense local heating at the interface increasing the thermal softening allowing the formation of a larger crater. The morphologies show largely negligible differences as expected from the comparison of flattening ratio, however, the adiabatic case does show a slightly more pronounced lip feature at the end of the impact, shown in Figure 5.9, where the solid black circles indicate the location of SPH particles in the conductive model and hollow red circles denote the adiabatic particle positions.

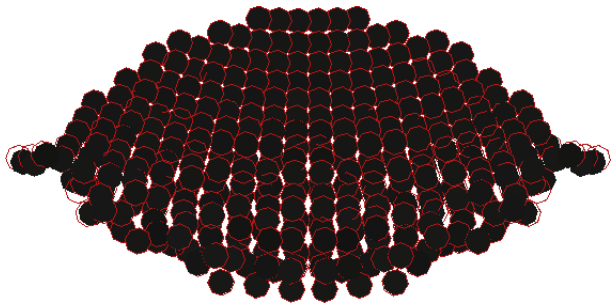

Figure 5.9: Comparison of splat morphology between the adiabatic model A (red) and the conductive model D (black).

In order to determine if there are differences in the distribution of key material properties such as temperature, yield strength EPS and EPS rate, the previously described contour plots of these properties will be compared. Since the effects of heat conduction are being examined, the distribution of heat within the splat will be discussed first (see Figures B.3 and B.20). There are significant differences in the heating profiles from the early stages of the impact. Unsurprisingly, the adiabatic model shows a greater degree of heating localisation and this results in a high degree of peak heating with maximum temperatures in the adiabatic feedstock reaching 714 K while those in the conductive feedstock only climb to 525 K (a 36% increase). Another significant difference is the cooling observed in the conductive model which results in the sharp temperature peak seen at the tleading edge of the lip feature gradually vanishing as heat is conducted into cooler surrounding material. In contrast, once peak heating is reached in the adiabatic model there is no cooling resulting in local yield strengths potentially being reduced by additional thermal softening. This softer material results in greater plastic strains explaining the more pronounced lip feature and the deeper crater seen in the adiabatic model. Upon examination of the yield strength distributions significant differences (see

Figures B.4 and B.19) are seen. The adiabatic model shows a dominance of hardening over thermal softening and peak hardening is experienced in a band of material across the middle of the splat body. There is distinctly less hardening found at the leading edge of the lip feature and this extends some way down the feedstock/substrate interface. The conductive model shows a different hardening profile as may be expected from the differences in the heating profiles; hardening in this case results in a peak yield strength of 461 MPa compared to the 420 MPa peak of the adiabatic model, representing a 9.76% change. The highest levels of hardening are seen at the flanks of the feedstock/substrate interface, with two zones of increased hardening reaching back into the splat body. Both models show reduced levels of hardening at the splat bottom centre and the lowest hardening overall is found at the splat top centre. There are also some disparities in the EPS rate distributions (see Figures B.5 and B.22) with a peak rate of 1.05×10^8 s^{-1} in the adiabatic model compared to 1.07×10^8 s^{-1} in the conductive model (a 1.9% variance). The higher EPS rate observed in the conductive model is caused by a larger region of the feedstock experiencing elevated temperatures when compared against the adiabatic model and therefore allowing a higher EPS rate. Although the adiabatic model experiences higher peak softening, the high degree of localisation has limited the overall EPS rate. Other than this slight difference in peak value, the EPS rate contours are in good agreement with each other. There is a corresponding increase in peak EPS in the conductive model with a final value of 0.904 compared to 0.871 in the adiabatic model representing a 3.65% difference. In general however there is good agreement between the EPS distributions for both models.

In addition to the previously described contour plots, the evolution of temperature, yield strength and EPS rate at the SPH particle that experiences the highest total EPS will be compared and comparative plots of these properties are given in Figure 5.10. Significant differences in the temperature profile (see Figure 5.10a) can be seen from 7 ns onwards, as the conductive model reaches its peak temperature and a period of gradual cooling follows as heat is conducted into colder feedstock and substrate regions; the adiabatic case in contrast shows a continued climb to its peak value at 17 ns with no sign of cooling over the whole time period considered. Early on in the impact, the yield strength profiles are in good agreement, however after the temperatures start to diverge at 7 ns, a similar divergence is seen in the yield strength profiles. The conductive model

continues to harden as thermal softening has less of an effect as the material cools, while the adiabatic model does not show this hardening as temperatures are high enough to maintain the thermal softening effect at significant levels. As expected from the contours of EPS rate in the feedstock (see Figures B.5 and B.22) there are slightly elevated EPS rates in the conductive model when compared to the adiabatic model.

Significant disparities between temperature and yield strength have been found, both in peak values and distributions within the feedstock. The rates of EPS seem largely unaffected but the conductive model shows elevated levels of final EPS when compared to the adiabatic model. Despite these differences, the final splat morphologies show only negligible differences and undergo the same amount of flattening and take the same time to reach a steady splat morphology.

5.1.2 Pair 2

The impact of 10μm feedstock with initial velocity and temperature of 600 m/s and 298 K, repectively, is considered with both heat conductive and adiabatic models and the effects of heat conduction on the splat formation are explored. Both splats show similar settling times with their morphologies reaching steady-state at 22 ns. The conductive splat undergoes slightly more flattening with a flattening ratio of 0.4018 compared to 0.4 for the adiabatic model whilst the adiabatic feedstock has penetrated the substrate to a slightly greater depth with P^* of 0.747 compared to 0.7466 in the conductive model. The final splat morphologies are plotted overlaid on each other in Figure 5.11. The conductive splat is represented with solid black circles and the adiabatic case with hollow red circles. From the comparative morphology cross-section plot, it can be seen that the splat bodies are in close agreement, with the most significant differences found at the material lip at the edge of the splat, where there is a slightly more pronounced lip in the adiabatic model.

In addition to these differences in the morphology, there are disparities in the magnitudes and distribution of material properties between the two splats; to illustrate these, the contours of temperature, yield strength, EPS rate and EPS are examined. The differences in temperature distribution (see Figures 5.3 and B.28) are significant, with the adiabatic model showing much more localisation of heating at the feedstock/substrate

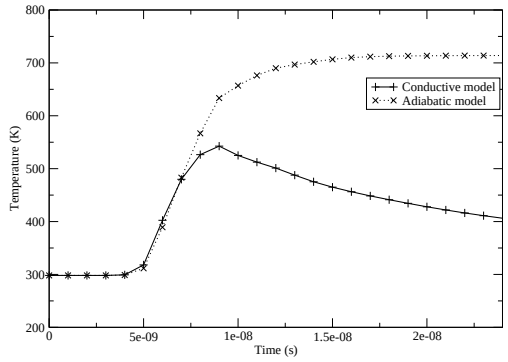

(a) Comaprison of jet region temperature for pair 1.

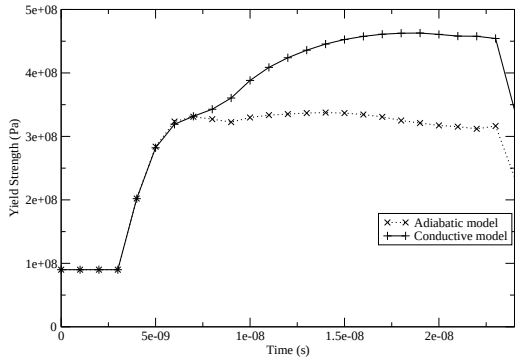

(b) Comaprison of jet region yield strength for pair 1.

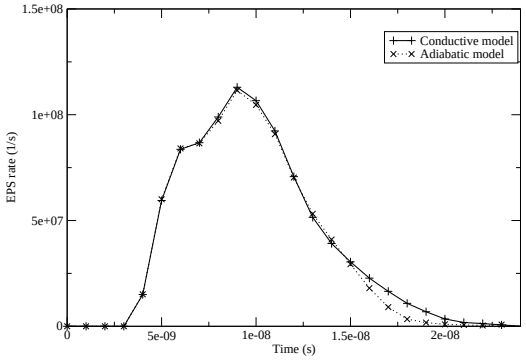

(c) Comaprison of jet region EPS rate for pair 1.

Figure 5.10: Comparison of properties in the high EPS region of models A and D.

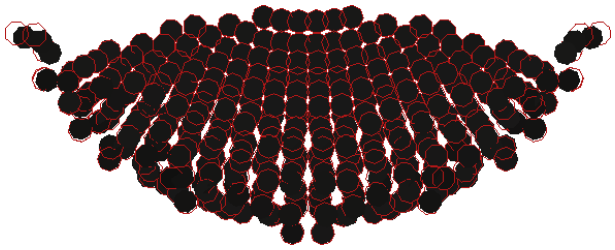

Figure 5.11: Comparison of splat morphology between the adiabatic model B (red) and the conductive model E (black).

interface for the full duration of the impact. The adiabatic model shows peak heating just below the leading edge of the lip feature whilst peak heating occurs across a larger region of the conductive feedstock and encompasses the leading edge. The conductive model shows cooling once the peak temperature is reached whilst the adiabatic model shows no cooling and maintains its elevated temperature. Maximum temperature in the conductive model is 673 K which is well below the material melting temperature, the adiabatic model however reaches a temperature of 1480 K exceeding the melt temperature and represents a 119.91% over prediction of local heating compared to the conductive model. The yield strength profiles also show significant differences (see Figures B.19 and B.27). The elevated temperature in the adiabatic model has increased thermal softening in the lip feature and at the point of peak heating, this has caused the complete loss of material strength due to melting. While the splat body shows the highest degree of hardening and reaches a peak yield strength of 426 MPa. The conductive model in contrast experiences peak hardening against the feedstock/substrate interface; there is a non-uniform distribution of hardening along the interface with hardening more pronouced at the flanks and less at the bottom centre of the splat. The splat body also shows hardening but to a much lesser extent than the interface with higher yield strengths found in the lower portion of the splat. Peak yield strength in the conductive model is 479 MPa which is a 12.4% increase over the adiabatic model. The distribution of EPS rate within the feedstocks (see Figures 5.5 and B.30) shows greater agreement than the temperature and yield strength distributions. The conductive model shows slightly less intense but more distributed EPS rates with peak rates of 1.24×10^8 s^{-1} found near the leading edge of the lip feature, the adiabatic model shows a very similar distribution with a slightly

lesser extent of strain but a higher peak value of 1.3×10^8 s^{-1} representing only a 4.84% variation in peak value. With these similarities between the EPS rate, it is unsurprising that the EPS contours are in close agreement with each other as well (see Figures 5.4 and B.29) although there is fractionally less localisation to the interface flanks in the conduction model. The largest difference is found in the magnitude of the peak EPS with the adiabatic model showing 1.36 whilst the conduction model reports a peak of 1.31 (a 3.82% change).

The evolutions of temperature, yield strength and EPS rate at the SPH particle that experiences the highest total EPS are shown in Figure 5.12. The temperature profile shows significant divergence from 4 ns when the conductive model reaches its peak temperature and cooling begins, while the adiabatic model continues to heat during this cooling period and reaches its peak temperature at 7 ns. These differences in heating has a dramatic effect on the yield strengths of the two models (see Figure 5.12b). The extreme heating in the adiabatic model makes thermal softening dominant over hardening from 3 ns when the temperature increases above the melting temperature causing a loss of material strength at 6 ns since there is no significant cooling, and therefore there is no recovery of strength for the remainder of the time considered. As the conductive model heats, it also shows a dominance of thermal softening over the strain hardening. This is of limited duration however, and results in a short period of reduced material strength before hardening becomes dominant as the material cools. The EPS rate profiles (see Figure 5.12c) show good agreement despite a slight increase in the adiabatic model, the peak rate of EPS is observed at 4 ns and coincides with the period of lowest yield strength in the conductive model.

The two models have produced very similar splat morphologies with similar flattening and penetration ratios into the substrate. Despite this there are significant differences in properties such as temperature and yield strength which affect patterns of plastic straining. The most significant difference is the extreme over heating seen in a small region of the adiabatic splat where the material melt temperature is exceeded, causing a loss of material yield strength. This level of heating is not seen in the conductive model and the splat remains in a solid state throughout the impact.

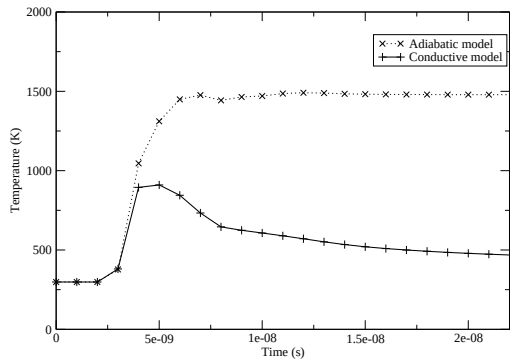

(a) Comaprison of jet region temperature for pair 2.

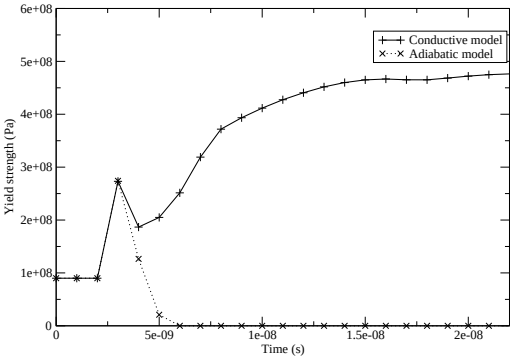

(b) Comaprison of jet region yield strength for pair 2.

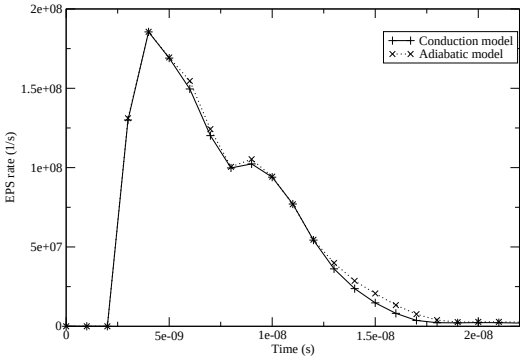

(c) Comaprison of jet region EPS rate for pair 2.

Figure 5.12: Comparison of properties in the high EPS region of models B and E.

5.1.3 Pair 3

The impact of 10μm copper feedstocks with initial velocity and temperature of 800 m/s and 298 K, respectively, are compared in order to highlight the effects of heat conduction on the splat formation. The settling times show a 1 ns variance with the adiabatic model taking 24 ns to reach a steady morphology whilst the conductive model reaches steady morphology in 23 ns. The splat morphology shows significant differences in the material lip at the edge of the splat, with the lip of the adiabatic model much more distinct than for the conductive model (see Figure 5.13), the adiabatic splat also shows greater flattening with a flattening ratio of 0.524 compared to 0.521 for the conductive model. Additionally the adiabatic feedstock has penetrated the substrate to a greater extent with a P^* of 1.004, the conductive model only reaches a P^* of 0.9917.

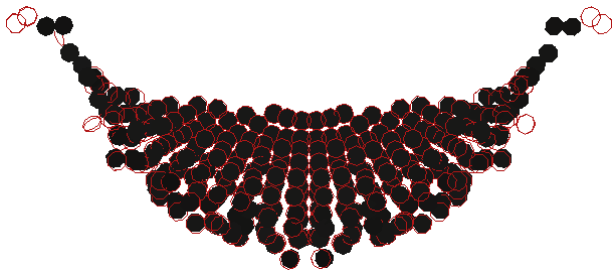

Figure 5.13: Comparison of splat morphology between the adiabatic model C (red) and the conductive model F (black).

The magnitude and distribution of key material properties show significant differences between the adiabatic and conductive models. The temperature contours are given in Figures B.13 and B.38. The adiabatic model shows very strong localisation of heat at the leading edge of the forming lip feature, where the peak temperature is reached towards the end of the impact and reaches 2080 K which is well over the material melt temperature. In contrast, the conductive model reaches a peak temperature of 890 K in the early stages of the impact (a 133.71% difference), and the splat shows significantly less localised heating as the conduction terms attempt to equalise the temperatures across the splat. These differences in temperature distribution have had a significant effect on the yield strength profiles of the two feedstocks (see Figures B.14 and B.36). The adiabatic feedstock shows a loss of material strength where temperatures have exceeded the melting temperature at the leading edge of the lip feature. The hardest material is found in the

splat body and the highest yield strength present is 420 MPa. The conductive feedstock shows quite a different pattern of hardening with peak values of 460 MPa seen at the feedstock/substrate interface representing a 9.52% increase over the adiabatic model. The body of the conductive feedstock still shows significant hardening with the lowest values seen at the splat top centre. The conductive feedstock shows a higher peak rate of EPS than the adiabatic model (see Figures B.13 and B.38), 1.25×10^8 s^{-1} compared to 1.12×10^8 s^{-1} which is a 11.6% increase. Despite these differences in magnitude the feedstocks share a similar EPS rate distribution. The EPS profiles of both feedstocks (see Figures B.12 and B.37) show some similarities, there is a concentration of plastic strain around the feedstock/substrate interface and peak values are seen towards the leading edge of the lip feature. The adiabatic feedstock experiences the highest peak EPS at 1.59 compared to 1.56 in the conductive feedstock (a 1.92% difference) due to the greater thermal softening resulting from the over estimation of local temperatures.

The evolutions of temperature, yield strength and EPS rate at the SPH particle that experiences the highest total EPS are plotted in Figure 5.14 for both the adiabatic and conductive feedstocks. The temperature profile shows significant divergence from 3 ns when the conductive feedstock shows some cooling whilst the adiabatic feedstock continues to heat locally. The adiabatic model continues heating until 5 ns where there is a brief period of cooling before the temperature stabilises above the melting temperature of the material. The yield strength profiles (see Figure 5.14b) also show significant variation between the feedstocks at 4 ns the adiabatic feedstock shows material melting reducing the yield strength to zero and with no significant cooling in this model the yield strength remains zero for the rest of the time considered. At the same time the local heating in the conductive feedstock has brought the material close to its melt temperature resulting in significant thermal softening but no complete loss of yield strength. As the conduction model cools the yield strength recovers as work hardening becomes dominant over thermal softening. Significantly less variation is seen in the rate of EPS between the two feedstocks in shown Figure 5.14c.

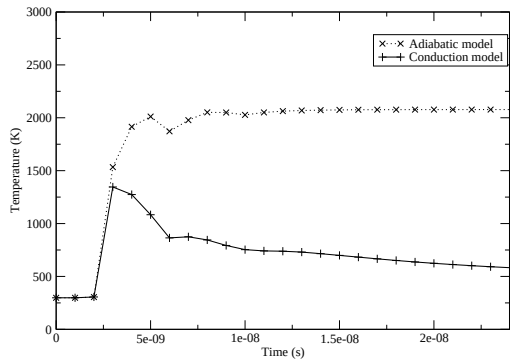

(a) Comaprison of jet region temperature for pair 3.

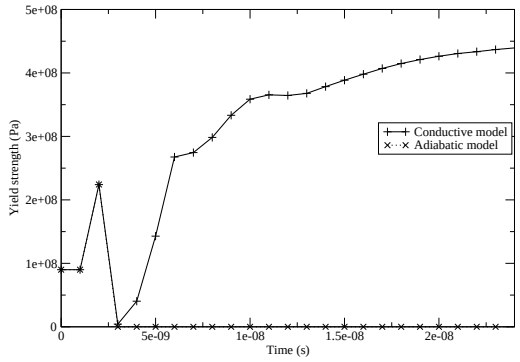

(b) Comaprison of jet region yield strength for pair 3.

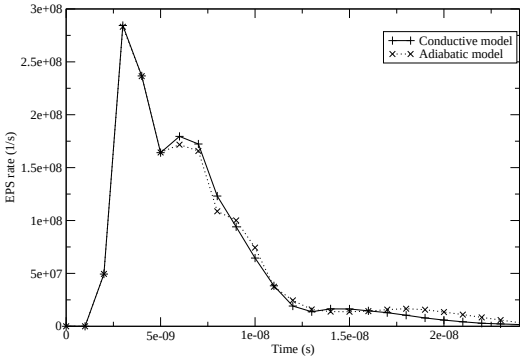

(c) Comaprison of jet region EPS rate for pair 3.

Figure 5.14: Comparison of properties in the high EPS region of models C and F.

5.1.4 Summary

The above discussion has highlighted the differences between an adiabatic and heat conductive model. Although morphological differences are minor, the distribution and evolution of key material properties such as temperature and yield strength show significant differences that prove that the adiabatic assumption is unacceptable for accurate modelling of the cold spray splat formation process. These differences became more significant as the impact velocity is increased for the cases considered in the current work; as impact velocity is increased the heating of the particles is increased as the energy of the impact increases. In the adiabatic models, this heating shows strong localisation to the interface between feedstock and substrate resulting in temperatures that exceed the melt temperature over a small portion of the interface. Heat conduction reduces this localisation and peak heating, with resulting temperatures well below the melt temperatures in the cases considered. As impact velocity is increased there is an increase in localised heating initially in the conduction model but because of the higher thermal gradients created in the feedstock results in a higher rate of heat transfer which acts to reduce the localisation. It is these differences in the pattern of heating that produce the observed variations in the material properties, the most direct effect is on the yield strength due to thermal softening which in turn controls the ease with which the material plastically deforms. The observed morphological differences were minor for this isolated splat formation model, the process of rapid successive feedstock impacts involved in physical coating formation is likely to produce significant differences between the two models. The heating in the adiabatic model is localised at the interface leaving the splat body and top centre relatively cool, increasing material hardening in the regions of the splat impacted by sucsessive feedstock. In the conductive case, the localisation of temperature is reduced resulting in a softer splat body and top centre which will deform more when impacted by a successive feedstock.

The effects of impact velocity on the splat formation will be considered in more detail in the next section. For this discussion it is sufficient to observe that the differences between the adiabatic and conductive models are present in at the entire range of velocities and so heat conduction is a fundamental requirement for modelling this process. For these reasons the following descriptions of splat formation will only consider conductive

models.

5.2 Impact Velocity Effects on Splat Formation

The impact of a 10μm diameter heat conductive copper feedstock with initial temperature of 298 K is modelled with impact velocities of $400, 600$ and 800 m/s in order to isolate the effects of velocity on the splat formation. The experimentally determined critical velocity for copper is 500 m/s and so below this velocity feedstock does not bond to the substrate. As impact velocity is increased the bonding becomes more likely until the erosion velocity is reached (for copper this is 1000 m/s [10]). As the impact velocity is increased the final feedstock morphologies show a greater amount of flattening and penetration into the substrate, the final values of which are given in Table 5.4. These differences can be seen in the splat morphologies in Figure 5.15. In addition to the flattening and penetration, the lip of material at the edge of the splat becomes more distinct as the velocity increases. Since this material lip indicates the possibility of a shear band instability, the increase in kinetic energy produced from the increase in impact velocity is likely increasing the intensity of this instability. To investigate this hypothesis, the evolution of temperature, yield strength, EPS rate and EPS at the SPH particle that experiences the total EPS are compared (see Figures 5.16 and 5.17) in each of the models this particle is typically found at the splat flank on the feedstock/substrate interface which is the location of material jetting. The temperature profiles (see Figure 5.16a) show that the 600 and 800 m/s feedstocks share a sharp period of peak heating which is not seen in the 400 m/s profile; as the impact velocity is increased this peak becomes sharper and also occurs earlier in the impact with a much higher rate of heating. All three profiles show a period of cooling after peak temperatures are reached. The higher heating rates and increase in peak temperature that occurs as the velocity is increased creates larger thermal gradients between the hot feedstock/substrate interface and the colder splat body and substrate away from the impact site, resulting in a short period of increased cooling before a more gradual cooling rate is reached. In the same way that the rate of heating increases with impact velocity, the rate of this cooling also increases with velocity.

These differences in heating/cooling rates and peak temperature have the most direct effect on the material yield strength via the thermal softening terms of the Johnson-Cook

model. As with the temperature profiles, the 600 and 800 m/s yield strength profiles share features that are absent in the 400 m/s model (see Figure 5.16b). In this case, they share a distinct period of thermal softening that coincides with the temperature spikes. As impact velocity is increased the feedstock shows greater softening in this region. Additionally this occurs earlier on in the impact and at a slightly higher rate as the velocity is raised. There is no sign of this thermal softening in the 400 m/s case and so the transient dominance of thermal softening appears key to material jetting. The formation of a material jet is observable in the EPS rate profiles (see Figure 5.17a) as a sharp spike in the early stages of the impact. This feature is not well developed in the 400 m/s profile but becomes more prominent as impact velocity is increased and is present in both the 600 and 800 m/s profiles coinciding with the period of peak temperature and thermal softening. The EPS profiles shown in Figure 5.17b demonstrate the earlier onset of plastic straining and the increase in rate of EPS as impact velocity is increased.

	400 m/s	600 m/s	800 m/s
Flattening ratio	0.306	0.4018	0.521
P^*	0.53	0.7466	0.992

Table 5.4: Comparison of the effect of impact velocity on final flattening ratio and penetration into the substrate.

Increasing impact velocity serves to increase the kinetic energy in the impact which is converted to a greater level of heating at the feedstock/substrate interface. The additional heating causes thermal softening to become dominant over strain and strain rate hardening at the flanks of the interface. The weakened material experiences an elevated EPS rate and a material jet is formed. This material jet serves to clean the interface of containments allowing the feedstock and substrate to come into contact via clean and hot material surfaces which under the impact pressures can metallurgically bond. The flow of plastically deforming material can also develop wave like features that allow mechanical interlocking between the feedstock and substrate. As the localised heating becomes very intense the higher thermal gradients, it promotes the conduction of heat away from the interface and this combined with the dissipation of energy as the the material plastically

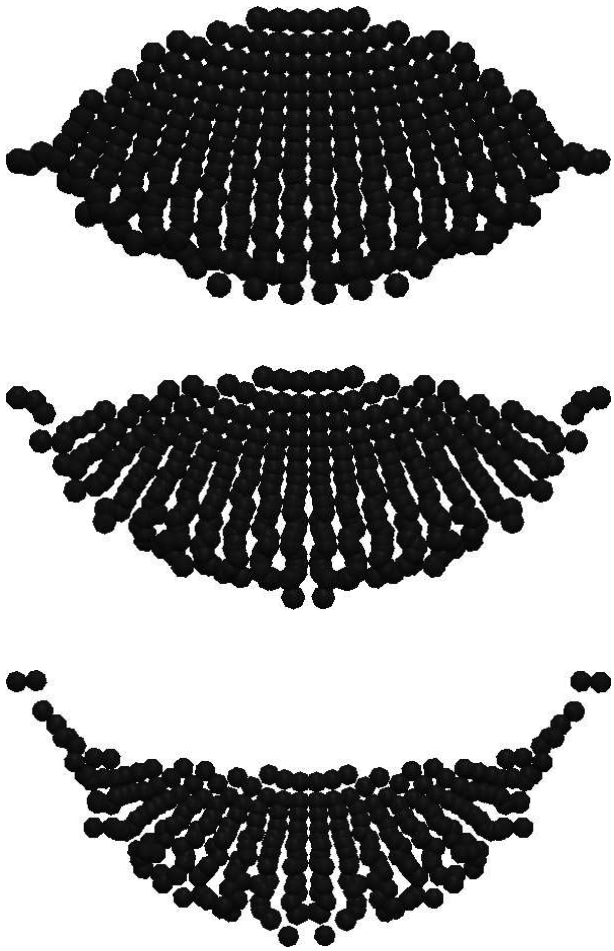

Figure 5.15: Comparison of final splat morphologies at $400, 600$ and 800 m/s impact velocities.

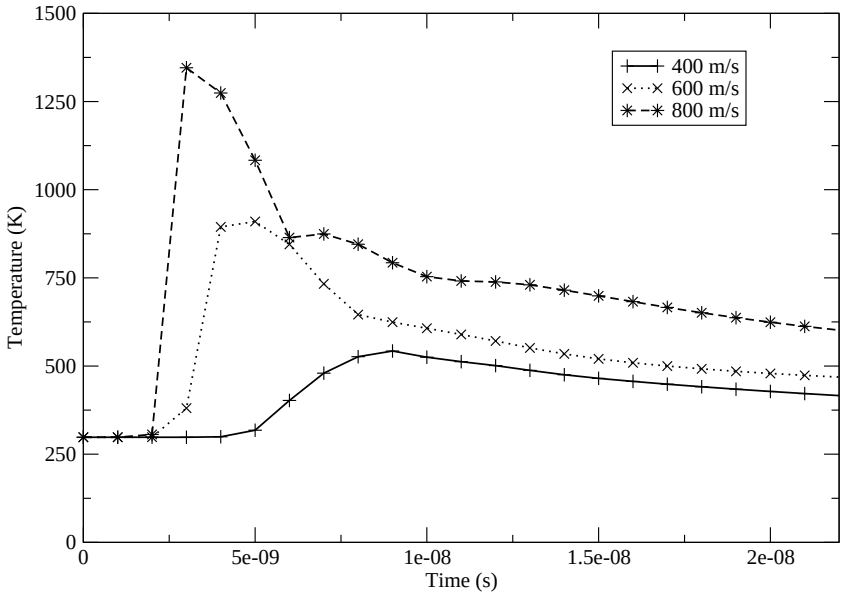

(a) Temperatures in the jet region.

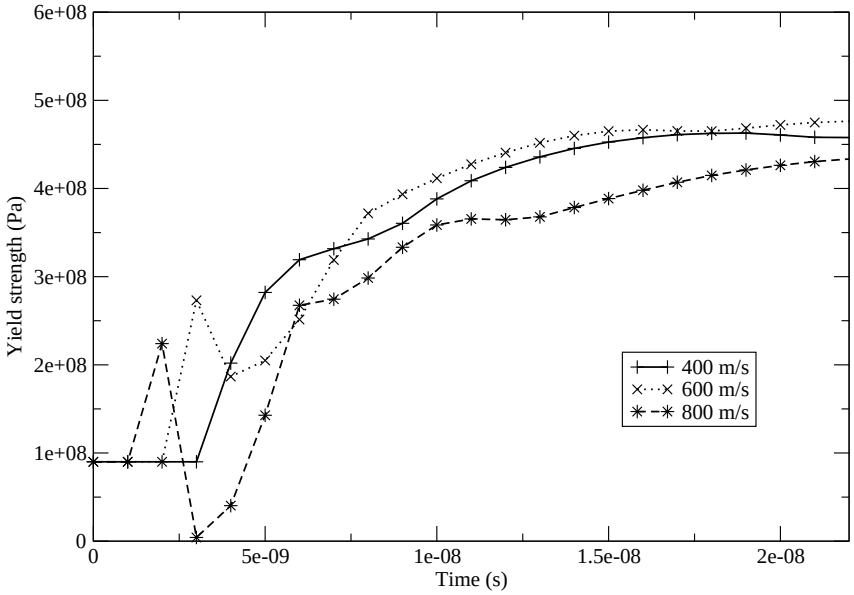

(b) Yield strength in the jet region.

Figure 5.16: Comparison of temperature and yield strength in the high EPS region with varying impact velocities.

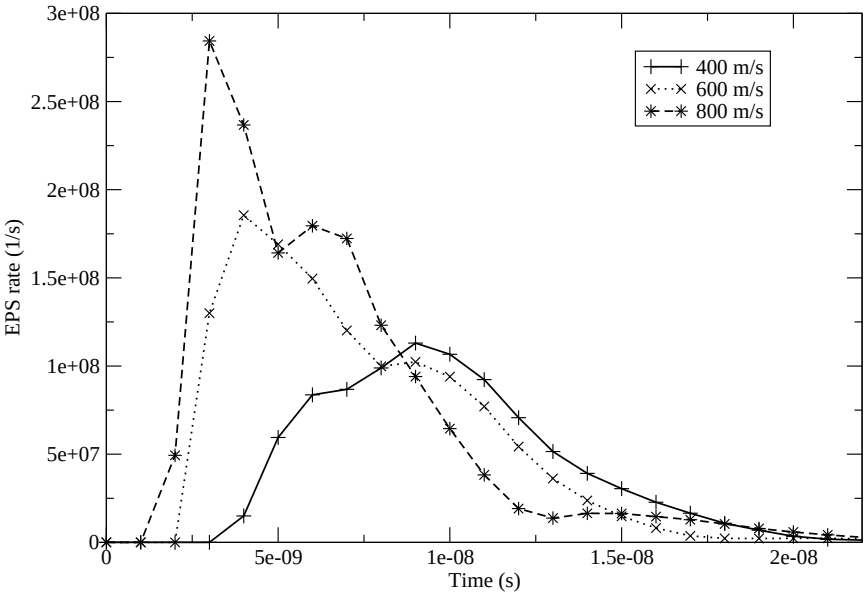

(a) EPS rate in the jet region.

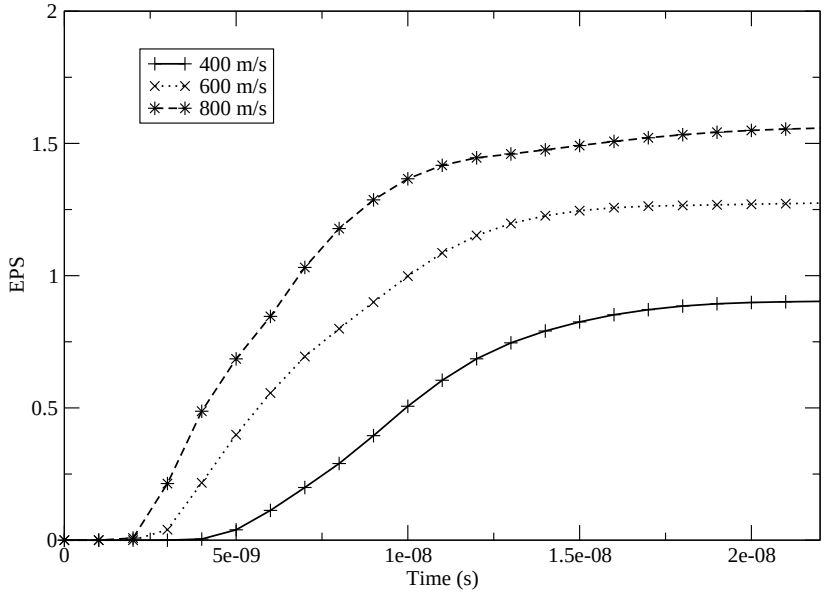

(b) EPS in the jet region.

Figure 5.17: Comparison of EPS rate and EPS in the high EPS region with varying impact velocities.

deforms causes material hardening to regain its dominance over thermal softening and eventually acts to shut off material jetting.

5.3 Feedstock Size Effect on Splat Morphology

The impact of heat conductive copper feedstocks with an impact velocity of 600 m/s and initial temperature of 298 K are considered using feedstock diameters of $2, 10$ and 20μm to illustrate the effects of the varying feedstock size on splat morphologies and material properties. The final flattening ratio and P^* values at steady-state are shown in Table 5.5, the time at which this stable state is reached is also presented. The most significant difference is the settling time of the splat morphologies, as feedstock diameter increases the time taken to reach steady-state also increases with the 20μm feedstock taking ten times as long to settle as the 2μm one. This feedstock diameter and settle time relationship is reflected in the peak rate of EPS experienced by each model. Examining the distributions of EPS rate within the feedstocks (see Figures B.30, B.62 and B.77), the location of peak EPS rate remains the same but the magnitude decreases as feedstock size is increased. The 10μm feedstock shows a peak EPS rate 6.95 times smaller than the 2μm feedstock and this is matched by a 9.94 times decrease between the 2μm and 20μm feedstocks. The elevated rate of EPS as feedstock size decreases, increases the rate of material hardening and so despite the much shorter impact duration peak yield strengths show some agreement between the three models (see Figures B.27, B.60 and B.76). Interestingly, there is a decrease in peak yield strength as feedstock size and, therefore, impact duration increases, while despite a 900% increase in impact duration a 14.7% decrease in peak yield strength is seen in the 20μm feedstock when compared to the 2μm feedstock. The distribution of yield strength within the splats show the same general trends with the hardest material found at the flanks of the feedstock/substrate interface and the lowest values at the splat top centre. Significant hardening is seen at the interface much earlier on in the impact in the 2μm feedstock than for the larger feedstocks.

The temperature distributions show some significant differences (see Figures B.28, B.59 and B.75). In the early stages of the impact the distribution of heating is very similar between all three feedstock sizes with peak heating seen at the tip of the forming

lip feature. The conduction of heat away from the interface and into the body of the feedstock becomes significant much earlier in the impact as feedstock size is decreased resulting in a much more even distribution of heat throughout the feedstock. This leads to a higher level of thermal softening in the splat body and a reduction of yield strength in the 2μm feedstock when compared to the larger feedstocks. By altering the feedstock dimensions whilst keeping all other variables constant, the kinetic energy of the impact varies, the 2μm diameter feedstock has the lowest impact energy of the three since it has the least mass and the largest feedstock at 20μm has the highest impact energy. The reduction in kinetic energy as the feedstock size decreases results in a reduction of the peak heating experienced at the interface. The lower level of heating at the feedstock/substrate interface found in smaller feedstocks reduces the thermal softening effect of the impact. The differences in heating distribution and yield strength has resulted in a more even distribution of EPS as particle size decreases with less localisation of peak values (see Figures B.29, B.61 and B.78). As a larger proportion of the feedstock undergoes more EPS, peak EPS at any one point in the feedstock reduces, for example, there is a 37.1% reduction in peak EPS in the 2μm feedstock when compared to the 20μm feedstock.

	2μm	10μm	20μm
Flattening ratio	0.3839	0.4018	0.373
P^*	0.7024	0.7466	0.704
Settling time (ns)	3.8	22	38

Table 5.5: Comparison of the effect of feedstock diameter on final flattening ratio and penetration into the substrate.

In order to investigate the effects of feedstock size on feedstock/substrate bonding, the evolution of temperature, yield strength and EPS rate at the SPH particle that shows the highest total EPS has been tracked and the results are shown in Figure 5.18. This particle is found at the flanks of the feedstock/substrate interface in the region where bonding is expected and so it's properties will indicate whether a shear band instability is present and therefore whether bonding has occurred. Due to the significant differences in feedstock settling time, the graphs in Figure 5.18 plot the material properties against

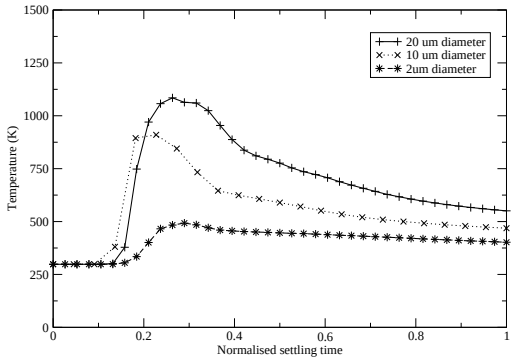

(a) Feedstock size effect on temperature in jet region.

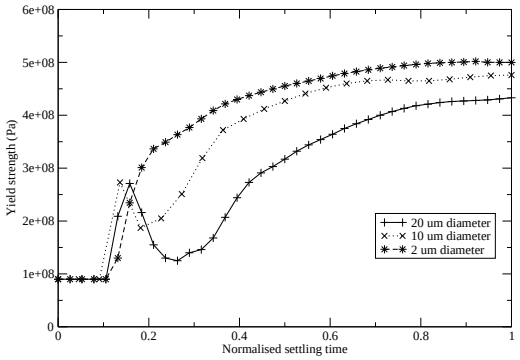

(b) Feedstock size effect on yield strength in jet region.

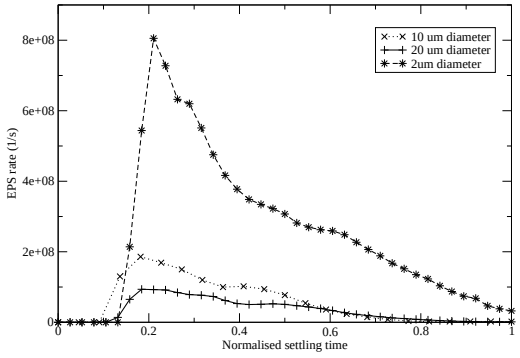

(c) Feedstock size effect on EPS rate in jet region.

Figure 5.18: Comparison of material properties in the high EPS flank region for a variety of feedstock diameters.

the normalised settling time t^*:

$$t^* = \frac{t}{t_{\text{settle}}} \tag{5.2}$$

where t is the current time and t_{settle} is the time taken for the variation in flattening ratio to drop below 1%.

The temperature profiles show significant differences in peak temperature as feedstock size is altered (see Figure 5.18a). The smaller feedstocks experience less intense heating compared to larger feedstocks impacting at the same velocity. The heating is caused by the deformation of the feedstock as it impacts the substrate and this is driven by the kinetic energy of the feedstock which varies with feedstock size; the 2μm feedstock impact has a kinetic energy of 6.76×10^{-9} J whilst the 10 and 20μm feedstocks have impact energies of 8.45×10^{-7} J and 6.76×10^{-6} J, respectively. The largest difference in kinetic energy is seen when the feedstock diameter is increased from 2 to 10μm and this is reflected in the peak temperatures experienced. The temperature differences have a direct effect on yield strengths (see Figure 5.18b) where significant thermal softening is seen for a short period of the impact in the 10 and 20μm feedstocks but not for the lower temperature 2μm feedstock impact. This period of weakened material coincides with the period of peak EPS rate and temperature and so indicates the presence of a shear band instability in the larger feedstocks whilst the lack of this feature indicates that the smaller feedstock does not develop this feature. However, the lower heating is not solely responsible for the complete dominance of material hardening over thermal softening in the 2μm feedstock, as it also experiences significantly higher rates of strain (see Figure 5.18c) which increases strain rate hardening at the time the feedstock is undergoing the most intense heating, which acts to prevent thermal softening becoming dominant and preventing the initiation of a shear band instability. This lack of a shear band instability in small scale feedstock impacts was also observed by Schmidt et al [10] but was explained by more even feedstock heating and as such offers a less complete description of the physics of the impact.

5.4 Feedstock Initial Temperature Effect on Splat Morphology

Impacts of 10μm heat conductive copper feedstocks on heat conductive copper substrates have been considered using initial velocities of 400 and 600 m/s and temperatures of 298 and 593 K in order to investigate the effects of the initial temperature of the feedstock. A range of velocities is used to assess the effect of feedstock pre-heating on the critical velocity for bonding. Impacts using 2 and 20μm feedstock travelling at 600 m/s with initial temperatures of 298 K and 593 K are also considered to examine the effect of feedstock size on the temperature effects. The entrainment time of the feedstock in the carrier gas is short and so typically feedstock does not heat completely to the gas temperature; for example feedstock entertained in a 700 K carrier gas was found to heat to 500 K experimentally [77]. The high temperature case considered here represents an extreme case of heating where the entire feedstock has heated to a typical carrier gas temperature of 593 K [3]. This extreme heating is used to exaggerate the heating effects without introducing melting in the feedstock. The substrate will undergo heating from the impinging gas jet and this has been shown to only become significant after jet impingement times of a number of seconds [83]. Additionally, the substrate temperature at steady-state is typically around half that of the gas temperature [83]. The impact of feedstock on previously uncoated substrate will be considered and so the substrate heating is neglected over the considered impact durations of a few nano seconds.

The temperature distributions within the 10μm feedstocks show a dependency on the initial temperature of the feedstock at both 400 and 600 m/s. As the initial feedstock temperature is increased, heat conduction away from the feedstock and into the colder substrate becomes more significant. At higher feedstock temperatures, this results in a colder layer of material at the feedstock/substrate interface relative to the splat body (see Figures B.43 and B.51). While the lower temperature feedstocks show the hottest material at the feedstock/substrate interface (see Figures B.20 and B.28), the less intense thermal gradients reduction the rate of conduction and increase the localisation of temperature. The interface cooling is more significant at lower impact velocities due to lower kinetic energy producing less heating in the feedstock/substrate interface region.

The 400 m/s impact shows a drop of 83 K from the initial temperature whilst the 600 m/s impact only shows a drop of 53 K. The 20μm diameter feedstocks show the same overall heating pattern as the 10μm feedstock (see Figures B.59 and B.67), and cooler material is found at the feedstock/substrate interface relative to the splat body when feedstock initial temperatures are higher than the substrates. The amount of cooling at the interface is reduced in the larger feedstock due to the additional heating from the increased kinetic energy of the impact and the temperature does not drop below 593 K. The smaller 2μm feedstocks also show cooling at the interface when the feedstock is hotter than the substrate, the amount of cooling is higher than both the 10 and 20μm feedstocks due to the lower impact heating resulting from lower impact kinetic energy. The amount of impact heating at the interface is a product of the feedstock mass and impact velocity and is independent of the feedstock initial temperature. It is the differences in initial temperatures between the feedstock and substrate that dictates the rate at which heat is conducted into the colder substrate; with higher temperature differences producing steeper thermal gradients across the substrate and therefore higher rates of heat conduction into the substrate.

The higher initial temperatures thermally soften the feedstock before the impact begins resulting in a lower yield strength and a more deformable material than lower temperature cases. A comparison of flattening ratios and normalised penetration into the substrate (P^*) is given in Table 5.6. As feedstock temperature is increased and the material becomes more deformable, the flattening ratio of the splat also increases. Interestingly, there is also greater penetration into the substrate. The increased feedstock heating is conducted across the interface and acts to thermally soften the substrate material allowing for deeper penetration of the feedstock. The greater deformation of both the feedstock and substrate increases the likelihood of mechanical interlocking bonds and the deeper penetration increases the possibility of a feedstock becoming partially encapsulated by the substrate. Additionally the elevated temperatures ease the formation of metallurgical bonds across the interface.

The slight differences in temperature distributions seen in the different sized feedstocks are caused by the variance in kinetic energy and are not a function of the feedstock preheat. The results shown in Table 5.6 show that the different sized feedstocks show similar effects from the increased initial temperature. For these reasons the 10μm

Feedstock diameter (μm)	Feedstock temperature (K)	Flattening ratio	P^*
2	298	0.384	0.644
2	593	0.426	0.738
10	298	0.402	0.747
10	593	0.446	0.781
20	298	0.373	0.644
20	593	0.426	0.738

Table 5.6: Comparison of the effect of feedstock initial temperature on final flattening ratio and penetration into the substrate for a variety of feedstock diameters.

impact results will be discussed in more detail and the conclusions can be applied in general terms to the other sized feedstocks. At an impact velocity of 600 m/s, the yield strength distribution within the feedstock shows (see Figures B.27 and B.52) reduction in overall strength at higher initial temperatures. The low temperature impact (Model E) shows higher levels of hardening at the feedstock/substrate interface than is seen in the splat body. Whilst this is observed in the higher temperature impact, the additional hardening is restricted to a much smaller area of the interface. This is a result of the additional softening and its effect on the distribution of EPS and rates of EPS. At higher temperatures the splat experiences plastic straining that is much less localised than in the colder impact (see Figures B.30 and B.54) which produces more uniform hardening profiles observed at higher temperatures. This is reflected in the EPS distributions which show a much larger proportion of the splat displaying significant levels of EPS at higher temperatures (see Figures B.29 and B.53).

In order to examine the effect of preheating on jet formation and therefore bonding, the temperature, yield strength and EPS rate in the jetting region are compared in Figure 5.19. The temperature profiles show the increased feedstock heating (see Figure 5.19a), where the peak heating caused by the impact is damped by the additional cooling caused by the temperature differential between the feedstock and substrate, resulting in proportionally less heating than is seen in the colder impact. The elevated temperature has had much less of an effect on the profile of EPS rate (see Figure 5.19b) with only a

slight increase seen at 593 K. The elevated temperature coupled with the smaller increase in strain rate has resulted in proportionally more softening during material jetting (see Figure 5.19c), the increased softening is visible for the full duration of the impact period considered. The same trends can be seen at a lower impact velocity of 400 m/s; at this velocity the yield strength profile still does not show the transient period of high softening that would indicate material jetting although there are signs of additional softening during the required time period. This indicates that raising the initial temperature of the feedstock reduces the critical velocity required for feedstock/substrate bonding. The deformation of the feedstock which is key to bonding is dependant on the energy (kinetic and/or thermal) being imparted to the feedstock being sufficient to create the high rates of deformation and interface temperatures required for bond formation and therefore, at lower temperatures a higher spray velocity is required and at higher temperatures lower impact velocities are needed. This dependency on the total balance of energy within the feedstock can be seen in other spray coating processes such as in plasma spray where higher temperatures are matched with lower spray velocities (Table 1.1). It is this reduction in material strength and subsequent increase in the deformability of the feedstock that is the key effect of feedstock temperature.

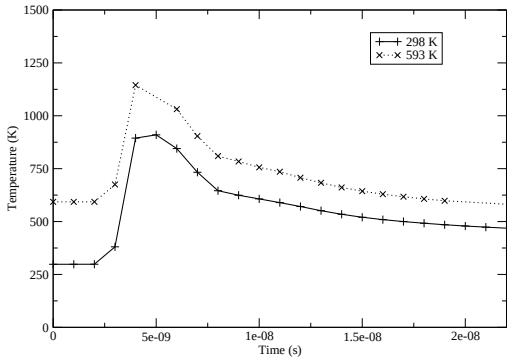

(a) Feedstock initial temperature effect on temperature in jet region.

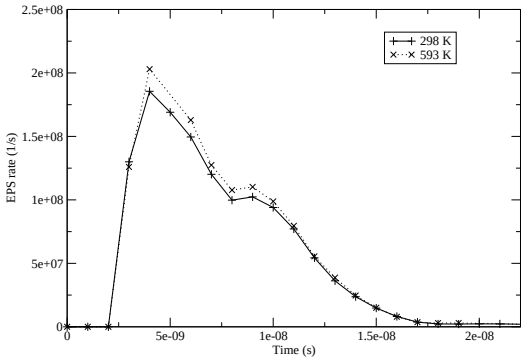

(b) Feedstock initial temperature effect on EPS rate in jet region.

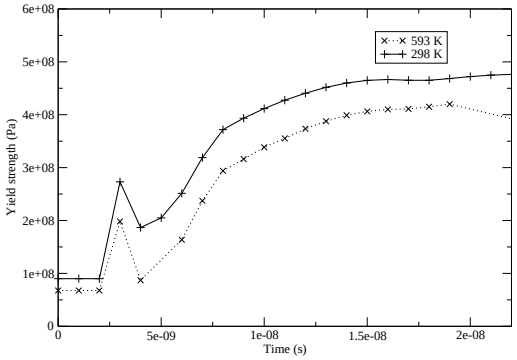

(c) Feedstock initial temperature effect on yield strength in jet region.

Figure 5.19: Comparison of EPS rate, temperature and yield strength in the high EPS region with impact velocity of 600 m/s and varying initial feedstock temperatures.

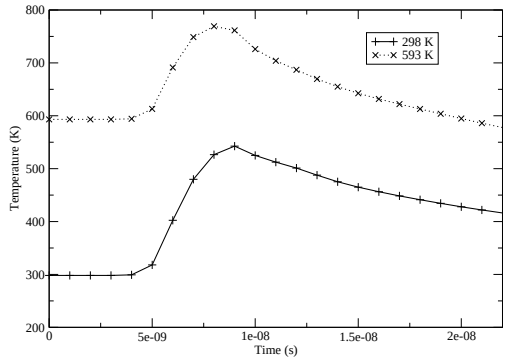

(a) Feedstock initial temperature effect on temperature in jet region.

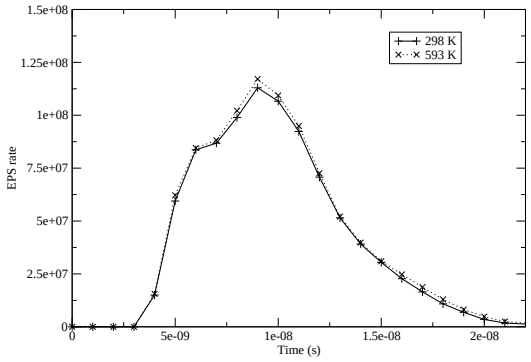

(b) Feedstock initial temperature effect on EPS rate in jet region.

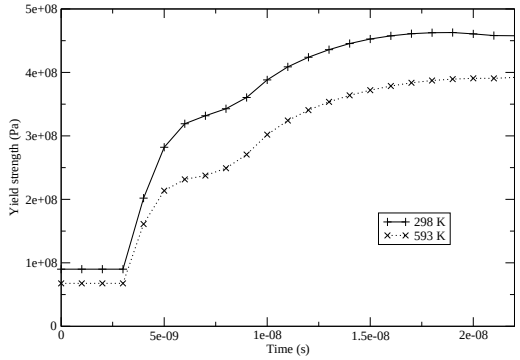

(c) Feedstock initial temperature effect on yield strength in jet region.

Figure 5.20: Comparison of EPS rate, temperature and yield strength in the high EPS region with impact velocity of 400 m/s and varying initial feedstock temperatures.

5.5 Feedstock/Substrate Bonding

In the previous descriptions of feedstock impacts and the effects of parameters such as feedstock velocity, temperature and size, the assessment as to whether a feedstock has bonded to the substrate has depended on detailed analysis of material properties at the feedstock/substrate interface. A transient dominance of thermal softening that coincides with a period of peak heating and EPS rate has been indicative of a bonded feedstock, the incidence of these features have been shown to coincide with the experimentally determined critical velocities.

The effect of feedstock size on the formation of shear band instabilities has been observed with smaller feedstocks showing no sign of the material jetting that would indicate the presence of an instability at impact velocities and temperatures where material jetting has been observed in larger feedstock. Feedstock with diameters of $2, 10$ and 20μm were investigated and the main effect of feedstock size was found to be in the kinetic energy at impact. The models used for the investigation have simplified the initial feedstock morphology to that of a sphere, in this case particle mass and therefore kinetic energy varies proportionally to the feedstock diameter cubed and so the diameter has a larger influence on impact energy than the impact velocity. The 2μm diameter feedstocks have 125 times less kinetic energy at impact than the 10μm feedstocks for example. This implies that using a critical velocity to describe the likelihood of bond formation does not adequately capture the full complexity of the coating process. Indeed current critical velocity measurements are defined for a particular feedstock material and average size resulting in a condition for bonding that actually requires two variables that indirectly describe the kinetic energy level within the feedstock. The use of critical velocities as a condition for bonding is useful for the production of coatings since this is an easily controlled process parameter and so determination of this parameter will always be a goal of any cold spray modelling method. The discussion of the effects of temperature on splat formation has shown that as the splat initial temperature is increased, there is an increase in material jetting as the thermal softening increases. This observation reinforces the hypothesis that total energy levels in the splat are what trigger bond formation. Previous works employed a qualitative assessment of the extent and strength of material jet formation to determine whether a splat has bonded to the surface. The

formation of this feature is observed at known experimental critical velocities. In order to improve the applicablity and impact of splat formation models a more quantitative condition for bonding is desirable. A new measure for strength of material jetting (and therefore bonding) refered to as a bonding coefficent will now be described.

The material jet caused by shear band instabilities has been proven a condition for bond formation, the material jet is a region of material undergoing significant rates of EPS implying a local energy level of sufficient strength to overcome the material yield strength by a significant margin. This indicates that jet formation can be determined by comparison of energy levels against the local material yield strength which describes the energy per unit volume needed to induce plastic deformation. In the current work, the SPH solver calculates energy per unit mass for each SPH particle, multiplication of this property by the local density will enable comparison with the local yield strength:

$$\Psi = \frac{E\rho}{y} \tag{5.3}$$

where Ψ is the ratio between energy and yield strength and will be referred to as the bonding coefficient, E is energy per unit mass and y is the current material yield strength which in the current work is calculated using the Johnson-Cook model and so takes thermal softening and work hardening into account.

The evolution of this bonding coefficient has been tracked in the region of the feedstock/substrate interface that experiences the highest EPS for a range of feedstock impact initial conditions in Figure 5.21. The initial conditions used in this plot span the range of non-bonded to bonded feedstock; the bonded feedstocks show a sharp increase in bonding coefficient at the same time that the presence of a shear band instability has been detected as a reduction in yield strength (see Figure 5.22). The unbounded feedstocks lack this rapidly forming feature and instead show a more gradual increase towards a significantly lower peak in bonding coefficient. After examination of the peak coefficient in all the feedstock impacts considered, the unbonded feedstocks show a bonding coefficient of less than 4 for the entire impact duration. Whilst bonded feedstocks show values higher than this for a significant portion of the impact duration. For this reason bonding coefficients above 4 across a significant proportion of the interface indicate that the impact was energetic enough to trigger the formation of a shear band instability and

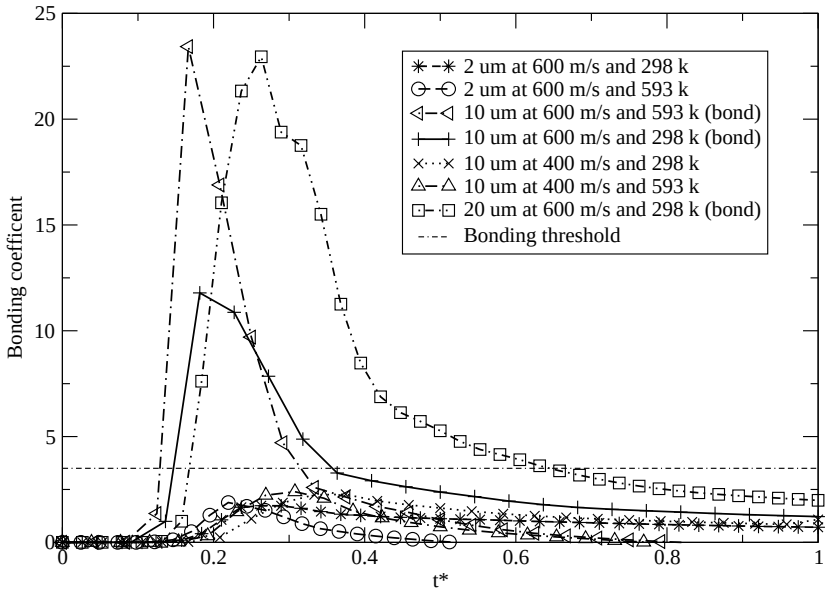

Figure 5.21: Comparison of bonding coefficient evolution in the material jets.

therefore cause feedstock/substrate bonding.

Figure 5.23 shows the evolution of bonding coefficent for both a bonded splat (impact velocity 600 m/s) and a non-bonded splat (impact velocity 400 m/s). In this figure the bonding coefficent is capped at 4 in order to illustrate when this threshold is crossed for each model. The peak bonding coeffiecent reached over the entire course of the impact is 3.8 for the non-bonded splat and 13.6 for the bonded splat. The bonded splat also maintians high levels of bonding coefficent for a significantly longer duration than the non-bonded splat, increasing the likelyhood of bond formation.

The bonding coefficient can be calculated for each SPH particle by the solver and monitored to determine bond formation. This simpler criterion for identifying shear band instabilities makes the determination of feedstock/substrate and feedstock/feedstock bonds in models of complex coating formation a much simpler task.

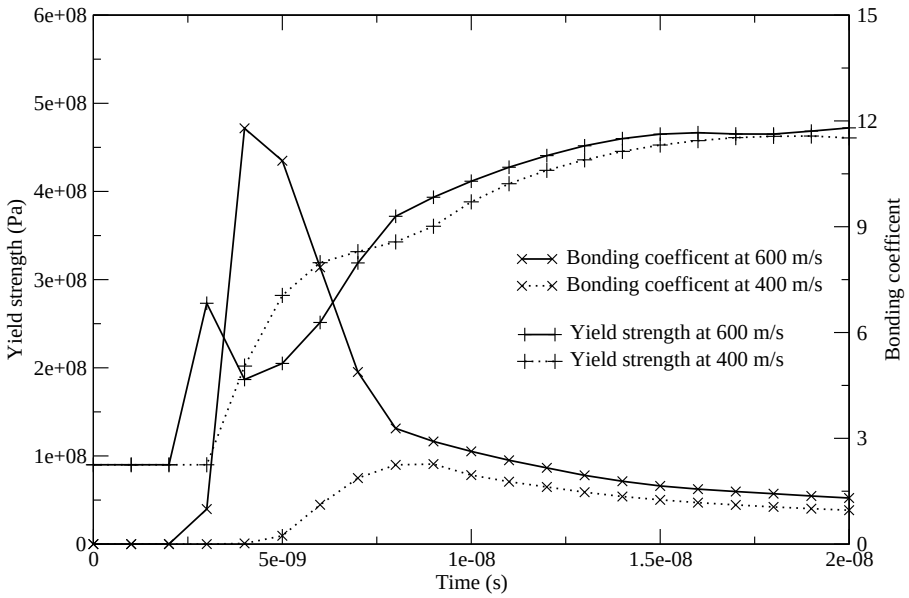

Figure 5.22: Comparison of bonding coefficient and yield strength evolution at the material jets.

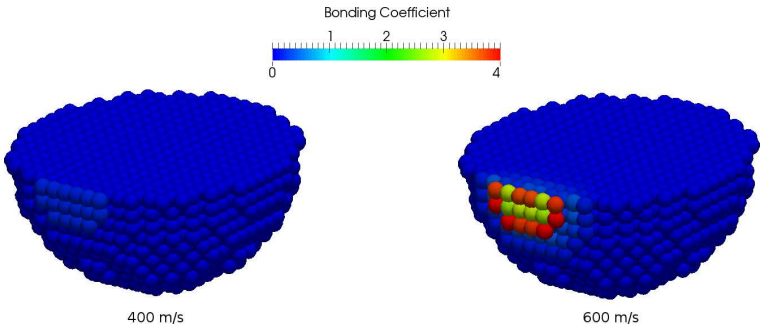

(a) 2 ns.

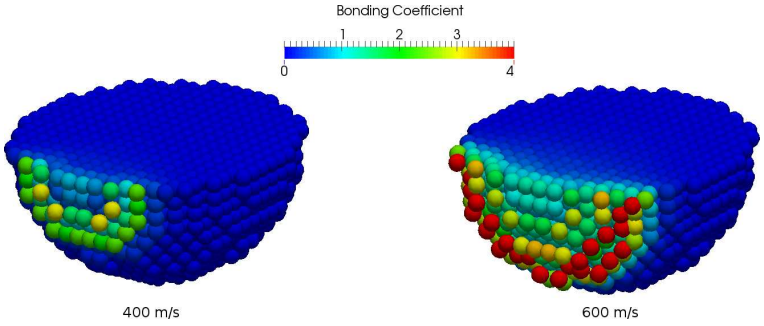

(b) 4 ns.

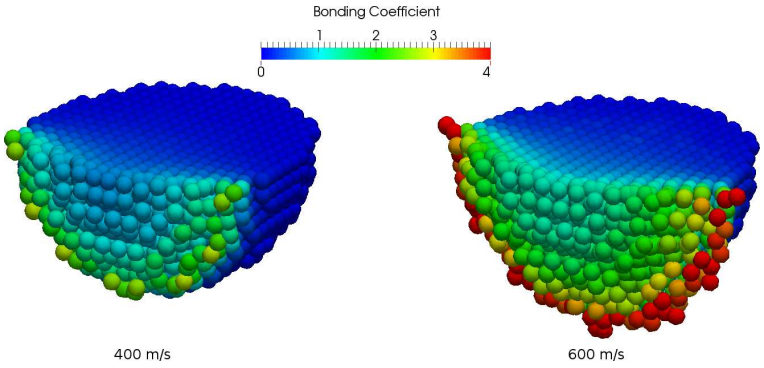

(c) 8 ns.

Figure 5.23: Comparison of the bonding coefficient at impact velosities of 400 m/s and 600 m/s.

Chapter 6

Coating Formation

The previous chapter described in detail the formation of an isolated splat morphology and explored the effects of spray parameters such as feedstock impact velocity, size, temperature, and conductivity. It also as developed a dimensionless number (bonding coefficient) that acts as a condition for feedstock/substrate bonding. The present chapter extends the three-dimensional models of isolated splat impacts to the simultaneous impact of multiple feedstocks to demonstrate the capabilities of the developed solver. The presented study is brief with only a single coating configuration considered, but the overview provided shows the potential for the current work to be extended to models of coating formation with ease.

6.1 Problem Definition

The successive impact of six three-dimensional copper feedstock particles onto a copper substrate is modelled, periodic boundaries are used to replicate a much larger three-dimensional coating process with a duration of 100 ns. The initial SPH particle deployment is shown in Figure 6.1 where material bodies are differentiated by colour. The substrate depth has been truncated in this figure to better show the feedstock deployments. In fact the substrate is 10 feedstock diameters deep along the y-axis and bounded by a dynamic boundary at its base. This depth ensures that shocks reflected by the dynamic boundary are negligible. The upper and lower x- and z-axis domain boundaries are treated with a periodic condition. The feedstock particles are 10μm in diameter and

have an initial temperature of 298 K and an impact velocity of 600 m/s along the y-axis. The SPH particles are deployed with a particle spacing of 0.5μm and an initial smoothing length, h, of 0.65μm.

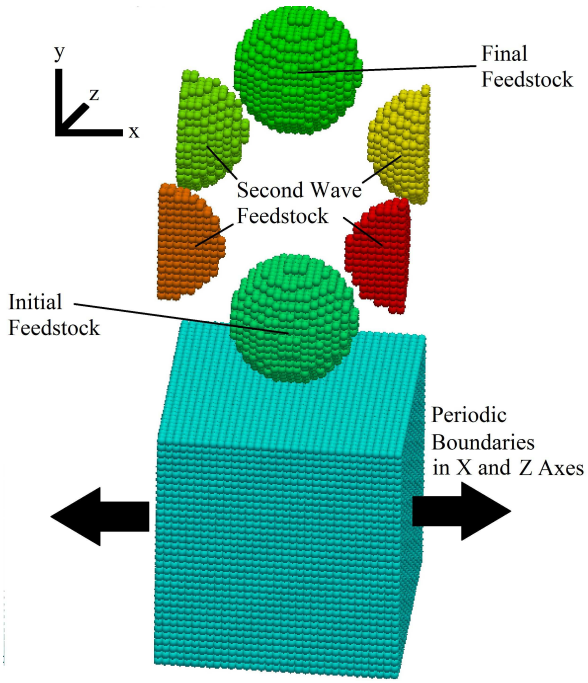

Figure 6.1: Coating model initial SPH particle positions.

An in-depth analysis of the modelled coating formation will be undertaken describing the evolution of morphology, temperature, EPS, yield strength and bonding coefficient within the feedstock and substrate.

6.2 Coating Analysis

A cross section of the coating morphology evolution is shown in Figure 6.2, where the cuut is made on the x-y plane and the individual feedstocks and substrate are emphasised with different colours. The first feedstock to impact the substrate does so in the centre of the modelled domain and for a large part of its splat formation resembles an isolated splat impact. A deviation from the previously discussed single splat morphology is seen once the next wave of feedstock impacts occur. These feedstocks impact at the corners of the domain, at the outer edge of the initial feedstock impact. The interaction of these newly impacting feedstocks with the initial splat has caused the substrate material to

fold back over the edges of the initial splat, resulting in encapsulation which was not seen in the isolated splat impacts and serves to increase the coatings adhesion to the substrate material. The final feedstock is positioned directly above the initial feedstock, because of the significant flattening experienced by the feedstock during splat formation, and this final feedstock shows little direct contact with the substrate material and is instead characterised by interactions with the already impacted feedstock below it. The effect of this impact on the already impacted feedstock is significant. The initial splat is tamped into the substrate material creating a deeper crater and flattening the splat even further. Material from this splat can be seen at the leading edge of the jet feature on the final splat indicating that the final splat has formed a crater in the initial splat and that the dominant bonds will be feedstock/feedstock. During the final impact, the crater formation has caused material from the substrate and initial feedstock to fold over the edges of the second wave feedstocks, thus, further increasing encapsulation. This pattern of encapsulation was not suggested by the single splat morphology study but appears quite often the coating formation under consideration, implying that coating bond strength can be higher than that expected from the formation of metallurgical bonds alone.

The coating temperature at 33, 66 and 99 ns is shown in Figure 6.3. The temperature in this figure is scaled to match the time periods chosen. When the whole impact duration is considered, a peak temperature of 1122.9 K is reached at the interface between the first and last feedstock to impact. The final feedstock impacts directly on top of the previously impacted feedstock, which has already undergone deformation and heating, while the subsequent impact further deforms the first feedstock increasing the temperature beyond the melting point of the material. This temperature is significantly larger than was observed in an isolated splat impact under these initial conditions, indicating that analysis of isolated splats does not capture the full dynamics of a coating formation event. In the early stages of the coating formation only a single splat is impacting the substrate. At this time, the patterns of heating show the expected agreement with the previous analysis of an isolated splat formation event. As the second wave of feedstock strikes the substrate, heating still shows the key characteristics of single splats, where heating is greatest in the splat flank regions and the top centre of the splat shows little heating. The initially impacted splat is starting to show more uniform heating as a result of the

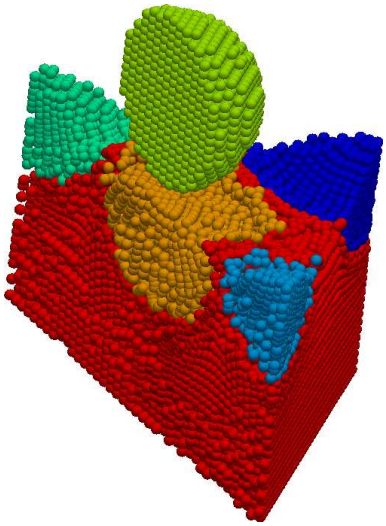

(a) 33 ns.

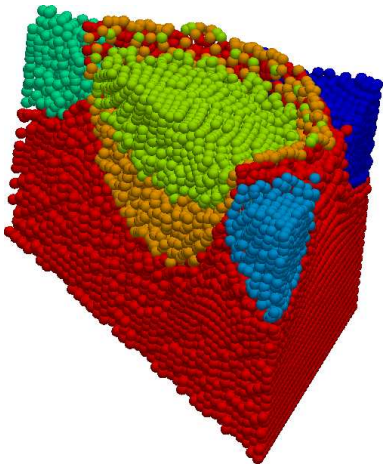

(b) 66 ns.

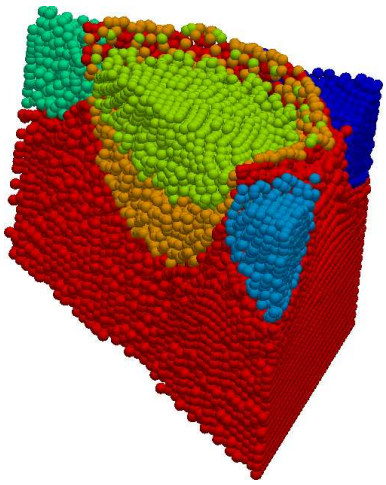

(c) 99 ns.

Figure 6.2: Coating morphologies at t = 33, 66, and 99 ns.

longer duration of this model when compared to the isolated splat model. The impact of the final feedstock has the most significant effect on the heating of the already impacted splats. The heating caused by this subsequent impact homogenises the temperatures in the existing layer of material but leaves a relatively hotter ring of material at the leading edge of the material jet.

The evolution of yield strength within the coating is shown in Figure 6.4. In the early stages of the coating formation, very distinct regions of hardening can be seen in the substrate and impacted feedstock. The highest yield strengths are seen in the high strain and strain rate splat flanks. This is in agreement with the observations of isolated splat impacts. The biggest deviation from these observations comes with the final feedstock impact. The final feedstock does show zones of increased hardness in its flanks as expected as it impacts on the previously deposited splats. The effect on the previously impacted feedstock is to increase the duration of elevated heating and causes further deformation. This results in a layer of material that displays a uniform yield strength representing significant hardening from the initial material properties. Zones of softer (lower yield strength) material can be seen at the top layer of the coating; these correspond to the top centres of the second and final wave feedstocks which have experienced the least strain throughout the coating event.

The state of EPS within the coating at 33, 66 and 99 ns is shown in Figure 6.5. At 33 ns the EPS distribution resembles that of the isolated splat impacts described in the previous chapter. The highest EPS is seen at the flanks of the impacting feedstocks, lower values are seen at the bottom centre of the splats and the splat bodies show little to no EPS. This pattern of plastic deformation holds true for the second wave feedstock splats for the duration of the coating event, the initial feedstock shows significant deviation from this norm however. The impact of the final feedstock directly on top of the initial feedstock has caused significant plastic straining throughout the entirety of the splat as the initial splat is tamped into the substrate, loosing the central peak feature seen at the top centre of splats in isolated impacts. Peak levels of EPS are observed in the interface region between these two splats where the already strained material is deformed to a greater extent by the final impact. Despite this additional strain, the final EPS distribution in the lower layers of the coating do not yet show the homogenisation seen in the temperature (Figure 6.3c), yield strength (Figure 6.4c), and bonding (Figure 6.6c)

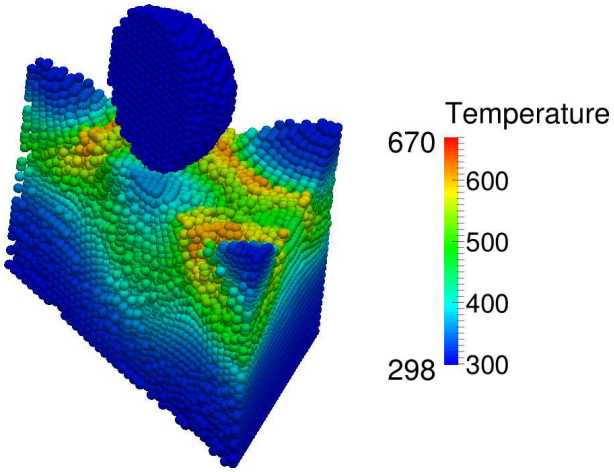

(a) 33 ns.

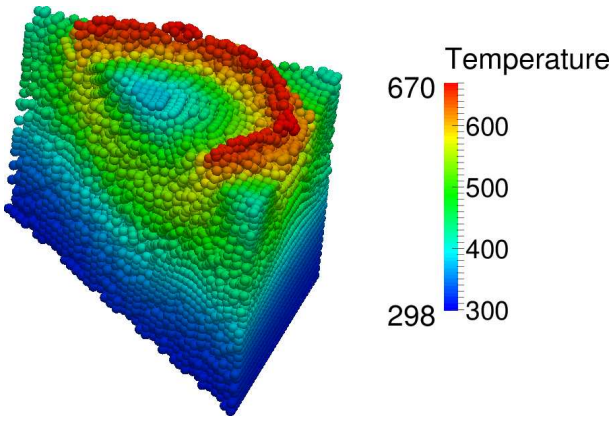

(b) 66 ns.

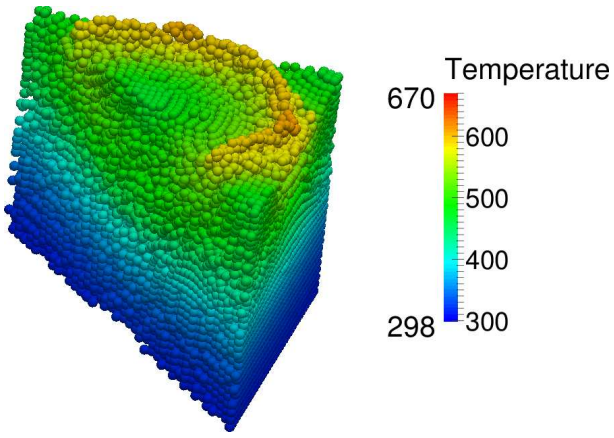

(c) 99 ns.

Figure 6.3: Coating temperature at t = 33, 66, and 99 ns.

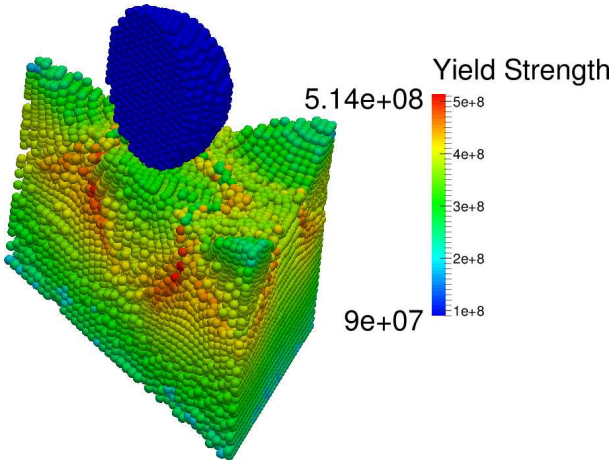

(a) 33 ns.

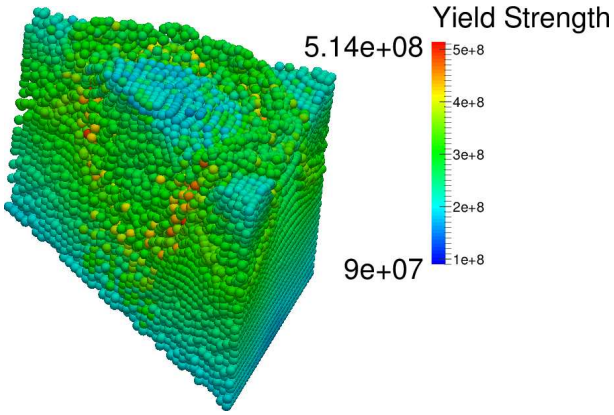

(b) 66 ns.

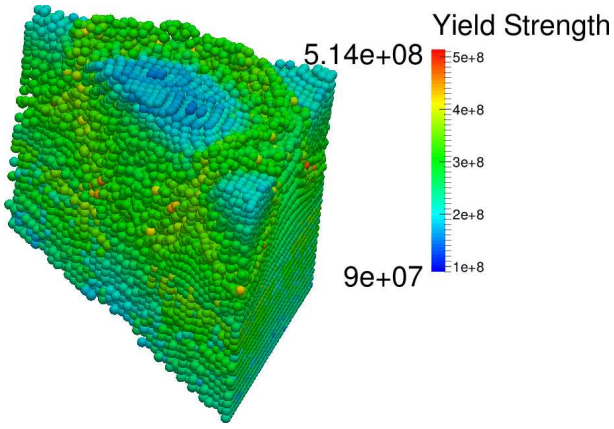

(c) 99 ns.

Figure 6.4: Coating yield strength at t = 33,66, and 99 ns.

evolution, with higher EPS levels observed at the flanks of the separate splats when compared to their splat body regions.

The description of splat morphologies indicated that feedstock encapsulation in existing coating layers plays a significant role in bond formation. In order to examine the possible extent of metallurgical bonds, the bonding coefficient described in Chapter 5 and Equation (5.3) has been calculated for every SPH particle used in this model. The development of this coefficient is shown in Figure 6.6. In the early stages of the impact the bonding patterns show similarities to those seen in isolated splat impacts with elevated bonding coefficients seen in the flank regions of the splats while low levels are observed in the splat bodies. In line with the previous observations of coating formation, the largest deviation from the isolated splat behaviour is seen with the impact of the final feedstock. The previously impacted layers of material have a more uniform distribution of bonding coefficient than earlier in the impact, this is caused by two factors. Firstly, the impact of fresh feedstock causes deformation in the impacted splat top centres, which previously had experienced only minor strains, creating the more uniform hardening patterns seen in Figure 6.4c. Secondly, the longer model duration coupled with heat conduction has resulted in more uniform heating (see Figure 6.3c). The final feedstock shows similar bonding coefficient trends to those seen in the isolated splat analysis. Interestingly the splat top centre shows high bonding coefficients towards the end of the coating event. This is likely due to heat conduction becoming evident due to the longer model duration and indicates that metallic bonding could be enhanced between this feedstock and a subsequent impact, were one to occur.

The examination of the overall coating properties has shown that the largest deviation in splat properties and evolution from the isolated splat analysis is observed at the initially impacted splat that has been subjected to the subsequent feedstock impacts. In order to better understand these differences, a 1μm cross-section has been taken through the centre of this feedstock and distributions of temperature, yield strength and EPS at 30, 40 and 50 ns are plotted in Figures 6.7, 6.8 and 6.9. Only moderate levels of heating are seen at at 30 ns in Figure 6.7; at this point in time the subsequent impact event has not initiated and splat properties are very similar to those of an isolated splat. There is a noticeable difference in the splat morphology when compared to an isolated impact, as this splat has been confined by the impact of neighbouring feedstock resulting in a fatter

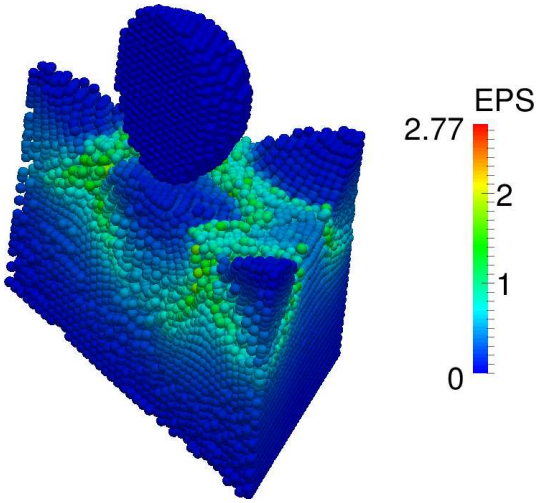

(a) 33 ns.

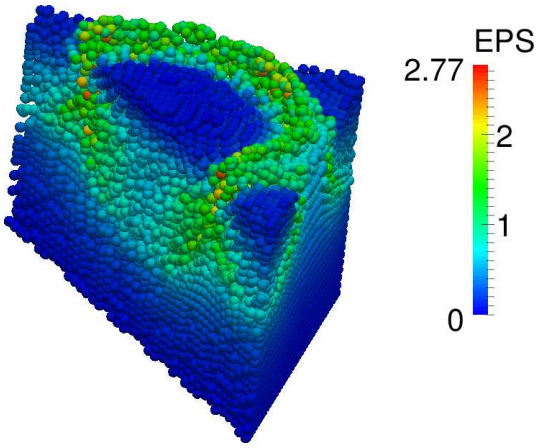

(b) 66 ns.

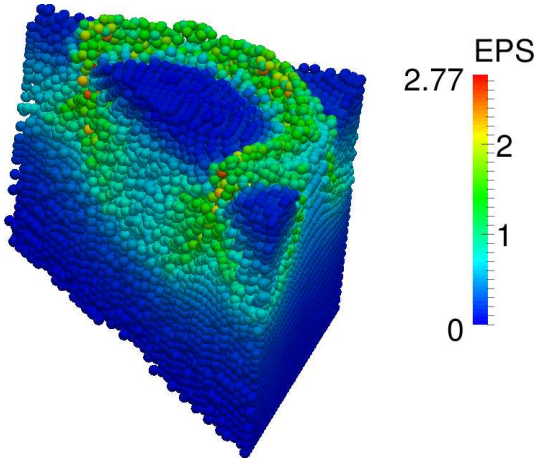

(c) 99 ns.

Figure 6.5: Coating EPS at t = 33, 66, and 99 ns.

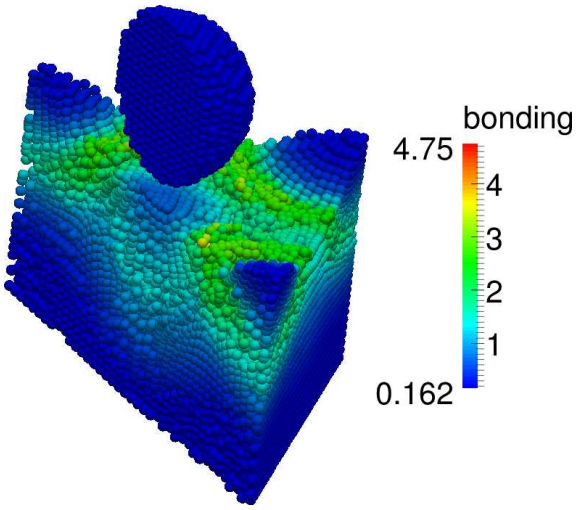

(a) 33 ns.

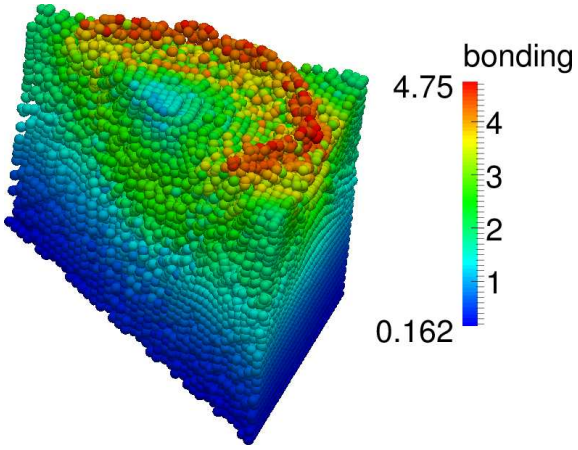

(b) 66 ns.

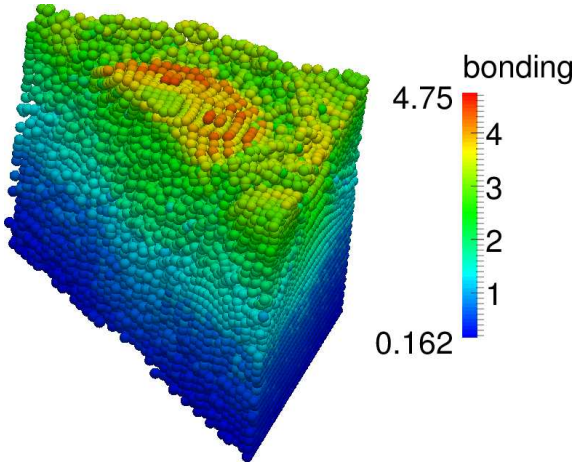

(c) 99 ns.

Figure 6.6: Coating bonding coefficient at t = 33, 66, and 99 ns.

splat body which has created a deeper crater in the substrate. At 40 ns, the subsequent impact is in progress and there is a corresponding effect on the splat morphology. The temperature distribution is also showing significant deviation from the isolated splat results with a region of extreme heating seen on the top surface of the splat. This elevated heating corresponds to the high strain flank regions of the impacting feedstock and it is this rapid straining that is producing the heating effect. At 50 ns cooling is observed in the feedstock as the large thermal gradients produce rapid cooling once the initial impact stages are completed.

A similar pattern is seen in the yield strength distributions shown in Figure 6.8. The high temperatures found on the top surface of the splat have increased thermal softening in this area resulting in a reduction in yield strength. Localised and transient thermal softening such as this has been observed indicating the presence of a shear band instability in isolated splat models and so it is expected that such an instability is formed in this region. The impact of the new feedstock has acted to increase hardening in the splat body whilst the extra heating has slightly softened the material in the initial splat's flank regions. The distribution of EPS (see Figure 6.9) has remained largely the same as that seen in isolated splat impacts with the highest strains seen at the splat flanks, lower values at the bottom centre and splat body and the lowest values at the top centre of the splat. However, the overall levels of EPS in the splat have increased significantly over those seen in isolated impacts, as the newly impacting feedstock causes additional plastic deformations.

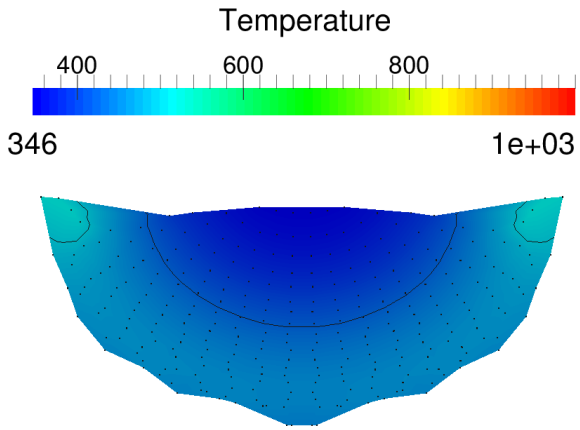

(a) 30 ns.

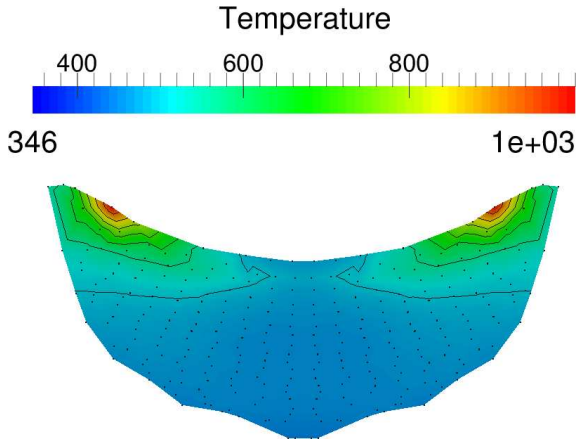

(b) 40 ns.

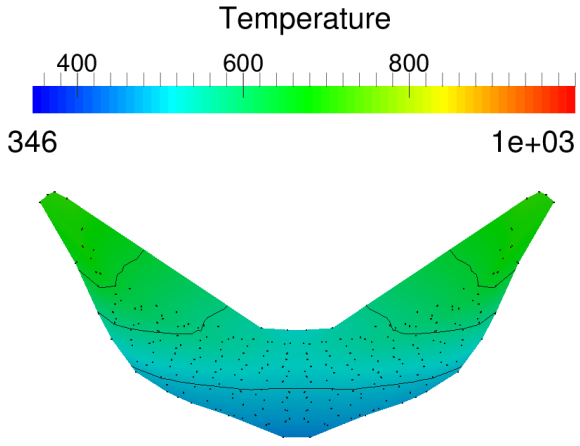

(c) 50 ns.

Figure 6.7: Temperature of initially impacted feedstock at t = 30,40, and 50 ns.

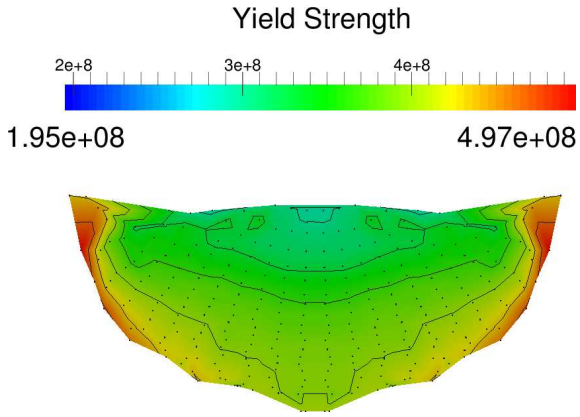

(a) 30 ns.

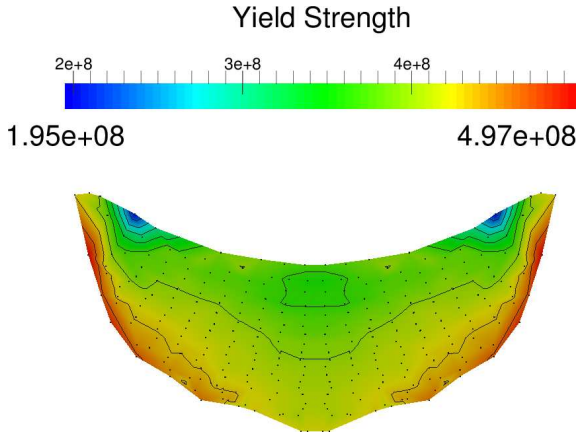

(b) 40 ns.

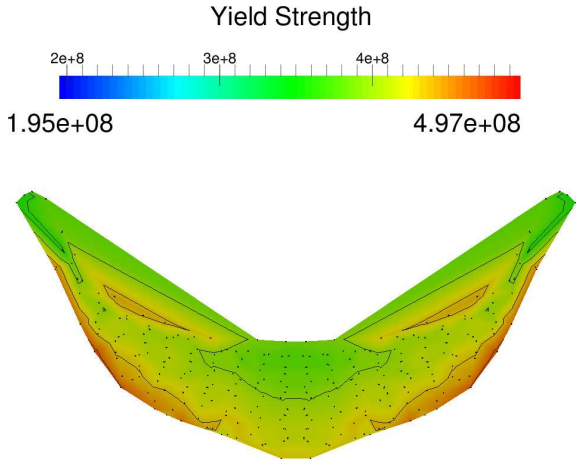

(c) 50 ns.

Figure 6.8: Yield strength of intiailly impacted feedstock at t = 30, 40, and 50 ns.

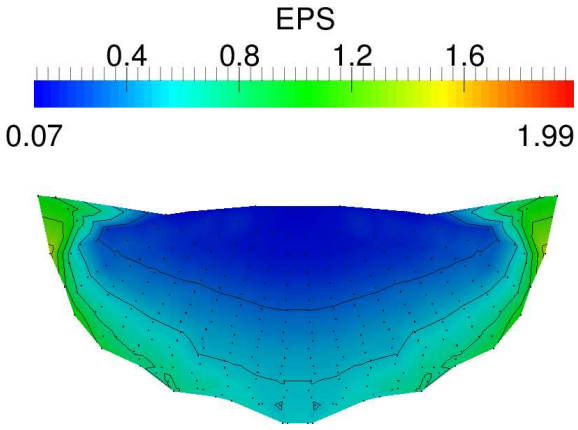

(a) 30 ns.

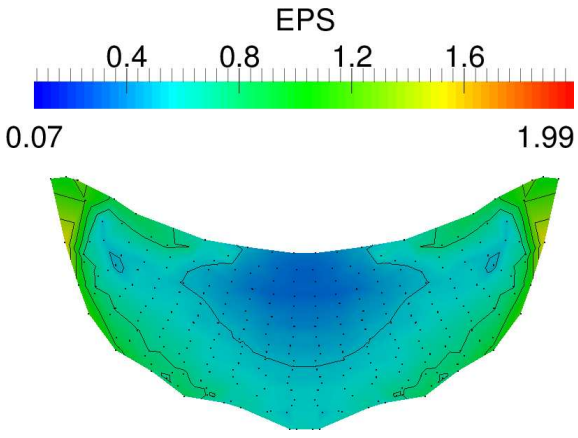

(b) 40 ns.

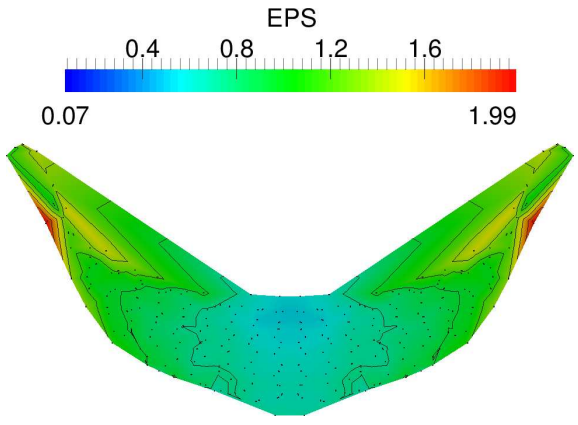

(c) 50 ns.

Figure 6.9: EPS levels in intiailly impacted feedstock at t = 30, 40, and 50 ns.

6.3 Summary

A simple coating formation event has been successfully modelled and the results analysed to demonstrate the capabilities of the developed solver. Significant differences between the isolated splat results and the coating presented in this chapter only appear with the impact of fresh feedstock onto already coated surfaces. The main effect of neighbouring impacts is to deform the splat morphology and potentially cause encapsulation as substrate material is folded over the lip features of neighbouring splats. Subsequent impact of feedstock acts to tamp the existing splats down into the existing coating and was observed to increase mechanical interlocking. Since the impact occurs on the top surfaces of the coating, previously unstrained regions are deformed homogenising coating properties when compared to single splat morphologies. The analysis of the initially impacted splat as it is impacted by a subsequent feedstock has shown that local heating can become much larger than that predicted by the isolated splat models. In some cases even exceeding the material melt temperature for a short duration when the isolated splat under similar conditions remained well below the melt temperature. The impact of fresh feedstock onto already deformed and heated feedstock causes this additional heating and is to be expected as the total kinetic energy of the coating formation is larger than that of isolated impacts. Although the coating event described in this chapter is a simplification of the conditions found in a physical coating, employing an idealised feedstock powder with identical and perfectly spherical particles all impacting at the same velocity and temperature, it is sufficient to demonstrate that the developed solver can be a powerful tool for the analysis of the cold spray process given sufficient time to conduct an in-depth study of coating formation. The following chapter will discuss the potential future applications as well as summarising the current research work.

Chapter 7

Conclusions and Future Work

The aim of this thesis is to improve on current capabilities for modelling splat morphologies produced by the cold spray process. This has been achieved by improving upon current SPH models of cold spray and by proposing a bonding coefficent that aims to predict the adhesion of splats from modelling data alone. The following chapter summaries what improvements have been implemented and how they improve upon existing methods. Lagrangian Finite Element Methods (FEM) are still the most common methodology used in the literature despite significant drawbacks such as a limit on obtainable resolution and a requirement for regular re-meshing, all of which stem from its meshed nature. Eulerian methods have also been applied and capture the large deformations with ease but inaccuracies arise with interface tracking and retrieval of material histories.

The current work utilised the Smoothed Particle Hydrodynamics (SPH) methodology to combine the advantages of both the above mentioned methods to better capture material histories and interfaces whilst enabling large strains. The application of SPH to the cold spray process is still in its infancy with only a handful of simple studies performed. Additionally, the application of SPH to solid mechanics problems is also relatively undeveloped when compared to the work done using FEM. The current work has extended the initial work of Libersky et al [114] on SPH solid mechanics, with the addition of heat conduction, zero impedance boundaries, tensile correction, and a viscous fluid material model. The developed solver is accelerated by the application of multi-threaded processing using the C++ 11 standard. The tensile instability correction of Monaghan has been extended to include the energy equation. Monaghan's work utilised the weakly

compressible equation of state which does not include energy dependant terms, however the current work follows that of Libersky and applies the Mie-Grunisen equation of state which depends on energy as well as compression. In order to maintain consistency, both the momentum and energy equations need to see the same state of material stress and so Monaghan's artificial stress is included in the energy gradient calculations. The accuracy of the developed solver has been rigorously verified against rebound tests, Pousielle and Couette flows, heat conduction in slabs, and Taylor bar impacts. The tensile stability of the methodology has also been proved with a pertubation test similar to that of Swegle [119]. The performance of the developed multi-threaded solver was benchmarked and was found to give a speed up of 3.4 with the use of 10 parallel threads resulting in significant savings in computational time.

An in-depth investigation of three-dimensional isolated cold sprayed copper feedstock impact events has been carried out and a detailed analysis of the resulting splat morphologies has been undertaken. In order to correctly and efficiently model the isolated splat impact, an investigation of boundary condition suitability was undertaken. It was found that periodic and untreated boundaries can affect the evolution of the splat morphology by reflecting or re-introducing the stress waves created by the impact. Whilst this could be mitigated by using larger substrates, doing so significantly increases the computational time required. A novel zero impedance boundary condition was developed in the current work which replicates an infinite domain without wrapping the domain as with a periodic treatment. The zero impedance boundary approximates the material conditions beyond the boundary by reflecting the actual material conditions over the boundary whilst preserving the sign of velocities and stresses. Stress waves are then allowed to propagate out of the domain and into the region of reflected material. The effects of this new boundary condition on splat morphologies was then studied in detail and found to provide an improvement over existing periodic and untreated conditions.

A range of process parameters have been considered in the isolated splat morphology study including impact velocity, temperature, feedstock size, and material heat conductivity. Impact velocity was varied from 400 to 800 m/s, a range that transitions from below the critical velocity for bonding (500 m/s) to well above it. At impact velocities in excess of the critical velocity, the heating induced by the extreme strain rates resulted in material softening localised at the flanks of the deforming feedstock; as the material weak-

ened the local strain rate increased, initiating a positive feedback loop and a shear band instability, resulting in the distinctive jet feature observed in cold sprayed splats. The formation of material jets has been experimentally linked to successful feedstock/substrate and feedstock/feedstock bonding and so the occurrence of the shear instability is considered a condition for bonding in the literature. Higher impact velocities produce increased levels of kinetic energy in the feedstock, enabling greater deformation and stronger material jetting. Feedstock size was also found to affect material jetting with small 2μm feestocks showing no sign of the instability at impact velocities of 600 m/s. The reduction in size and therefore mass has resulted in a corresponding reduction in the kinetic energy of the impact, causing a reduction in heating and material softening, thus, preventing the formation of a shear band instability.

The inclusion of heat conduction models has been shown to dramatically change the properties of impacted splats. The early work by Assadi et al [3] on modelling the cold spray process assumed an adiabatic impact and was very successful at reproducing the morphology of experimentally produced splats. The later work of Schmidt [10] and Yokohama et al [84] proved that heat conduction affects the splat morphologies but did not provide a detailed analysis. The effects on the splat properties have been examined in detail in the current work. It was found to have only a minor effect on the final shape of the splat but a significant alteration was seen in the patterns of material hardening and softening within the splat. The adiabatic models often result in a complete loss of material strength in the flank regions of a splat due to extreme thermal softening, resulting in a break down of shear stresses in this region. The models inclusive of heat conduction showed less extreme local heating and material temperatures remained well below the melting point. Clearly, heat conduction has to be considered when modelling the cold spray process and becomes even more important when multiple feedstock impacts are considered in models of complete coating formation. The incorrect patterns of thermal softening and residual stresses seen in adiabatic splats alter the deformation and properties of successive feedstock impacts, causing further deviation from the expected coating formation and properties.

The single splat analysis showed that the various process parameters can have significant effects on the final splat morphologies and that this effect can be traced back to the energy of the impact and the resistance of the feedstock and substrate material

to deformation. A shear band instability is initiated in the splat flank region when the impact energy exceeds a material dependant threshold. In the current work, a novel bonding coefficient:

$$\Psi = \frac{E\rho}{y} \tag{7.1}$$

is proposed that aims to determine clearly and concisely when a shear band instability is present and therefore whether a particular feedstock particle can be expected to successfully bond to surrounding material. The bonding coefficient combines material energies, densities and yield strengths to provide an easily calculated threshold for bond formation in cold spray processes. The suitability of the bonding coefficient has been shown numerically by analysis of a range of splat impacts and has also been applied to a more complicated coating formation model in order to highlight patterns of bonding within the final coating. A brief study of an idealised coating formation process shows the capability of the solver to model the complex dynamics involved and its potential to further extend the understanding of coating properties. The coating study showed that successive feedstock impacts increase the likelihood of splat encapsulation, homogenise material properties in the lower layers of the coating and increases peak heating when compared to isolated splat impacts.

The developed solver provides a powerful tool for accurately and efficiently modelling the cold spray process. However, a more detailed analysis of coating formation remains to be performed, extending the analyses to include factors such as impact angle and feedstock/substrate material changes. A strength of the SPH method is its ability to model both solid and fluid mechanics with ease, the developed solver is equipped with both viscous fluid and elastic-plastic material models which provides the potential to model both the carrier gas jet and the feedstock particles to produce a more holistic model of the physical system. Material melting is currently approximated by loss of material yield strength through the Johnson-Cook model. With the addition of more advanced models of melting and solidification, the developed solver could also be extended to a wider range of thermal coating processes such as plasma and HVOF, as well as laser sintering of metal powders for additive manufacturing. A recent study by Rahmati et al [144] has shown that the Johnson-Cook flow stress model utilised in the literature and

the current work may not be suitable for application to the cold spray process; the study shows preliminary results and further work is required to determine to what extent the Johnson-Cook model is in error and which model should be used in its place.

Despite the success of the applied multi-threading in the current work, there remains much that could be improved upon. The solver is restricted to operation in a shared memory environments, therefore, placing limitations on problem sizes and the amount of resources that can be applied to their solution. Future development should equip the solver for distributed memory systems through the application of MPI processes in addition to the existing multi-threading capabilites, the use of accelerators and co-processors such as Graphics Processing Units (GPU) and Intel's Many Integrated Core (MIC) architecture should also be considered.

In the current work, a novel SPH solver has been developed for application to the cold spray processes. The solver models viscous fluids, elastic-plastic solids, heat conduction, shockwaves, work hardening and thermal softening. Stability is ensured by an extension of Monaghan's artificial stress correction and a new zero impedance boundary condition has been developed to facilitate modelling infinite domains. Computational efficiency improvements have been made by considering pairwise interactions and multi-threaded performance. The solver has been applied to isolated splat impacts in addition to coating formations; the analysis of these results has been used to describe the effect of varying several process parameters, all of which can be considered by their effect on the energy at impact. The dependence of splat bounding on impact energies has been encapsulated in a new non-dimensional bonding coefficient.

Appendix A

Boundary Condition Selection Test Results

This appendix contains a detailed description of the different boundary condition test results disscussed in Chapter 4.

A.1 No Boundary Condition

The first test case considers substrate boundaries which are given no special treatment, with SPH particles deployed away from the computational domain boundaries allowing the substrate to expand if required. Due to the rotational symmetry of the three-dimensional problem, a two-dimensional slice through the centre of the substrate will be used to illustrate the characteristics and properties of the impact. The flattening ratio (see Equation (3.23)) and splat centre height, plotted in Figure A.1, is used to determine when the feedstock impact is completed. The splat shows a steadily increasing flattening ratio which reaches a steady value of 0.402 at 22 ns when the variation in flattening ratio drops below 1%; from this time onwards the height of the splat centre also shows negligible variation. In order to properly highlight the effects of the boundary condition on the substrate, it will be considered separately to effects on the feedstock, a cut section 1μm wide has been taken along the impact axis (y-axis) aligned with the splat centre as shown in Figure 4.2.

Figures A.2 to A.5 show the time evolution of energy, Von Mises stress, temperature

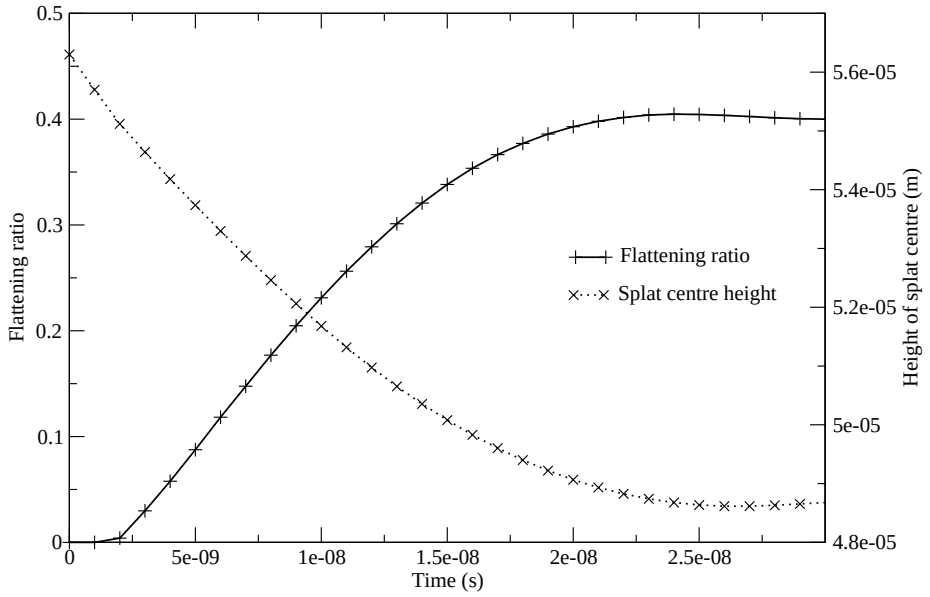

Figure A.1: Flattening ratio and splat centre height for basic boundary condition model

and EPS along this cross-section respectively. An increase in energy is seen in the immediate vicinity of the impact site, which rapidly becomes insignificant. Energy at the interface peaks at 20 ns and can be seen to be conducted away from the interface. The boundary condition has no effect on the total energy due to energy localisation around the impact site. Material temperatures are strongly linked to the material energies and the temperature profile in Figure A.4 shows the expected similarities, peak heating at the interface is seen in the 20 ns plot with subsequent conduction into the substrate and the heating profile shows no effect from the boundary condition. The EPS evolution along the cross section in Figure A.5 also shows strong localisation at the interface with no effect from the boundary condition, however, the Von Mises profiles plotted in Figure A.3 are more complex. An increase in stress is seen at the interface between 10 and 20 ns as the initially spherical feedstock is strained and deformed into the final splat morphology by the impact. There is a reduction in stress after completion of the impact after 22 ns and this is seen in the 30 ns profile in Figure A.3. This reduction is due to the relief of elastic strains once the impact energy is exhausted by deforming the feedstock

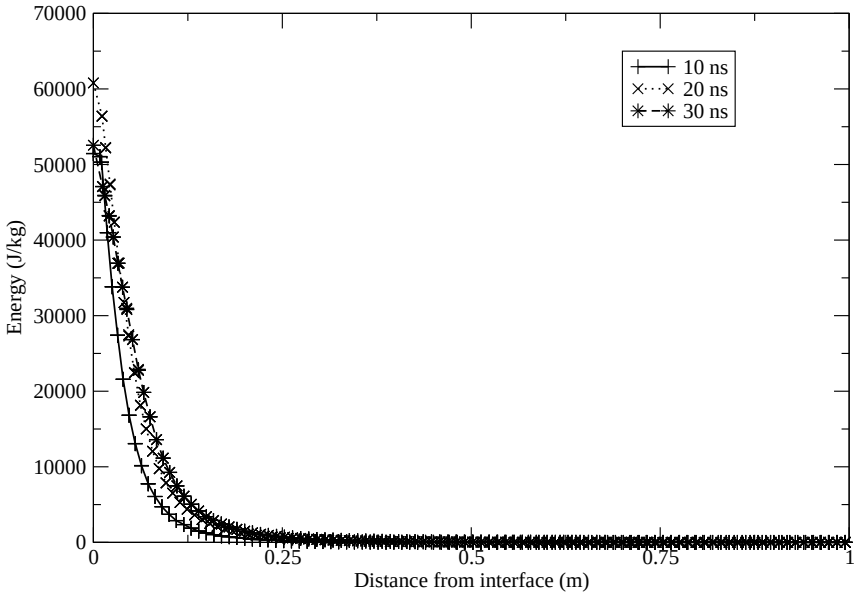

Figure A.2: Basic domain energy profile along the y-axis at 10, 20 and 30 ns.

and substrate. Additionally, the stress wave propagating outwards from the impact site has travelled to the edge of the substrate. With no special treatment, the boundary condition in this case replicates a physical material edge and so stress reflections occur at the boundary, thus, altering the stress distribution in the substrate when compared to an infinite substrate. From 20 ns onwards, this effect can be seen as an oscillatory feature against the substrate boundary in the Von Mises profiles (Figure A.3), where a smooth reduction in stress would be expected from an infinite substrate.

In addition to the y-axis cross-section shown schematically in Figure 4.2 and discussed above, an additional 1μm wide cross section is taken parallel to the x-axis and is aligned with the base of the impact crater as shown in Figure 4.3 to analyse the boundary effects across the width of the substrate. Profiles of Von Mises stress, energy, temperature and EPS along this x-axis cross section are shown correspondingly in Figures A.6 to A.9, respectively, and are plotted against the normalised distance from the impact centre rather than the impact interface. The results show that starting from the centre of the crater edge highlights the peaks of stress, temperature and EPS in the flank regions that

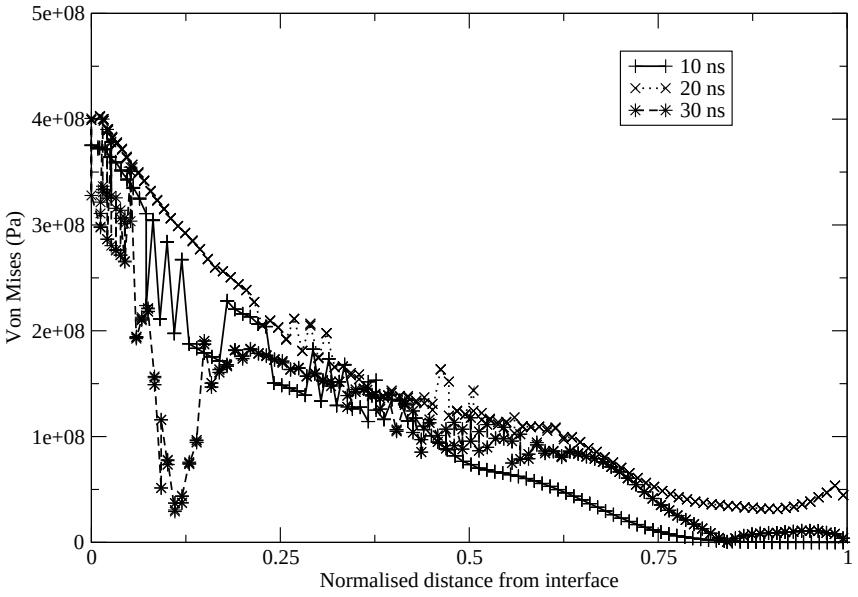

Figure A.3: Basic domain Von Mises profile along the y-axis at 10, 20 and 30 ns.

initiate material jetting. The raw data appears noisy because the cross-section is made such that it cuts a straight line across the hemispherical impact features. In order to improve clarity of the general trends along this cross-section, a 10 point moving average filter has been applied to the data.

The Von Mises profiles in Figure A.6 show an increase in stress between 10 and 20 ns in the early stages of splat formation. This is followed by a reduction in stress at the impact site by 30 ns, caused by the initial impact being over and the splat entering a relief phase. At 10 ns the profile shows a zero stress at the substrate edge, which is located 30μm away from the splat centre. The sound speed of the material used in this test is 3940 m/s and so the stress wave resulting from the impact will have travelled 39.4μm from the initial impact point 10 ns into the impact, while the distance from the initial impact point to the substrate edge is only 30μm. If the boundary treatment has no effect on the stress distribution when compared to an infinite substrate, the stresses present would decrease smoothly from the initial impact site to a distance of 39.4μm, beyond this distance the material remains unstressed. The stress profile (Figure A.6)

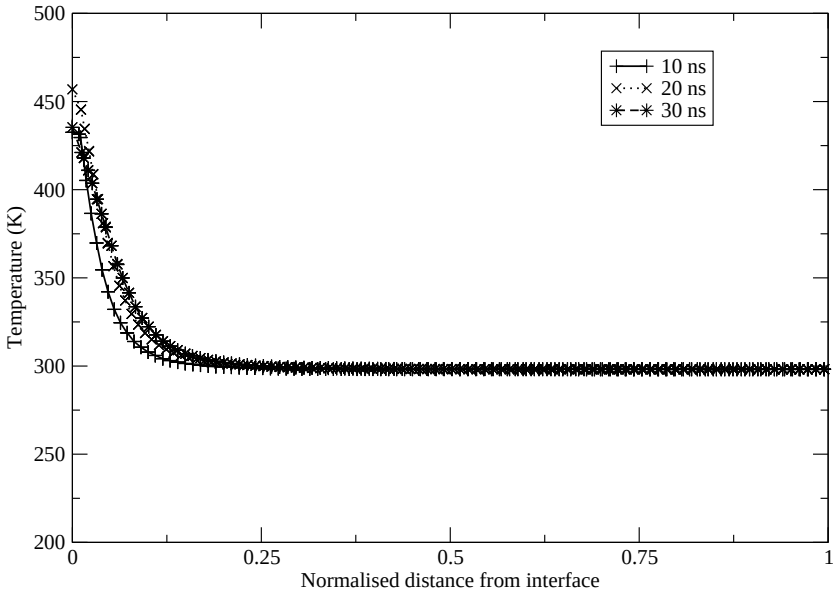

Figure A.4: Basic domain temperature profile along the y-axis at 10, 20 and 30 ns.

instead shows a rapid decrease in stresses around a normalised distance from the splat centre of 0.7 along the x-axis and no stress is seen at the edge of the substrate, which is a clear deviation from the expected values for an infinite substrate.

Figure A.7 plots the energy profile along this x-axis cross-section, showing that there is strong localisation at the interface region and so the profiles remain unaffected by the boundary. At 10 ns the peak energy is located at the flanks of the impact crater and coincides with the peak of EPS at this time, indicating material jetting in this region due to a shear instability. From 20 ns, this sharp peak feature has disappeared, the strongest period of material jetting is over and heat is being conducted away from the flank regions into the rest of the substrate/feedstock. As expected the temperature profiles in Figure A.8 share the features of the energy profiles and show no disturbance caused by the boundary. The EPS profiles (see Figure A.9) are also unaffected by the boundary and exhibit a strong peak at the impact crater flanks. This peak is present in all the EPS profiles and there is a general increase in the amount of EPS between 10 and 30 ns as the feedstock particle is deformed from its initial spherical shape to the final splat

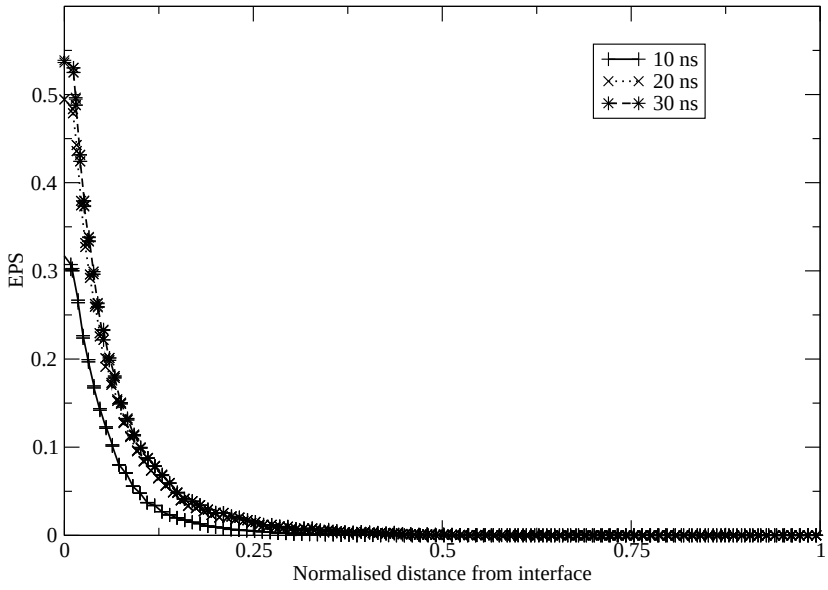

Figure A.5: Truncated basic domain EPS profile along the y-axis at 10, 20 and 30 ns.

morphology.

The examination of the substrate has shown that there is no effect of the boundary on energies, temperatures and levels of EPS, while the Von Mises stress profiles show some effect from the boundary condition. To facilitate the comparison between different boundary conditions, the state of Von Mises stress in the feedstock is shown in Figure A.10. These contour plots are produced by taking a 0.5μm slice through the centre of the feedstock, the data is then flattened to produce a two-dimensional slice of feedstock on the x-y plane which is passed through a two-dimensional Delaunay filter. In order to demonstrate the effects of the Delaunay filter, the SPH particle positions are included in the contour plots.

The contours in Figure A.10 demonstrate the feedstock flattening and forming the distinctive material jets on its flanks. There is a general increase in stress between the 10 and 20 ns contours which is followed by a reduction in overall stress by 30 ns once the initial impact phase has completed and the splat is in a relief phase. Peak stresses are found in the interface region with the lowest values in the splat top centre, corresponding

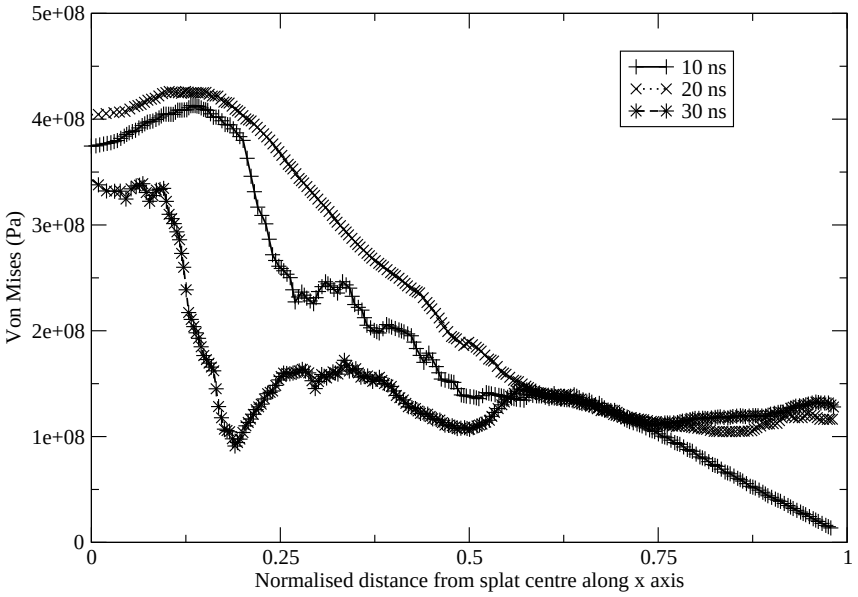

Figure A.6: Basic domain Von Mises profile along the x-axis at 10, 20 and 30 ns.

with the amount of strain these regions have experienced. The interface undergoes the most straining during the impact, whilst the splat top centre experiences relatively little strain.

The feedstock impact model without special treatment of the substrate boundaries has successfully modelled the splat formation with EPS, energy and temperature showing no interaction with the boundary. Von Mises stresses, however, show interactions with the boundary condition resulting in reflections and therefore causing the state of stress to deviate from that expected in an infinite substrate.

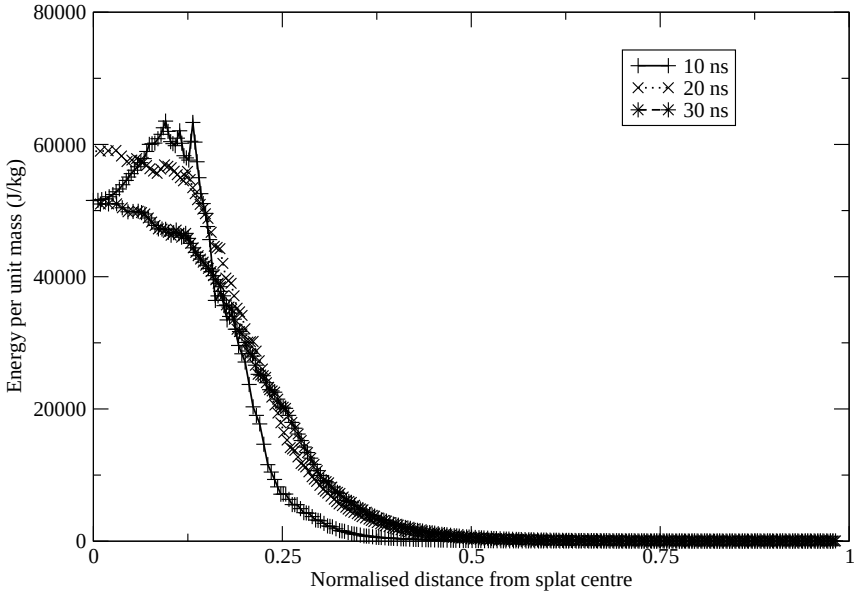

Figure A.7: Basic domain energy profile along the x-axis at 10, 20 and 30 ns.

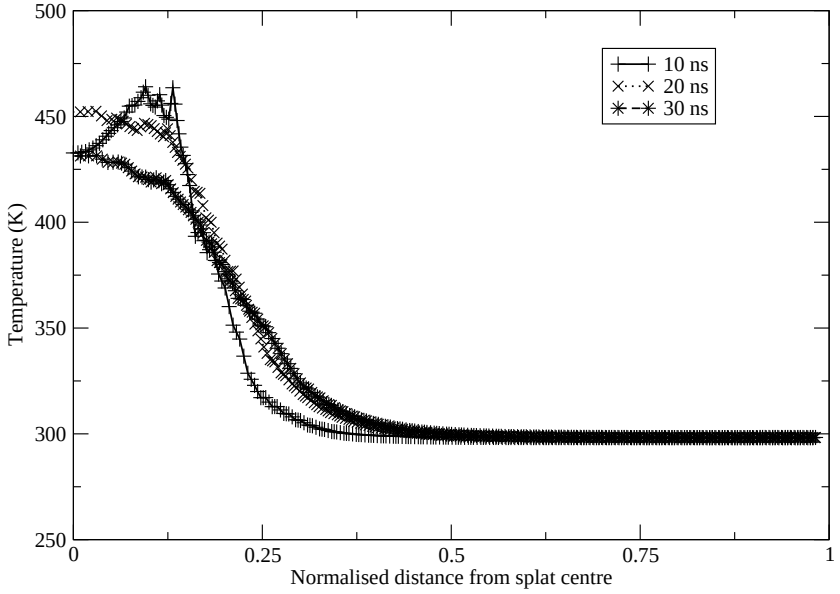

Figure A.8: Basic domain temperature profile along the x-axis at 10, 20 and 30 ns.

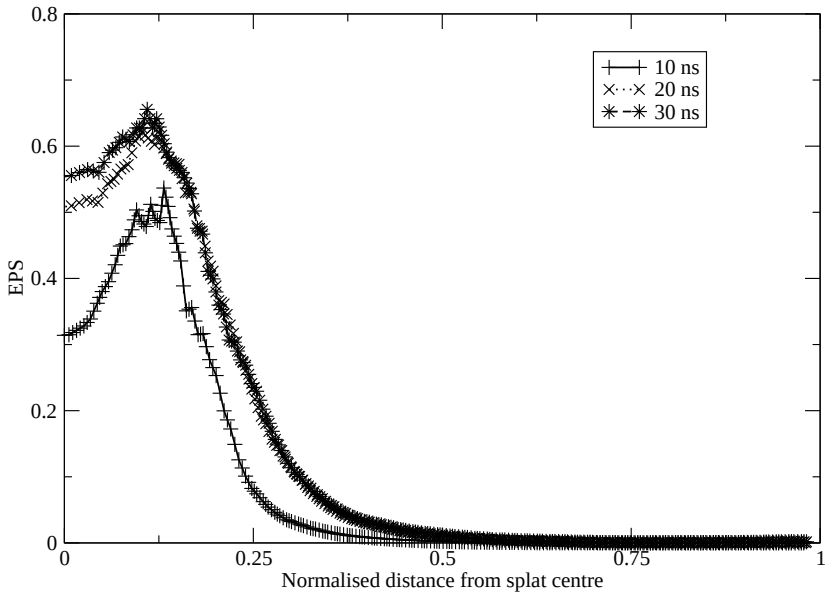

Figure A.9: Basic domain x-axis EPS profile at 10, 20 and 30 ns.

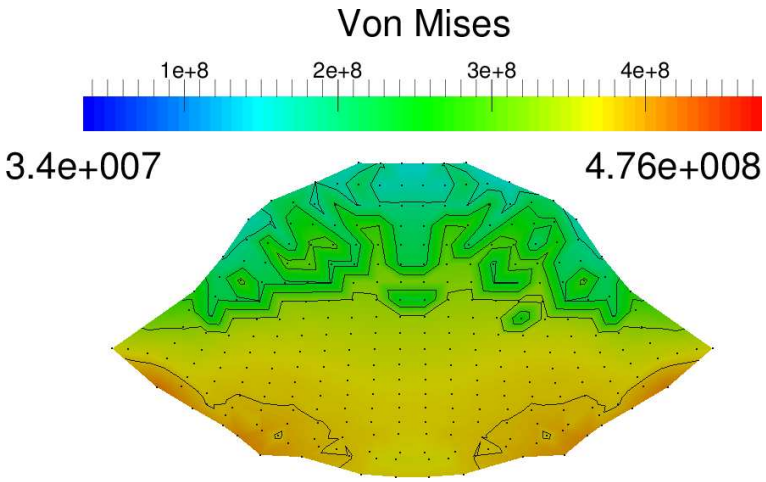

(a) Von Mises at 10 ns.

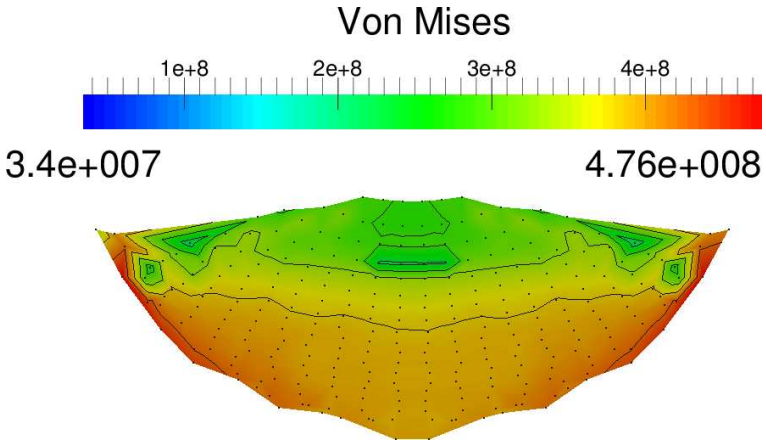

(b) Von Mises at 20 ns.

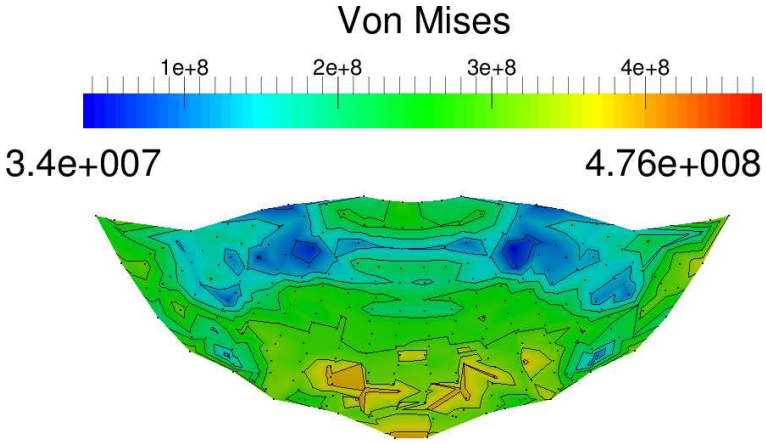

(c) Von Mises at 30 ns.

Figure A.10: Basic domain contours of Von Mises stress in feedstock.

A.2 Periodic Boundary Condition

For this test the substrate boundaries in both the x- and z-axis are given a periodic condition whilst the bottom of the substrate in the impact axis (y-axis) is given no special treatment. As with the basic domain substrate properties will be examined along the two cross-sections shown in Figures 4.2 and 4.3.

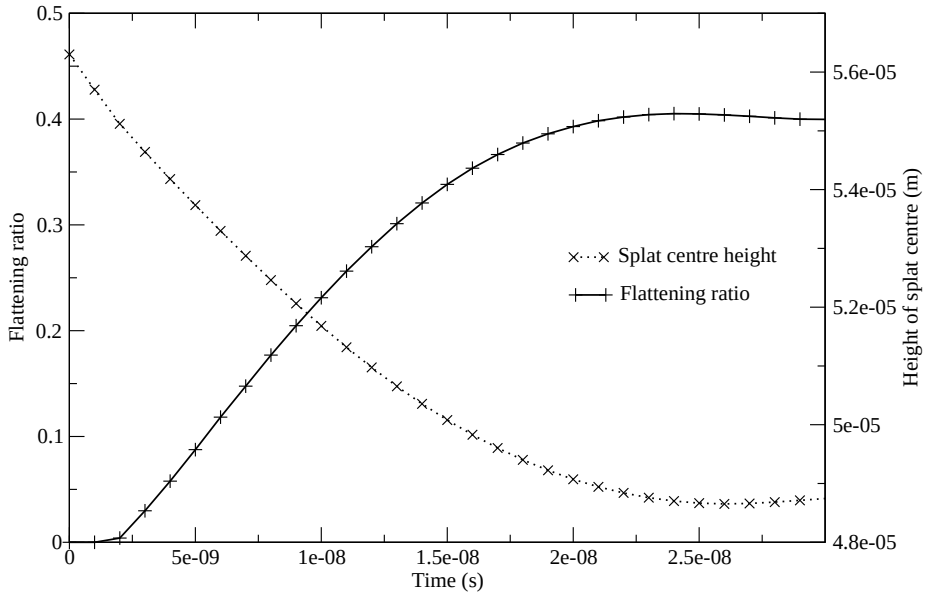

Figure A.11: Flattening ratio and splat centre height for periodic boundary model.

The evolution of flattening ratio and splat centre height is plotted in Figure A.11. The flattening ratio gradually increases until 22 ns when the variation in this ratio drops below 1%. The splat has also reached a steady penetration depth into the substrate at this time, indicating that the majority of the impact energy has been expended.

The profiles of energy, Von Mises stress, temperature and EPS along the y-axis cross-sections are shown respectively in Figures A.12 to A.15. As expected the levels of energy, temperature and EPS are restricted to the impact site and show no interaction with the boundary conditions. Figure A.15 shows a general increase in plastic strain across the time period considered, however, the majority of plastic straining appears to occur between 10 and 20 ns. The energy and temperature profiles show an increase in this

property for the first 20 ns before a reduction in peak levels as it is conducted away from the interface. The Von Mises profile on the other hand shows interaction with the boundary producing some stress reflections.

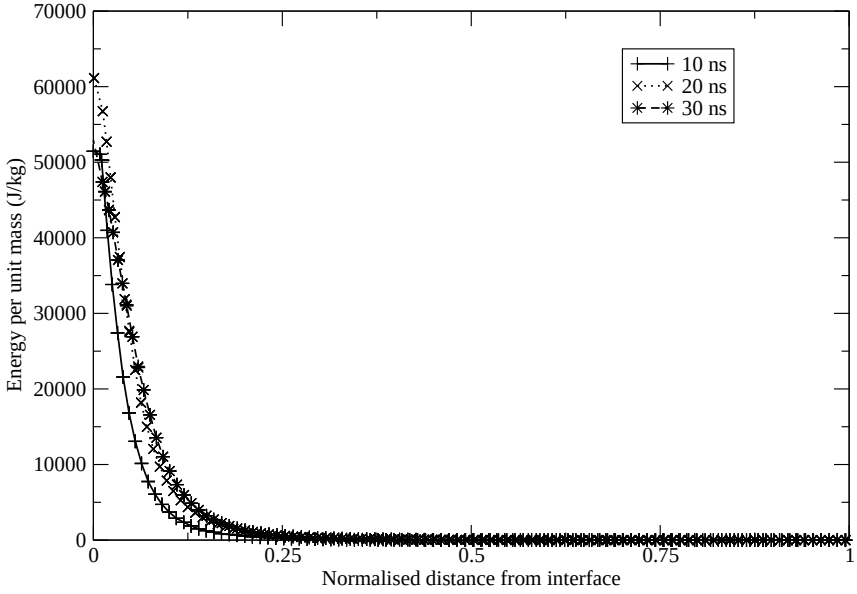

Figure A.12: Periodic domain energy profile along the y-axis at 10, 20 and 30 ns.

Profiles of Von Mises stress, energy, temperature and EPS along the x-axis cross-section are shown correspondingly in Figures A.16 to A.19. The energy, temperature and EPS values show the jetting and expected localisation characteristics with no interaction with the boundary conditions. The Von Mises stress profile shows interaction with the boundary condition for all three time instances considered. The periodic condition that operates at the upper and lower boundaries transmit the stress wave to the opposite boundary approximating a series of neighbouring impacts rather than the desired isolated splat formation event. There is a relaxation of stress between the 20 and 30 ns profiles and this corresponds to the stabilisation of flattening ratio and depth of crater, further supporting the hypothesis that these values indicate the completion of splat formation.

Contours of Von Mises stress in the feedstock, shown in Figure A.20, show that there is a general increase in stress levels between the 10 and 20 ns contours followed by a

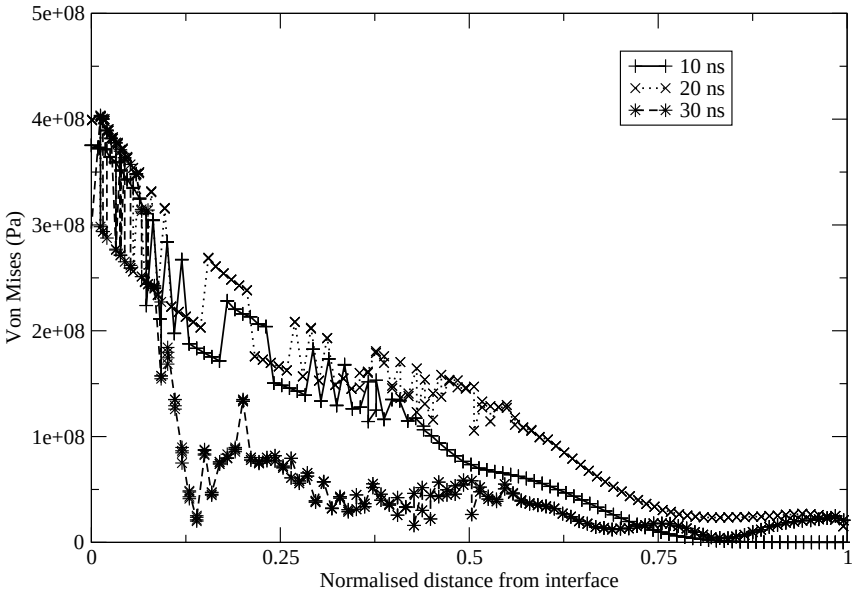

Figure A.13: Periodic domain Von Mises profile along the y-axis at 10, 20 and 30 ns.

reduction at 30 ns. Peak stresses are seen in the interface region on the splat flanks whilst the bottom centre and splat body show much lower levels of stress. These high stress regions match the expected location of shear instabilities and indicate the possibility of material jetting.

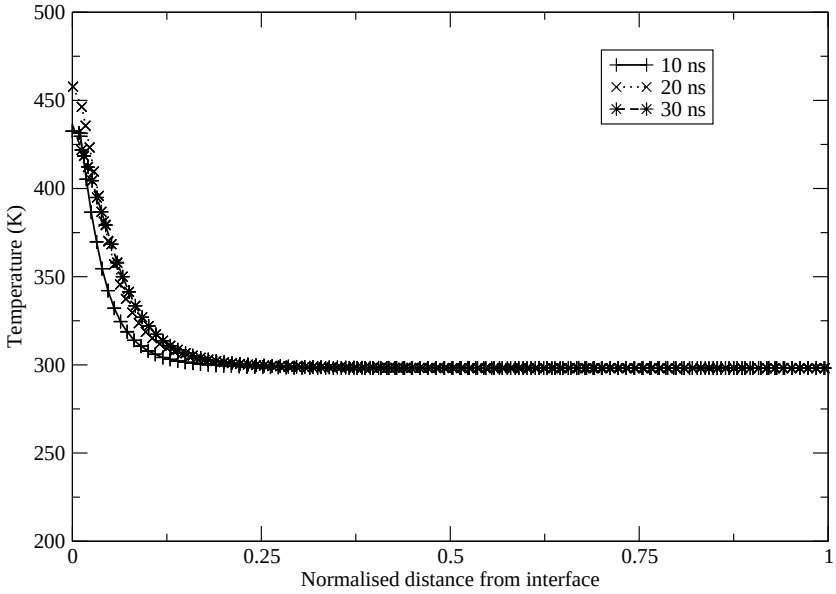

Figure A.14: Periodic domain temperature profile along the y-axis at 10, 20 and 30 ns.

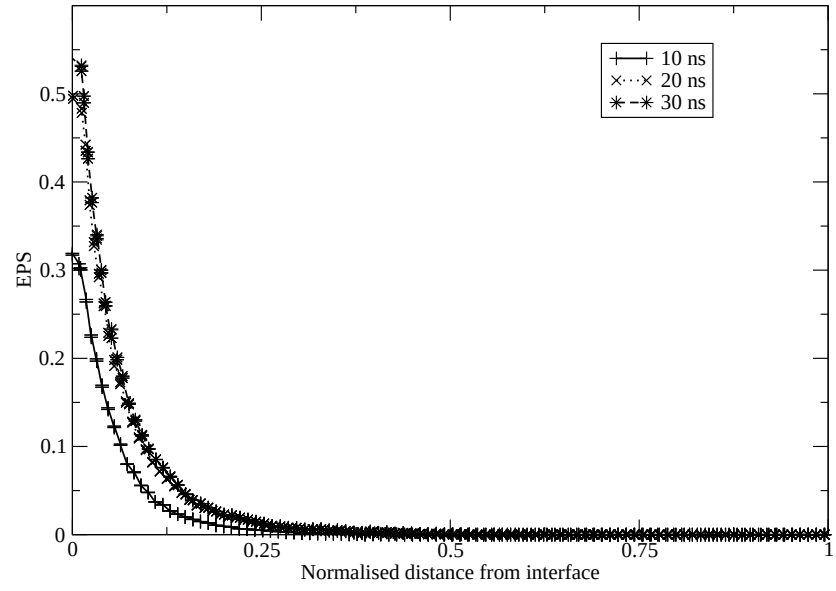

Figure A.15: Periodic domain EPS profile along the y-axis at 10, 20 and 30 ns.

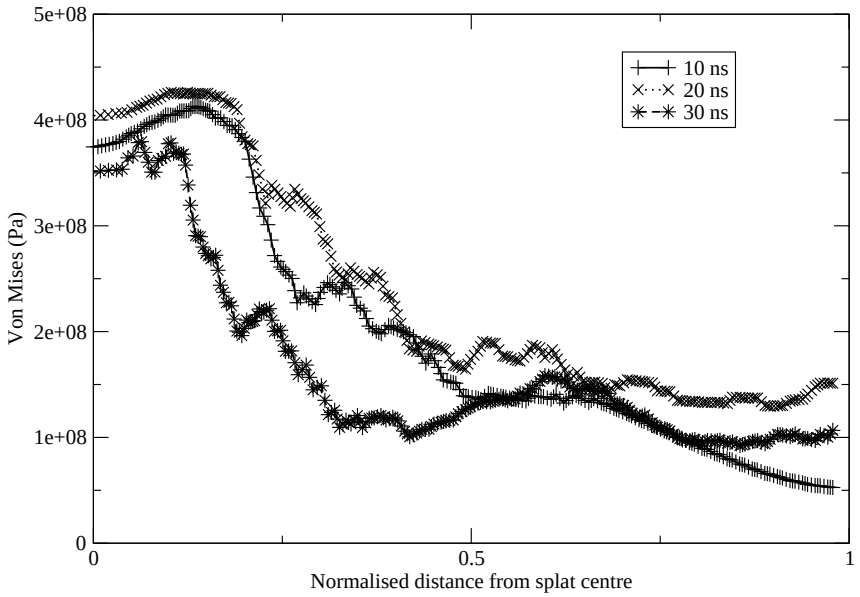

Figure A.16: Peridoic domain Von Mises profile along the x-axis at 10, 20 and 30 ns.

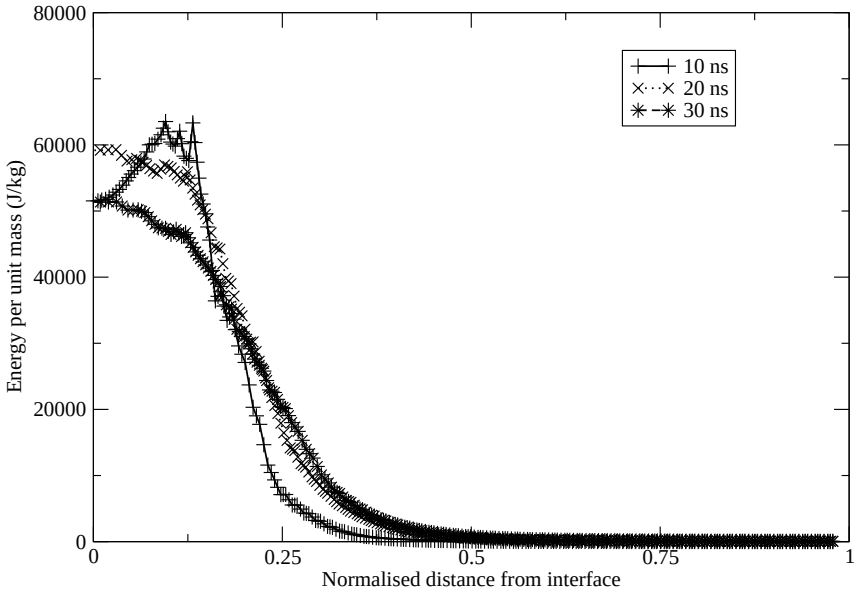

Figure A.17: Periodic domain energy profile along the x-axis at 10, 20 and 30 ns.

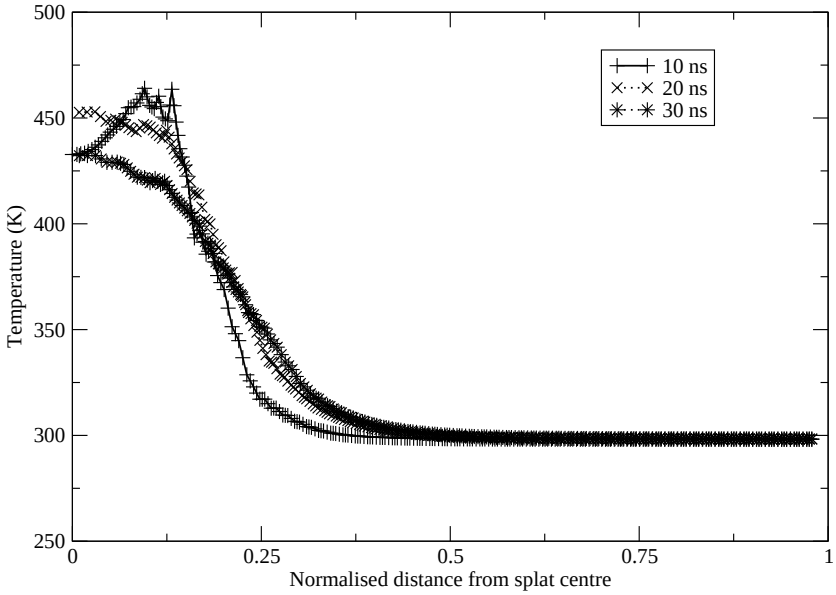

Figure A.18: Peridoic domain temperature profile along the x-axis at 10, 20 and 30 ns.

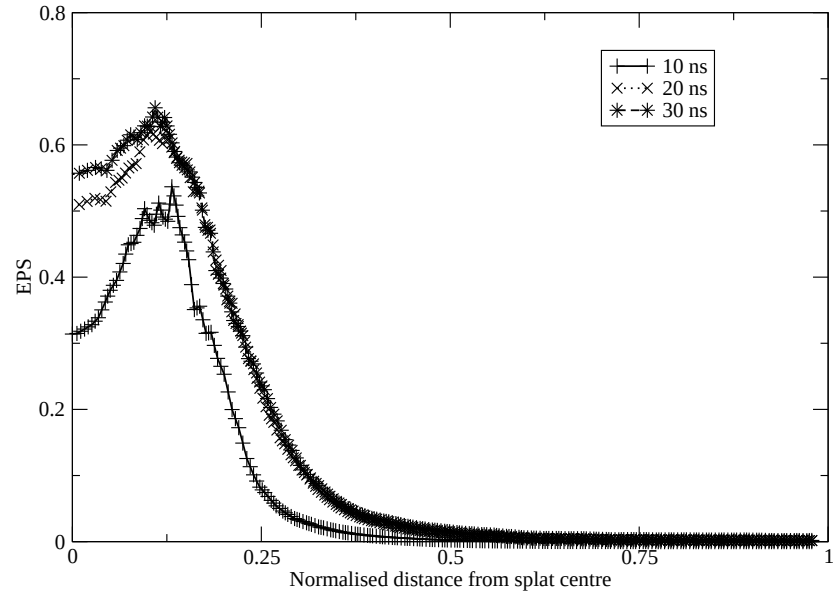

Figure A.19: Peridoic domain x-axis EPS profile at 10, 20 and 30 ns.

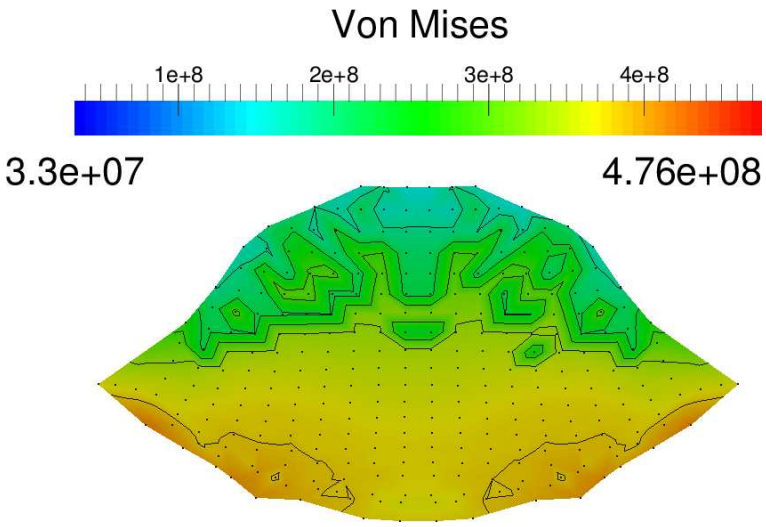

(a) Von Mises at 10 ns.

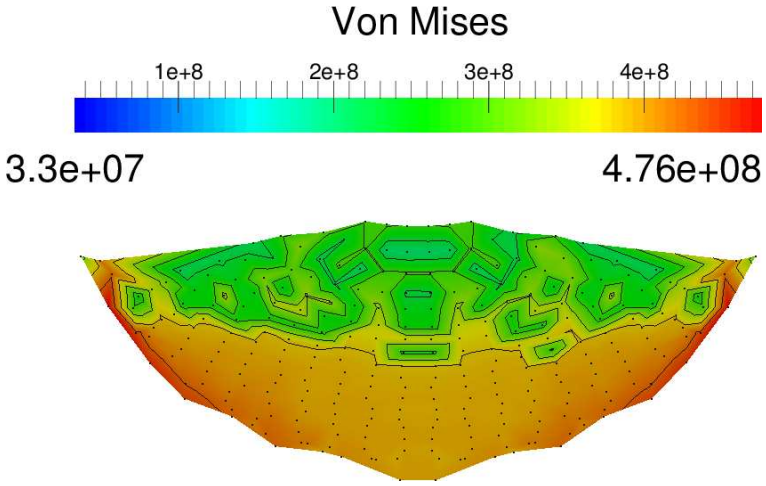

(b) Von Mises at 20 ns.

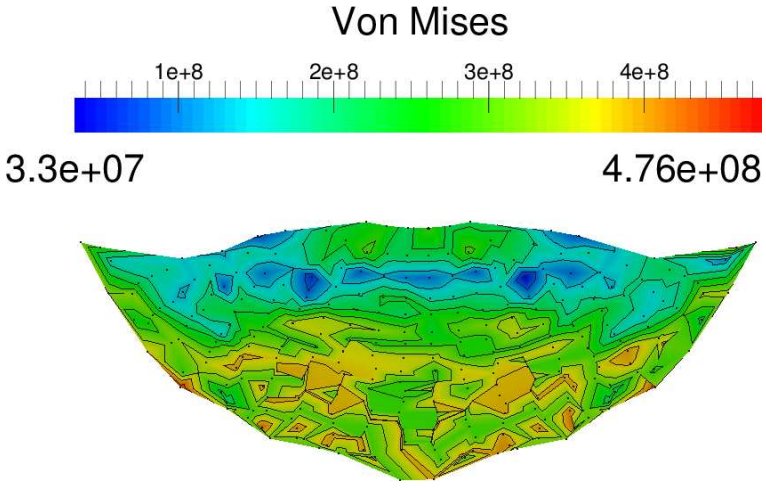

(c) Von Mises at 30 ns.

Figure A.20: Periodic domain contours of Von Mises stress in feedstock.

A.3 Zero Impedance Boundary Condition

For this model the substrate boundaries are treated with a zero impedance condition, and unlike the previous periodic condition model, the zero impedance condition can be applied to the lower boundary along the y-axis providing additional shockwave damping.

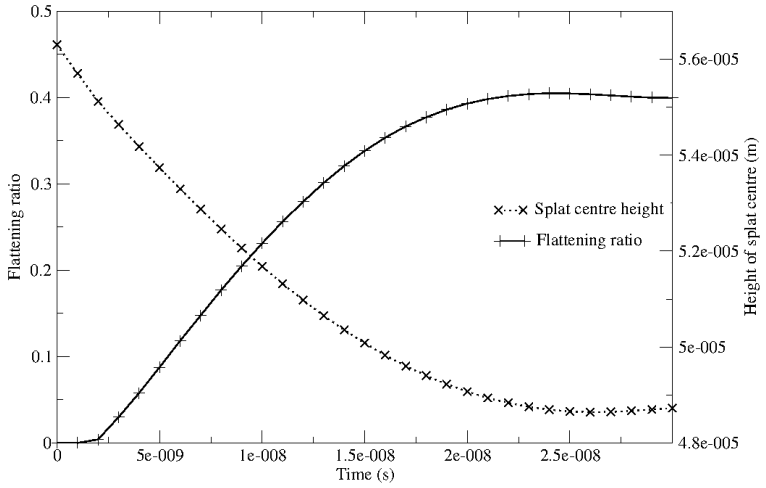

Figure A.21: Flattening ratio and splat centre height for zero impedance boundary model.

The flattening ratio and splat centre height is shown in Figure A.21. The variation in flattening ratio is below 1% from 22 ns onwards and so the splat morphology shows negligible further changes in profile.

The y-axis profiles of energy, Von Mises stress, temperature and EPS are shown correspondingly in Figures A.22 to A.25. As expected, the profiles of temperature, EPS and energy show no interaction with the boundary condition and this holds true for the x-axis contours shown in Figures A.27 to A.29. In both the x- and y-axis cross-sections the Von Mises stress profile shows interaction with the boundary conditions. In the y-axis profile the stress shows none of the large scale oscillatory behaviours of the periodic and no special treatment boundary conditions, there is instead a generally smooth decrease in the overall stress towards the boundary. Although the boundary condition has caused some small oscillations in the stress profile in the immediate vicinity of the boundary, this is of low amplitude and so does not affect the overall characteristics of the stress profile significantly. The stress profiles in this case show a much greater agreement with the expected stress pattern in an infinite substrate with stress waves propagating out of the substrate material, resulting in negligible reflections and no reintroduction of stress

waves at the opposite boundary as was seen in the periodic boundary condition models.

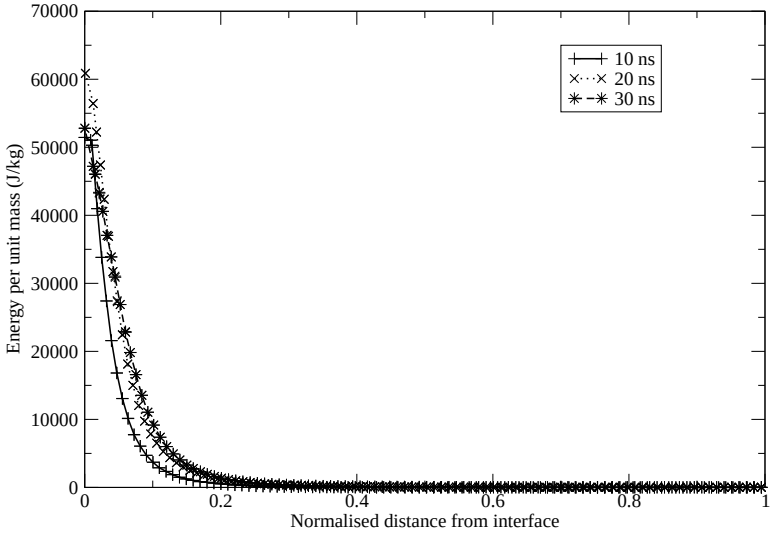

Figure A.22: Zero impedance domain energy profile along the y-axis at 10, 20 and 30 ns.

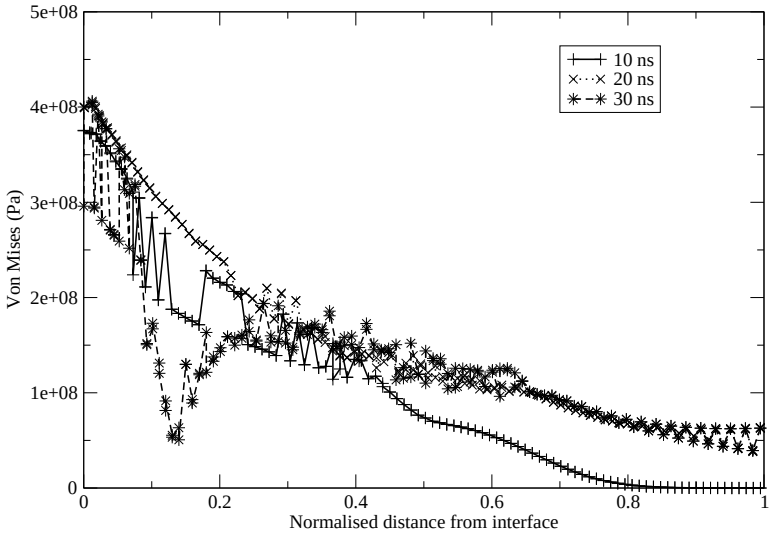

Figure A.23: Zero impedance domain Von Mises profile along the y-axis at 10, 20 and 30 ns.

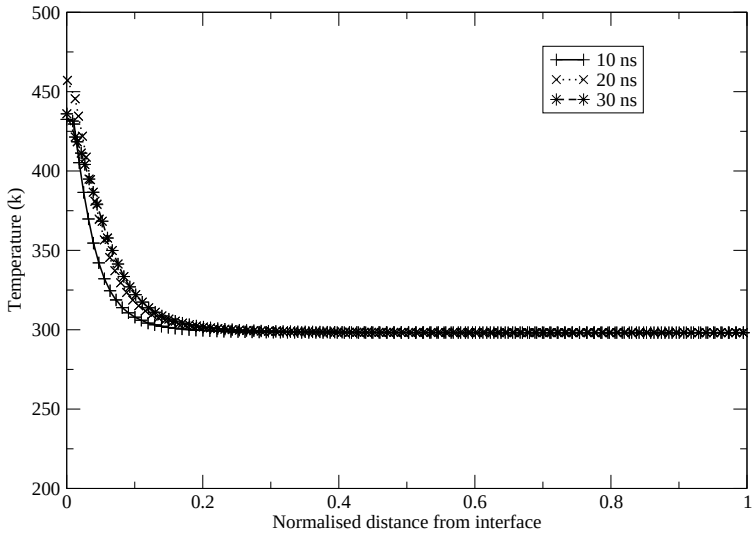

Figure A.24: Zero impedance domain temperature profile along the y-axis at 10, 20 and 30 ns.

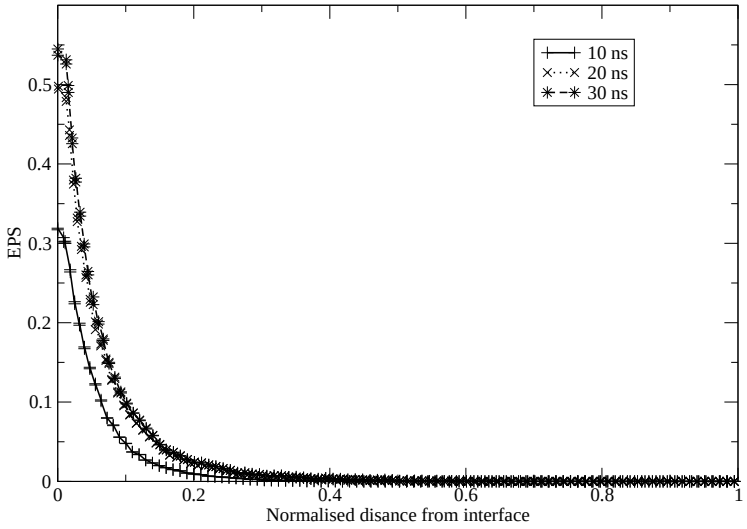

Figure A.25: Zero impedance domain EPS profile along the y-axis at 10, 20 and 30 ns.

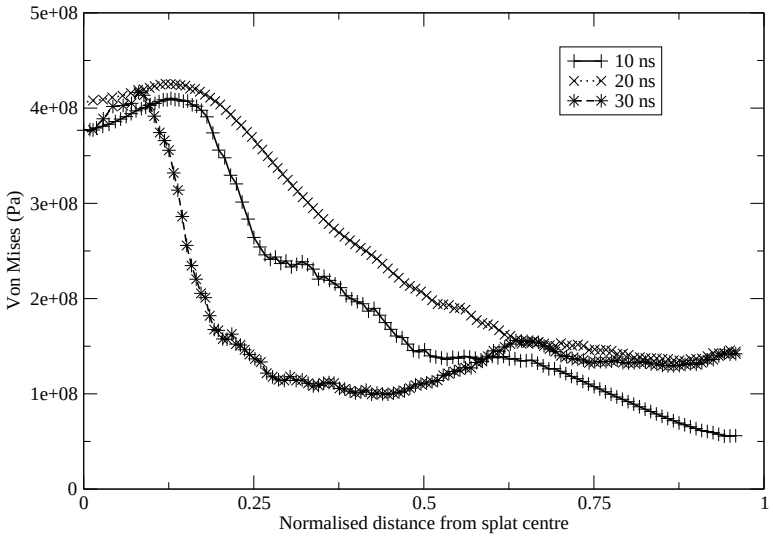

Figure A.26: Zero impedance domain Von Mises profile along the x-axis at 10, 20 and 30 ns.

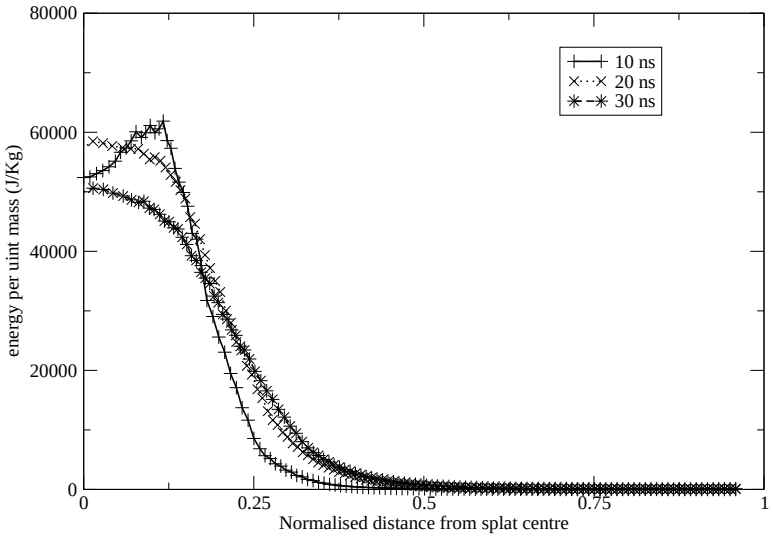

Figure A.27: Zero impedance domain energy profile along the x-axis at 10, 20 and 30 ns.

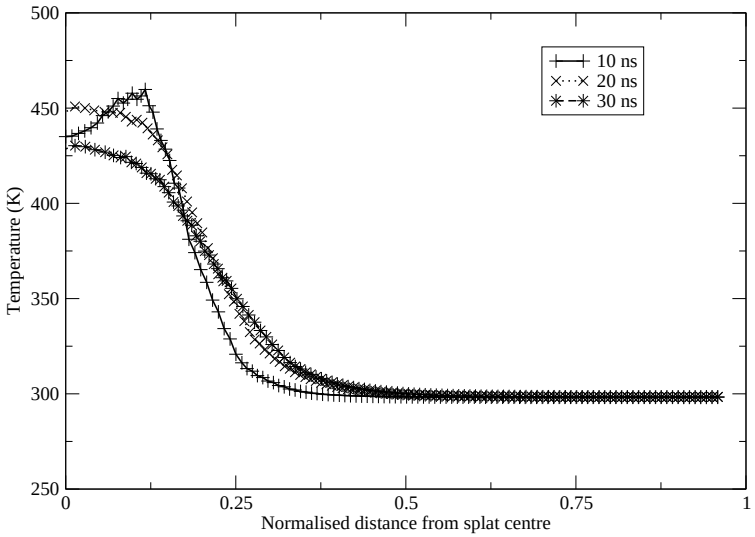

Figure A.28: Zero impedance domain temperature profile along the x-axis at 10, 20 and 30 ns.

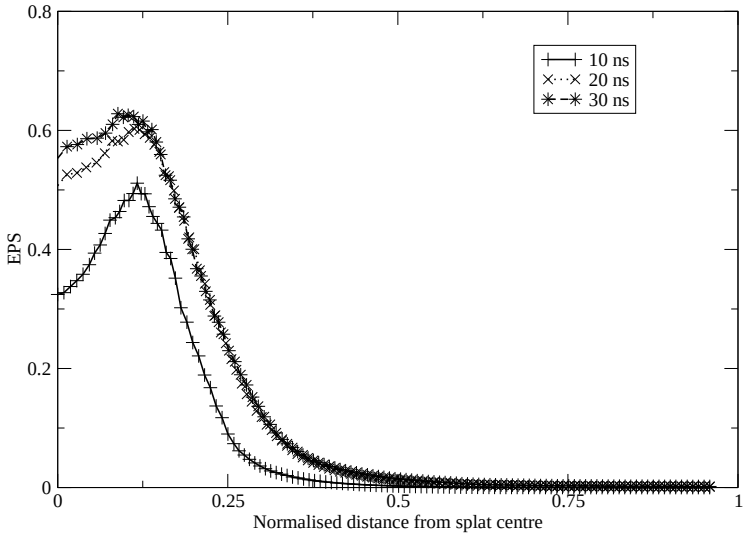

Figure A.29: Zero impedance domain x-axis EPS profile at 10, 20 and 30 ns.

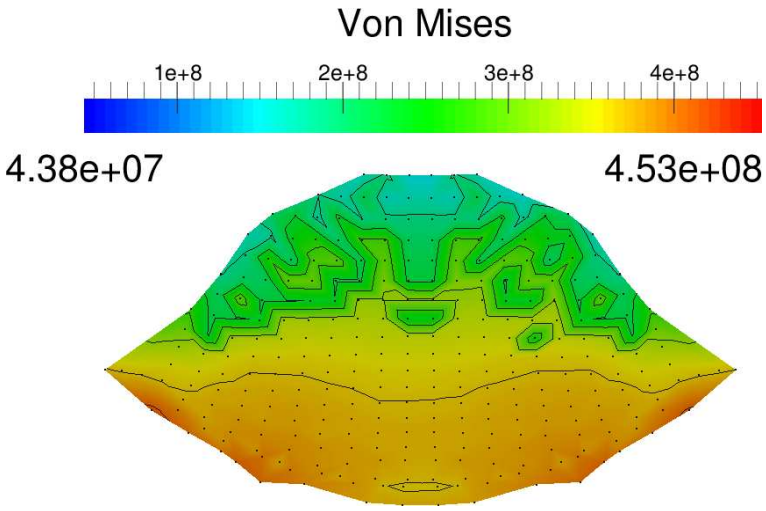

(a) Von Mises at 10 ns.

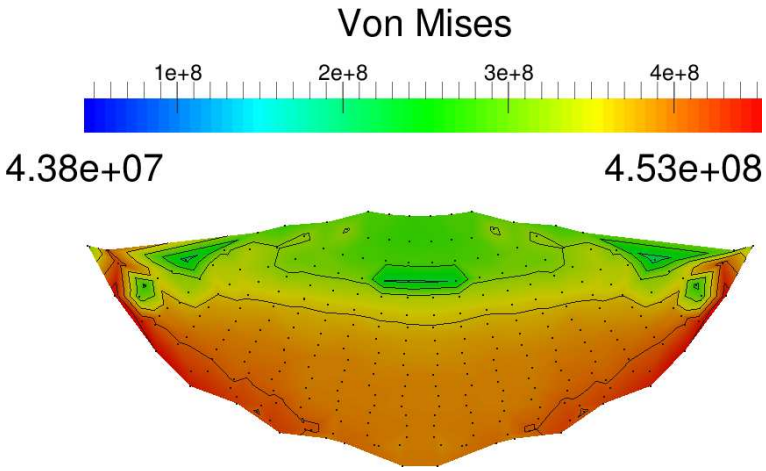

(b) Von Mises at 20 ns.

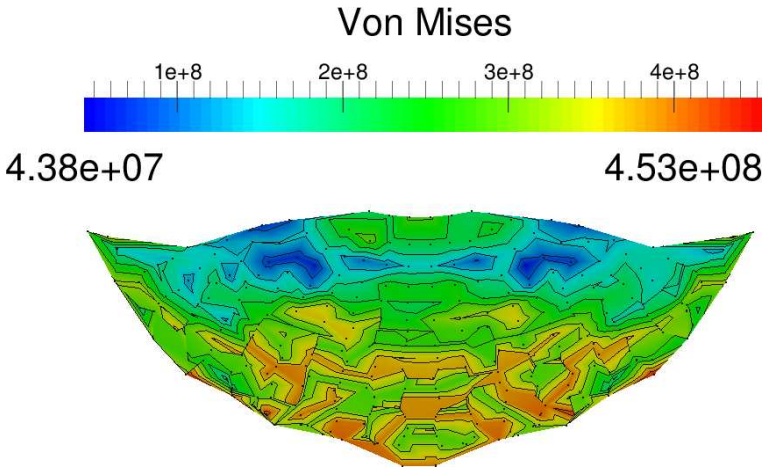

(c) Von Mises at 30 ns.

Figure A.30: Zero impedance domain contours of Von Mises stress in feedstock.

Appendix B

Single Splat Impact Test Results

B.1 Adiabatic Models

B.1.1 Model A

The impact of a 10μm diameter three-dimensional adiabatic copper feedstock particle travelling at 400 m/s with an initial temperature of 298 K is considered in this section. The flattening ratio and height of the splat centre is monitored and is used to establish when the impact event is completed; these properties are plotted against time in Figure B.1. The flattening ratio shows a steady increase culminating in a steadily decreasing oscillation around a peak value. The height of the splat centre is used to monitor the depth of penetration of the feedstock into the substrate, and the profile in Figure B.1 shows a steady decrease towards a decreasing oscillation around a minimum value. At 24 ns the variation in height permanently falls below 0.1%, while the flattening ratio shows less than 1% variation. From this time onwards the splat morphology is expected to undergo no further significant variation and so the feedstock impact is considered complete for the purposes of this analysis.

The flattening ratio, splat centre height and P^* at 24 ns is shown in Table B.1. The data shows that the feedstock particle has penetrated the substrate by half of its initial diameter whilst flattening by one third of its intial diameter. The initially spherical feedstock has falttened into an elipse during the impact and this flattening ratio is measured at the thickest part of the splat which is found along the splat central axis. The flattening ratio describes the total deformation of the splat and a high level of flattening is

indicitative of a high quality coating with little porosity [21].

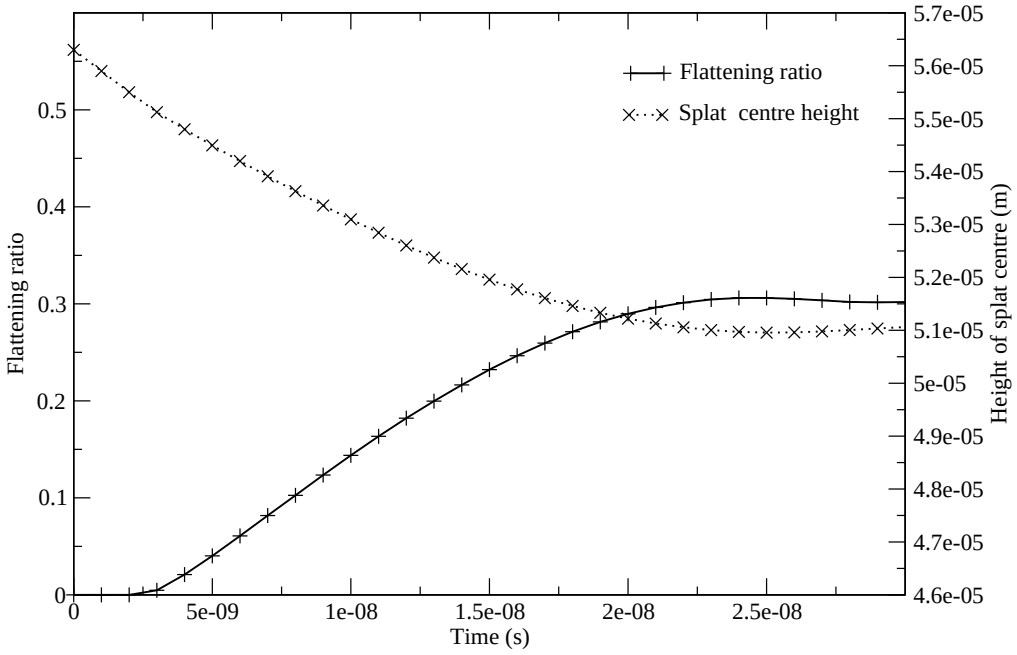

Figure B.1: Flattening ratio plot for an adiabatic feedstock at 298 K and 400 m/s

Flattening ratio	0.306
Splat centre height (μm)	50.97
P^*	0.5297

Table B.1: Model A flattening ratio, P^* and splat centre height data at 24 ns.

Figures B.3 to B.6 show the distribution of heat, yield strength, EPS rate and EPS within the splat at 10, 20 and 24 ns into the impact, respectively. The splat shows some flattening (see Figure B.2) although this is minimal as indicated by the final flattening ratio of 0.306, the splat also lacks a pronounced lip feature. The initial velocity used for this model was 400 m/s and this is under the critical velocity for bonding of 500 m/s that has been determined experimentally for copper [10]. Therefore, the reduced flattening and lack of splat lip is expected. The lack of lip indicates that material jetting was weak

at best and since this feature has been strongly linked to splat/substrate bonds in the past this potentially indicates a failure of the splat to bond to the substrate.

The heat distribution shown in Figure B.3 shows a strong localisation to the interface between feedstock and substrate. The interface does not experience uniform heating with peak temperatures of 714 K reached only at the tip of the small lip feature whilst the splat bottom centre show distinctly less heating overall. The splat bottom centre does show heating when compared to the splat body and to the initial temperature of 298 K. Peak temperatures for this case do not exceed the melt temperature of copper indicating a completely solid phase impact.

The distribution of yield strength as calculated from the Johnson-Cook model (Equation (2.94)) as shown in Figure B.4. Strain and strain rate hardening is dominant across the whole splat with the weakest region of material found towards the top of the splat showing only a 125.5% increase from the initial value of 90 MPa at 24 ns. The most hardening is seen in the splat body close to but slightly removed from the feedstock/substrate interface; this region exhibits two larger lobes close to the splat flanks and narrows towards the splat bottom centre which corresponds to the EPS rate contours shown in Figure B.5. The tips of the lip feature show less hardening and this coincides with the highest temperatures present in the splat resulting in higher material softening.

Figure B.5 shows the distribution of EPS rate, it can be seen that the highest rate of EPS occurs early on in the impact event when velocities are at their highest. The peak EPS rate is seen at the tip of the lip feature with two prominent lobe features extending from the feedstock/substrate interface flanks into the body of the splat; this region of elevated EPS rate does not extend to the splat bottom centre where strain rates close to those found in the splat body are evident.

EPS distributions are shown in Figure B.6. The feedstock/substrate interface shows elevated levels of EPS with a peak value at the tip of the lip feature whilst the splat bottom centre shows the lowest EPS levels found in the interface region corresponding to the distribution of EPS rate shown in Figure B.5. The levels of EPS decrease further from the interface as expected with the splat top centre showing the lowest EPS of 0.0141, demonstrating that the whole splat has undergone plastic deformation to some extent. It is widely accepted that the formation of a material jet is a requirement of successful feedstock/substrate bonding and so the evolution of this feature is of particular interest.

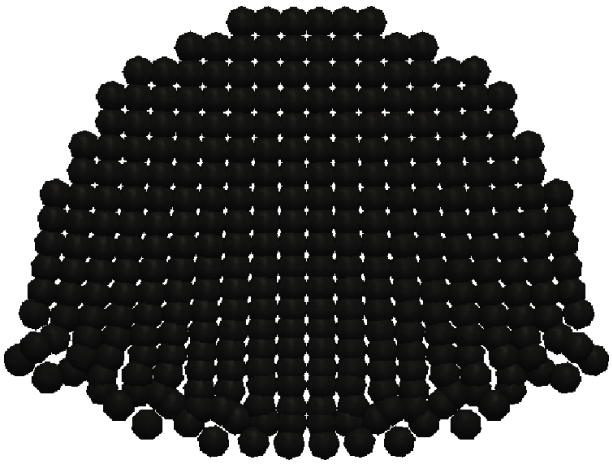

(a) 10 ns.

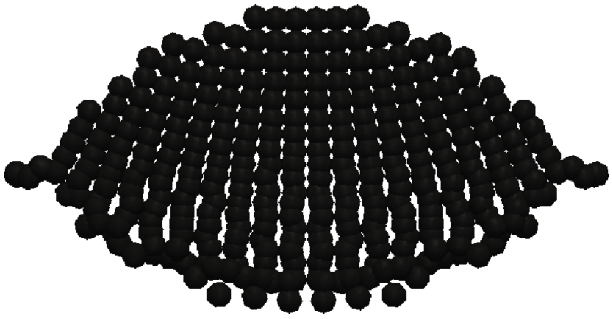

(b) 20 ns.

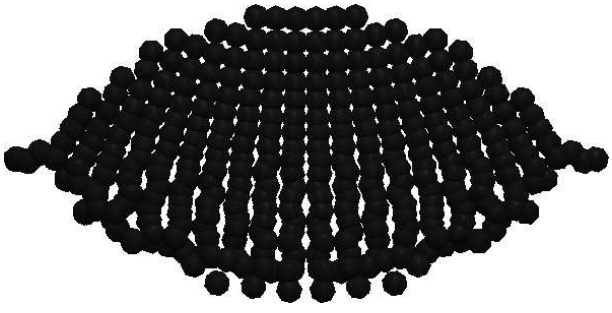

(c) 24 n.s

Figure B.2: Model A, cross section through centre of 3-D splat morphology.

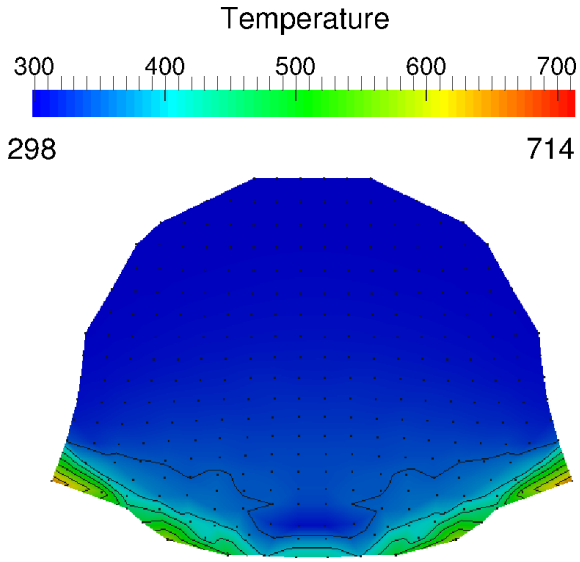

(a) 10 ns.

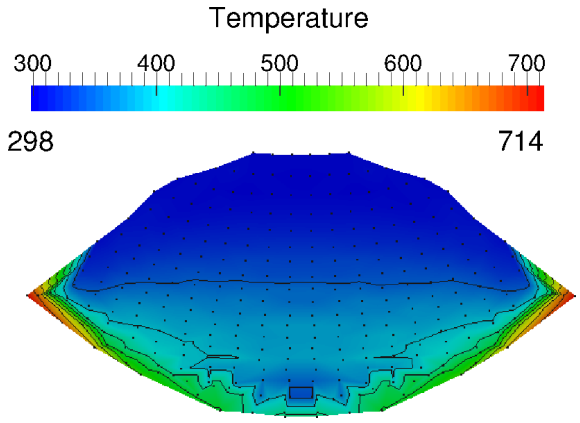

(b) 20 ns.

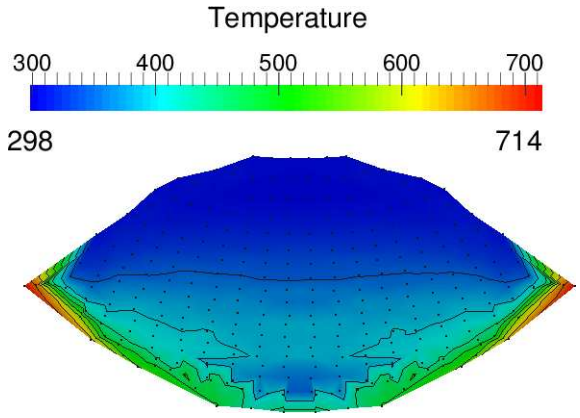

(c) 24 ns.

Figure B.3: Model A, temperature cross section through centre of 3-D splat morphology.

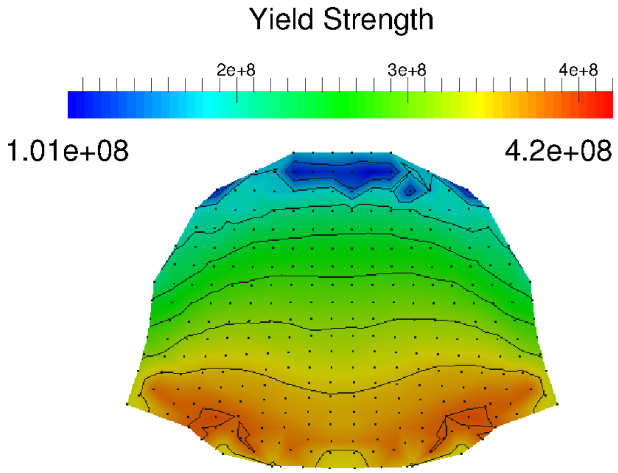

(a) 10 ns.

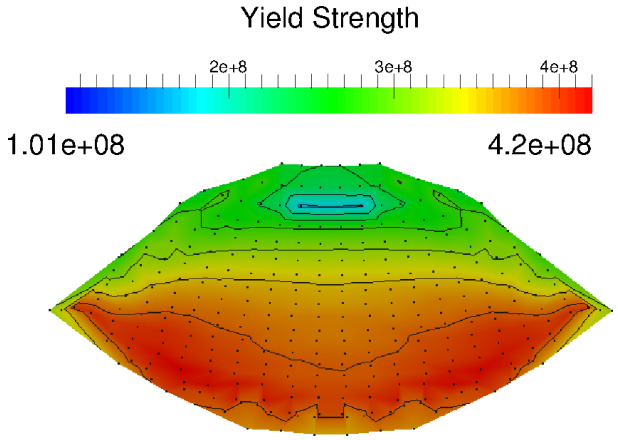

(b) 20 ns.

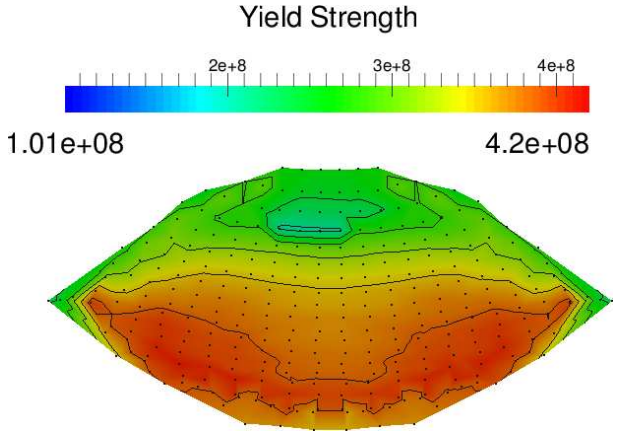

(c) 24 ns.

Figure B.4: Model A, yield strength cross section through centre of 3-D splat morphology.

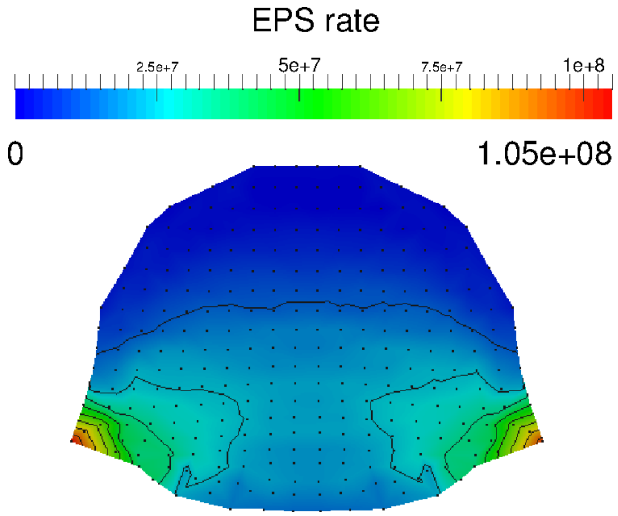

(a) 10 ns

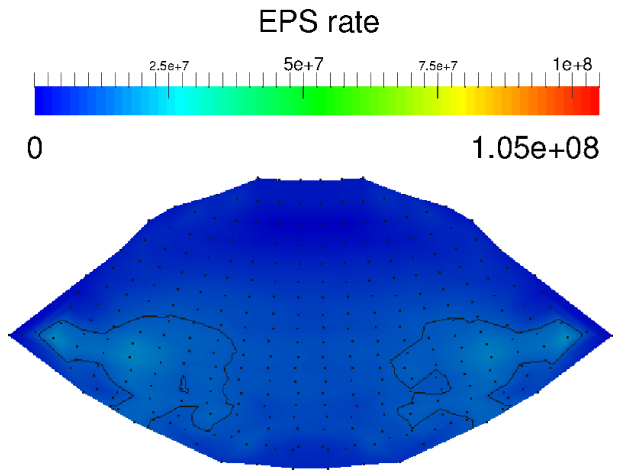

(b) 20 ns

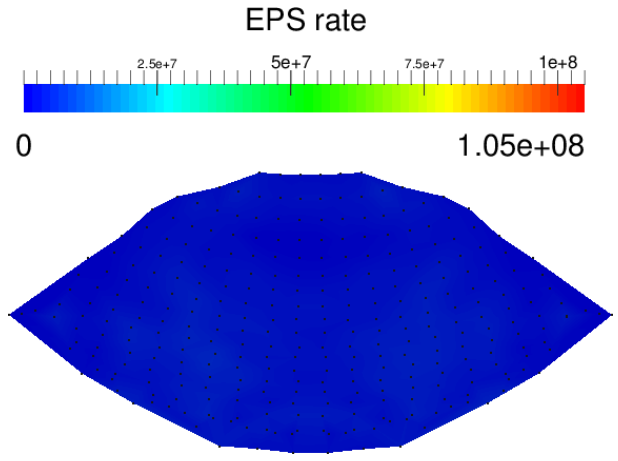

(c) 24 ns

Figure B.5: Model A, EPS rate cross section through centre of 3-D splat morphology.

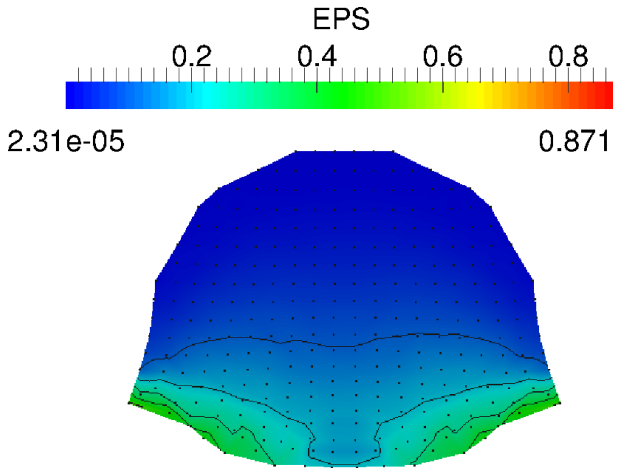

(a) 10 ns

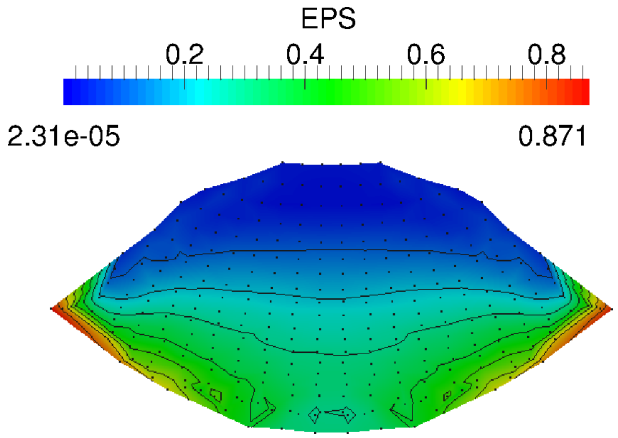

(b) 20 ns

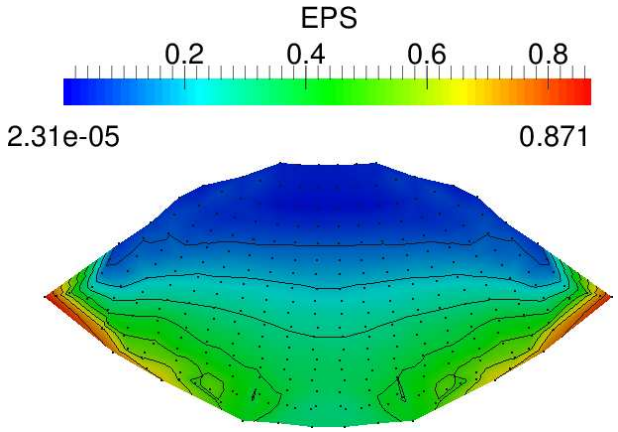

(c) 24 ns

Figure B.6: Model A, EPS cross section through centre of 3-D splat morphology.

Therefore, the SPH particle that has the highest level of EPS at the end of the impact will be monitored and its properties are shown in Figures B.7 and B.8. This particle is typically observed in the splat flank regions where jetting is expected.

The temperature evolution at the lip region (see Figure B.7a) shows a sharp increase between 5 and 10 ns before slowly approaching its peak value of 714 K, no decrease in temperature is evident over the time period considered by this study. The EPS plot (see Figure B.7b) shows a steady increase in EPS from 4 to 20 ns when the peak value is reached.

An increase in yield strength is seen between 3 and 7 ns (see Figure B.8a), there is no significant decrease in yield strength over the duration examined which would make the splat susceptible to shear band instability formation that would result in strong material jetting. The reduction in yield strength seen at 25 ns is caused by the EPS rate reducing to an insignificant level in the Johnson-Cook strength model. The highest rate of EPS is seen at 9 ns in Figure B.8b, but this only corresponds with a very minor drop in yield strength at the same time the occurrence of peak stress at a time where the yield strength of the material is still elevated appears to have prevented the formation of a shear band instability and the state of material jetting that is required for bonding.

With the limited flattening and no obvious sign of a shear band instability, it is concluded that this splat would not bond to the substrate and this corresponds to the experimentally derived critical velocity of 500 m/s.

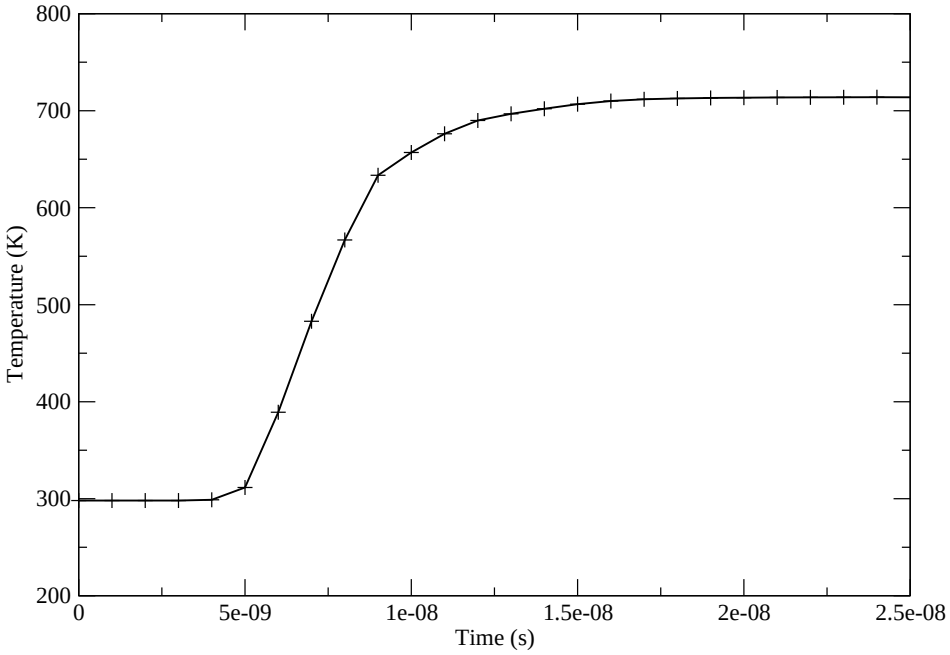

(a) Model A, temperature evolution in high EPS material jet region

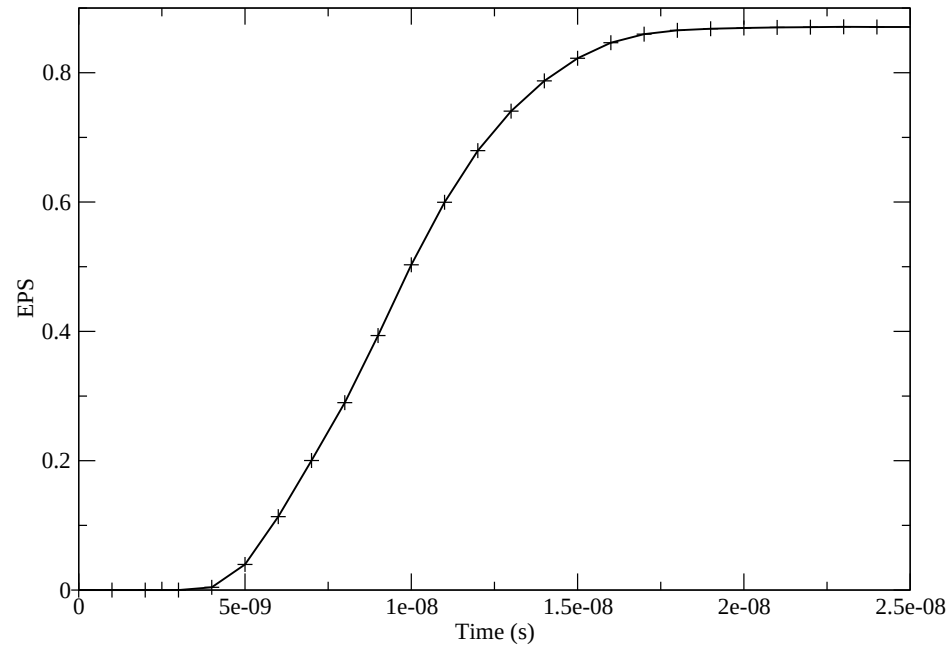

(b) Model A, EPS evolution in high EPS material jet region

Figure B.7: Model A, evolution of temperature and EPS in material jet.

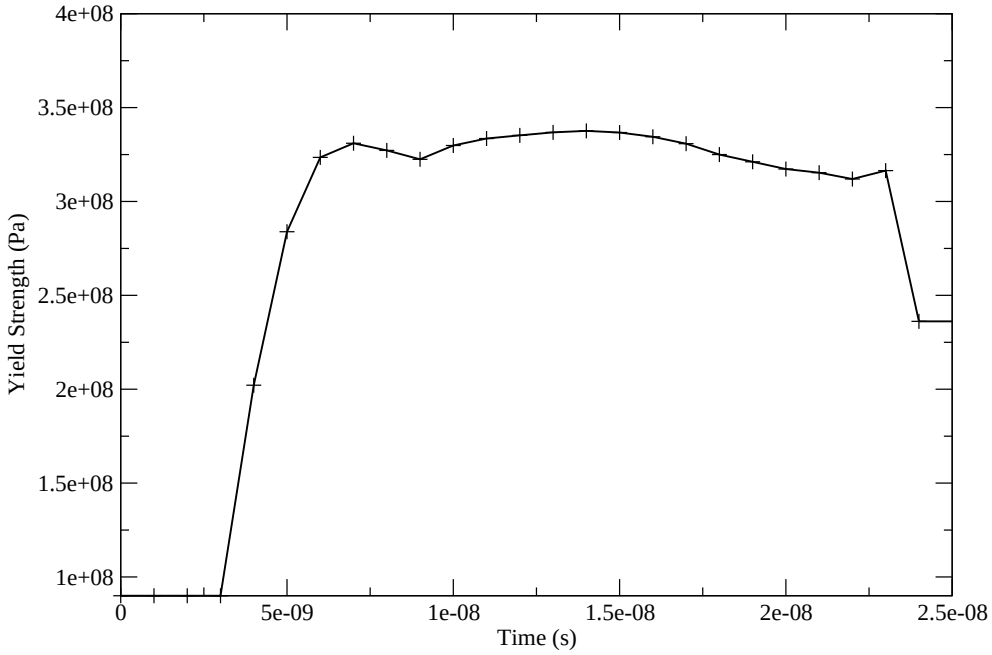

(a) Model A, yield strength evolution in high EPS material jet region.

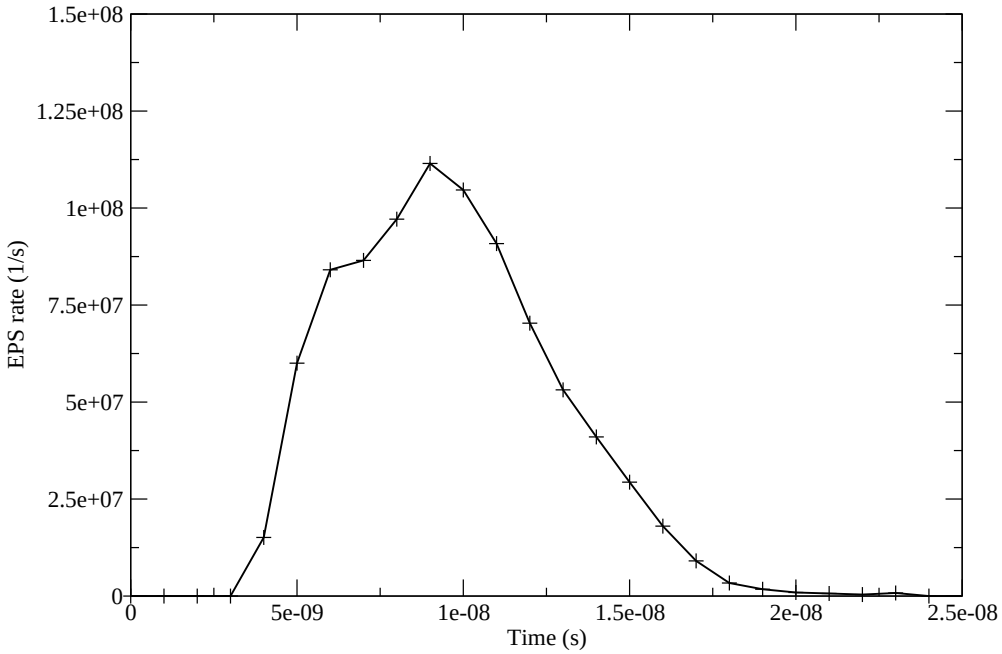

(b) Model A, EPS rate evolution in high EPS material jet region.

Figure B.8: Model A, evolution of yield strength and EPS rate in material jet.

B.1.2 Model C

The flattening ratio and splat centre height evolution for a adiabatic feedstock travelling at 800 m/s with initial temperature 298 K is shown in Figure B.9. There is a steady increase in flattening ratio until the variation drops below 1% at 24 ns and results in a peak value of 0.524. At this time, the variation in splat centre height is less than 1% and decreasing, resulting in a final settling height of 46.2μm and a P^* of 1.0004. This value of P^* indicates an impact crater as deep as the initial particle diameter, which serves to increase the contact area between feedstock and substrate. A crater this deep could result in feedstock encapsulation, thus, enhancing the strength of mechanical bonds. The feedstock shows a high flattening ratio of 0.524, a significant total deformation and indicitive of a high quality coating. The properties at 24 ns are summarised in Table B.2.

Flattening ratio	0.524
Splat centre height (μm)	46.2
P^*	1.004

Table B.2: Model C flattening ratio, P^* and splat centre height data at 24 ns.

A cut section through the three-dimensional splat morphology at 24 ns is shown in Figure B.10 the most distinctive feature is the large lip of material at the edges of the splat. The lip forms early on in the impact and is visible in the 10 ns morphology plot (see Figure B.10a) and is made up of a thin layer of material one SPH particle wide; this lip indicates strong material jetting and therefore the presence of a shear band instability.

The distribution of heat at $10, 20$ and 24 ns is shown in Figure B.11, where the splat shows strongly localised heating limited to the flanks of the feedstock/substrate interface whilst the splat body and bottom centre show little to no heating. Peak temperatures are found just behind the tip of the lip feature at the interface and at 2080 K are well in excess of the material melt temperature although this temperature is limited to a single SPH particle. Which indicates that melted material only makes up a small fraction of the total interface.

The distribution of EPS (see Figure B.12) shows some localisation at the feedstock/substrate interface although to a lesser extent than the temperature contours in

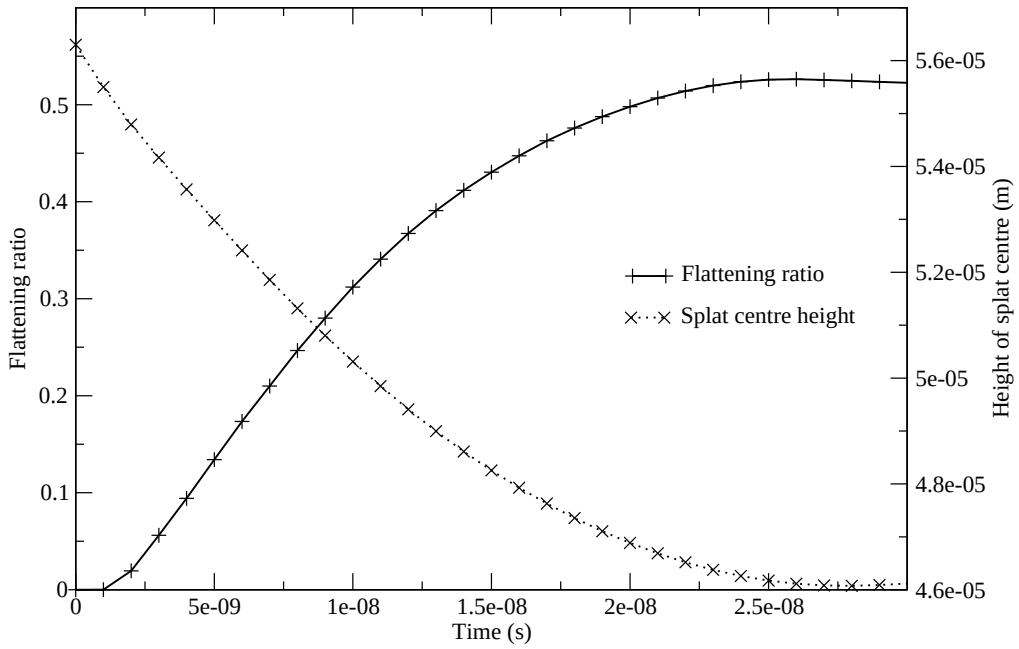

Figure B.9: Flattening ratio plot for a three-dimensional adiabatic feedstock at 298 K and 800 m/s.

Figure B.11. The peak EPS is found at the same point as the peak heating just below the tip of the lip feature with a decrease in levels of EPS along the interface at the bottom centre of the splat. The lowest levels of EPS are found at the splat top centre and although this is minor, this region of the splat has still experienced plastic straining.

The highest rates of EPS (see Figure B.13) occur early on in the impact when the impact velocity is at its highest. At 10 ns the highest rates of EPS are found at the flanks of the feedstock/substrate interface but does not stretch to the splat bottom centre. Beyond 20 ns significant rates of EPS are found in the lower half of the splat and along the interface but these decline rapidly.

Due to the high temperatures reached in the region of material jetting, the yield strength distribution (see Figure B.14) shows a loss of strength at the lip feature. Away from this area material hardening is dominant over thermal softening with the highest levels of hardening found in the splat body and the lowest levels at the top centre of the splat.

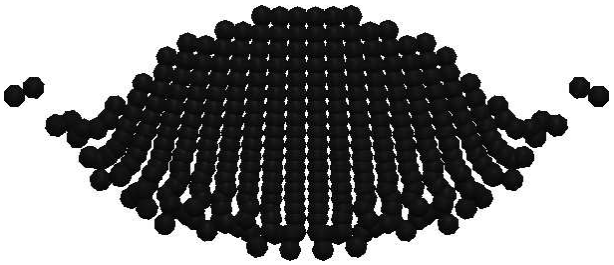

(a) 10 ns.

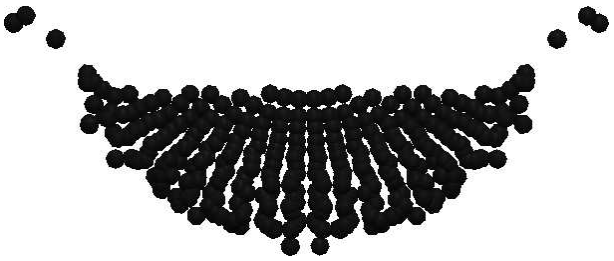

(b) 20 ns.

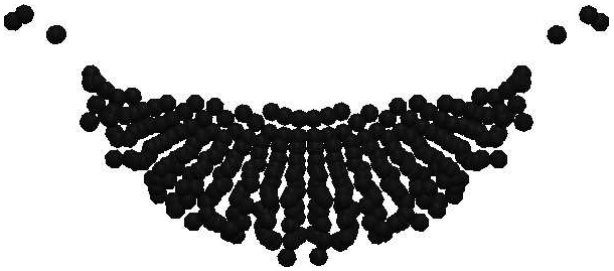

(c) 24 ns.

Figure B.10: Model C, cross section through centre of 3-D splat morphology.

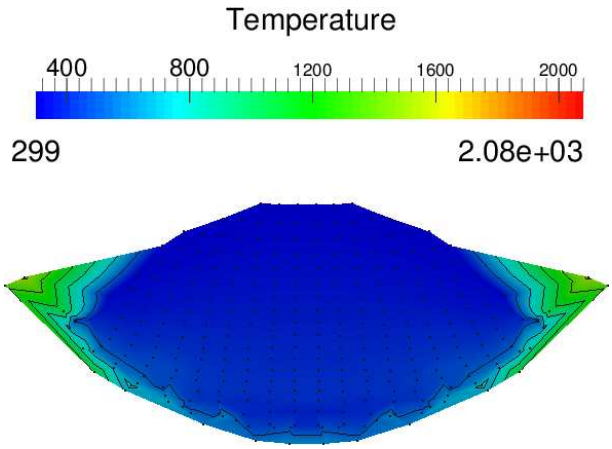

(a) 10 ns.

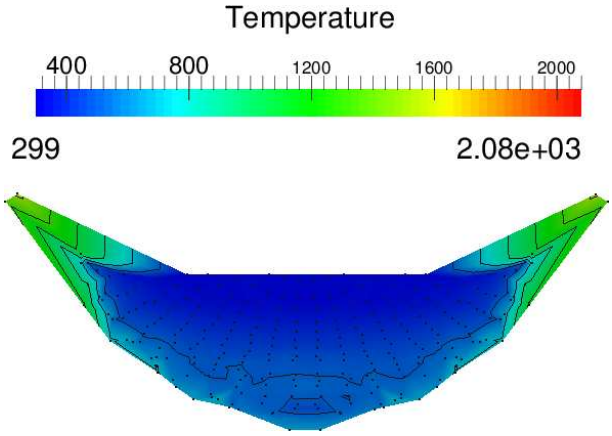

(b) 20 ns.

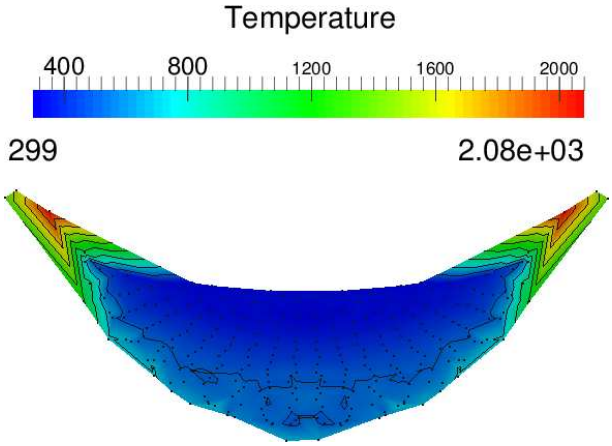

(c) 24 ns.

Figure B.11: Model C, temperature cross section through centre of 3-D splat morphology.

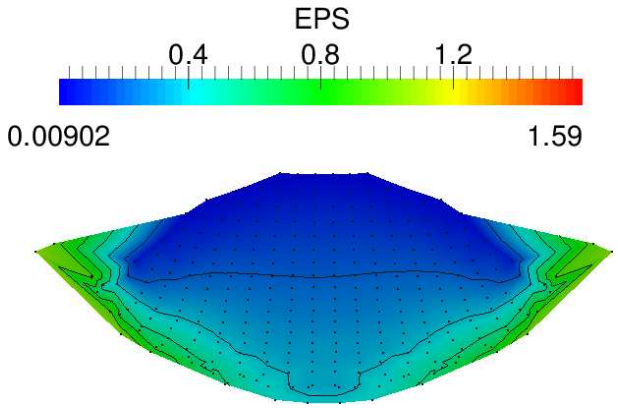

(a) 10 ns.

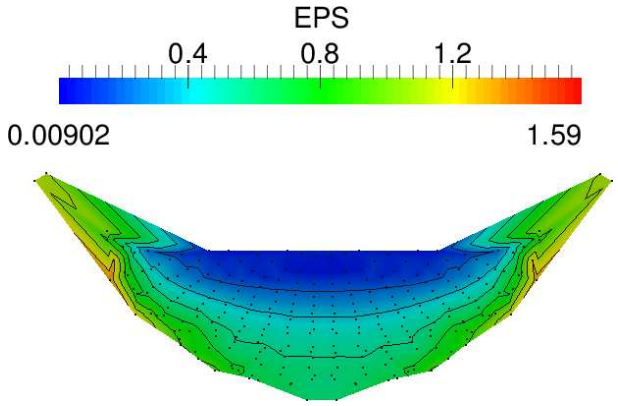

(b) 20 ns.

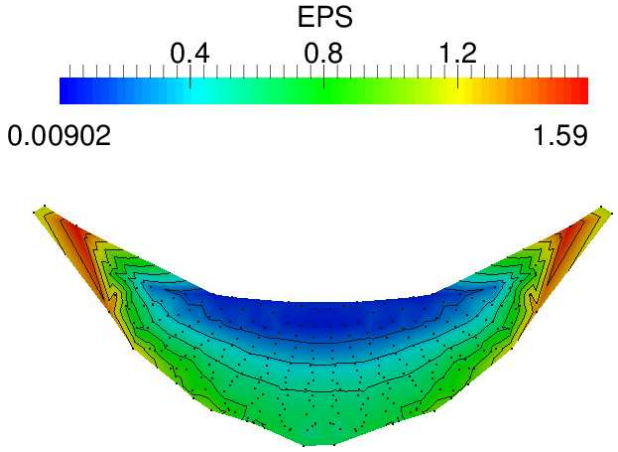

(c) 22 ns.

Figure B.12: Model C, EPS cross section through centre of 3-D splat morphology.

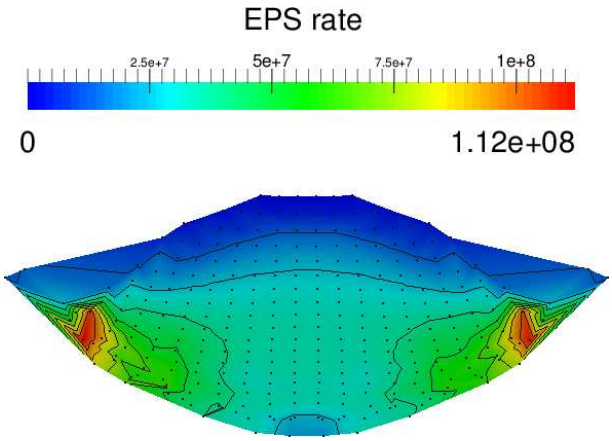

(a) 10 ns.

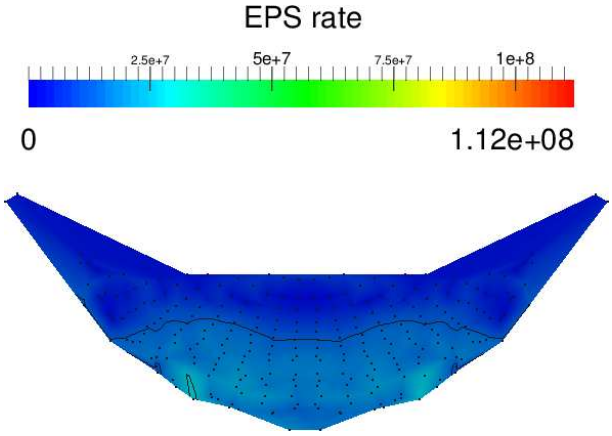

(b) 20 ns.

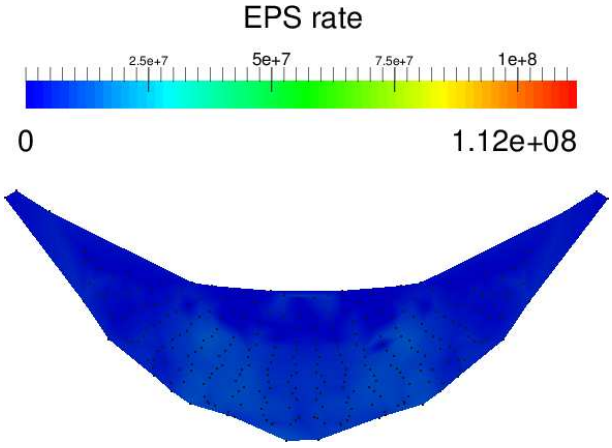

(c) 24 ns.

Figure B.13: Model C, EPS rate cross section through centre of 3-D splat morphology.

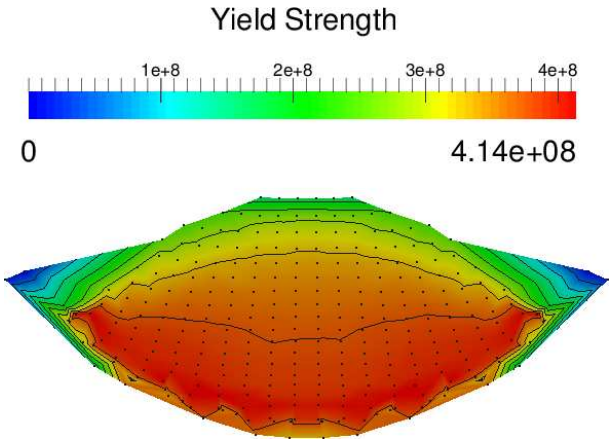

(a) 10 ns.

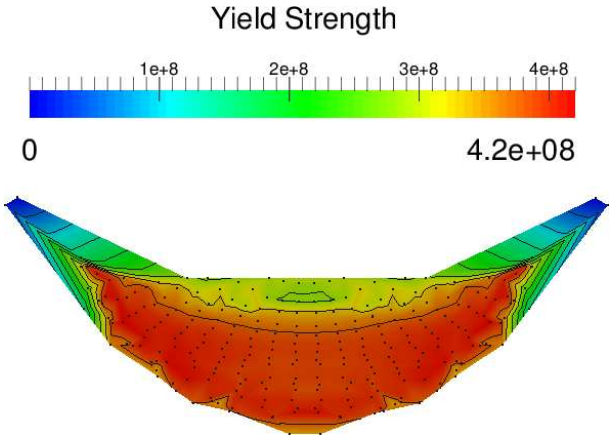

(b) 20 ns.

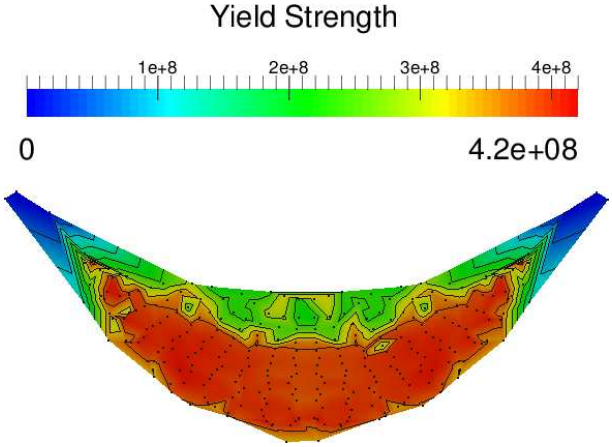

(c) 24 ns.

Figure B.14: Model C, yield strength cross section through centre of 3-D splat morphology.

The evolution of temperature, EPS, EPS rate and yield strength at the SPH particle exhibiting the highest total EPS are given in Figures B.15 and B.16. This SPH particle is located in the splat flank region near to the tip of the lip feature. The temperature plot (see Figure B.15a) shows a rapid increase in temperature until 6 ns into the impact when there is a slight dip in temperature before a continued rise to a peak value of 2080 K. Other than this short duration reduction in temperature, there is no significant cooling during the time period considered. The EPS profile (see Figure B.15b) shows an increase in EPS levels across the time period considered with the highest rate of increase over after 10 ns.

The evolution of material yield strength calculated using the Johnson-Cook model is shown in Figure B.16a. Due to the local heating exceeding the melt temperature, there is a complete loss of yield strength at 3 ns. The reduction in temperature at 6 ns is not significant enough to restore yield strength and with no further cooling of the material the yield strength stays zero throughout the time period considered. The peak in the rate of EPS (see Figure B.16b) coincides with this loss of yield strength and could indicate the presence of a shear band instability. There is a general decrease in rates of EPS from this point on with a notable exception of a plateau between 5 and 7 ns which coincides with the temperature drop at 6 ns.

The initial velocity in this case was well in excess of the experimental critical velocity for copper. A large amount of flattening was observed along with strong material jetting. Additionally, local heating in the material jet was significant enough to cause material melting and this has been accounted for by zero yield strength in these regions.

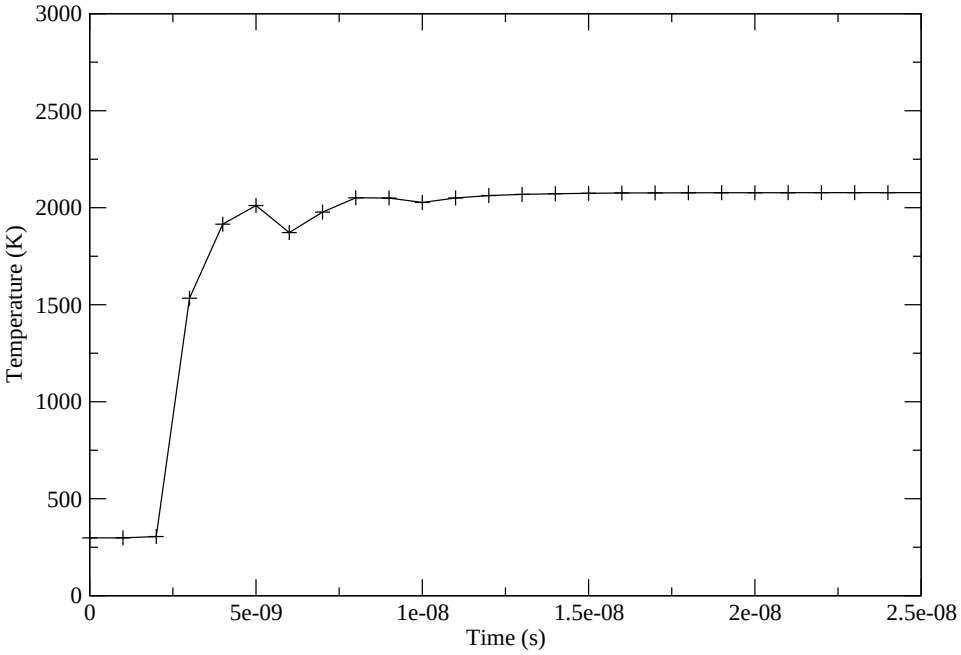

(a) Model C, temperature evolution in high EPS material jet region.

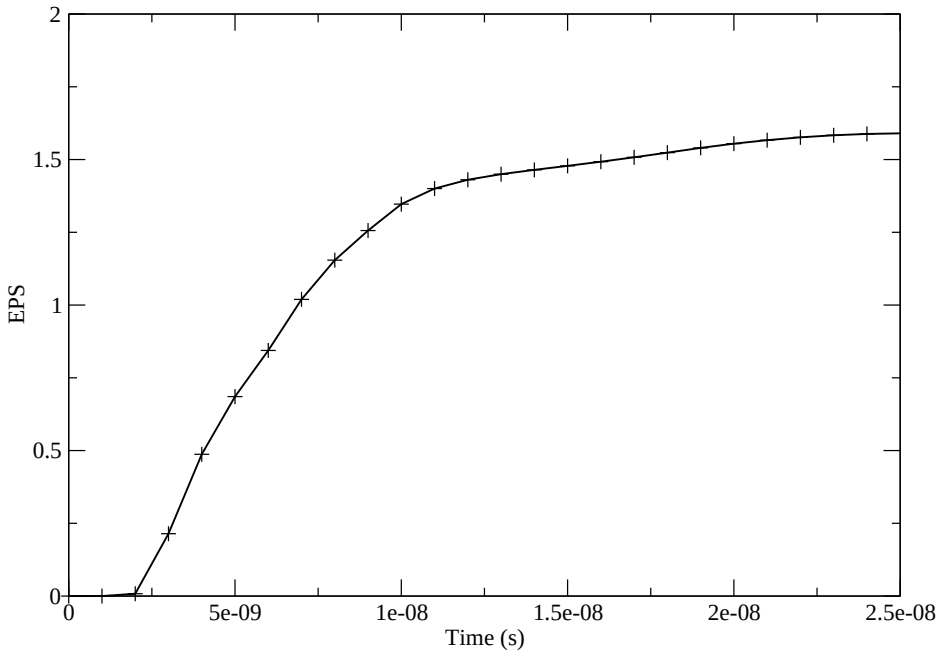

(b) Model C, EPS evolution in high EPS material jet region.

Figure B.15: Model C, evolution of temperature and EPS in material jet.

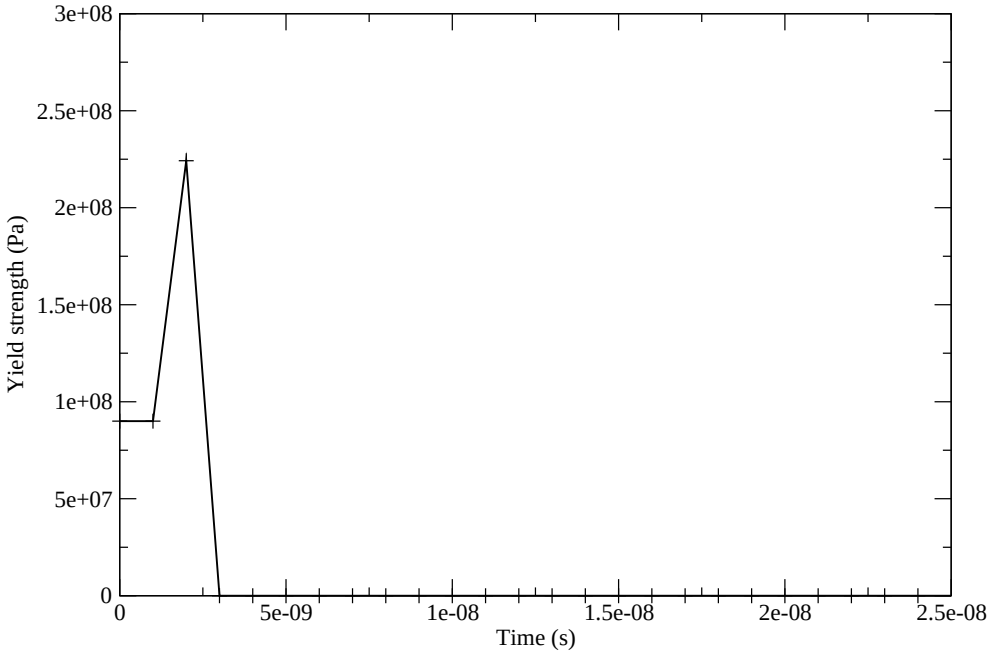

(a) Model C, yield strength evolution in high EPS material jet region.

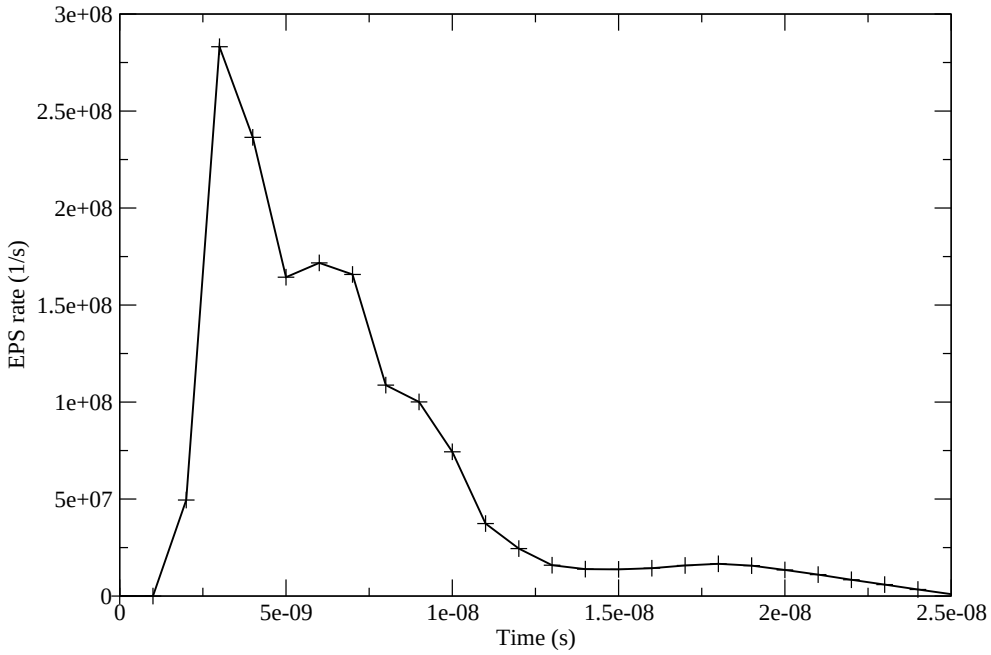

(b) Model C, EPS rate evolution in high EPS material jet region.

Figure B.16: Model C, evolution of yield strength and EPS rate in material jet.

B.2 Heat Conduction Models

B.2.1 Model D

The previous sections have described the impact of three-dimensional adiabatic feedstocks over a range of velocities and a series of conductive feedstocks will now be considered using the same initial conditions in order to examine the effect of heat conduction on splat morphology. The effects of including heat conduction will be disscussed in detail in section 5.1. Although heat conduction has been shown to have an effect on the splat formation an in detail comparison is lacking in the literature. In the following test case, a 10μm in diameter feedstock impacts the substrate at 400 m/s and 298 K. The flattening ratio plot in Figure B.3 shows a smooth increase towards a steady final value and variation in this value drops below 1% at 24 ns. At this time the variation in splat centre height falls below 0.1% and variation in both flattening ratio and splat centre height continues to reduce for the remainder of the time considered. Final values of flattening ratio, splat centre height and P^* are shown in Table B.3. From the P^* value it can be seen that the feedstock has created a crater half its initial diameter deep, which makes encapsulation of the feedstock unlikely. Relatively little flattening has occured during the impact due to the low kinetic energies involved, and as a consequence a low quality coating would be expected from impacts at this velocity.

Flattening ratio	0.306
Splat centre height (μm)	50.97
P^*	0.53

Table B.3: Model D flattening ratio, P^* and splat centre height data at 24 ns.

The splat morphology as shown in Figure B.18, shows a very small lip at the edge of the splat from 20 ns onwards; the splat has not undergone a lot of flattening and the final morphology shows a reasonably rounded shape.

The yield strength contours (see Figure B.19) show the dominance of thermal softening across the whole splat, peak hardening is seen at the feedstock/substrate interface although the hardening is uneven along this interface with the splat bottom centre show-

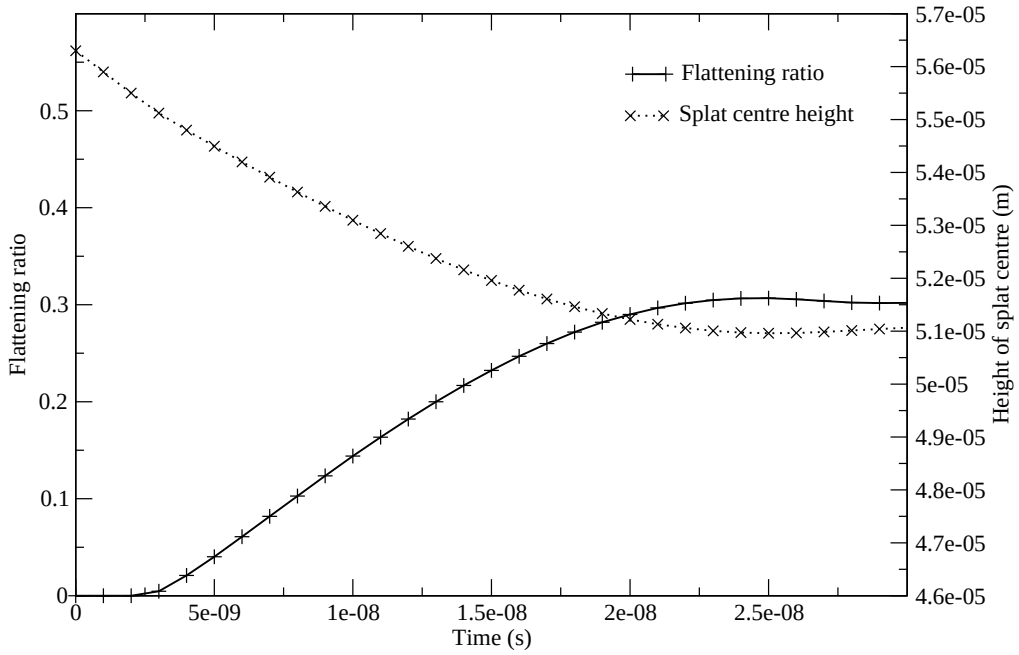

Figure B.17: Flattening ratio plot for a conductive feedstock at 298 K and 400 m/s.

ing less hardening than the flanks. The lowest hardening is seen towards the top centre of the splat.

Peak heating takes place in the early stages of the impact and can be seen to be localised to the flanks of the feedstock/substrate interface as shown in Figure B.20. The conductive terms act to reduce this localisation as heat is conducted away from the interface into the feedstock and substrate and this becomes significant under the high thermal gradients and small scale of the feedstock particles. Peak temperatures do not approach the melting point of the copper material at any point over the time considered.

The distribution of EPS within the splat is shown in Figure B.21 and the peak value of 0.904 is measured at the tip of the small lip feature on the splat flanks. Despite the increased levels of EPS at the interface between the feedstock and substrate, the entire splat has undergone plastic straining with the lowest strains found at the splat top centre.

The highest rate of EPS is found at the tip of the developing lip feature early on in the impact (see Figure B.22) when impact velocity and heating are at their highest. Two large regions of elevated EPS rate extend into this region from the lip tip and the flanks

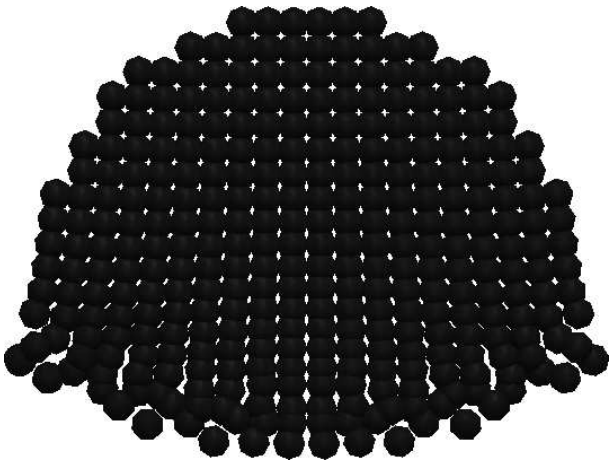

(a) 10 ns.

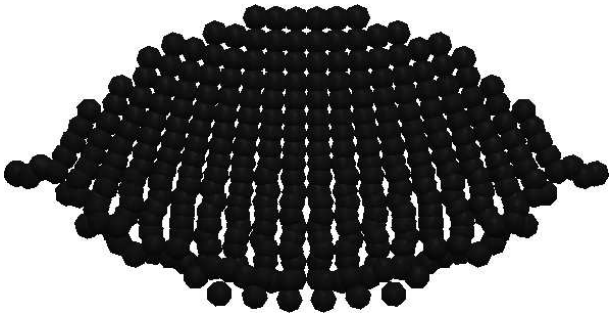

(b) 20 ns.

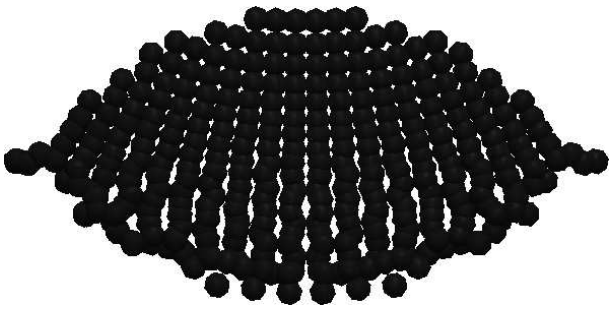

(c) 24 ns.

Figure B.18: Model D, cross section through centre of 3-D splat morphology.

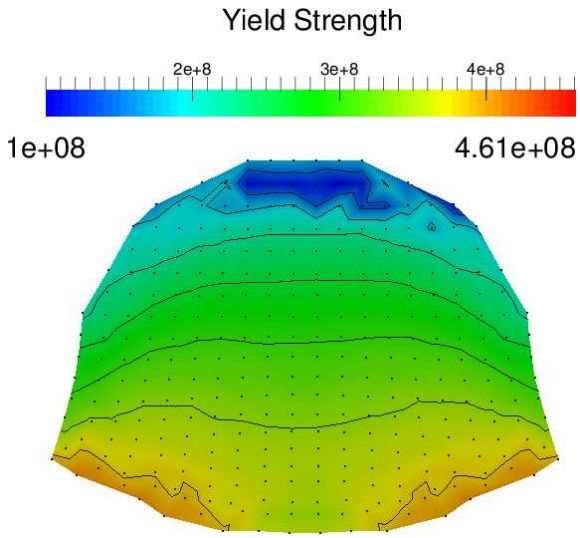

(a) 10 ns.

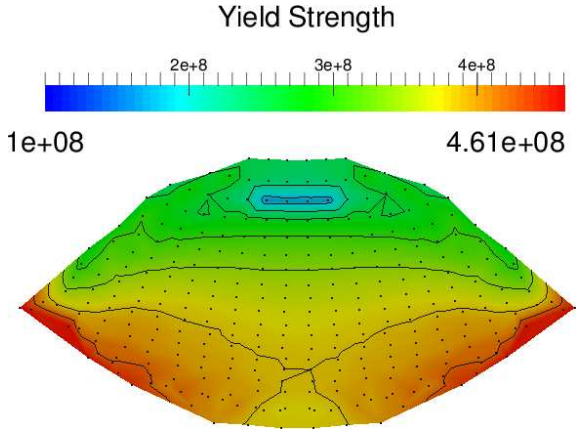

(b) 20 ns.

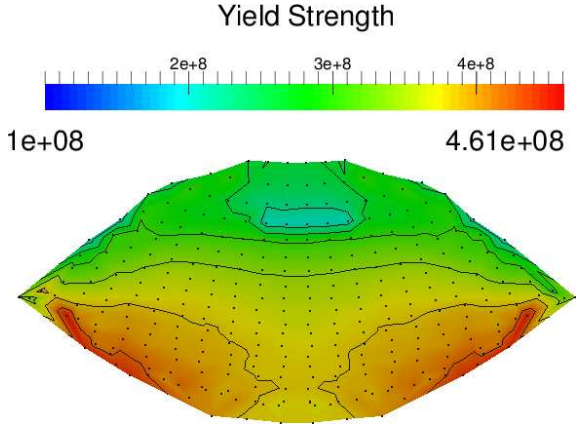

(c) 24 ns.

Figure B.19: Model D, yield strength cross section through centre of 3-D splat morphology.

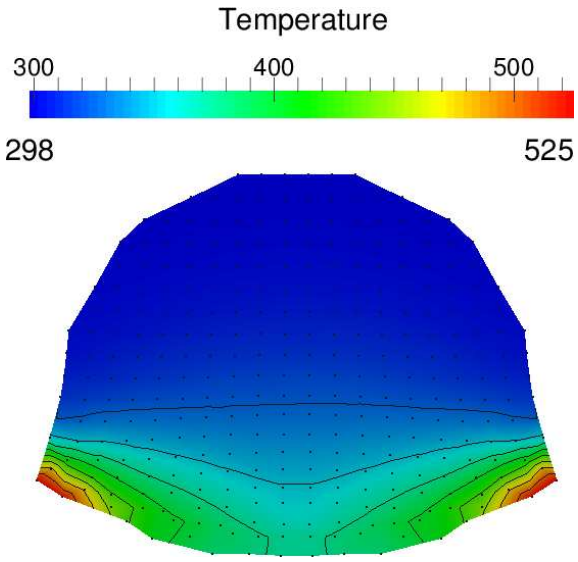

(a) 10 ns.

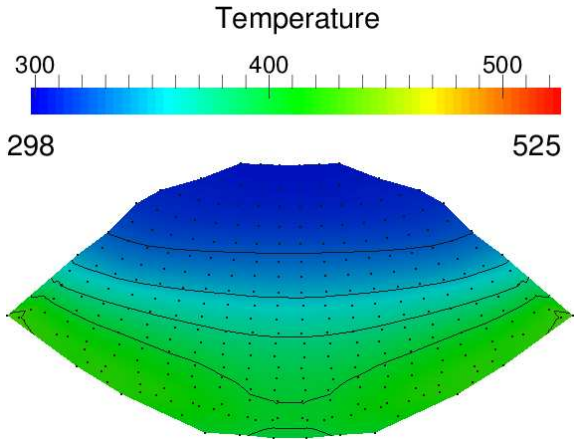

(b) 20 ns.

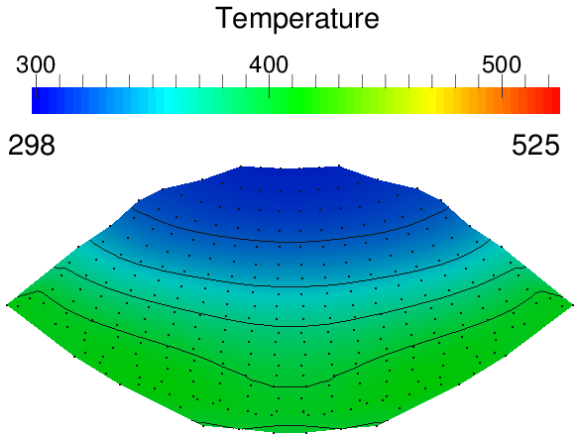

(c) 24 ns.

Figure B.20: Model D, temperature cross section through centre of 3-D splat morphology.

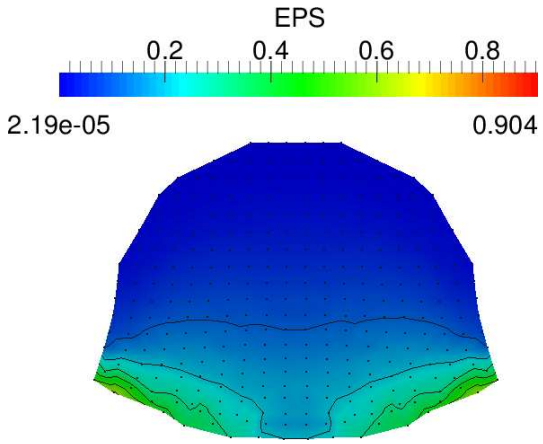

(a) 10 ns.

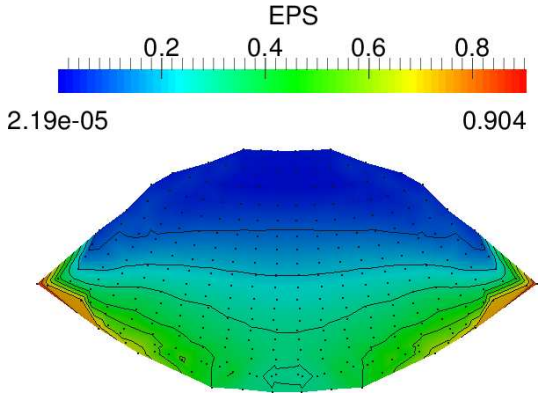

(b) 20 ns.

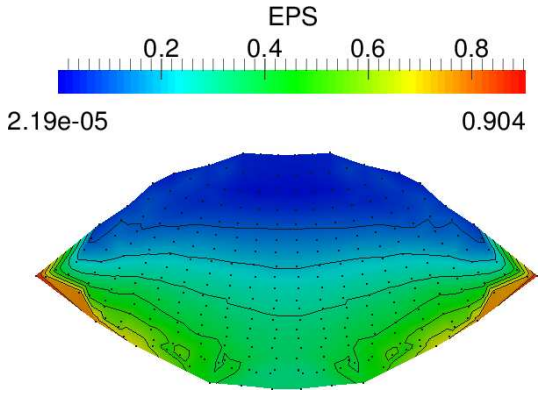

(c) 24 ns.

Figure B.21: Model D, EPS cross section through centre of 3-D splat morphology.

of the interface. After this period of rapid straining the EPS rate quickly reduces across the whole splat.

The evolution of temperature, EPS, EPS rate and yield strength in the splat at the point of highest total EPS are plotted in Figures B.23 and B.24. The temperature in this region starts to show a significant increase around 4 ns and this becomes a sharp rise to its peak value at 9 ns before a period of gradual cooling. The evolution of EPS shows a smooth approach to the peak value from 4 to 24 ns.

Material hardening in the yield strength plot (see Figure B.24a) is observed after 4 ns into the impact there is slight reduction in the rate of hardening between 6 and 9 ns and this shows some correlation to a period of time where there is a reduction in the EPS rate gradient in Figure B.24b. The rate of EPS shows a steep increase from 3 ns until a peak value is reached at 9 ns before a steady decline is observed. This peak in EPS rate happens at the same time as the peak temperature and therefore experiences the largest levels of thermal softening.

The lip feature that could indicate a region of shear band instability is barely observed for this impact; here the yield strength profiles in the lip region (see Figure B.24a) do not show any dominance of thermal softening for even a short duration and this is also true for the splat as a whole. Taking this into account as well as the initial velocity being below the experimentally derived critical velocity leads to the conclusion that the splat has not bonded to the substrate.

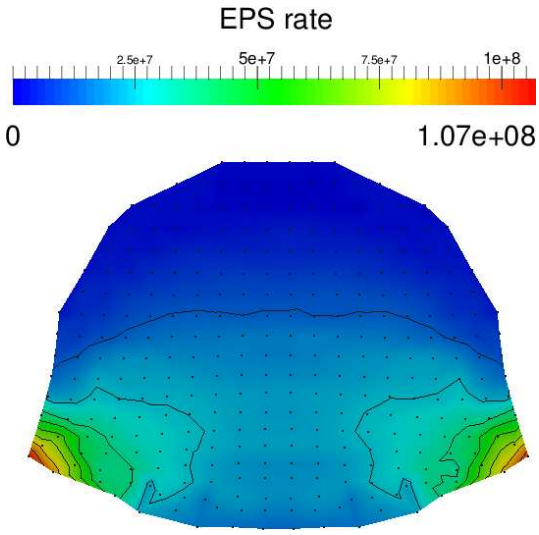

(a) 10 ns.

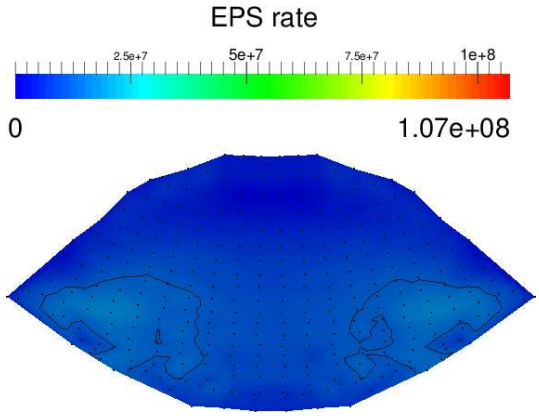

(b) 20 ns.

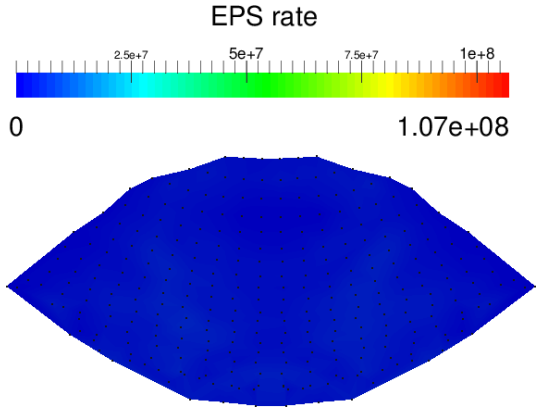

(c) 24 ns.

Figure B.22: Model D, EPS rate cross section through centre of 3-D splat morphology.

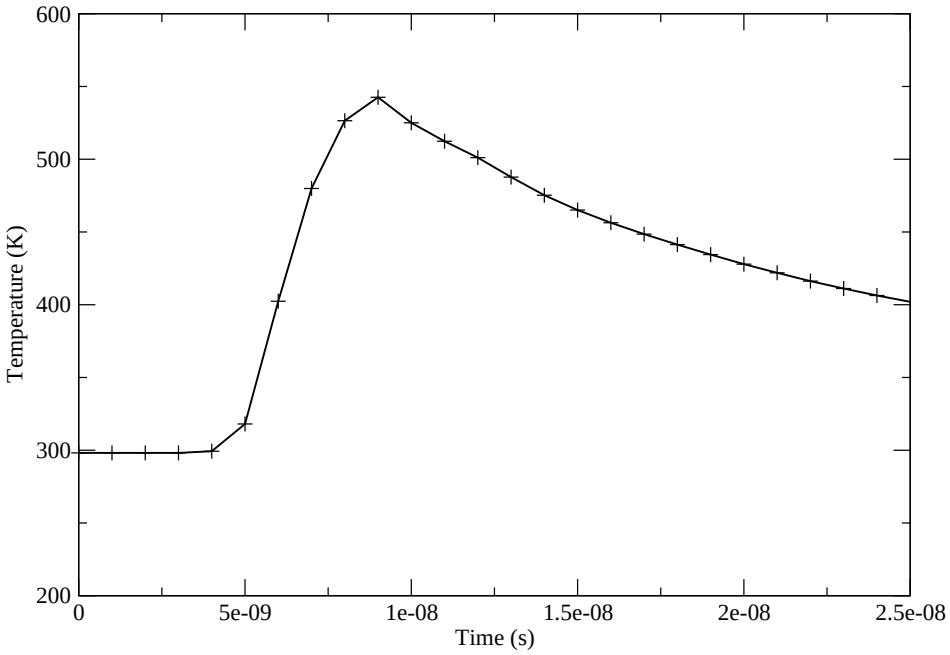

(a) Model D, temperature evolution in high EPS material jet region.

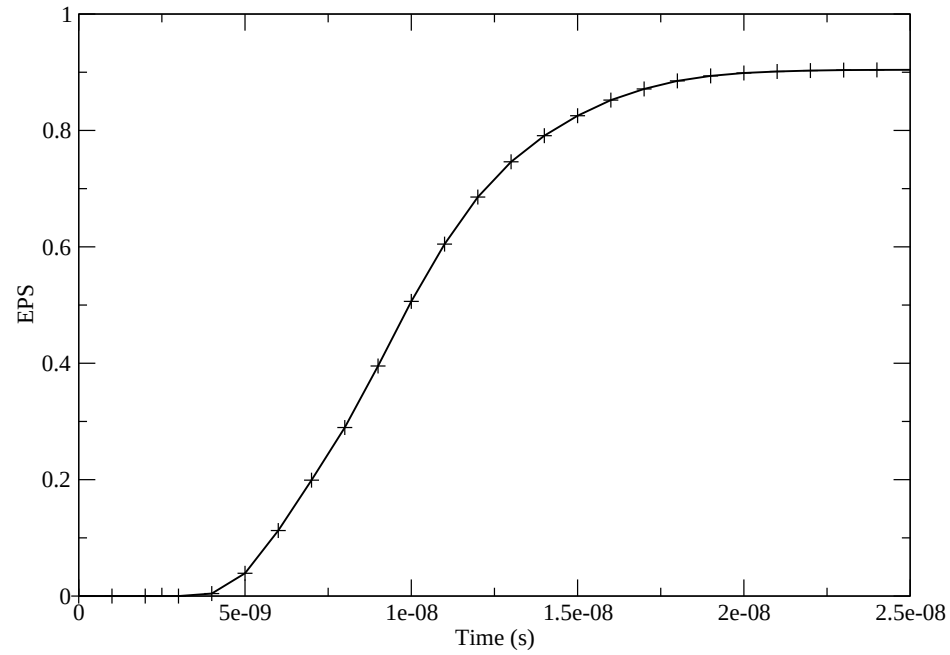

(b) Model D, EPS evolution in high EPS material jet region.

Figure B.23: Model D, evolution of temperature and EPS in material jet.

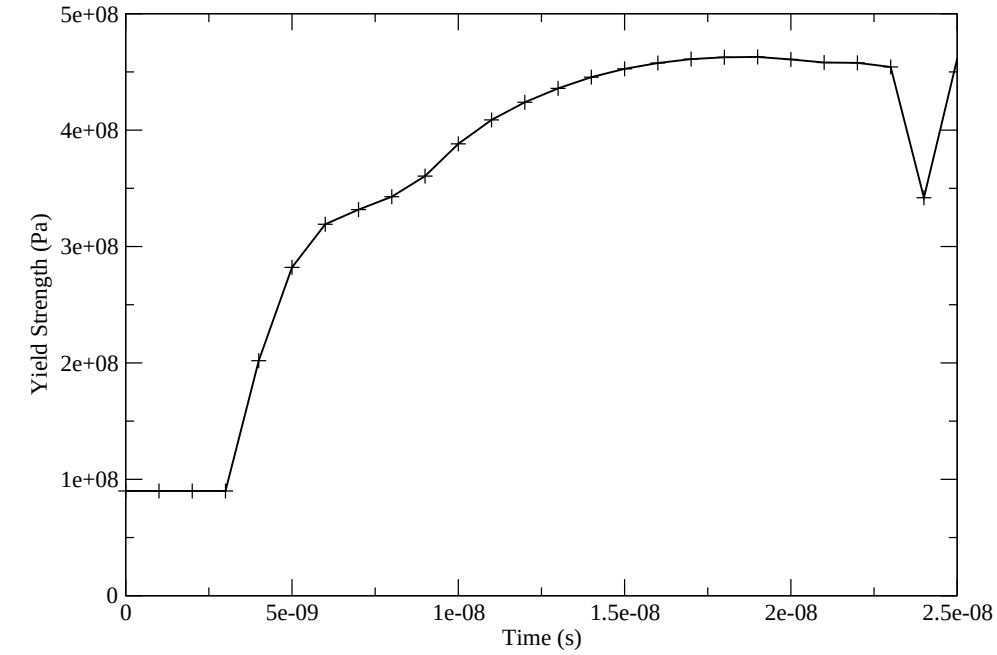

(a) Model D, yield strength evolution in high EPS material jet region.

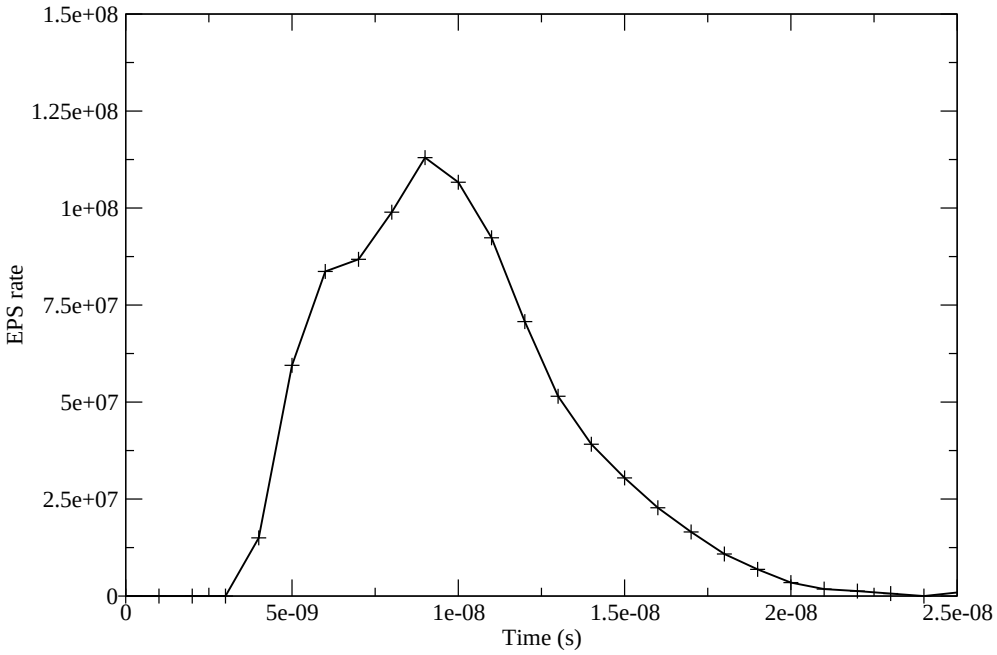

(b) Model D, EPS rate evolution in high EPS material jet region.

Figure B.24: Model D, evolution of yield strength and EPS rate in material jet.

B.2.2 Model E

The impact of a 10μm diameter copper feedstock travelling at 600 m/s with an initial temperature of 298 K is now considered. The variation of flattening ratio and splat centre height is shown in Figure B.25. The fluctuation of flattening ratio drops below 1% at 22 ns and at this time, the height of the splat centre is varying by as little as 0.2% and so the splat morphology is assumed to have reached a steady state. Peak values of flattening ratio, splat centre height and P^* are given in Table B.4. The feedstock has created a significant crater in the substrate, increasing the interfacial area over which bonding can occur. Significant flattening is also observed as a result of the impact and indicates a good quality coating can result from impacts at this velocity.

Flattening ratio	0.4018
Splat centre height (μm)	49.07
P^*	0.7466

Table B.4: Model E flattening ratio, P^* and splat centre height data at 22 ns.

The development of the splat morphology is shown in Figure B.26, a distinct lip of material at the splat edge can be seen from the 10 ns plot onwards indicating material jetting. The splat morphology shows overall flattening and widening as the impact progresses.

The distribution of material yield strength is shown in Figure B.27. Peak hardening is found at the flanks of the feedstock/substrate interface with reduced levels measured at the splat bottom centre, the lowest levels of hardening are found near the splat top centre where the splat has experienced the least strain. Material hardening is dominant over thermal softening across the whole splat for the full time period considered, due to the high strains experienced compared to lower levels of heating.

Temperature contours within the feedstock are given in Figure B.28. Peak heating is found at the tip of the lip feature early on in the impact before heat conduction reduces the localisation of the heating. No part of the feedstock exceeds the material melting temperature over the duration considered.

The distribution of EPS is shown in Figure B.29. There is a strong localisation to

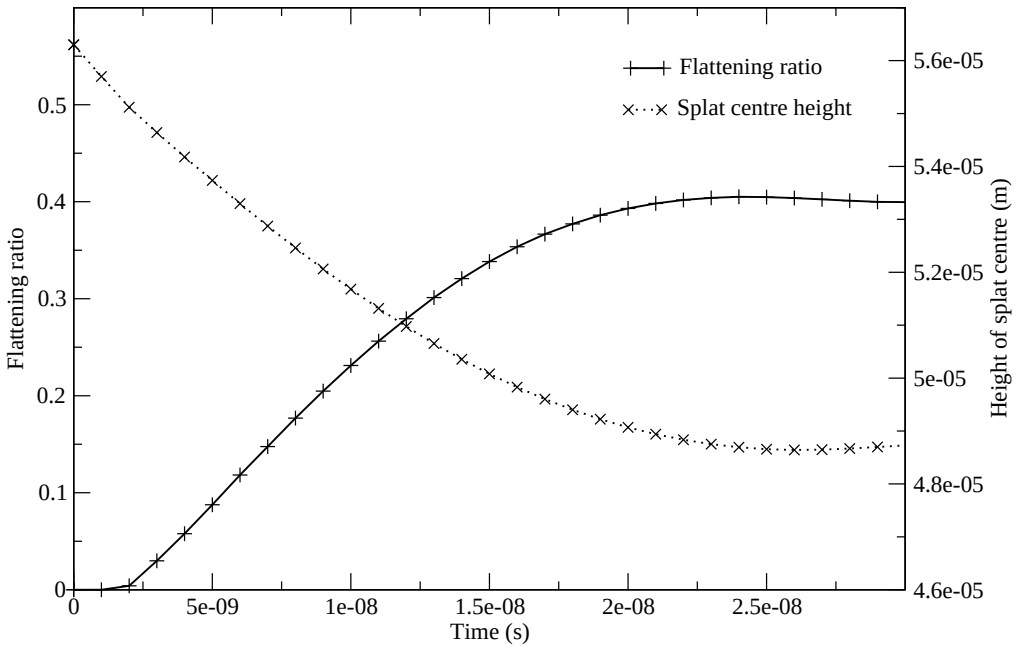

Figure B.25: Flattening ratio plot for a conductive feedstock at 298 K and 600 m/s.

the flanks of the feedstock/substrate interface early on in the impact, although as time goes on, the level of plastic strain experienced by the splat as a whole increases as the feedstock deforms into the final splat morphology. Peak EPS is seen just behind the tip of the lip feature on the substrate interface with levels at the interface decreasing towards the splat bottom centre.

The highest rate of EPS is seen at this point just behind the lead edge of the lip feature in the early stages of the impact (see Figure B.30), coinciding with the highest impact velocites. This period of heightened plastic strain rate is brief and the rate of EPS across the splat decreases quickly as the splat deaccelerates into the substrate. The entire interface does not experience the same rate of EPS with the splat bottom centre showing the lowest levels of the whole interface, whilst the lowest levels of EPS rate in the splat as a whole are found at the splat top centre where little strain is experienced.

The evolution of temperature, EPS, yield strength and EPS rate in the region of peak total EPS is plotted in Figures B.31 and B.32. They show a sharp increase in temperature from 2 ns until 5 ns when a sudden decrease in temperature is followed by a period of

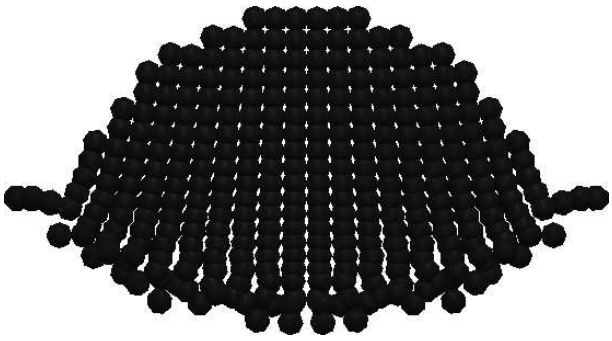

(a) 10 ns.

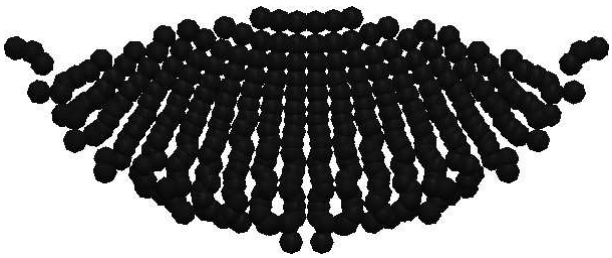

(b) 20 ns.

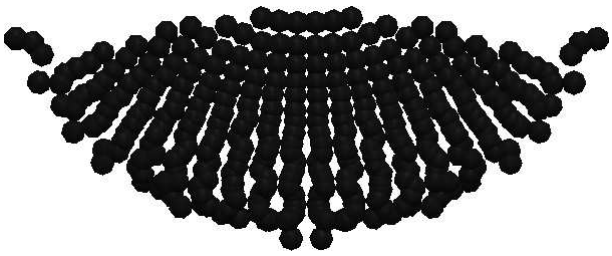

(c) 22 ns.

Figure B.26: Model E, cross section through centre of 3-D splat morphology.

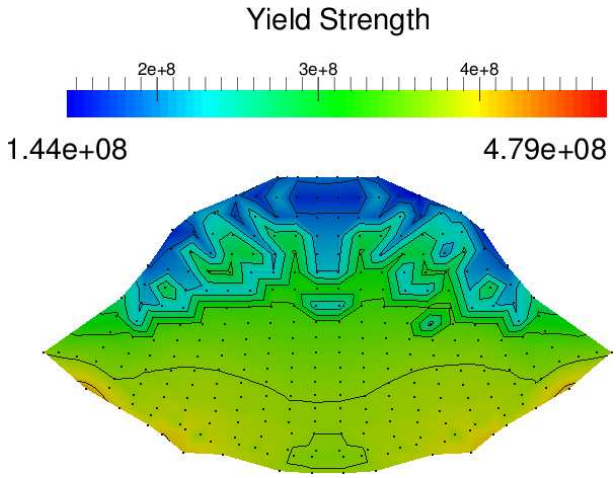

(a) 10 ns.

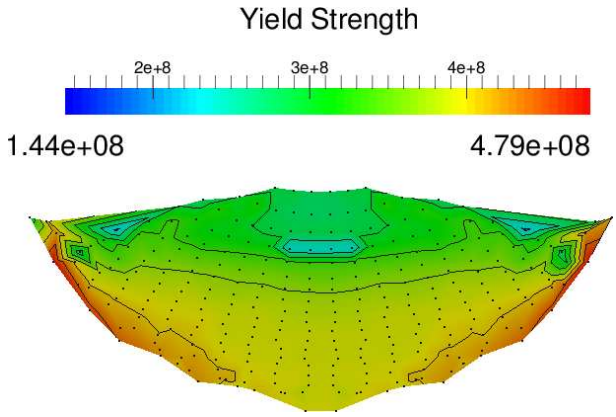

(b) 20 ns.

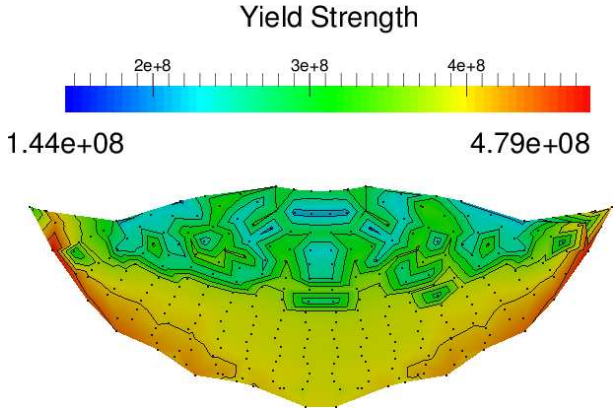

(c) 22 ns.

Figure B.27: Model E, yield strength cross section through centre of 3-D splat morphology.

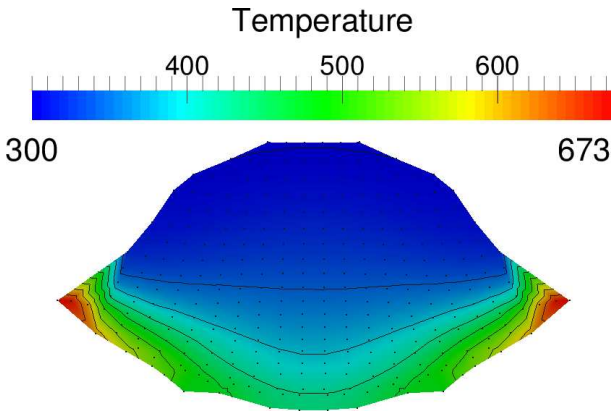

(a) 10 ns

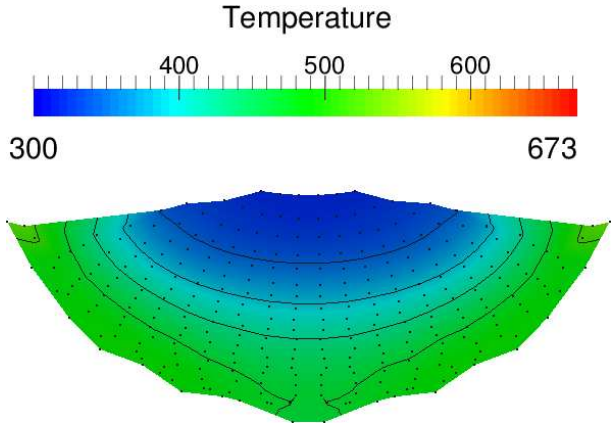

(b) 20 ns

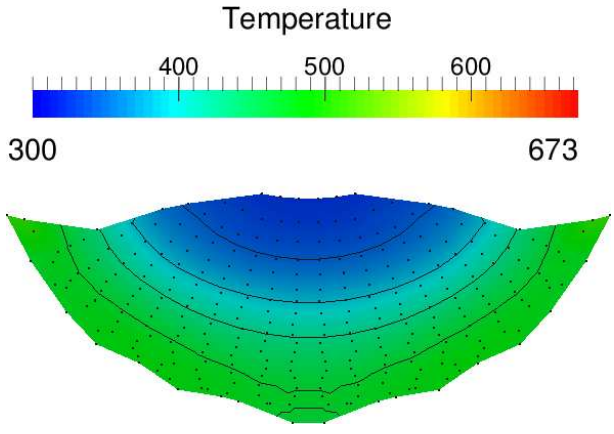

(c) 22 ns

Figure B.28: ModelE, temperature cross section through centre of 3-D splat morphology

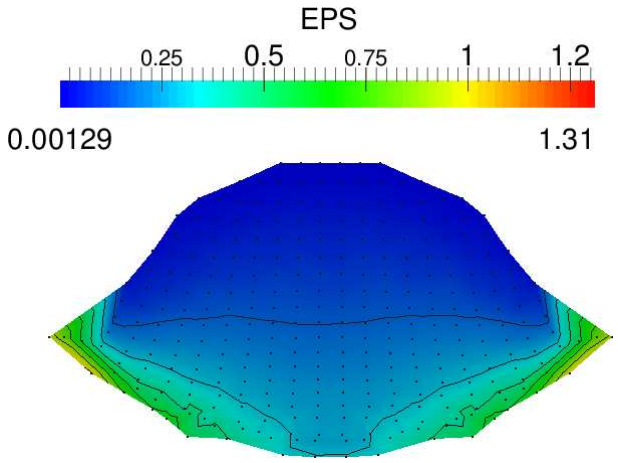

(a) 10 ns.

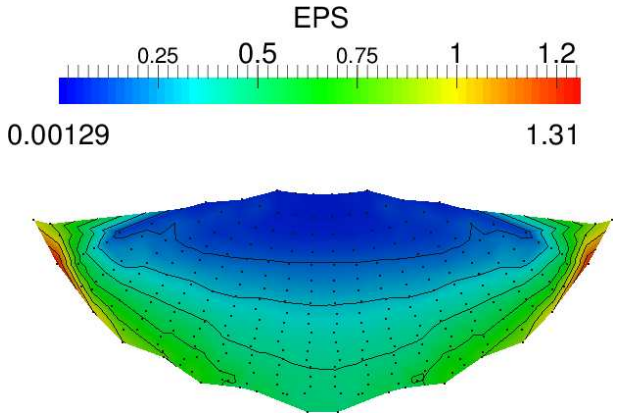

(b) 20 ns.

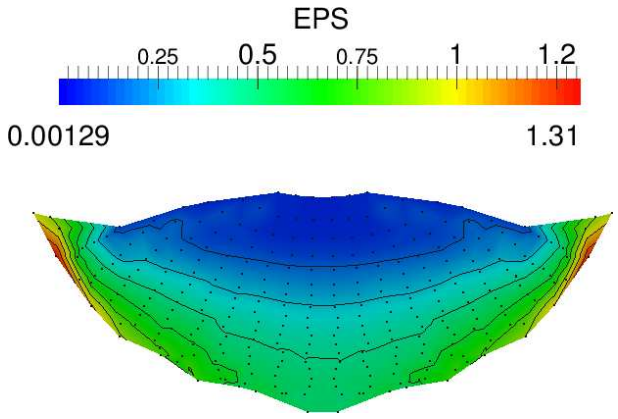

(c) 22 ns.

Figure B.29: Model E, EPS cross section through centre of 3-D splat morphology.

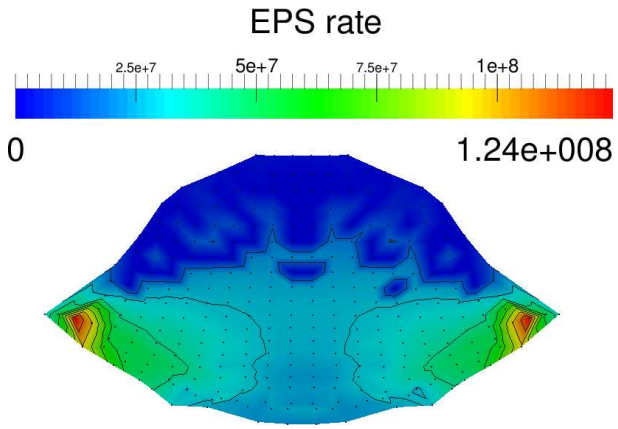

(a) 10 ns.

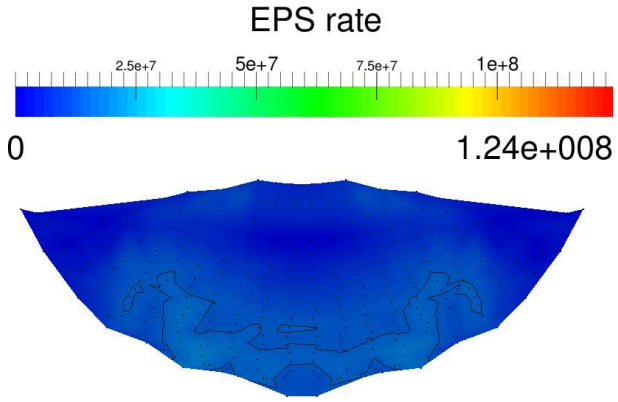

(b) 20 ns.

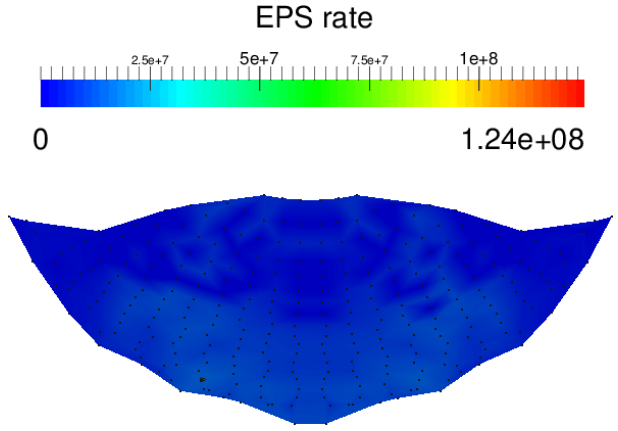

(c) 22 ns.

Figure B.30: Model E, EPS rate cross section through centre of 3-D splat morphology.

much slower cooling from 8 ns (see Figure B.31a). The EPS evolution in Figure B.31b shows an increase from 2 ns until the peak value is reached, idicating the deformation is the splat has halted.

The yield strength profile (see Figure B.32a) shows a sharp increase in hardening at 2 ns which is followed by a period of material softening with the material reaching its highest softening at 4 ns before hardening becomes dominant again and remains so for the remainder of the time period considered. This dip in yield strength happens at the same time that peak EPS rate is reached (see Figure B.32b) and is in the vicinity of the period of peak heating; this momentary dominance of thermal softening coincides with elevated EPS rate indicates the presence of a shear band instability and material jetting.

The distinct lip feature seen in the splat morphology coupled with the evidence of high plastic strain rates during a period of weakened material strength in the lip region indicates strong material jetting at the flanks of feedstock/substrate interface and that bonding is likely to occur. This is in agreement with the experimentally derived critical velocity of 500 m/s.

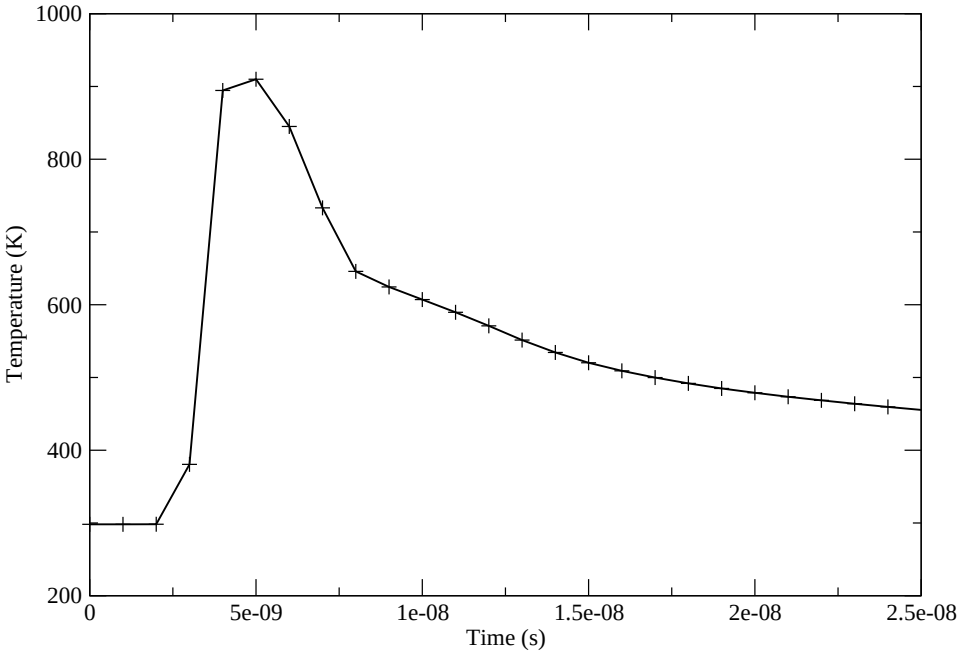

(a) Model E, temperature evolution in high EPS material jet region.

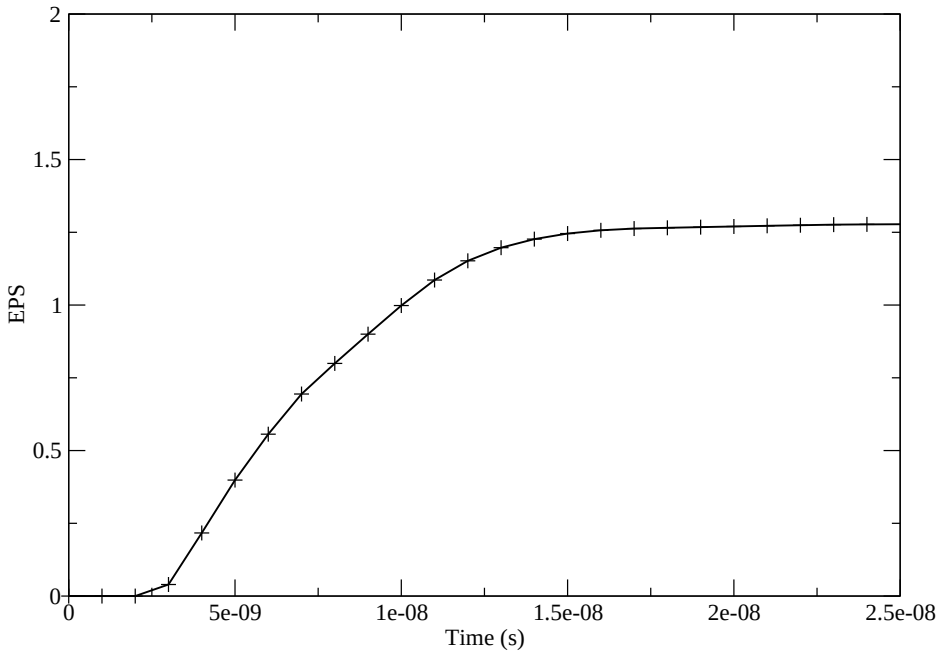

(b) Model E, EPS evolution in high EPS material jet region.

Figure B.31: Model E, evolution of temperature and EPS in material jet.

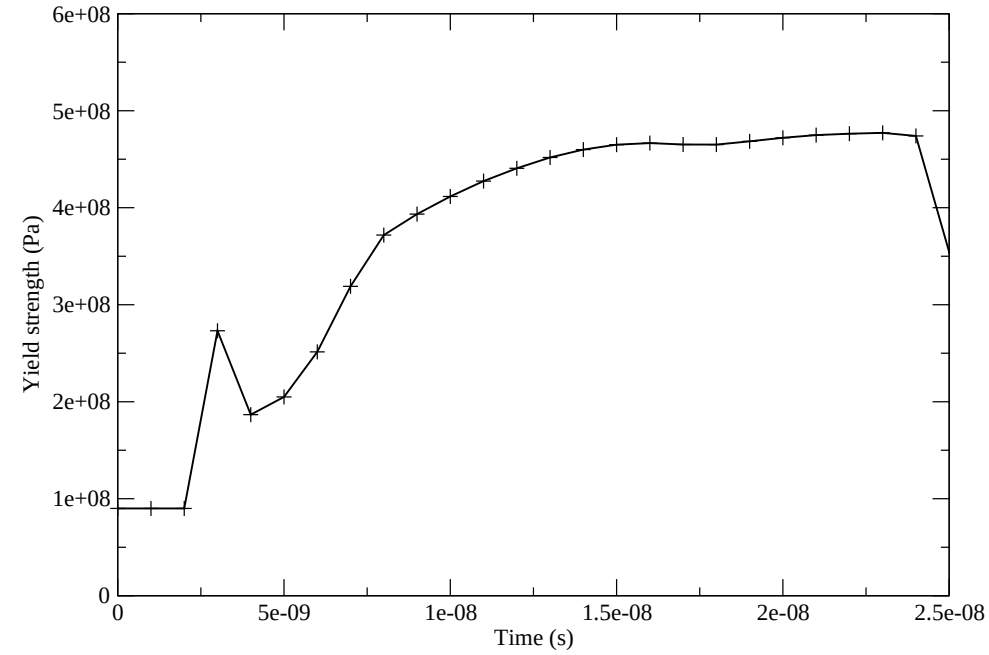

(a) Model E, yield strength evolution in high EPS material jet region.

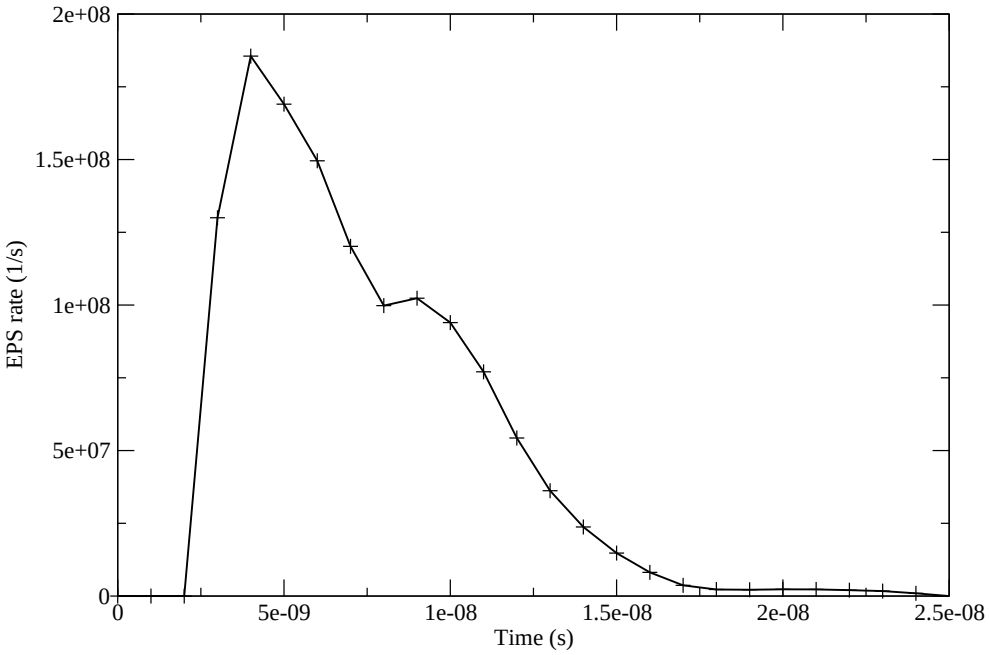

(b) Model E, EPS rate evolution in high EPS material jet region.

Figure B.32: Model E, evolution of yield strength and EPS rate in material jet.

B.2.3 Model F

The impact of a heat conductive copper feedstock with an initial diameter of 10μm, velocity 800 m/s and temperature 298 K is now examined. The splat morphology is found to reach a stable state at 23 ns when the variation in flattening ratio decreases below 1% and the variation in slat centre height is at 0.3%. Final values of flattening ratio, splat centre height and P^* are given in Table B.5. The feedstock has flattened by 52% of its inital diameter during the impact whilst forming a deep crater in the substrate. This indicates the feedstock has significantly deformed and has a large interfacial contact area with the substrate with a possibiltiy of feedstock encapsulation for less spherical initial morpholgies.

Flattening ratio	0.521
Splat centre height (μm)	46.383
P^*	0.9917

Table B.5: Model F flattening ratio, P^* and splat centre height data at 23 ns.

The splat morphology shows a developing lip at the edge of the splat at 10 ns which grows in size as the impact evolution progress, while the remainder of the splat shows a significant level of flattening.

Peak heating is seen in the early stages of the impact at the leading edge of the lip feature (see Figure B.35) and at this time, strong localisation is seen at the feedstock/substrate interface. Temperature distribution along the interface is not uniform with the splat bottom centre experiencing significantly lower levels of heating. The conduction terms act to reduce the localisation as the impact progresses and the feedstock experiences more uniform heating.

The distribution of yield strength within the feedstock is shown in Figure B.36. In the early stages of the impact the lower portion of the splat experiences the highest levels of hardening although this is over taken by increased hardening at the splat flanks against the feedstock/substrate interface by 20 ns into the impact. There is an overall dominance of hardening over softening over the entire impact due to high strain and strain rates relative to the heating caused by the impact.

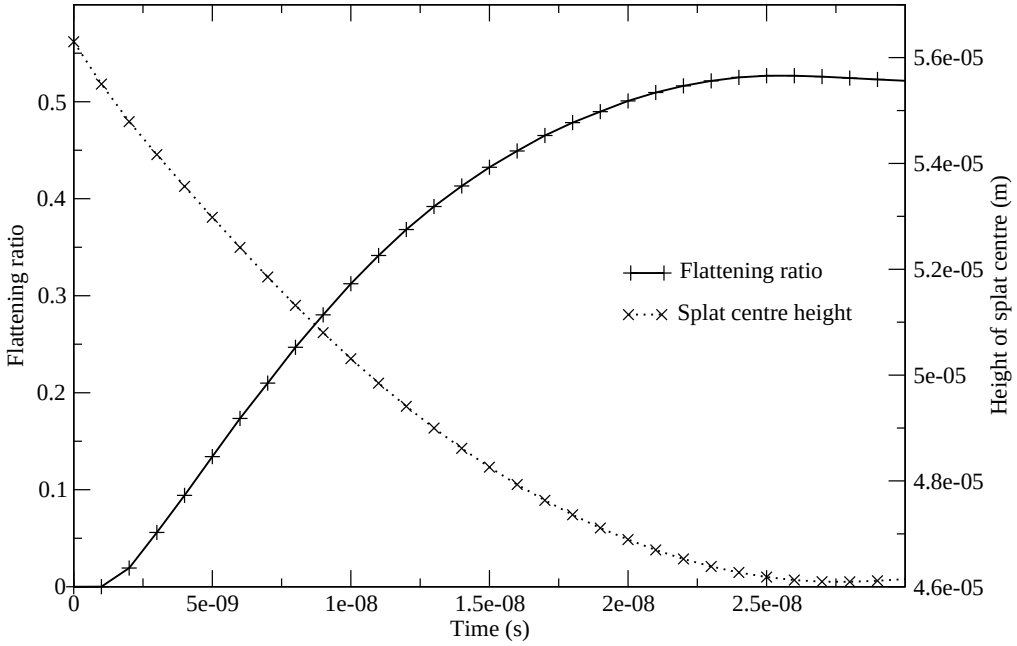

Figure B.33: Flattening ratio plot for a conductive feedstock at 298 K and 800 m/s.

The highest EPS levels are found just behind the leading edge of the lip feature (see Figure B.37) at the feedstock/substrate interface. The distribution of EPS along this interface is not uniform with the splat bottom centre showing lower strains than those found in the flank areas, this non-uniform distribution is caused by the pattern of feedstock deformation throughout the impact. The material in the flank regions is subjected to higher shear stresses as the feedstock flattens and creates a crater in the substrate, it is these shear stresses that cause the high levels of plastic strain and trigger jet formation. In comparison, the splat top centre undergoes significantly less strain and so shows the least EPS of the whole splat.

Contours of EPS rate within the feedstock are shown in Figure B.38. The highest rate is seen early on in the impact at the flanks of the interface region with a zone of increased EPS rate radiating from these regions into the splat body. As the impact nears completion there is a general reduction of EPS rate as the kinetic energy is nearly spent and the splat approaches steady state.

The development of temperature, EPS, yield strength and EPS rate has been moni-

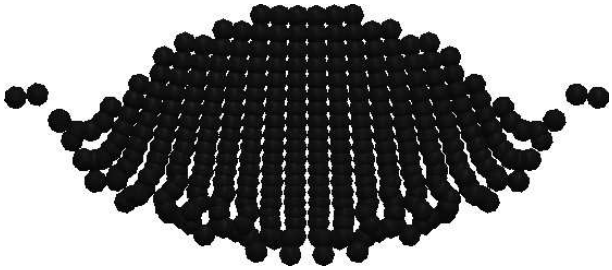

(a) 10 ns.

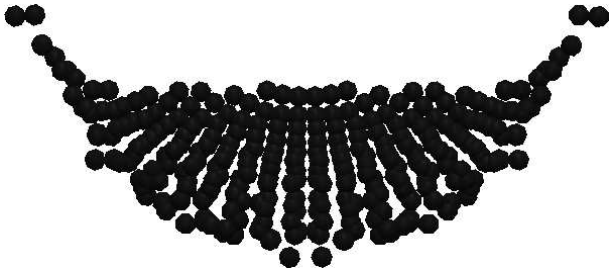

(b) 20 ns.

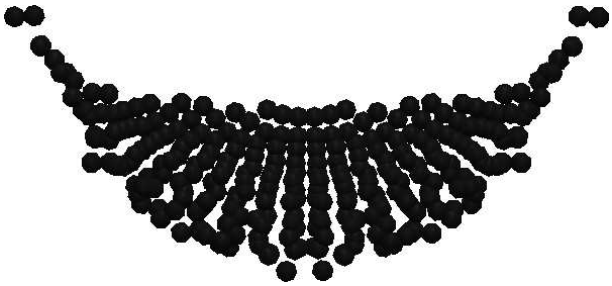

(c) 23 ns.

Figure B.34: Model F, cross section through centre of 3-D splat morphology.

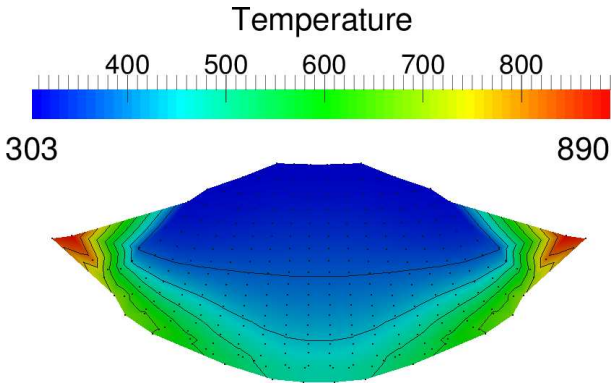

(a) 10 ns.

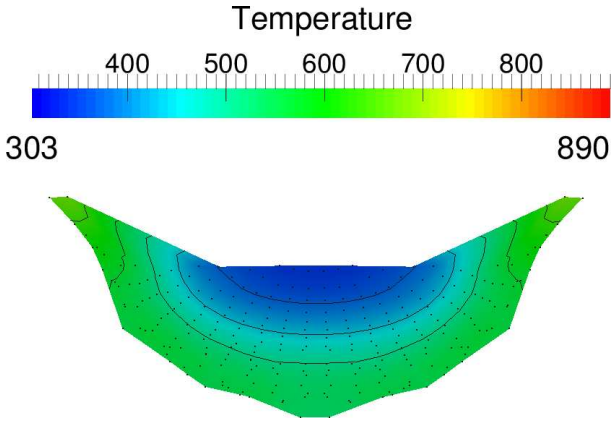

(b) 20 ns.

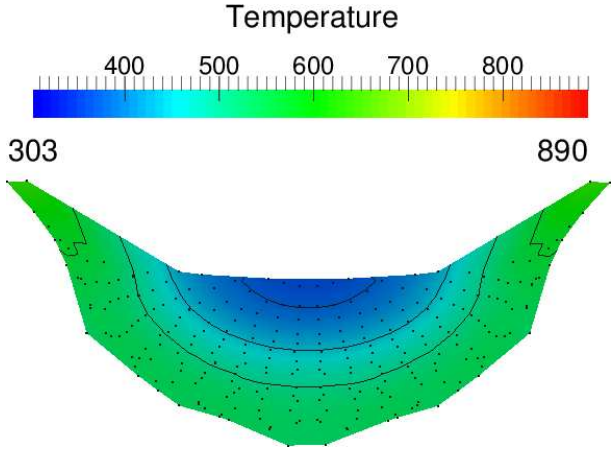

(c) 23 ns.

Figure B.35: Model F, temperature cross section through centre of 3-D splat morphology.

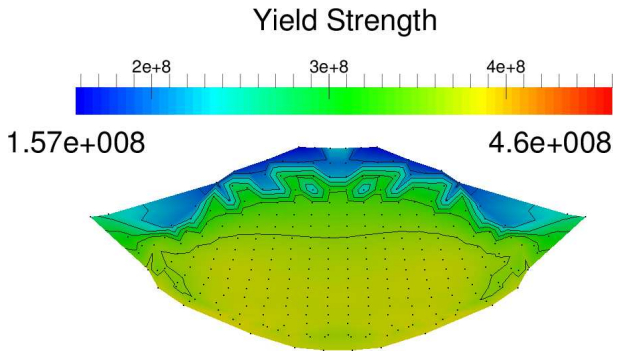

(a) 10 ns.

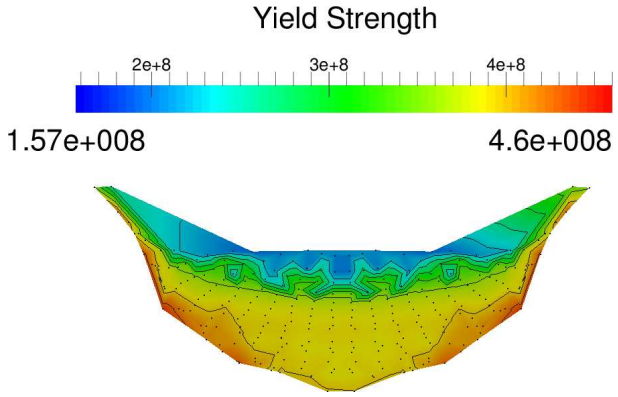

(b) 20 ns.

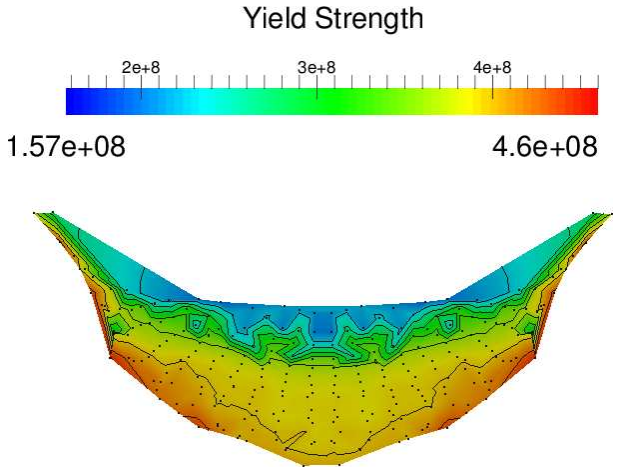

(c) 23 ns.

Figure B.36: Model F, yield strength cross section through centre of 3-D splat morphology.

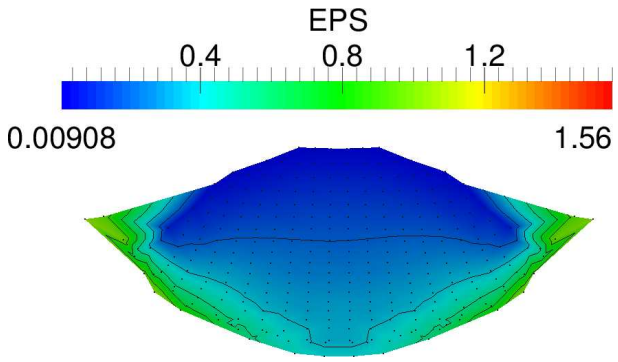

(a) 10 ns.

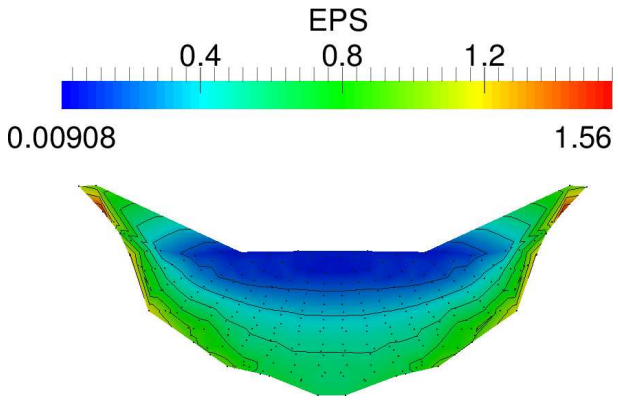

(b) 20 ns.

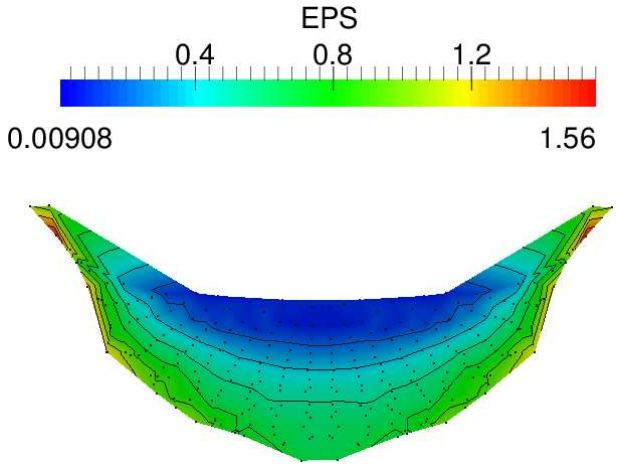

(c) 23 ns.

Figure B.37: Model F, EPS cross section through centre of 3-D splat morphology.

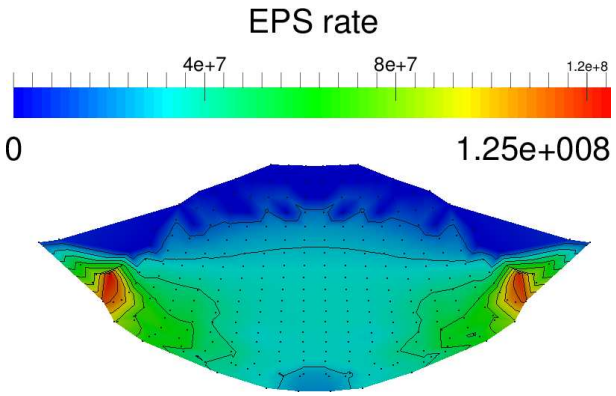

(a) 10 ns.

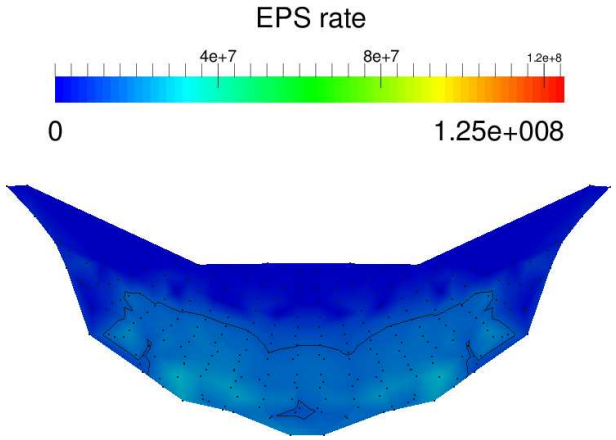

(b) 20 ns.

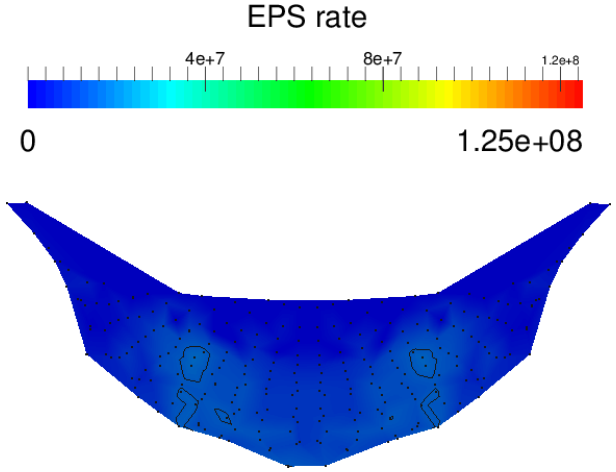

(c) 23 ns.

Figure B.38: Model F, EPS rate cross section through centre of 3-D splat morphology.

tored in the region of the lip feature that experiences the highest total EPS and profiles are shown in Figures B.31 and B.40. There is a sharp rise in heating at 2 ns (see Figure B.39a) that reaches a peak at 3 ns before experiencing rapid cooling until 6 ns when the rate of cooling reduces, there is a short period of heating between 6 and 7 ns. The peak temperature approaches but does not exceed the material melt temperature and so the splat remains in a solid state throughout the impact. The levels of EPS (see Figure B.39b) show a steady increase towards a peak value.

The profiles of yield strength (see Figure B.40a) and EPS rate (see Figure B.40b) show some interesting correlations. After a short period of hardening there is a sharp reduction in yield strength at 2 ns as thermal softening becomes locally dominant due the high level of heating experienced at this time (see Figure B.39a); this period of softened material lasts until 6 ns and coincides with the highest experienced rate of EPS. After 3 ns there is a rapid reduction in EPS rate until a plateau feature indicating a brief increase in EPS rate is seen between 5 and 7 ns before a return to decreasing EPS rate matched by increasing material yield strength.

The formation of a large lip of material at the splat periphery and the observed localised material softening and resulting high EPS rates seen at the flanks of the feedstock/substrate interface indicate the presence of a shear band instability. This causes strong material jetting in areas of the splat that correspond to experimentally observed regions of feedstock/substrate bonding. Additionally, the initial velocity used in this case is above the experimentally determined critical velocity and so the splat is assumed to have bonded to the substrate.

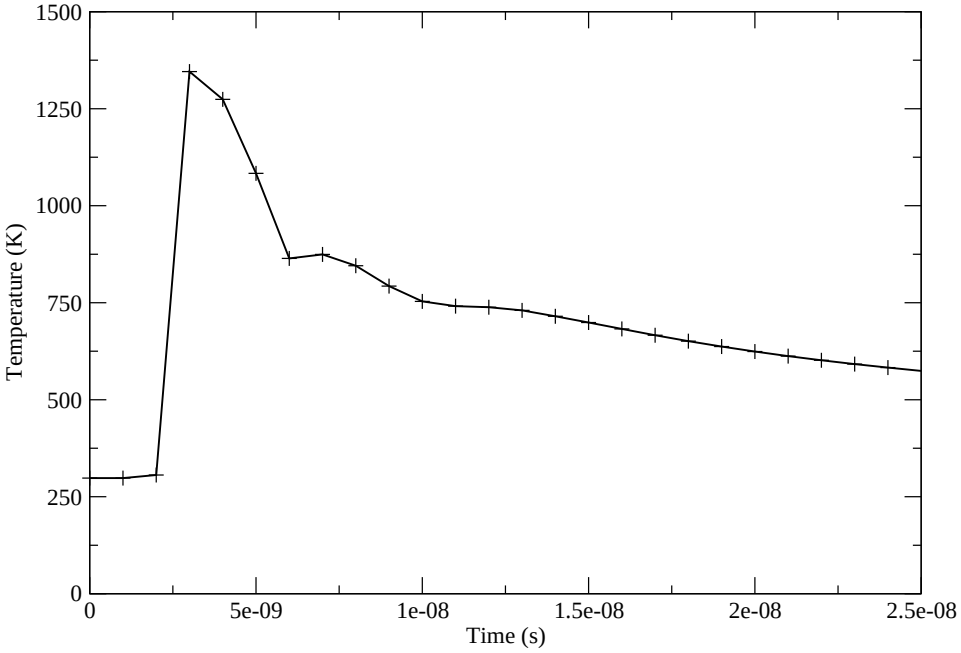

(a) Model F, temperature evolution in high EPS material jet region.

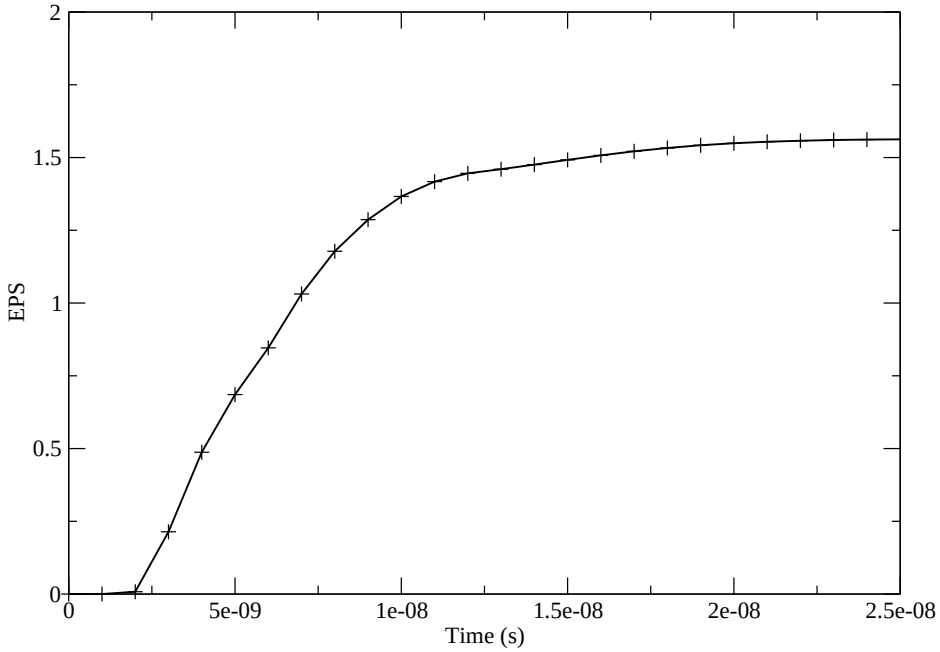

(b) Model F, EPS evolution in high EPS material jet region.

Figure B.39: Model F, evolution of temperature and EPS in material jet.

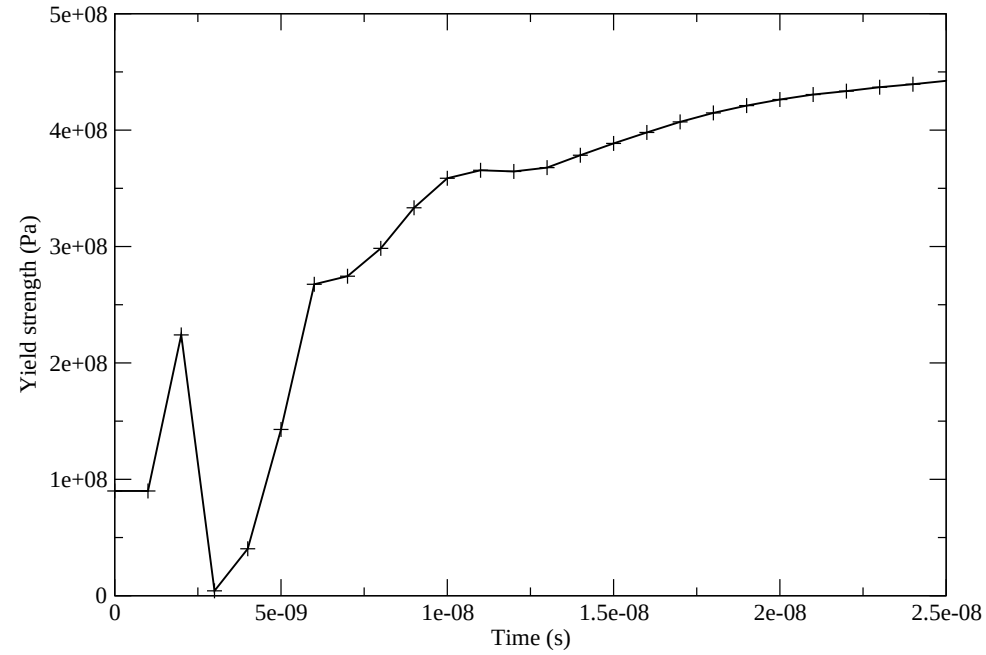

(a) Model F, yield strength evolution in high EPS material jet region.

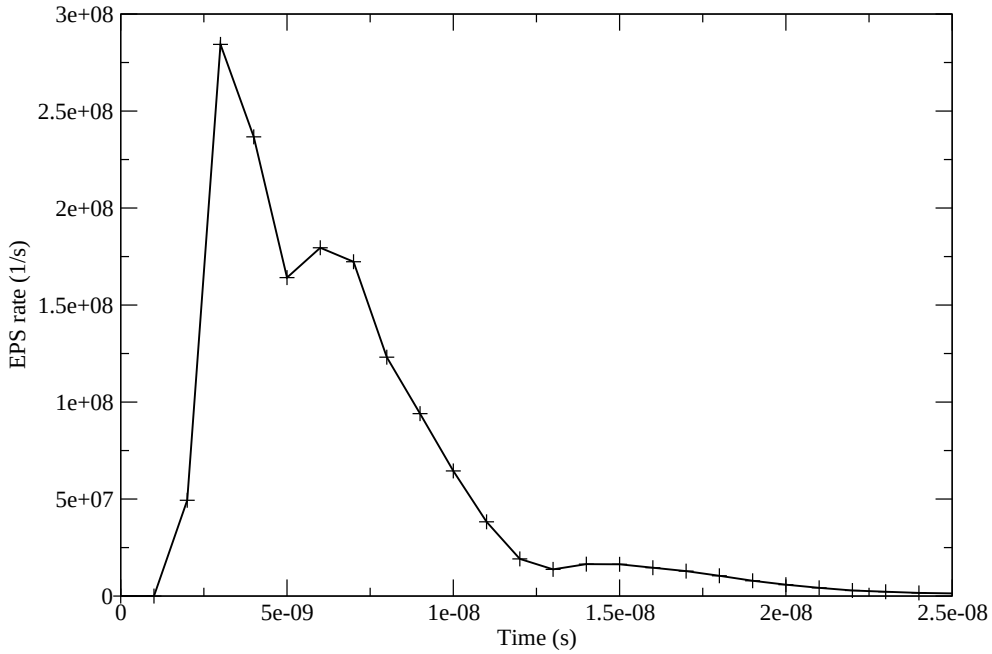

(b) Model F, EPS rate evolution in high EPS material jet region.

Figure B.40: Model F, evolution of yield strength and EPS rate in material jet.

B.2.4 Model G

The following study investigates the impact of a 10μm conductive copper feedstock with initial velocity and temperature of 400 m/s and 593 K respectively onto a copper substrate with initial temperature of 298 K. Figure B.41 shows that the feedstock flattens and embeds itself into the substrate over the duration of impact. The flattening ratio steadily increases to a peak value at 26 ns when variation in flattening drops below 1% and at this time variation in splat centre height is 0.03% wherethe splat morphology is considered to have reached a steady state. Final values of flattening ratio, splat centre height, P^* are given in Table B.6. At this low impact velocity relatvely little flattening is observed and a modest crater is formed in the substrate indicating a reduced interface area and low feedstock deformation.

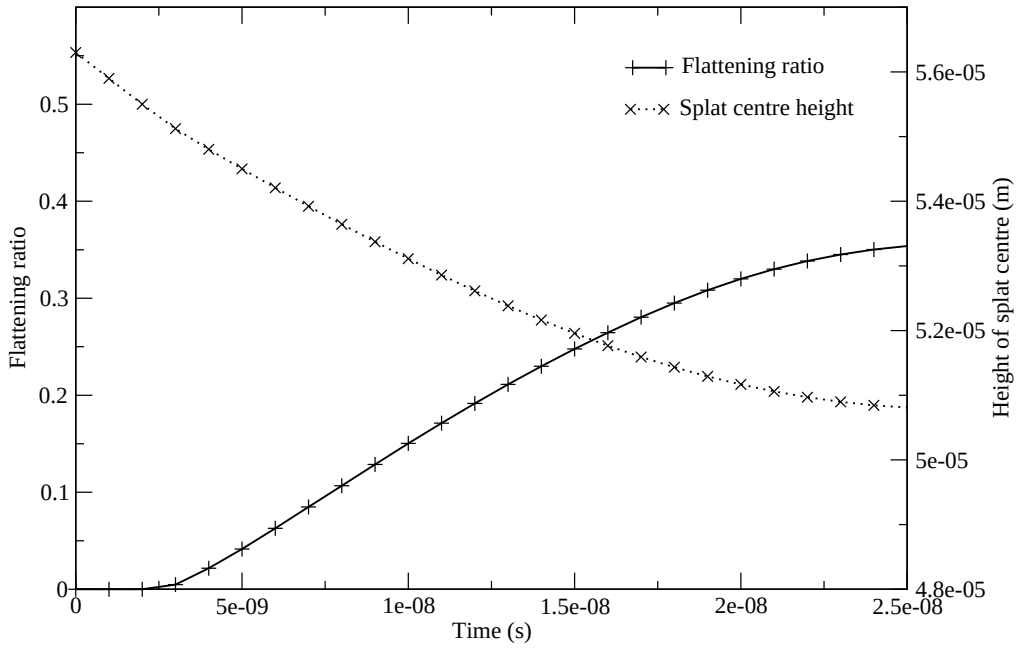

Figure B.41: Flattening ratio plot for a conductive feedstock at 593 K and 400 m/s

The splat morphology shows a limited amount of flattening as expected from the final value of flattening ratio, however from 10 ns onwards, there is a small lip feature forming at the splat edges but this feature is not particularly significant.

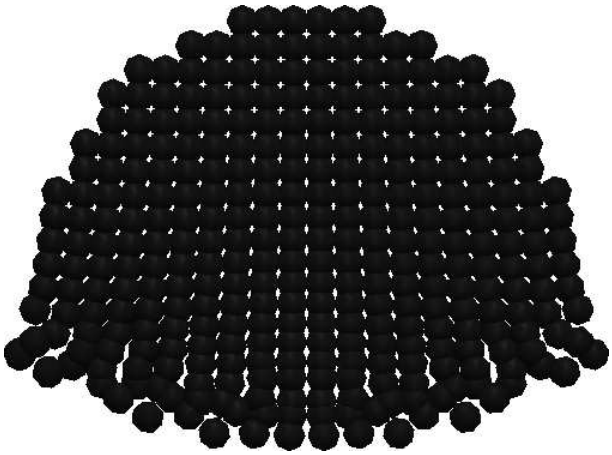

(a) 10 ns.

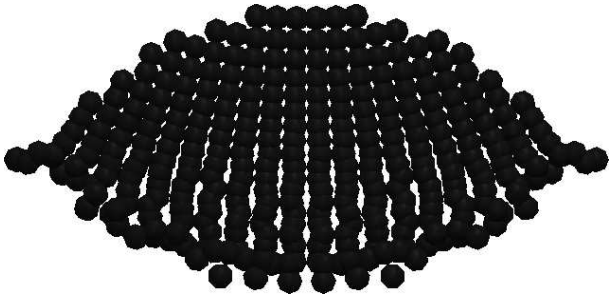

(b) 20 ns.

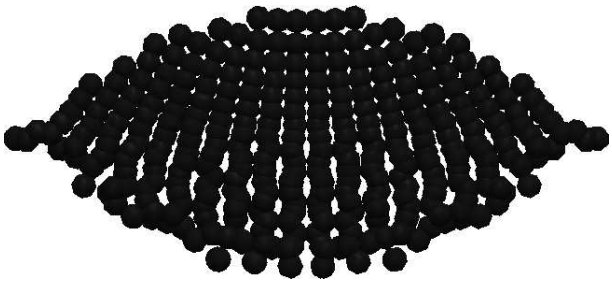

(c) 26 ns.

Figure B.42: Model G, cross section through centre of 3-D splat morphology.

Flattening ratio	0.356
Splat centre height (μm)	50.8
P^*	0.551

Table B.6: Model G flattening ratio, P^* and splat centre height data at 26 ns.

Peak heating is seen early on in the impact (see Figure B.43) at the leading edge of the lip feature, in this case the substrate is 295 K cooler than the impacting feedstock and so conduction of heat from the feedstock to the substrate is observed at the feedstock/substrate interface. At 10 ns this cooler zone observed at splat bottom centre gradually spreads up the splat flanks as the impact progresses.

Although the feedstock has been thermally softened by 25% by the elevated initial temperature, the splat in general has been dominated by hardening during the course of the impact as the splat strains and cools via conduction into the colder substrate. Peak hardening is found at the flanks of the feedstock/substrate interface but does not extend to the splat bottom centre, while the upper portion of the splat body shows the least hardening.

Peak rates of EPS are seen in the early stages of the splat formation (see Figure B.45) and occur at the leading edge of the forming lip feature with zones of increased EPS rate stretching into the feedstock body from these areas. There is a rapid reduction in rates of EPS from 20 ns onwards as the splat approaches steady state, elevated rates can be seen in a band across the splat body and at the flanks of the feedstock/substrate interface throughout the impact.

As expected, the EPS distribution (see Figure B.46) matches the distribution of the EPS rate (see Figure B.45), showing peak values at the flanks of the feedstock/substrate interface with reduced levels at the splat bottom centre and the lowest overall levels at splat top centre.

The development of temperature, yield strength, EPS rate and EPS in the region of the splat that experiences the highest total EPS is plotted in Figures B.47 and B.48. This region is found at the feestock/substrate interface at the splat flanks. A sharp increase in heating is evident between 4 and 8 ns which is followed by gradual cooling of the feedstock. The EPS profiles shows an increase towards a steady value throughout the

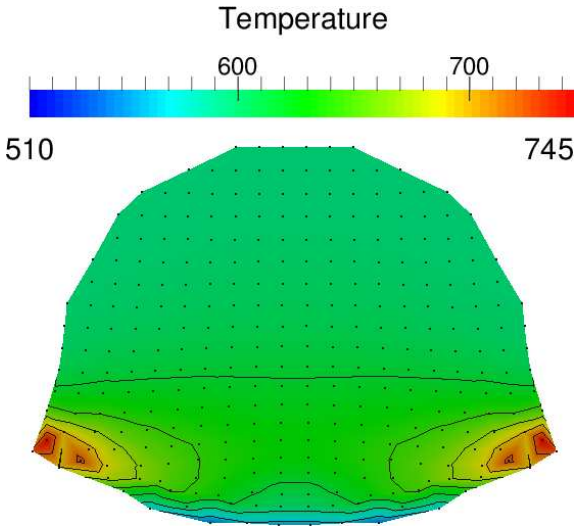

(a) 10 ns.

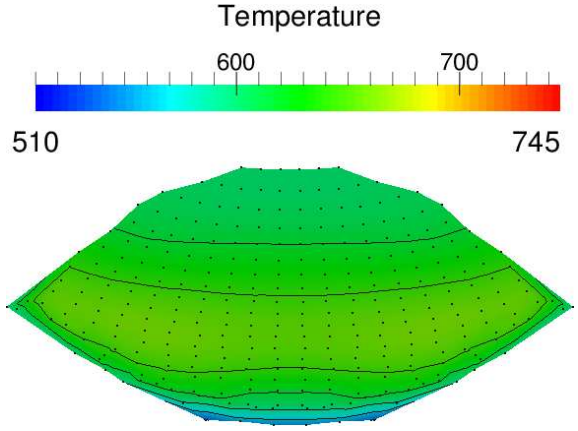

(b) 20 ns.

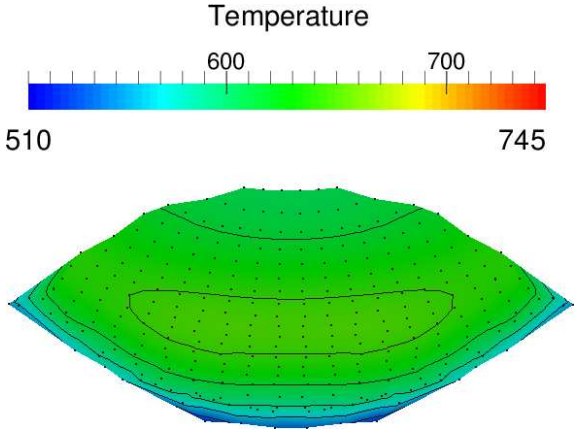

(c) 26 ns.

Figure B.43: Model G, temperature cross section through centre of 3-D splat morphology.

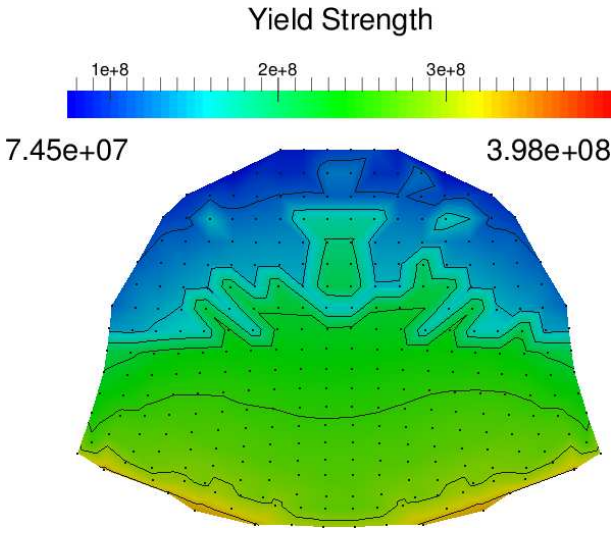

(a) 10 ns.

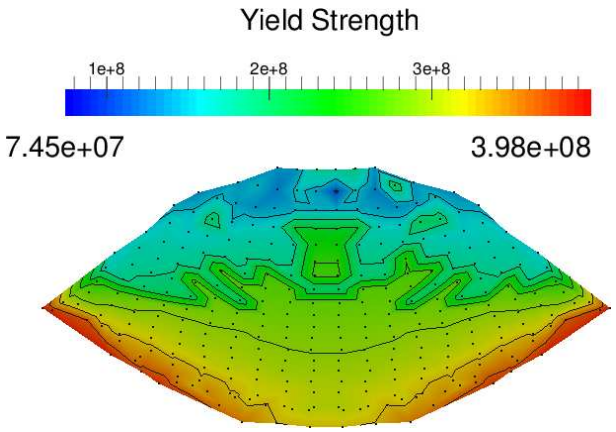

(b) 20 ns.

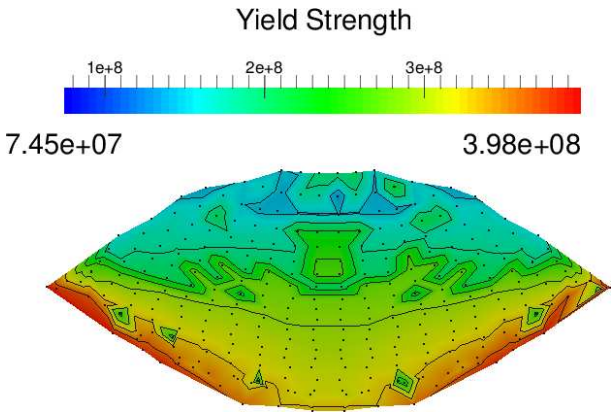

(c) 26 ns.

Figure B.44: Model G, yield strength cross section through centre of 3-D splat morphology.

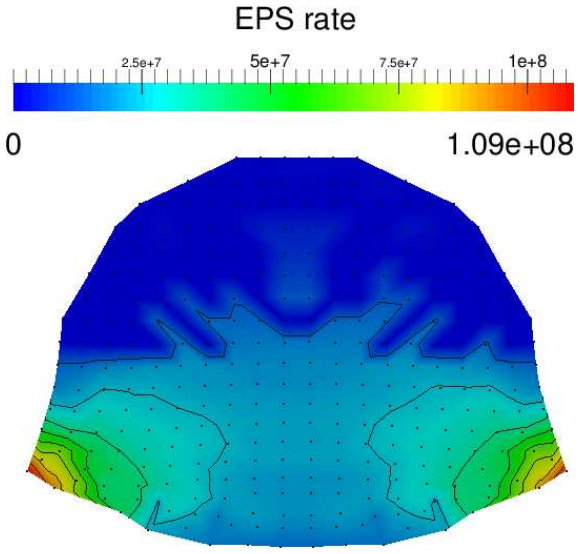

(a) 10 ns.

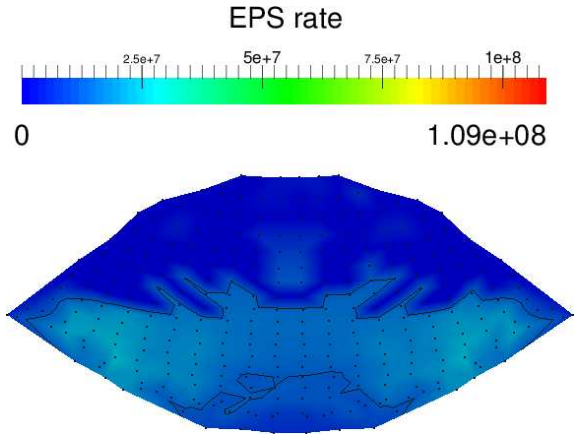

(b) 20 ns.

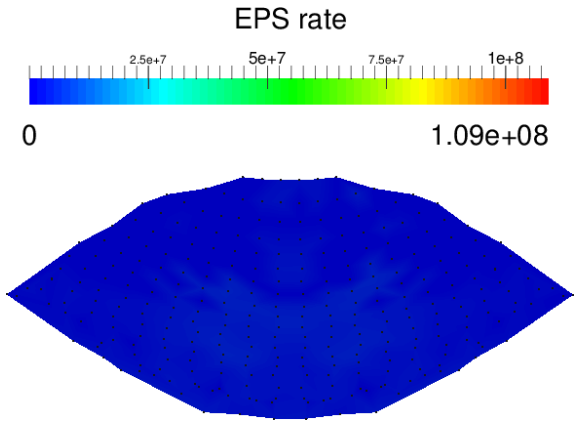

(c) 26 ns.

Figure B.45: Model G, EPS rate cross section through centre of 3-D splat morphology.

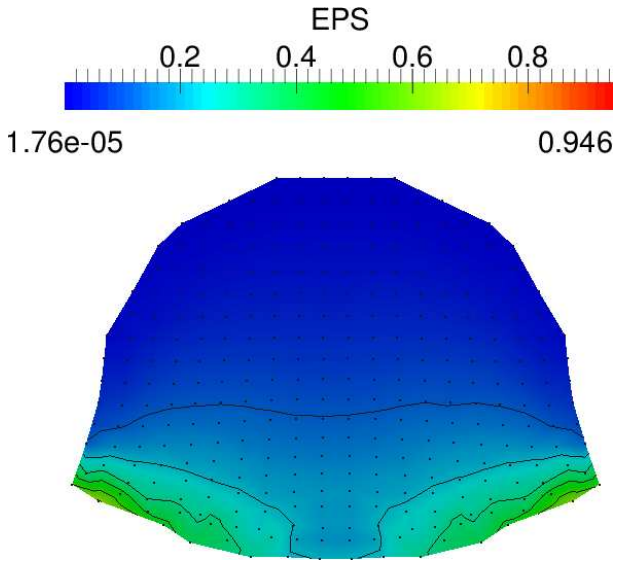

(a) 10 ns.

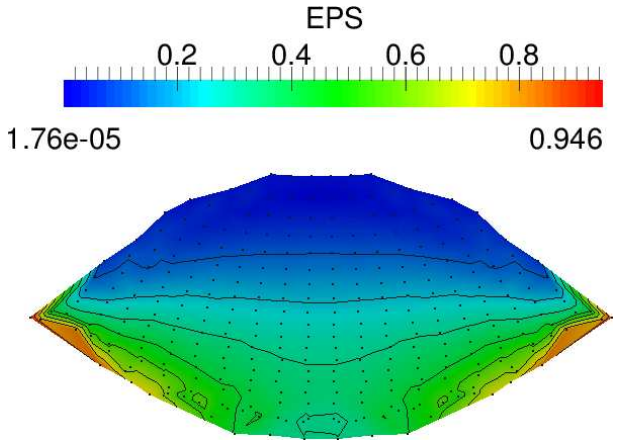

(b) 20 ns.

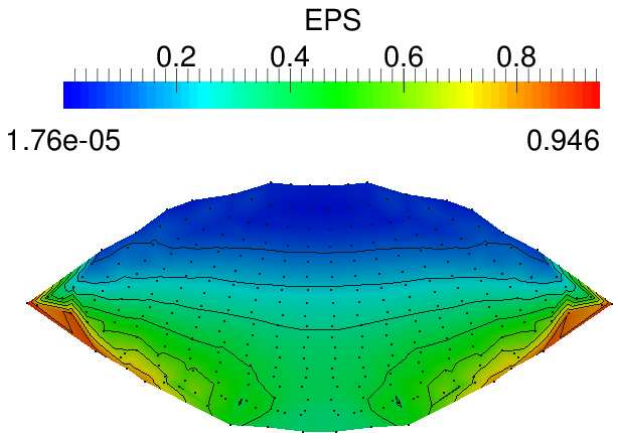

(c) 26 ns.

Figure B.46: Model G, EPS cross section through centre of 3-D splat morphology.

impact.

The evolution of yield strength (see Figure B.48a) as shows the dominance of hardening over thermal softening over the entire impact event. The rate of EPS climbs to a peak value at 9 ns before declining towards zero as the impact velocity is expended deforming the feedstock and substrate.

There is no sign of a shear band instability forming in the feedstock since there is no sign of significant localised and transient material softening at the feedstock/interface flanks and only an under developed lip feature is seen. These observations are in agreement with the initial impact velocity being below the experimentally determined critical velocity.

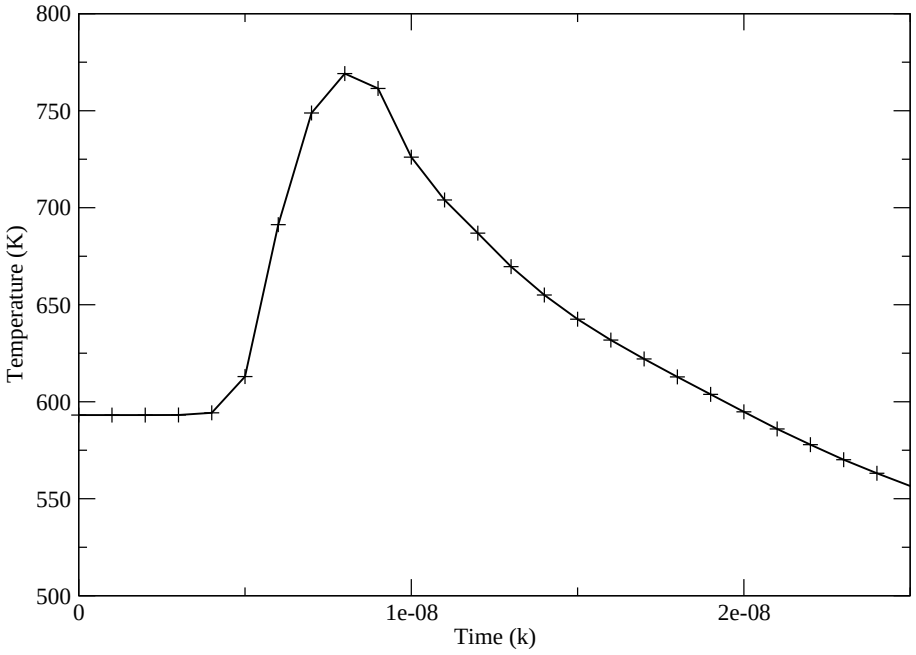

(a) Model G, temperature evolution in high EPS material jet region.

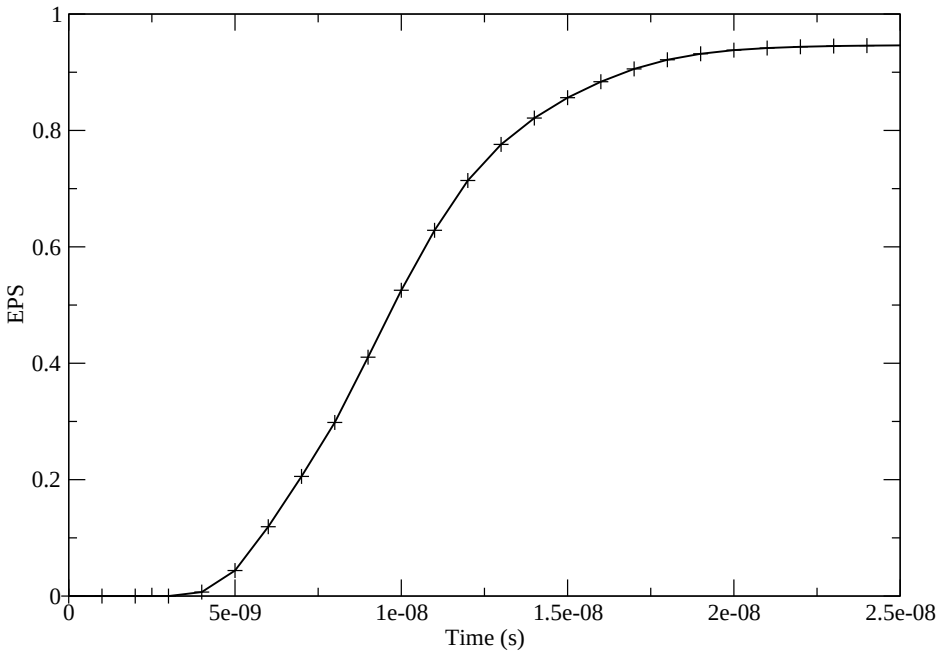

(b) Model G, EPS evolution in high EPS material jet region.

Figure B.47: Model G, evolution of temperature and EPS in material jet.

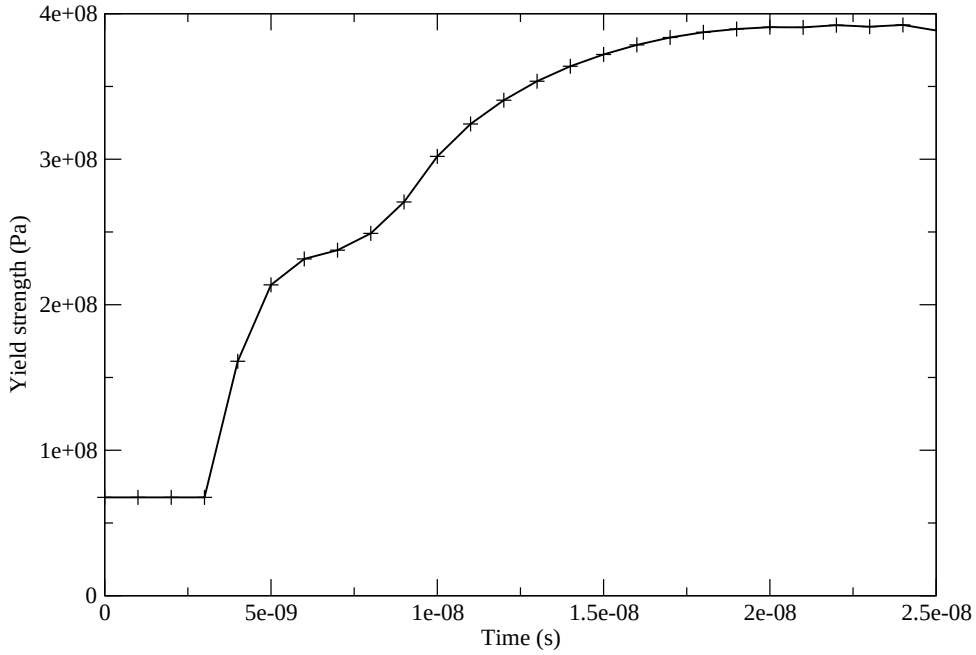

(a) Model G, yield strength evolution in high EPS material jet region.

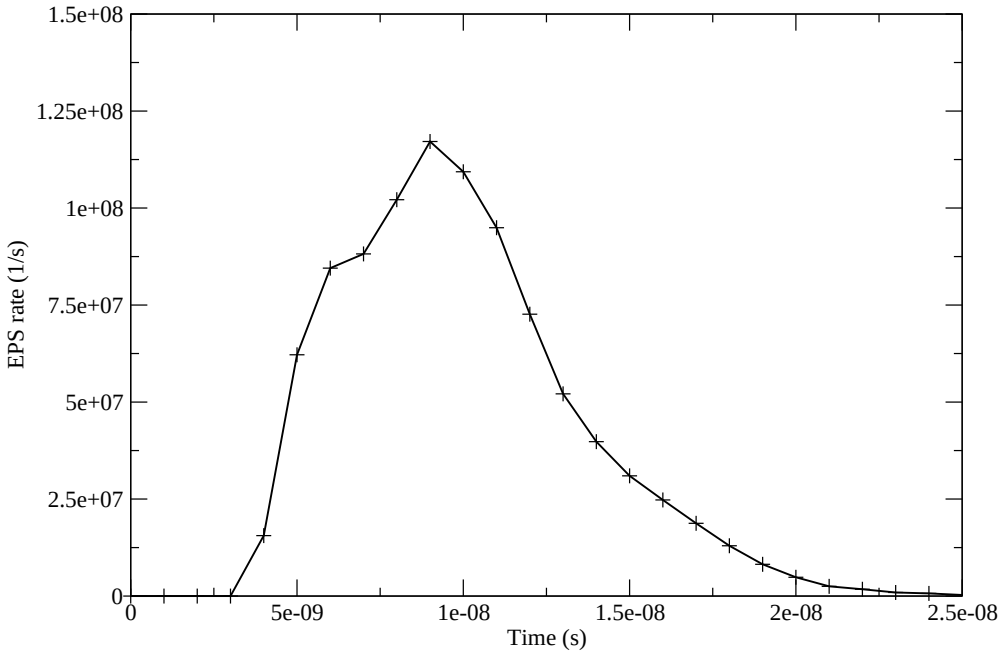

(b) Model G,EPS rate evolution in high EPS material jet region.

Figure B.48: Model G, evolution of yield strength and EPS rate in material jet.

B.2.5 Model H

The impact of a three-dimensional 10μm diameter conductive copper feedstock with an initial velocity and temperature of 600 m/s and 593 K on a copper substrate with initial temperature 298 K is now considered. Figure B.49 shows the flattening ratio and splat centre height of the feedstock during the impact. The splat morphology is considered to have reached a steady state when the variation of flattening ratio drops below 1% at 24 ns, where at this time the splat centre height shows a 0.168% variation. Final values of flattening ratio, splat centre height and P^* are given in Table B.7 and show a significant crater has been created increasing the contact area for bonding whilst the feedstock has flattened noticeably indicating a high level of EPS. The splat morphology shows a distinct lip feature at the edge of the feedstock from the early stages of the impact and this grows steadily as the impact progresses.

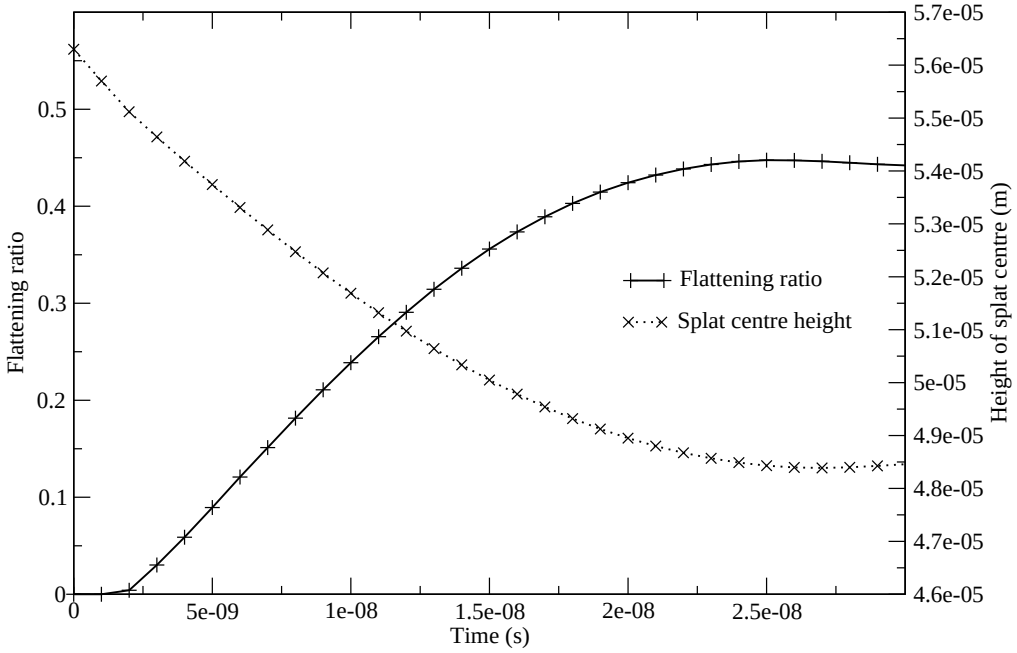

Figure B.49: Flattening ratio plot for a conductive feedstock at 593 K and 600 m/s.

The highest temperatures are found at the start of the impact and are located at the leading edge of the lip feature against the feedstock/substrate interface. Heating

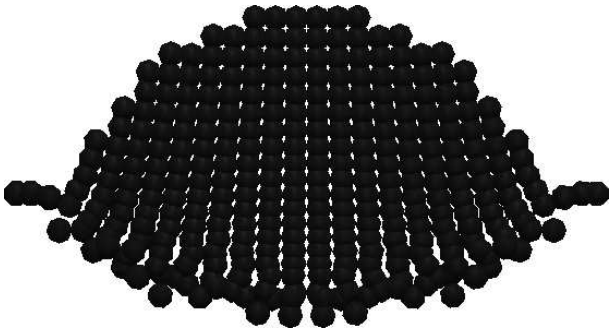

(a) 10 ns.

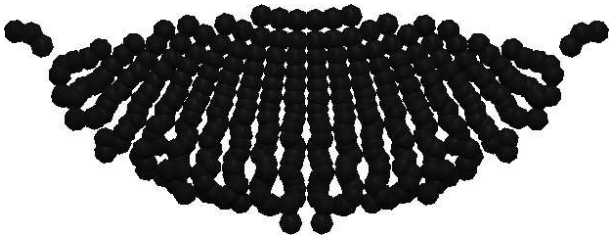

(b) 20 ns.

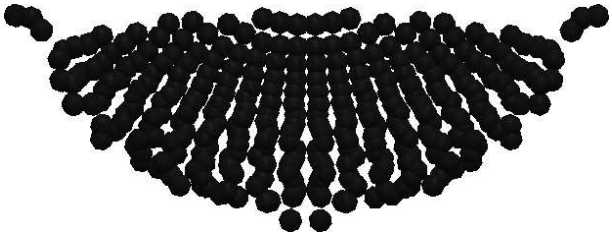

(c) 24 ns.

Figure B.50: Model H, cross section through centre of 3-D splat morphology.

Flattening ratio	0.446
Splat centre height (μm)	48.49
P^*	0.7812

Table B.7: Model H flattening ratio, P^* and splat centre height data at 24 ns.

against this interface is not uniform with the splat bottom centre experiencing less heating than the lip. As the impact progresses heat is conducted away from the warm feedstock/substrate interface into the colder portions of the substrate and splat; this forms a colder layer of material at the interface and a warmer band of material is found in the splat body.

The yield strength profiles are shown in Figure B.52. The splat shows an overall dominance of material hardening which reaches its maximum value at the interface between the feedstock and substrate. The distribution of hardening along the interface is not even with the flanks increasing in yield strength the most whilst the splat bottom centre undergoes the least hardening. The splat body shows a mostly even hardening profile in comparison with the lowest levels found towards the splat top centre.

In the early stages of the impact the EPS is localised to the interface region with the most EPS found at the leading edge of the forming lip feature and the splat bottom centre showing the lowest EPS value across the whole interface (see Figure B.53). As the impact develops, more of the splat experiences significant plastic straining and so the localisation of EPS decreases.

The distribution of EPS rate within the feedstock is shown in Figure B.54, showing peak strain rates are found early on in the impact when velocities are at their highest. This high EPS rates are found at the leading edge of the forming lip feature and result in large zones of increased EPS rate stretching into the splat body. The EPS rate quickly reduces and the location of peak strain rate moves into a band across the centre of the splat body.

The evolution of temperature, yield strength, EPS and EPS rate in the high strain lip region is monitored and plotted in Figures B.55 and B.56. The EPS profiles show the expected smooth rise to its peak value in Figure B.55b. The temperature evolution (see Figure B.55a) shows a period of rapid heating from 2 to 4 ns which is followed by period

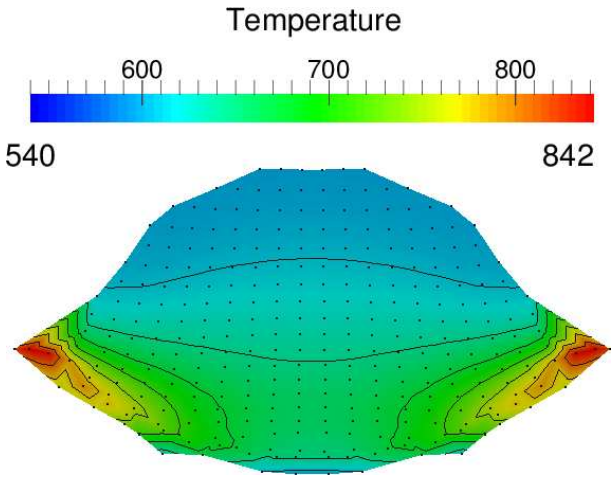

(a) 10 ns.

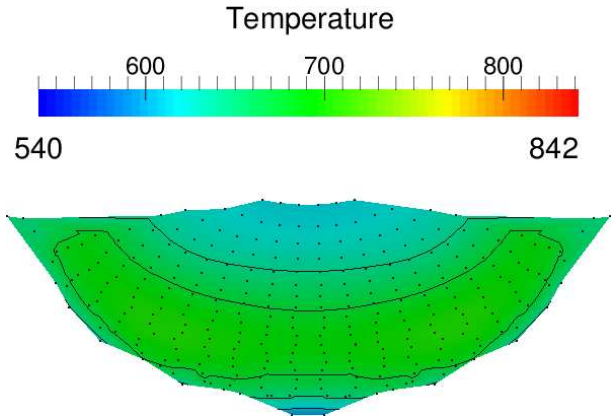

(b) 20 ns.

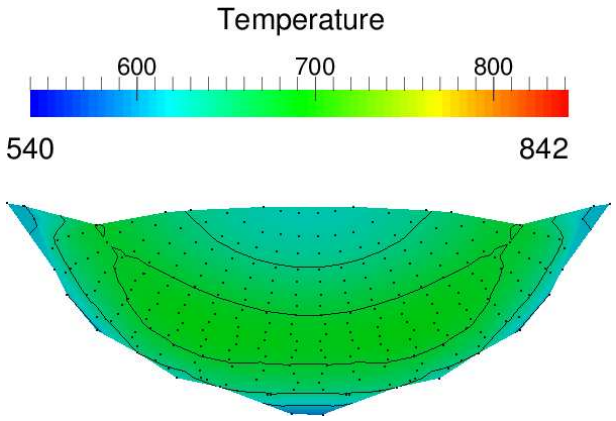

(c) 24 ns.

Figure B.51: Model H, temperature cross section through centre of 3-D splat morphology.

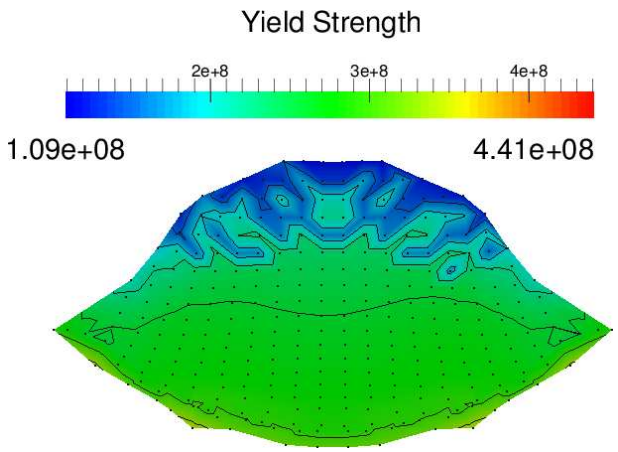

(a) 10 ns.

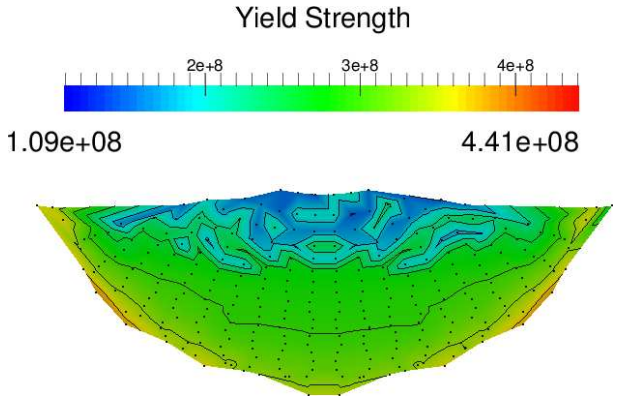

(b) 20 ns.

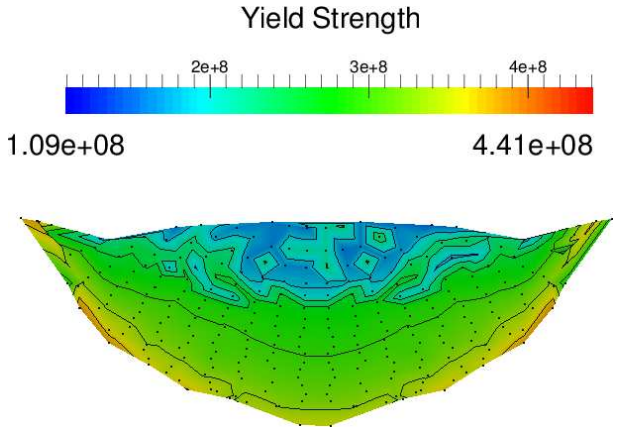

(c) 24 ns.

Figure B.52: Model H, yield strength cross section through centre of 3-D splat morphology.

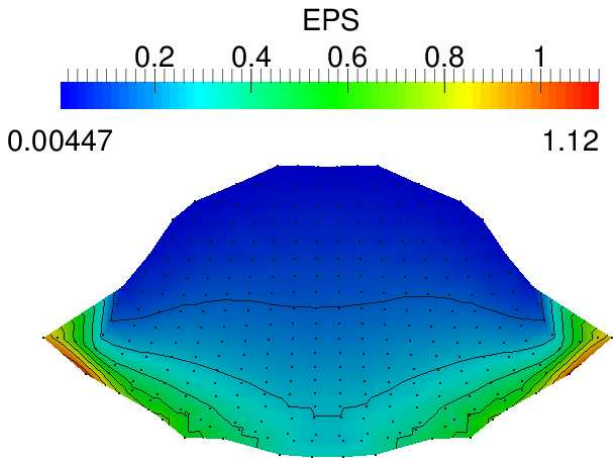

(a) 10 ns.

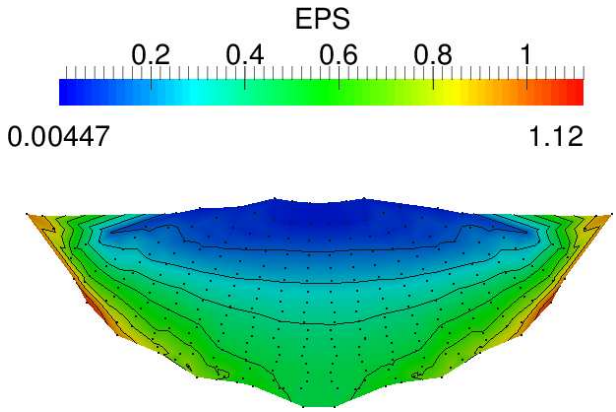

(b) 20 ns.

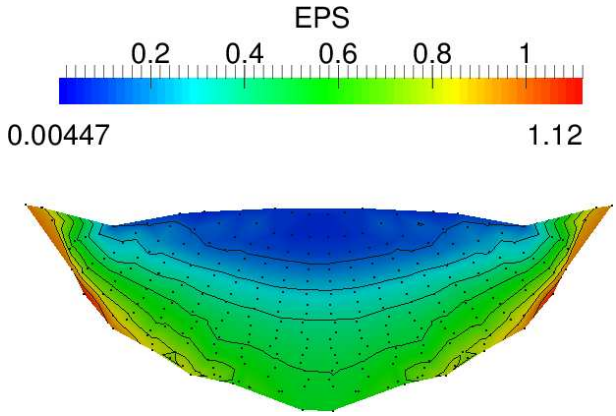

(c) 24 ns.

Figure B.53: Model H, EPS cross section through centre of 3-D splat morphology.

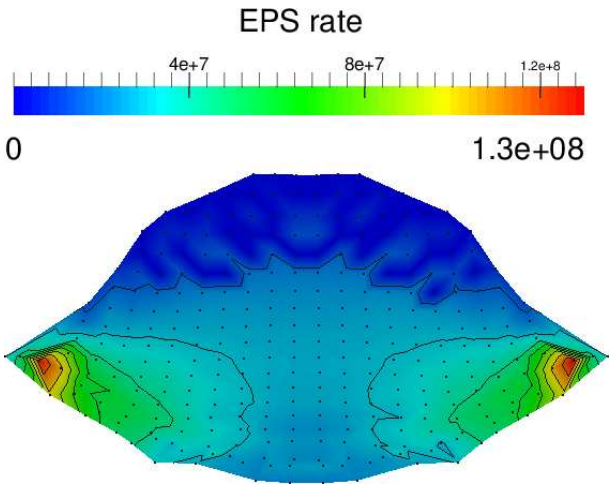

(a) 10 ns.

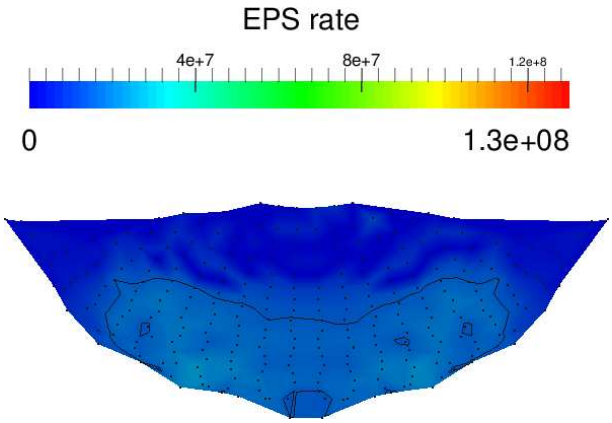

(b) 20 ns.

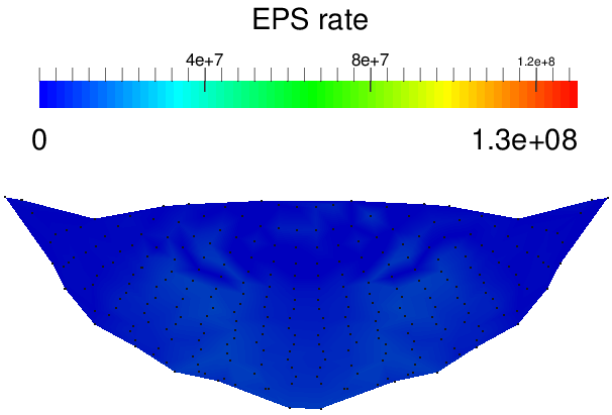

(c) 24 ns.

Figure B.54: Model H, EPS rate cross section through centre of 3-D splat morphology.

of cooling for the remainder of the time considered.

Over the course of the entire impact, there is a dominance of material hardening over thermal softening, as seen in Figure B.56a. There is however, a short period where thermal softening dominates in this region of the feedstock. This period of softening coincides with the highest experienced EPS rate (see Figure B.56b). The occurrence of this period of softened material and high EPS rates indicates the presence of a shear band instability. This instability is located on the flanks of the feedstock/substrate interface and is the area where material bonding has been experimentally observed. These observations indicate that the splat has bonded to the substrate material and this hypothesis is supported by the velocity at impact exceeding the experimentally derived critical velocity of copper (500 m/s).

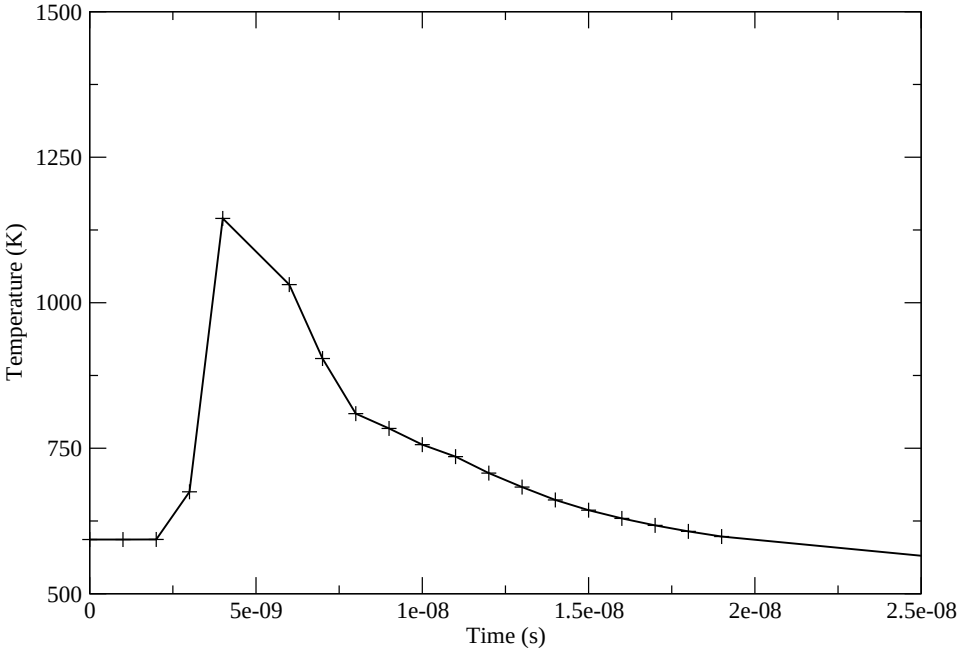

(a) Model H, temperature evolution in high EPS material jet region.

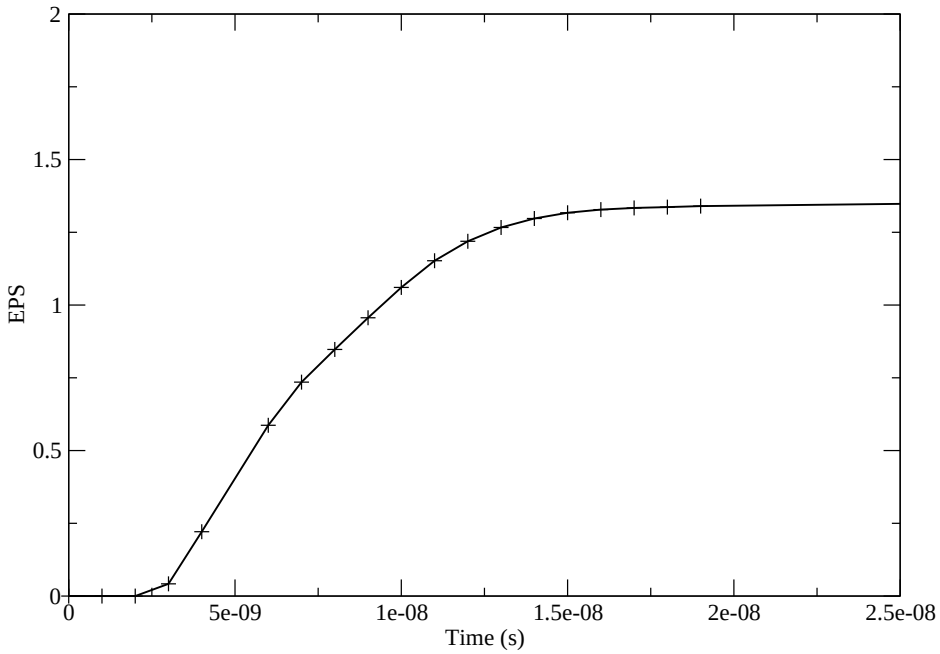

(b) Model H, EPS evolution in high EPS material jet region.

Figure B.55: Model H, evolution of temperature and EPS in material jet.

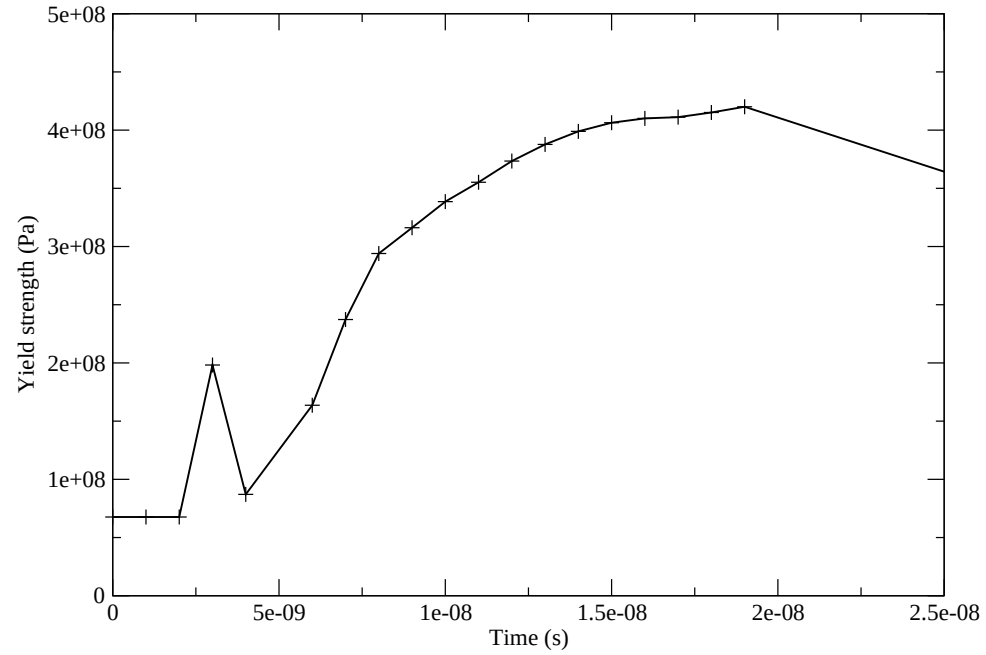

(a) Model H, yield strength evolution in high EPS material jet region.

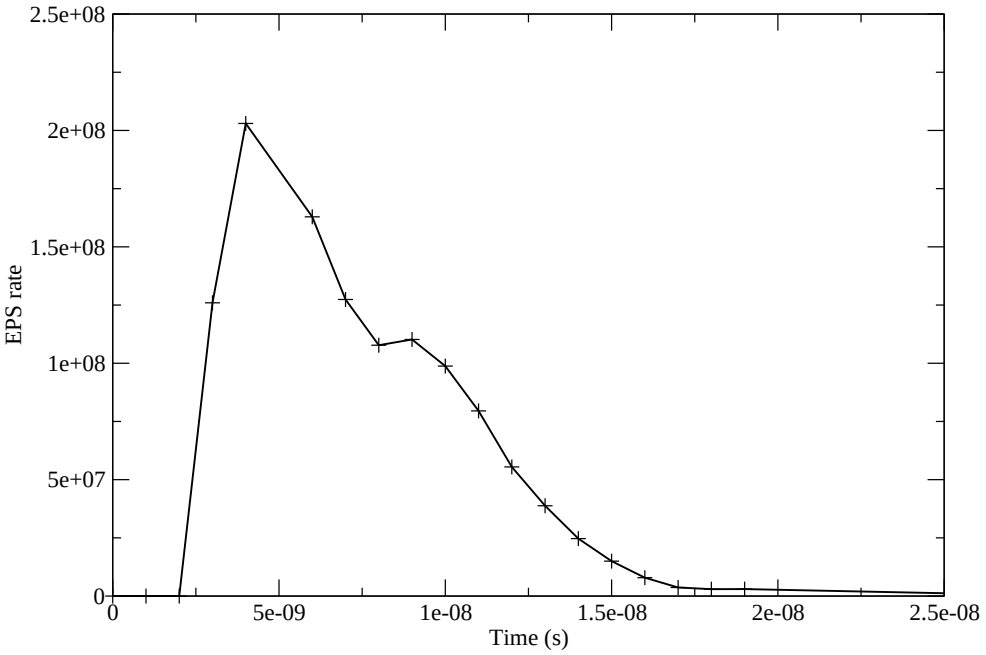

(b) Model H, EPS rate evolution in high EPS material jet region.

Figure B.56: Model H, evolution of yield strength and EPS rate in material jet.

B.3 Larger Conductive Feedstocks

B.3.1 Model I

The impact of a three-dimensional 20μm diameter conductive copper feedstock with initial velocity and temperature of 600 m/s and 298 K onto a copper substrate with initial temperature of 298 K is considered. The feedstock flattening ratio and centre height development is shown in Figure B.57 and shows the expected approach to steady values. The morphology is assumed to have reached a steady-state when the variation in flattening ratio drops below 1% at 38 ns and at this time the variation in splat centre height is 0.22%. Final values of flattening ratio, splat centre height and P^* are given in Table B.8. A low level of flattening is seen with the final splat remaining at 63% of its initial diameter, producing a deep crater and therefore increasing the contact area between feedstock and substrate. The splat morphology shows a lip feature developing at the splat edge at 20 ns in Figure B.58 and this indicates material jetting in this region.

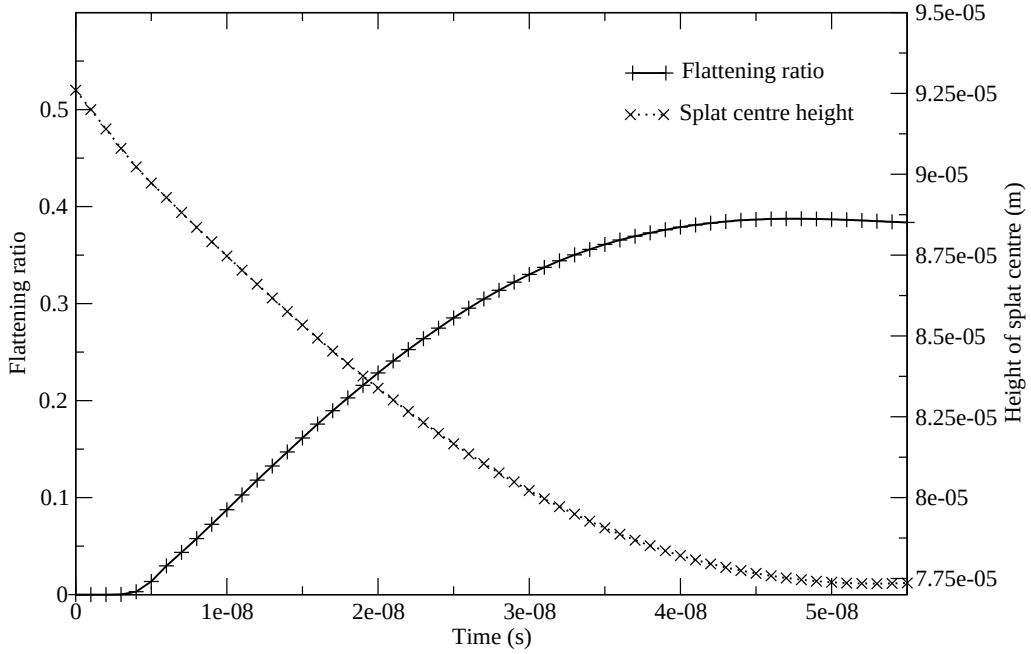

Figure B.57: Flattening ratio plot for a 20μm diameter conductive feedstock at 298 K and 600 m/s.

Flattening ratio	0.373
Splat centre height (μm)	78.5
P^*	0.704

Table B.8: Model I flattening ratio, P^* and splat centre height data at 38 ns.

The distribution of heating with the feedstock at several time instances during the impact are shown in Figure B.59. During the early stages of the impact, there is a strong localisation of heating at the feedstock/substrate interface. This heating is not uniform and higher temperatures are observed at flanks of the interface whilst the splat bottom centre shows lower heating. As the impact progresses, more of the splat is strained and heated in addition to heat being conducted out of the warm interface region into cooler parts of the feedstock and substrate, which leads to less localisation in the temperature contours.

The yield strength contours (see Figure B.60) show a dominance of hardening over softening thrughout the impact event. The flank regions that experience the highest strains show the highest levels of work hardening as expected.

The EPS distribution is shown in Figure B.61. In the early stages of the impact there is localisation at the interface and the expected non-uniform distribution along the interface with peak values found at the leading edge of the lip feature and lower strains seen at the splat bottom centre. As the splat flattens this localisation reduces as the previously unstrained material is affected by the impact. Despite this, the location of peak EPS remains at the flanks of the feedstock/substrate interface with the lowest observed EPS found at the splat top centre.

Figure B.62 shows the development of EPS rate over the course of the splat formation. Highest rates are seen in the early stages of the impact and are located near the leading edge of the forming lip feature with a zone of elevated EPS rate radiating into the splat body; these regions are subjected to the highest shear stress rates as they are push up and away from the bottom centre of the forming crater. There is a rapid reduction in EPS rate after peak values are reached with highest rates towards the end of the impact found in the splat body.

The evolution of temperature, EPS, EPS rate and yield strength in the region of

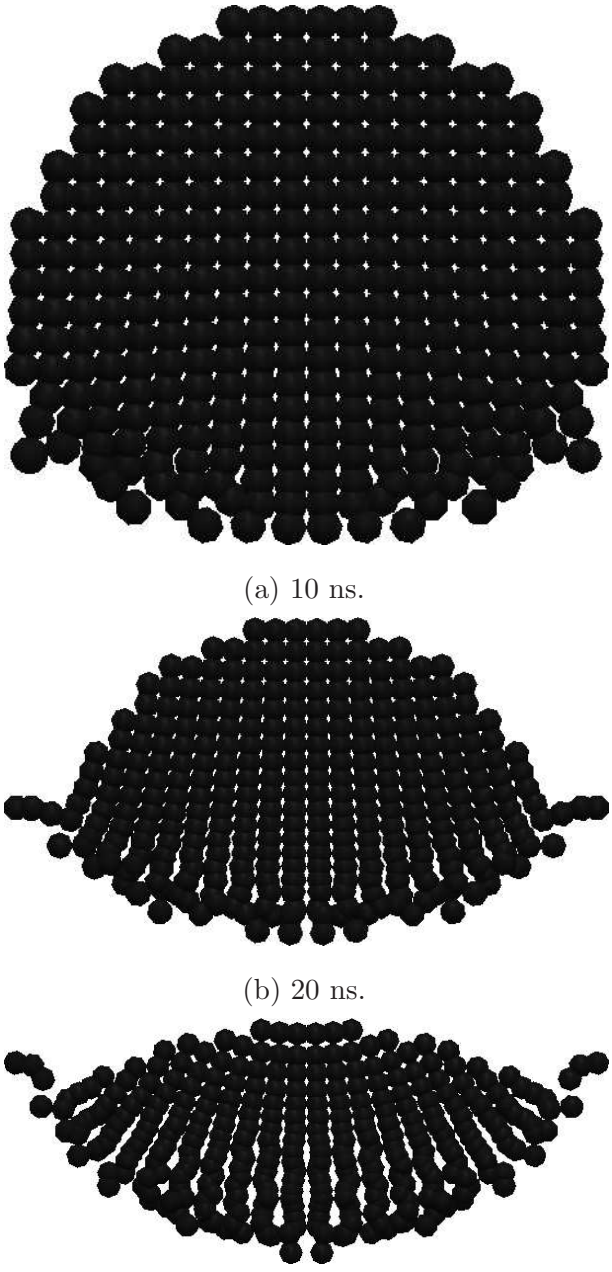

(a) 10 ns.

(b) 20 ns.

(c) 38 ns.

Figure B.58: Model I, cross section through centre of 3-D splat morphology.

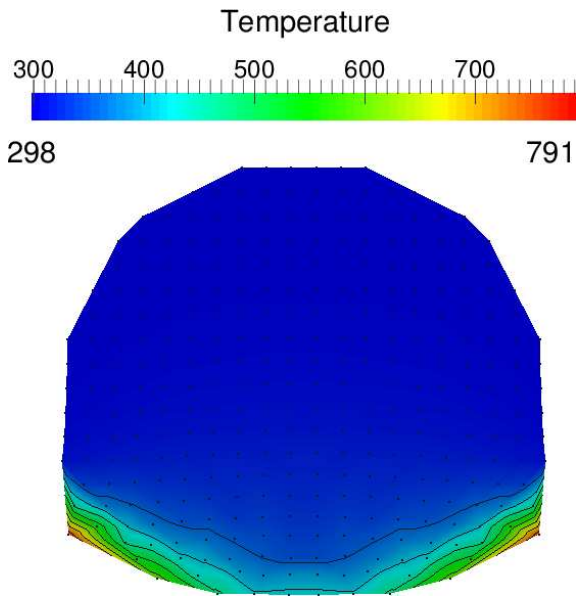

(a) 10 ns.

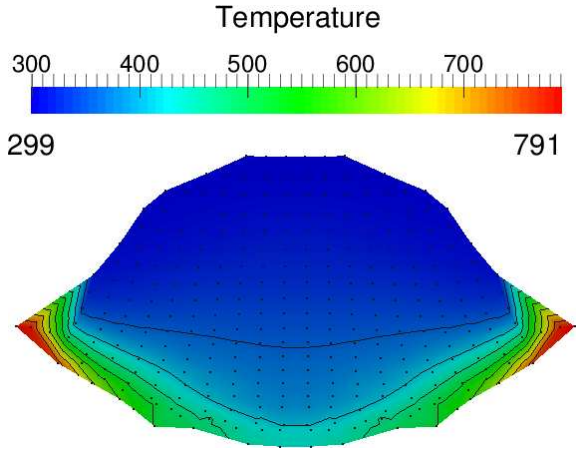

(b) 20 ns.

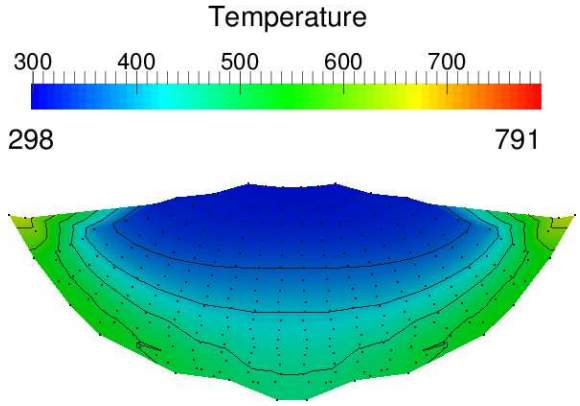

(c) 38 ns.

Figure B.59: Model I, temperature cross section through centre of 3-D splat morphology.

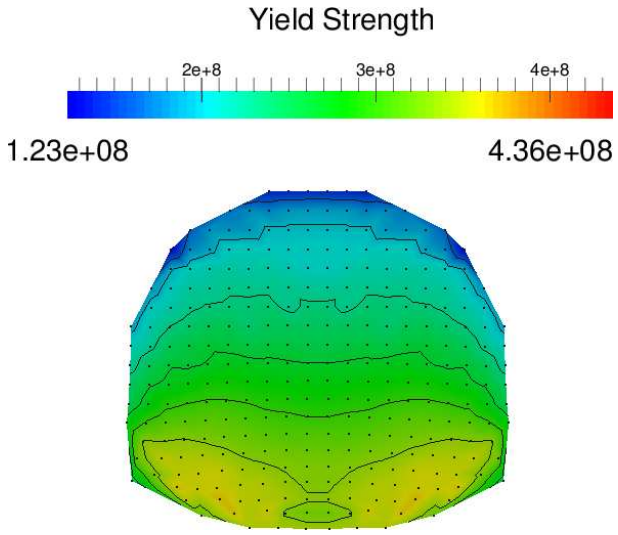

(a) 10 ns.

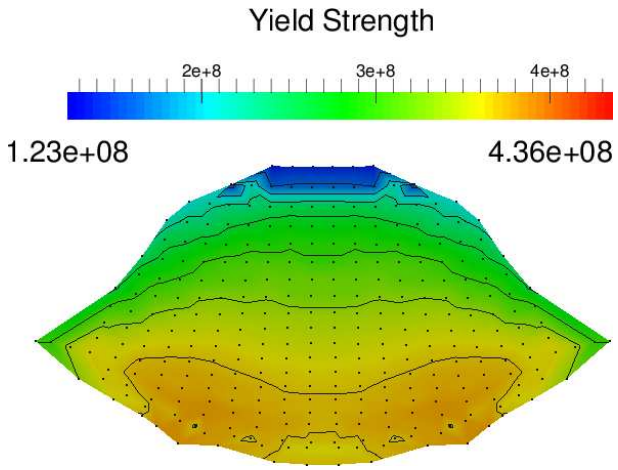

(b) 20 ns.

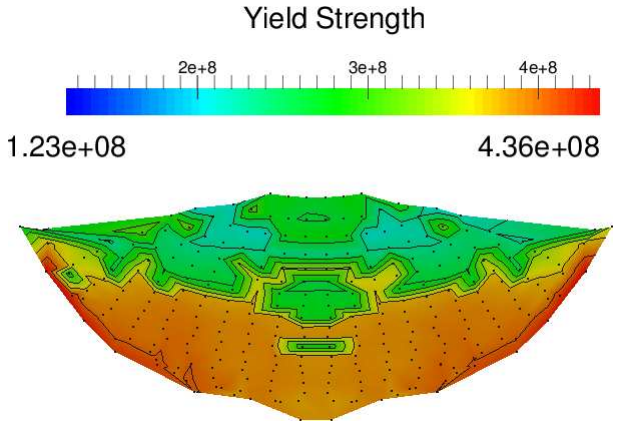

(c) 38 ns.

Figure B.60: Model I, yield strength cross section through centre of 3-D splat morphology.

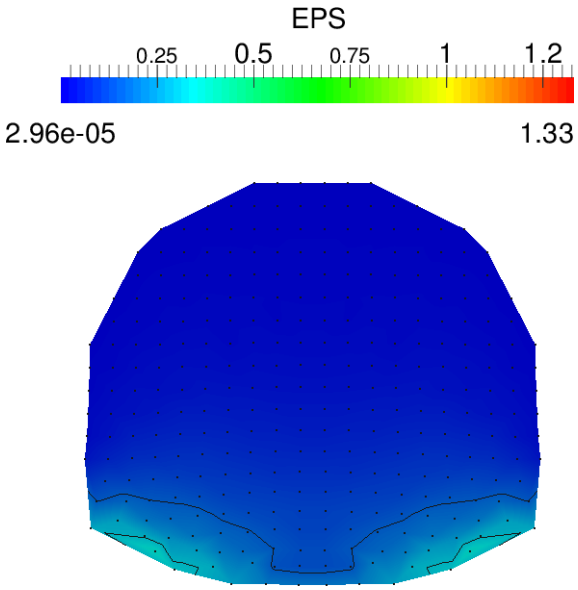

(a) 10 ns.

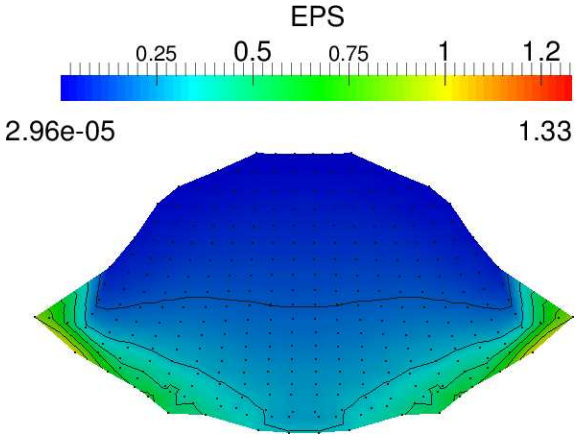

(b) 20 ns.

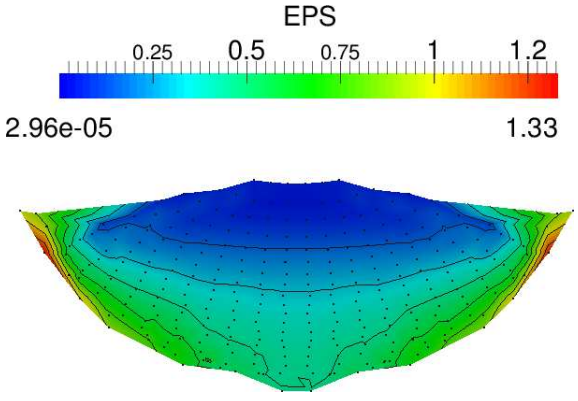

(c) 38 ns.

Figure B.61: Model I, EPS cross section through centre of 3-D splat morphology.

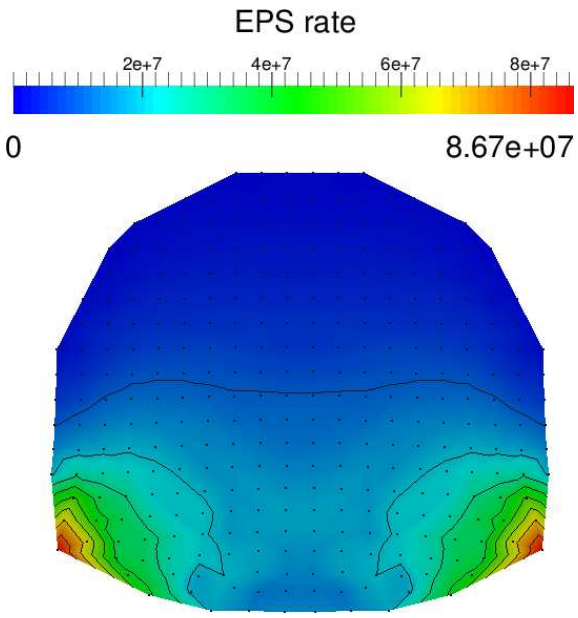

(a) 10 ns.

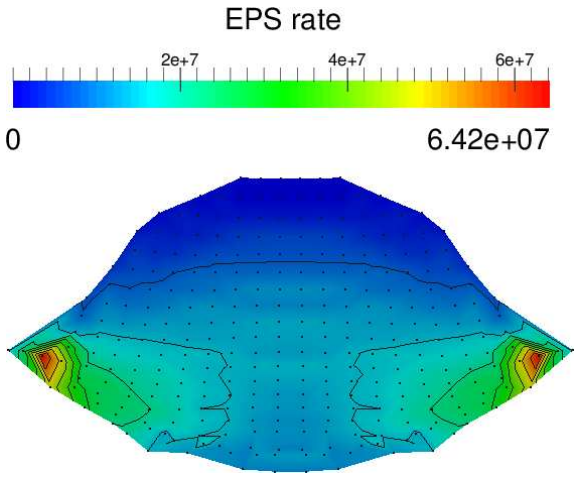

(b) 20 ns.

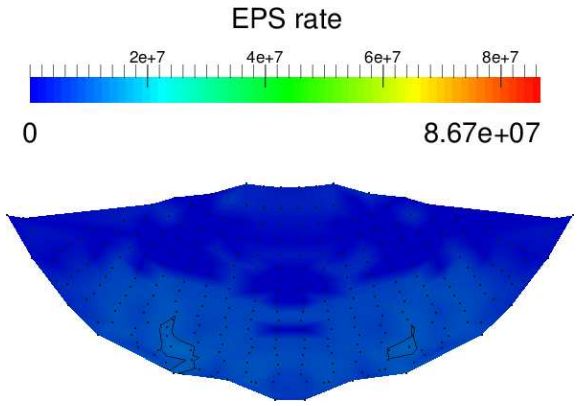

(c) 38 ns.

Figure B.62: Model I, EPS rate cross section through centre of 3-D splat morphology.

the lip that experiences the highest total EPS has been monitored throughout the splat formation and the evolution of these properties is shown in Figures B.63 and B.64. The EPS profiles show the expected rise towards a steady peak value in Figure B.63b. The temperature profile shows a period of rapid heating in the early stages of the impact before a more gradual cooling for the remainder of the time considered.

The yield strength profile (see Figure B.64a) shows an overall dominance of material hardening with the only exception being a brief period of localised thermal softening in the early stages of the impact. This period of weakened material coincides with a period of heightened EPS rate and indicates the existence of a shear band instability that is causing significant material jetting.

With the presence of a shear band instability causing material jetting it is highly possible this feedstock has bonded to the substrate.

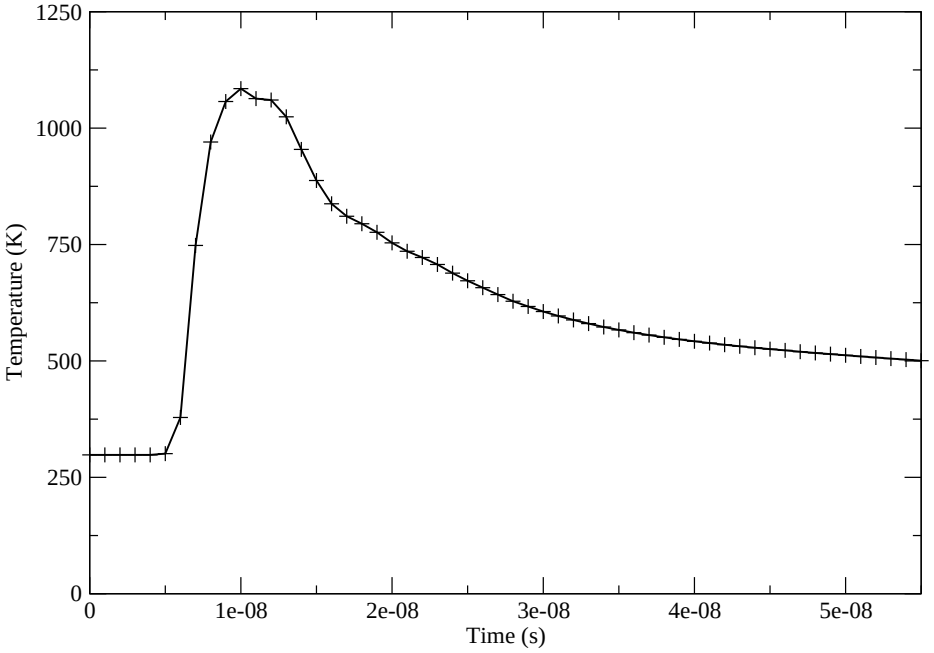

(a) Model I, temperature evolution in high EPS material jet region.

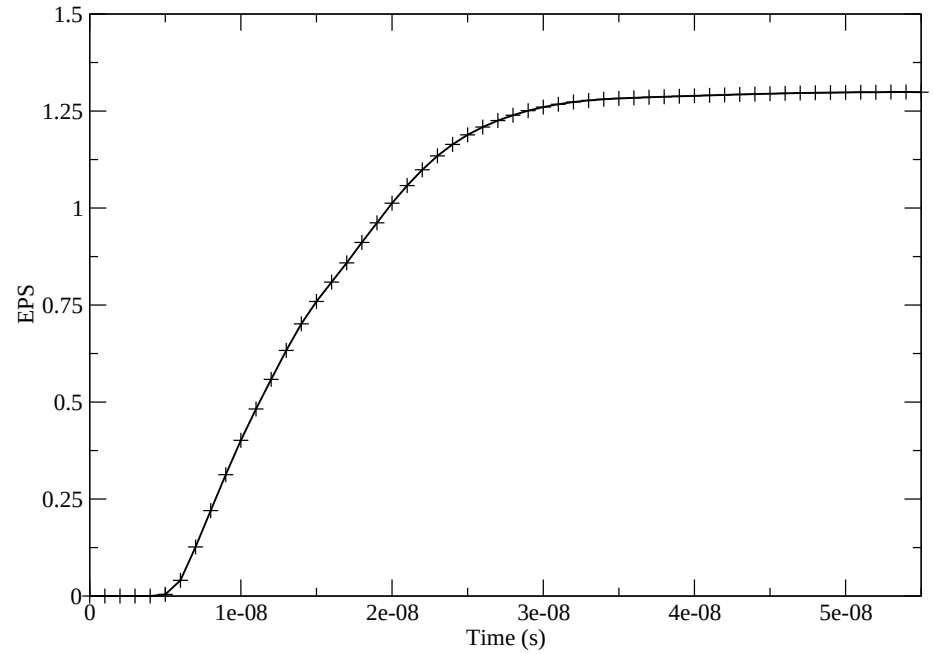

(b) Model I, EPS evolution in high EPS material jet region.

Figure B.63: Model I, evolution of temperature and EPS in material jet.

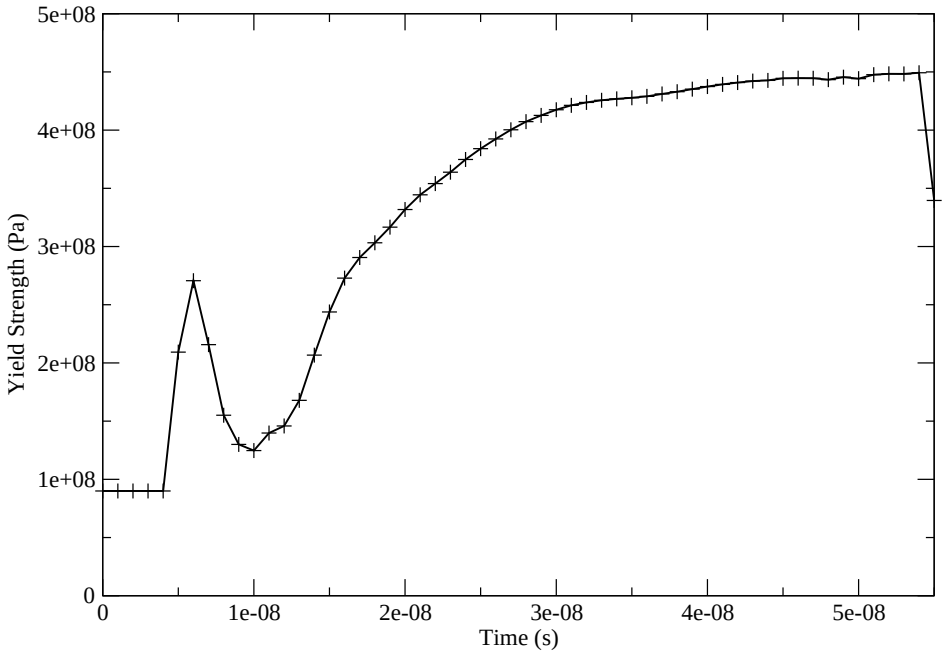

(a) Model I, yield strength evolution in high EPS material jet region.

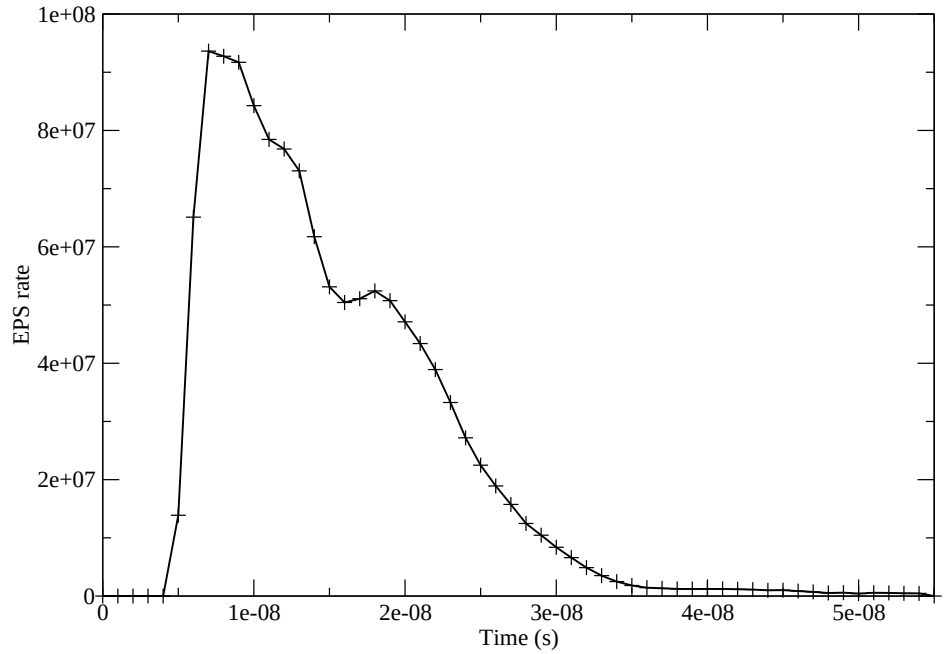

(b) Model I, EPS rate evolution in high EPS material jet region.

Figure B.64: Model I, evolution of yield strength and EPS rate in material jet.

B.3.2 Model J

The impact of a 20μm diameter heat conductive copper feedstock with initial velocity of 600 m/s and temperature 593 K against a heat conductive copper substrate with initial temperature 298 K is considered. The evolution of splat flattening ratio and the height of the splat centre is shown in Figure B.65, an increase towards a steady value of flattening ratio of 0.409 is observed. The splat reaches its final penetration depth into the substrate at 40 ns and at this time the variation in splat centre height is less than 0.21%. The final values of flattening ratio, splat centre height and P^* are given in Table B.9, where the splat has flattened by 41% whilst penetrating the substrate to a depth of 73% of its initial diameter.

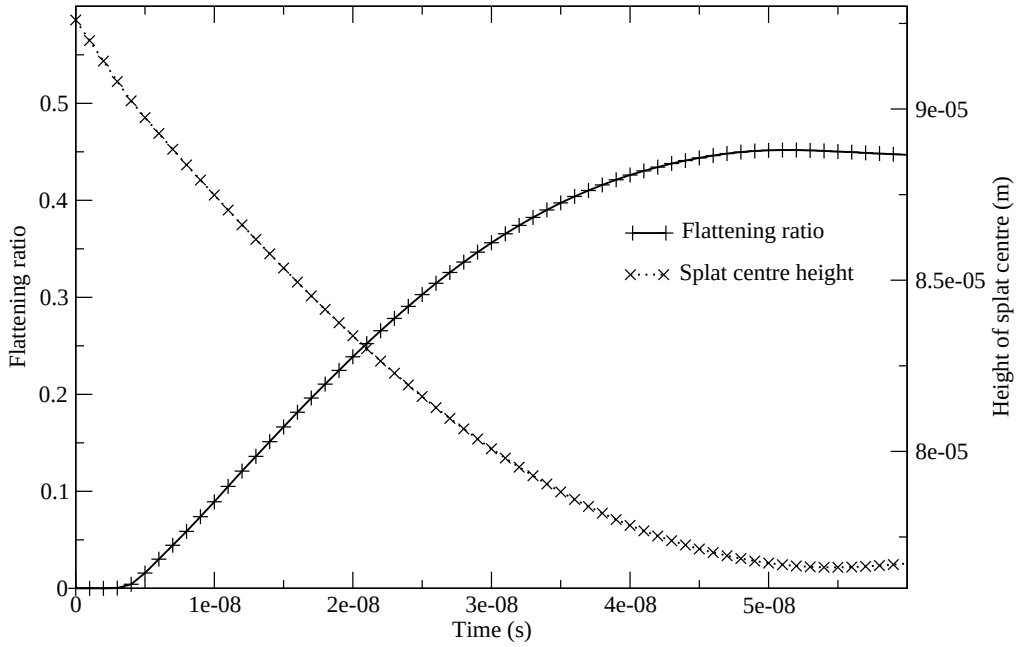

Figure B.65: Flattening ratio plot for a 20μm diameter conductive feedstock at 593 K and 600 m/s.

The deformation and flattening of the splat can be seen in the morphologies shown in Figure B.66 where the position of the SPH particles are shown. A distinct lip of material can be seen in the morphologies at the outer edges of the splat, indicating a shear band

Flattening ratio	0.409
Splat centre height (μm)	78
P^*	0.73

Table B.9: Model J flattening ratio, P^* and splat centre height data at 40 ns.

instability has formed during the impact.

Peak temperatures are seen in the early stages of the impact (see Figure B.67) and are located at the leading edge of the forming lip feature, the peak heating approaches but does not exceed the material melting temperature of 1356 K. Conduction of heat from the hotter feedstock into the substrate becomes significant after the initial stages of impact and this produces a cooler layer of material at the feedstock/substrate interface; this results in the hottest region of the splat forming a band across the middle of the splat body. This pattern of heating is reflected in the yield strength profiles (see Figure B.67), where weaker material is found in the high temperature region at the leading edge of the lip feature in the initial impact stages but as the interface cools, material hardening becomes significant. By the end of the impact, the hardest material is seen at the interface between feedstock and substrate. The rate of EPS peaks early on in the impact and shows strong localisation to the tip of the forming lip feature (see Figure B.70), the rate of EPS quickly reduces as the impact progresses with peak values found along the feedstock/substrate interface. The whole splat undergoes plastic strains to some extent (see Figure B.69), however peak values are restricted to the flanks of the interface region.

The presence of a distinct lip feature indicates the existence of a shear band instability; in order to confirm this, the evolution of temperature, EPS, EPS rate and yield strength at the flanks of the feedstock/substrate interface are monitored and the results are presented in Figures B.71 and B.72. The EPS profiles show a rapid rise towards a peak value (see Figure B.71b). A rapid rise in temperature can be seen from 4 ns with peak values reached at 10 ns (see Figure B.71a). This is followed by gradual cooling for the remainder of the time considered. This sharp spike in heating is matched by a period significant thermal softening (see Figure B.72a), where the peak of softening is reached at the same time as the peak heating and as the material cools, hardening becomes progressively more

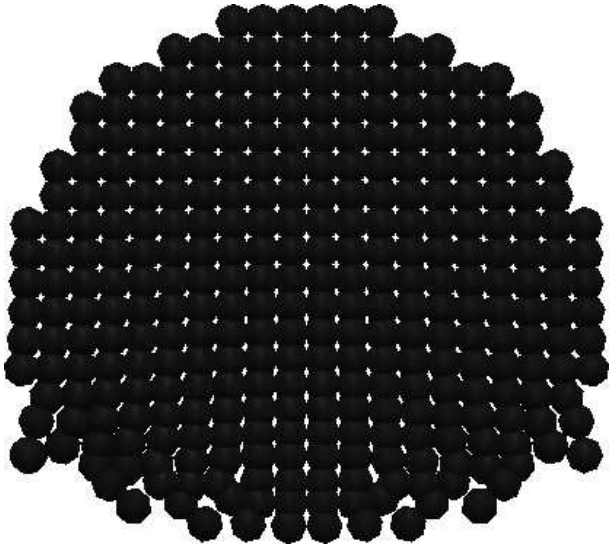

(a) 10 ns.

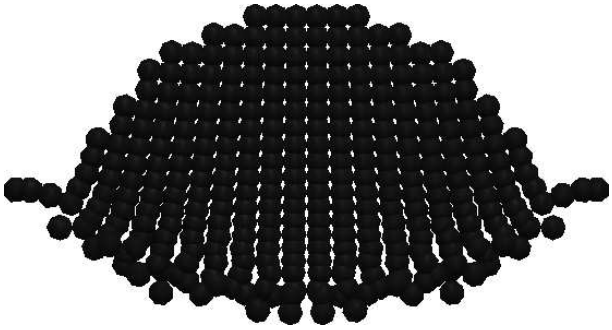

(b) 20 ns.

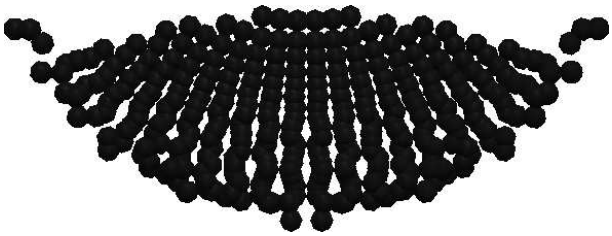

(c) 40 ns.

Figure B.66: Model J, cross section through centre of 3-D splat morphology.

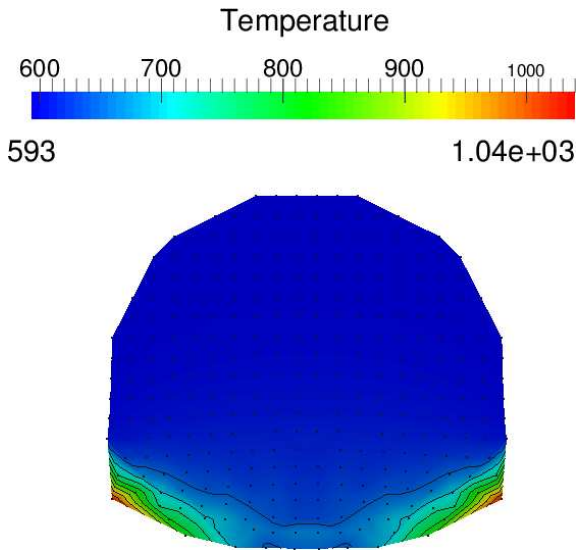

(a) 10 ns.

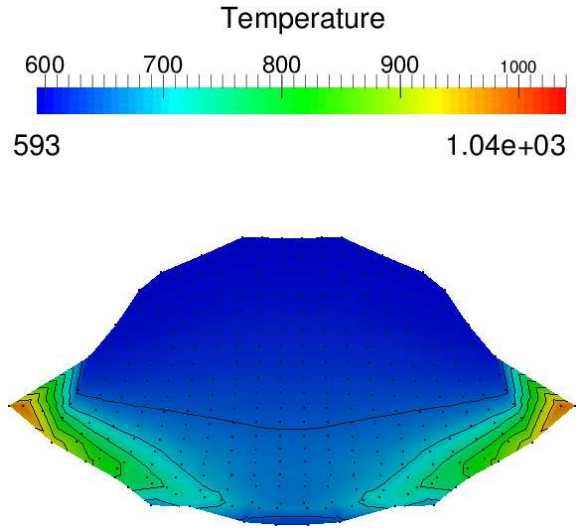

(b) 20 ns.

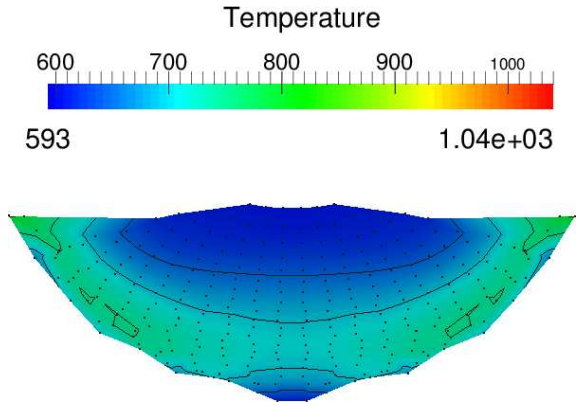

(c) 40 ns.

Figure B.67: Model J, temperature cross section through centre of 3-D splat morphology.

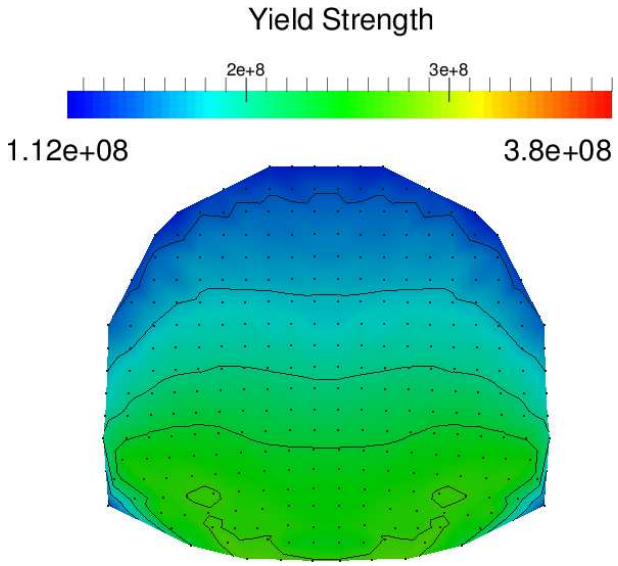

(a) 10 ns.

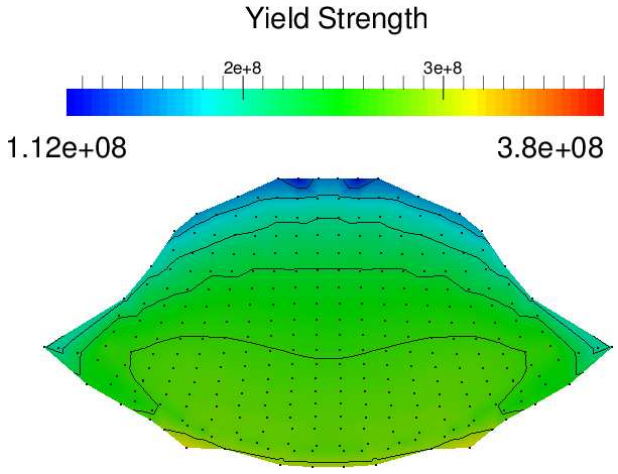

(b) 20 ns.

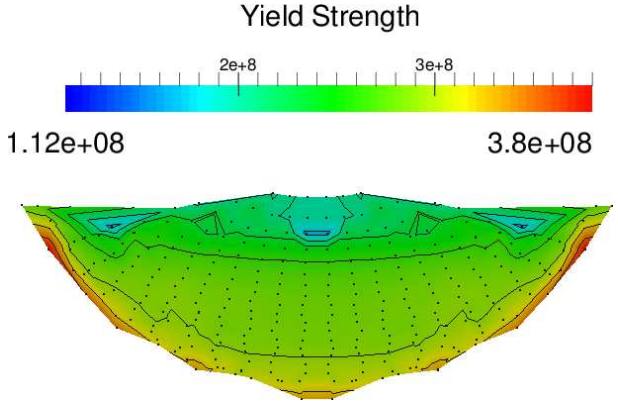

(c) 40 ns.

Figure B.68: Model J, yield strength cross section through centre of 3-D splat morphology.

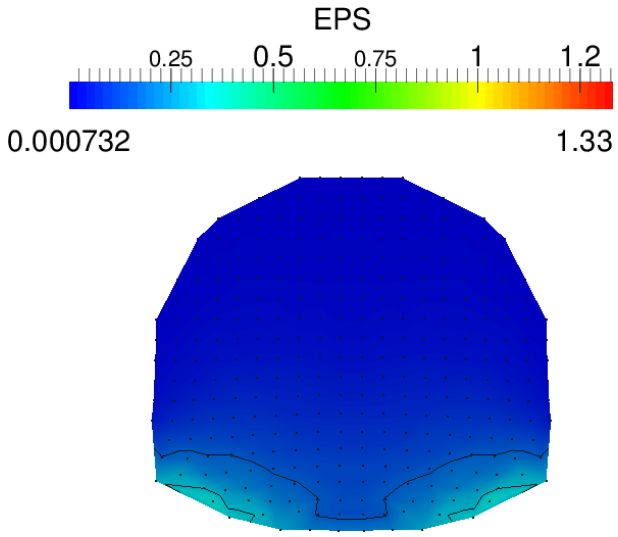

(a) 10 ns.

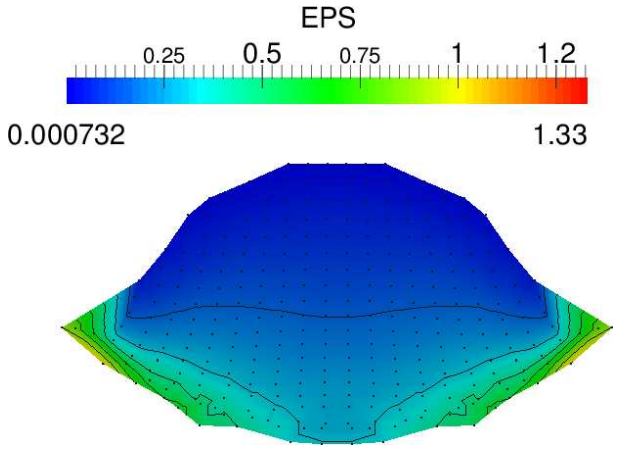

(b) 20 ns.

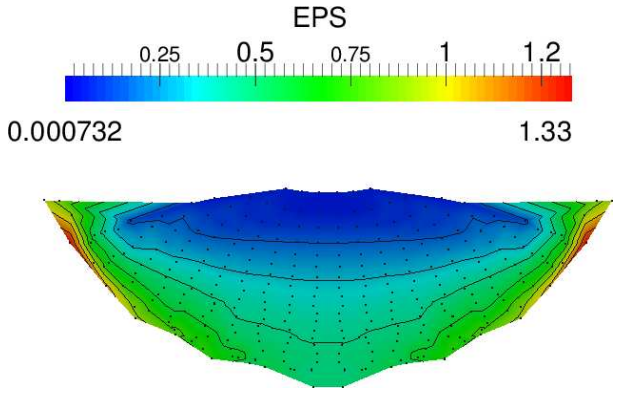

(c) 40 ns.

Figure B.69: Model J, EPS cross section through centre of 3-D splat morphology.

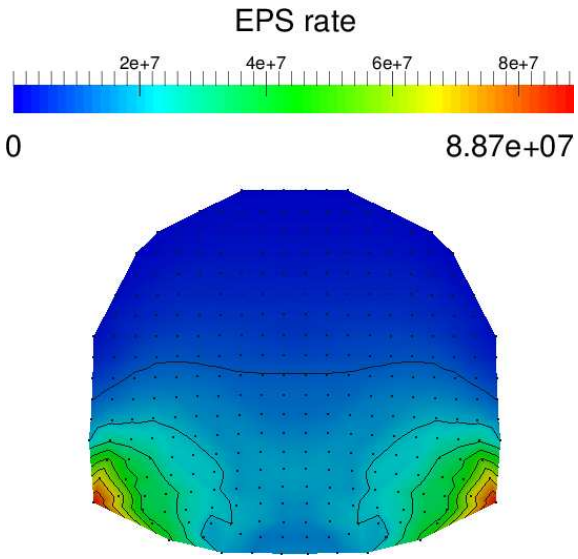

(a) 10 ns.

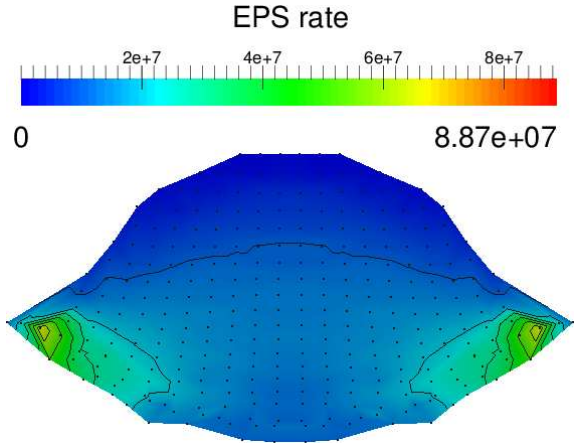

(b) 20 ns.

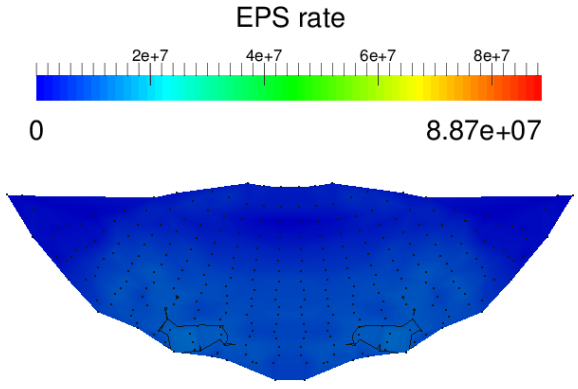

(c) 40 ns.

Figure B.70: Model J, EPS rate cross section through centre of 3-D splat morphology.

significant. Peak temperatures and thermal softening coincide with the period of highest EPS rate (see Figure B.72b), the simultaneous formation of all three of these features indicates that a shear band instability has indeed formed and that the splat has bonded to the substrate.

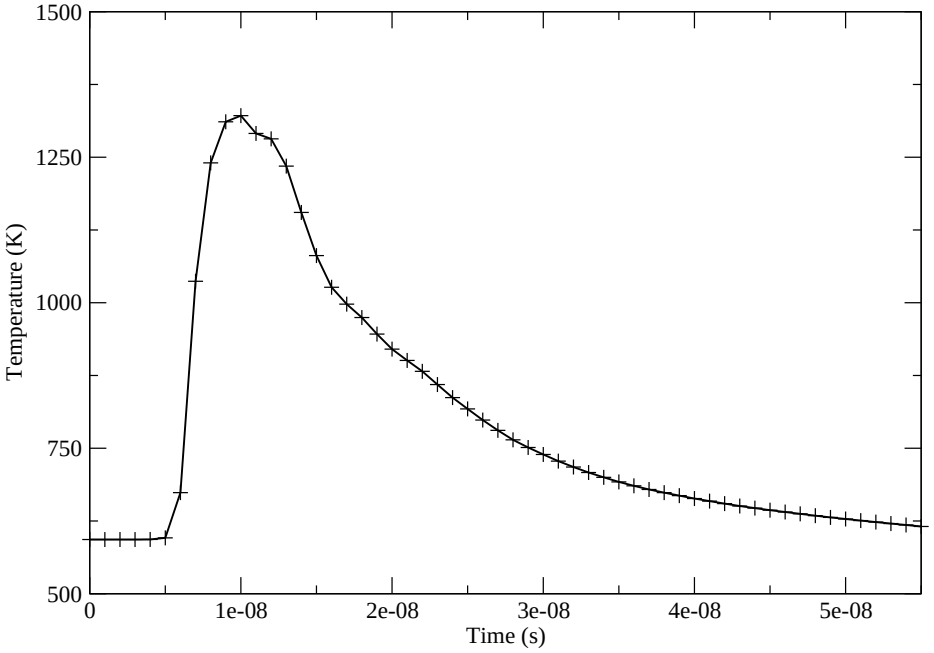

(a) Model J, temperature evolution in high EPS material jet region.

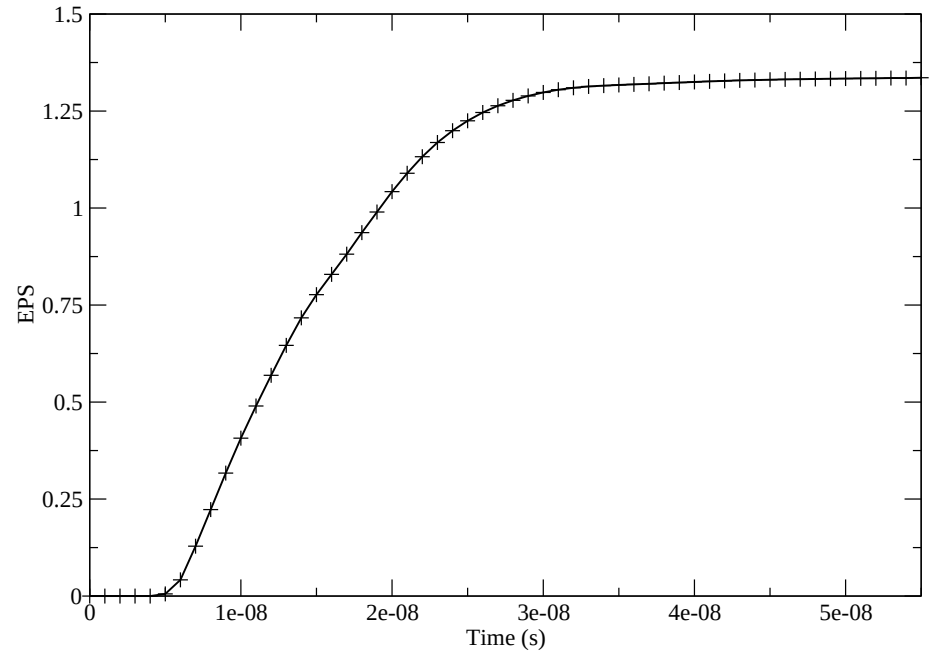

(b) Model J, EPS evolution in high EPS material jet region.

Figure B.71: Model J, evolution of temperature and EPS in material jet.

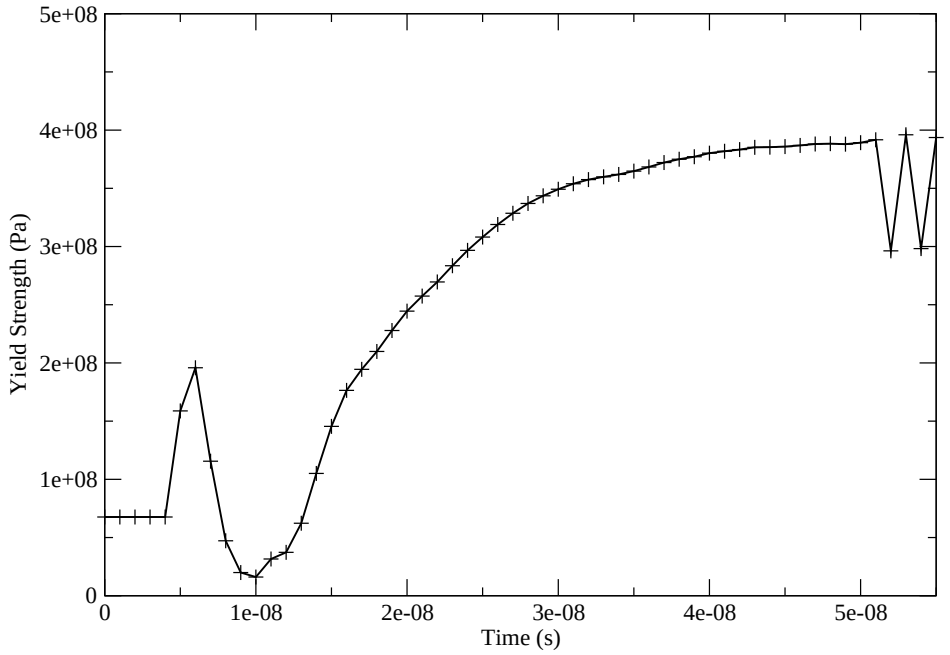

(a) Model J, yield strength evolution in high EPS material jet region.

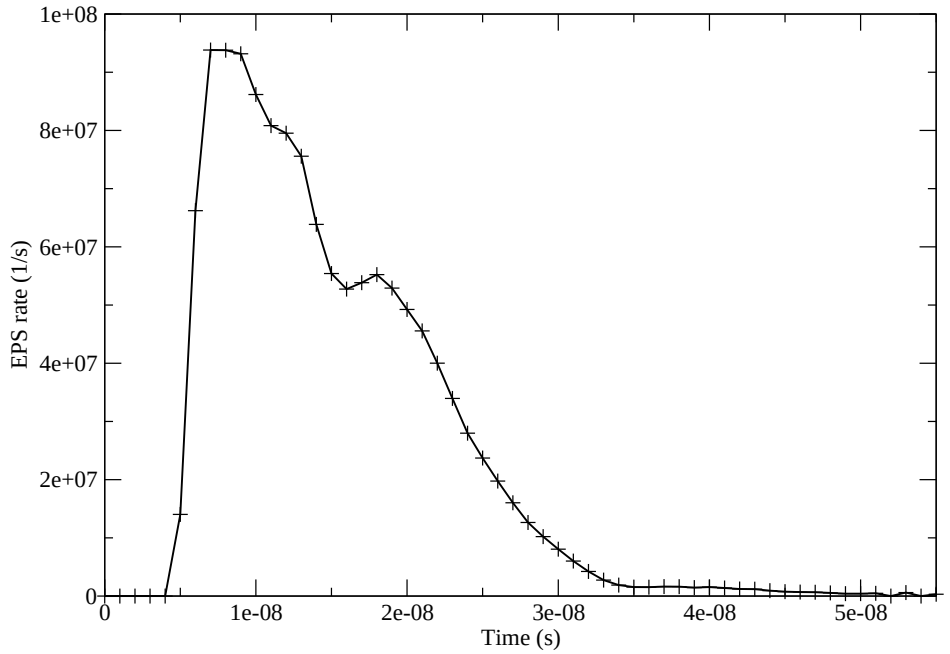

(b) Model J, EPS rate evolution in high EPS material jet region.

Figure B.72: Model J, evolution of yield strength and EPS rate in material jet.

B.4 Smaller Conductive Feedstocks

B.4.1 Model K

The impact of a small 2μm diameter heat conductive copper feedstock with initial velocity and temperature of 600 m/s and 298 K, respectively is considered against a heat conductive copper substrate with initial temperature 298 K. The evolution of flattening ratio and splat centre height is shown in Figure B.73. The flattening ratio increased to its peak value of 0.384 in 3.8 ns at which point the time dependant variation in this property drops below 1% and the variation in splat centre height is negligible while a peak normalised penetration into the substrate (P^*) of 0.703 is obtained at this time. The final values of flattening ratio, splat centre height and P^* are given in Table B.10. The final splat morpholgy shows reasonable flattening and a deep penetration into the substrate indicating large plastic deformations and a good sized interfacial contact area promoting bond formation.

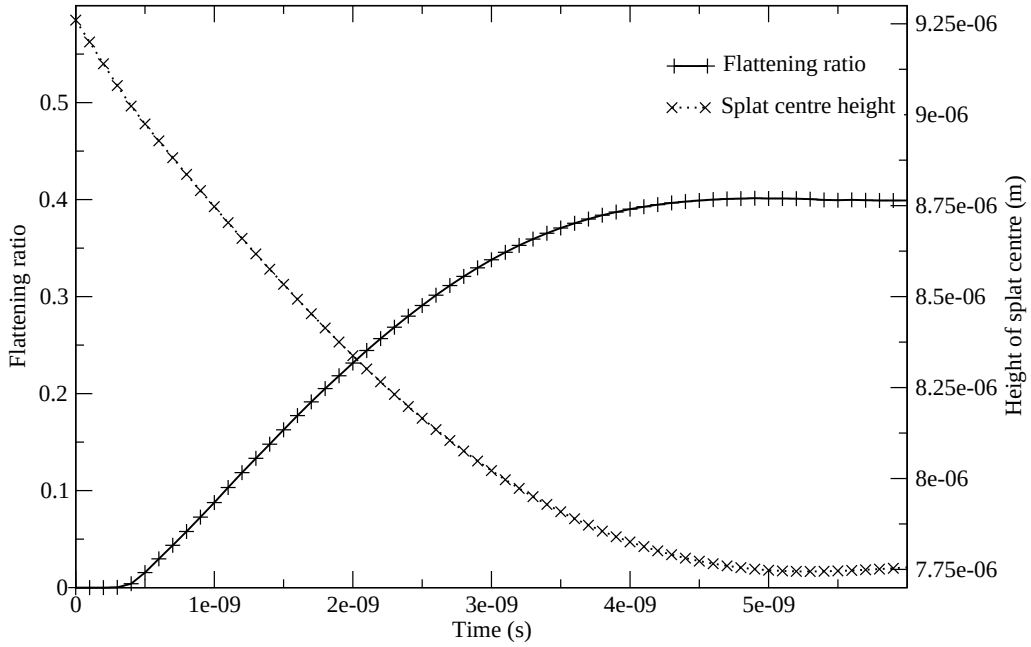

Figure B.73: Flattening ratio plot for a 2μm diameter conductive feedstock at 298 K and 600 m/s.

Flattening ratio	0.384
Splat centre height (μm)	7.855
P^*	0.703

Table B.10: Model K flattening ratio, P^* and splat centre height data at 3.8 ns.

The splat morphology shows a lip of material protruding from the splat edge. This lip indicates that a shear band instability may have formed during the impact enabling bonding between the feedstock and substrate. The temperature profiles (see Figure B.75) show that in the early stages of the impact the heating is localised at the leading edge of the forming lip feature. However, as the impact progresses this localisation decreases until the whole splat is at a nearly constant temperature. Peak temperatures remain well below the material melting temperature for the full duration of the impact event. Material hardening has been dominant across the whole splat (see Figure B.76), with peak hardening seen at the flanks of the feedstock/substrate interface. Peak rates of EPS are found early on in the impact and are located at the leading edge of the forming lip feature. These rates of EPS diminish rapidly from their peak values as the impact progresses (see Figure B.77). It is seen that the whole feedstock has been subjected to some level of plastic strains although the flanks of the feedstock/substrate interface shows the highest total EPS.

The evolution of temperature, EPS, EPS rate and yield strength in the feedstock/substrate interface flanks have been monitored and the results are presented in Figures B.79 and B.80. There is a sharp increase in temperature at 0.5 ns (see Figure B.71a) with peak temperature reached at 1.1 ns. This is followed by cooling for the remainder of the impact. The increase in heating is matched by a rapid rise in EPS rate at 0.5 ns which reaches a peak at 0.8 ns before declining as the impact progresses (see Figure B.72b). Despite the sharp rise in temperature, the yield strength profile shows no significant thermal softening at any point and peak heating has only increased by 200 K from intial values with high EPS rates at this period of heating maintaining the dominance of strain and strain rate hardening over thermal softening. If a shear band instability were present, significant softening of the material would have been expected as the temperature increase and subsequent material softening initiates a positive feedback loop further increases the

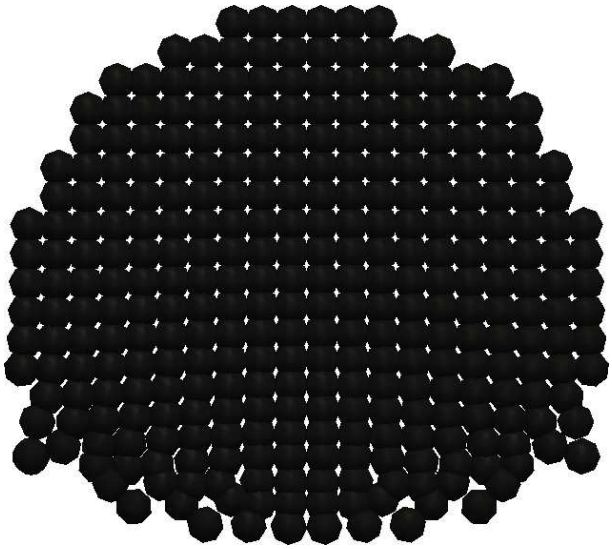

(a) 1 ns.

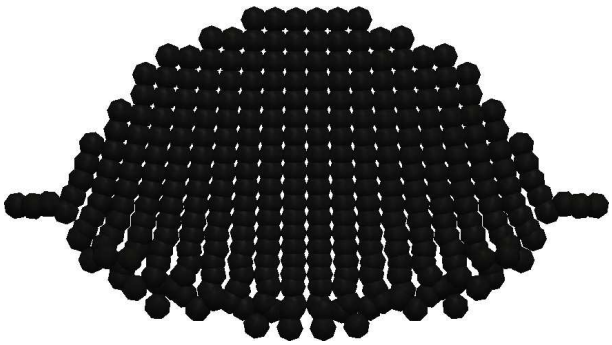

(b) 2 ns.

(c) 3.8 ns.

Figure B.74: Model K, cross section through centre of 3-D splat morphology.

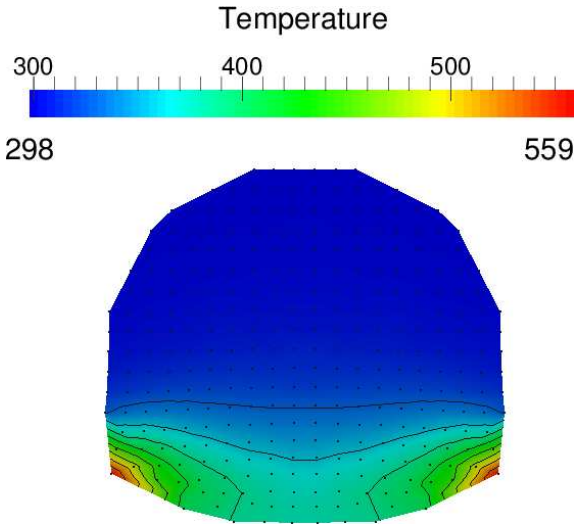

(a) 1 ns.

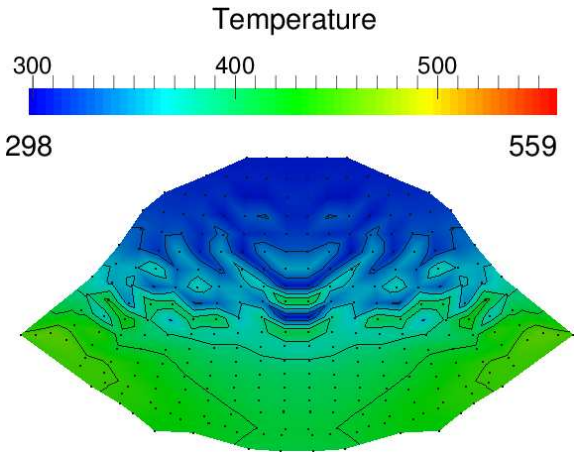

(b) 2 ns.

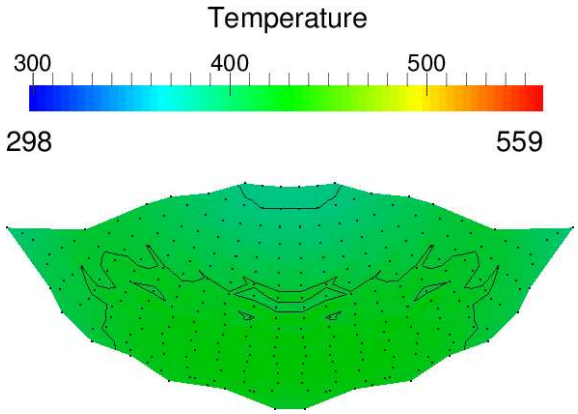

(c) 3.8 ns.

Figure B.75: Model K, temperature cross section through centre of 3-D splat morphology.

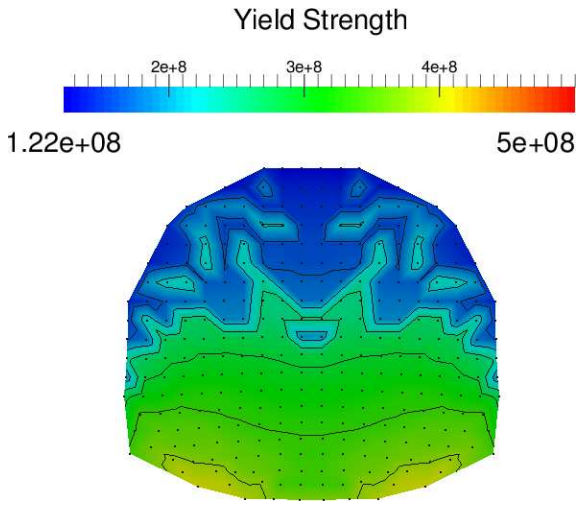

(a) 1 ns.

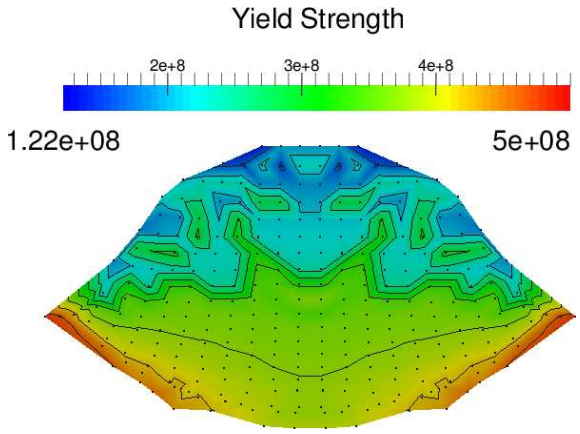

(b) 2 ns.

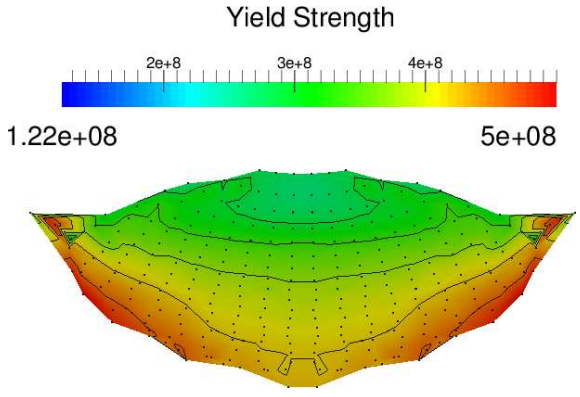

(c) 3.8 ns.

Figure B.76: Model K, yield strength cross section through centre of 3-D splat morphology.

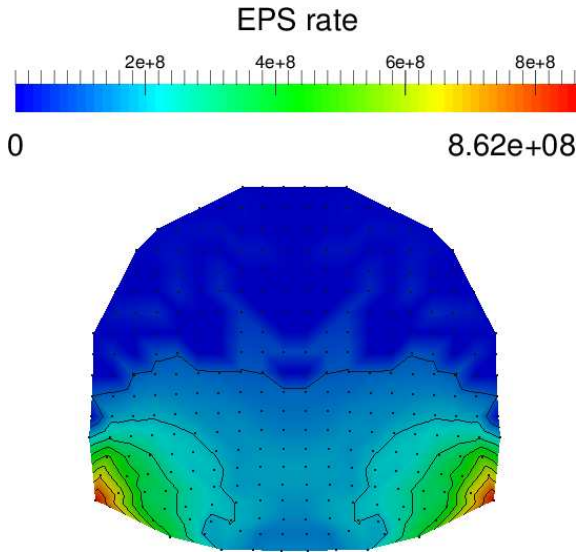

(a) 1 ns.

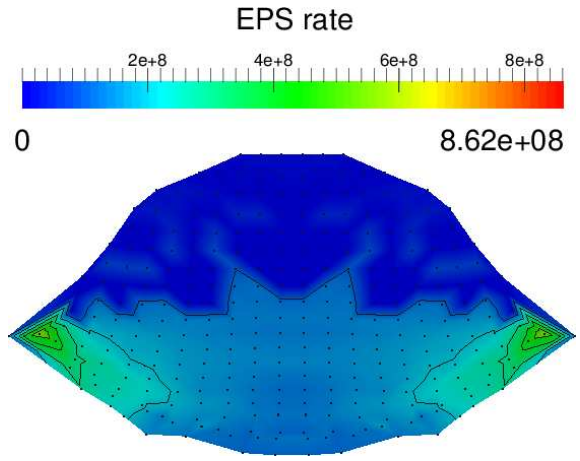

(b) 2 ns.

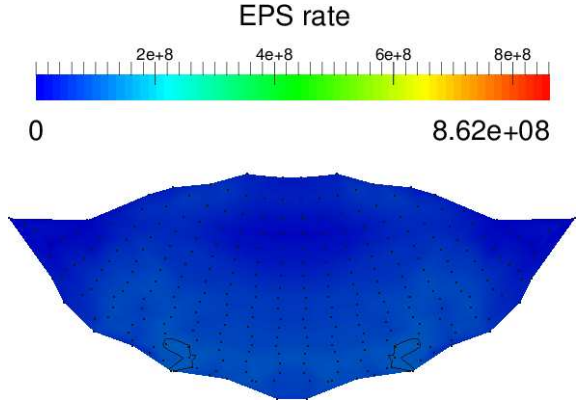

(c) 3.8 ns.

Figure B.77: Model K, EPS rate cross section through centre of 3-D splat morphology.

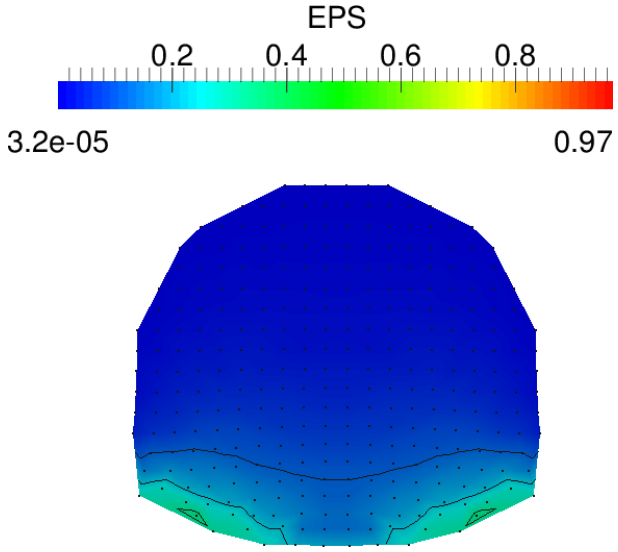

(a) 1 ns.

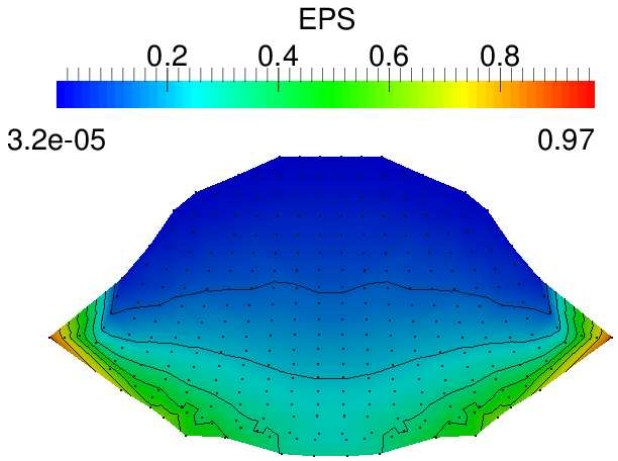

(b) 2 ns.

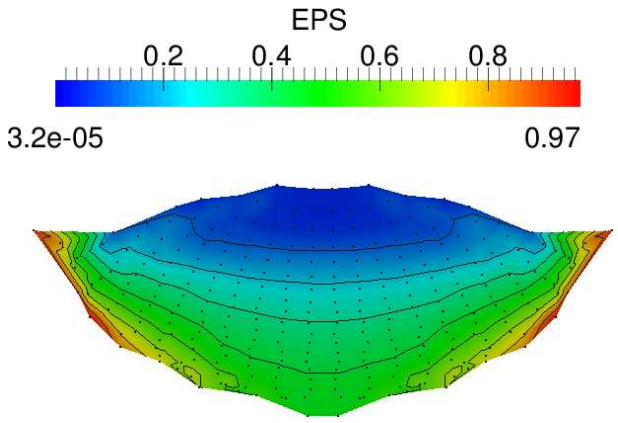

(c) 3.8 ns.

Figure B.78: Model K, EPS cross section through centre of 3-D splat morphology.

EPS rate, heating and thermal softening until the impact energy is expended and material cooling can act to shut off the material jetting. Without these features, the splat is unlikely to bond to the substrate and is assumed to have rebounded, the observed lack of a material jet matches observations by Schmidt et al [10].

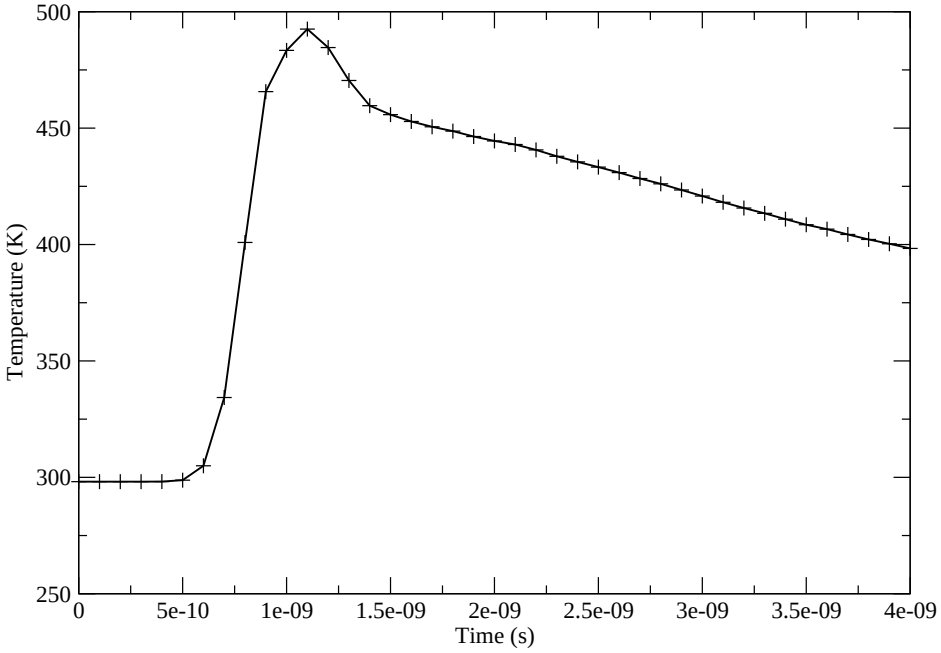

(a) Model K, temperature evolution in high EPS material jet region.

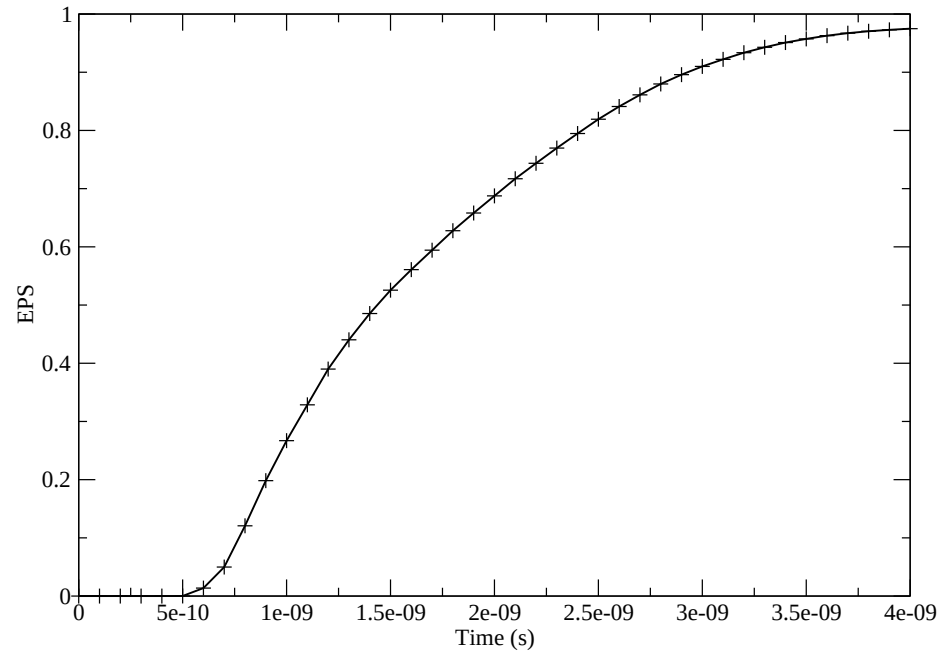

(b) Model K, EPS evolution in high EPS material jet region.

Figure B.79: Model K, evolution of temperature and EPS in material jet.

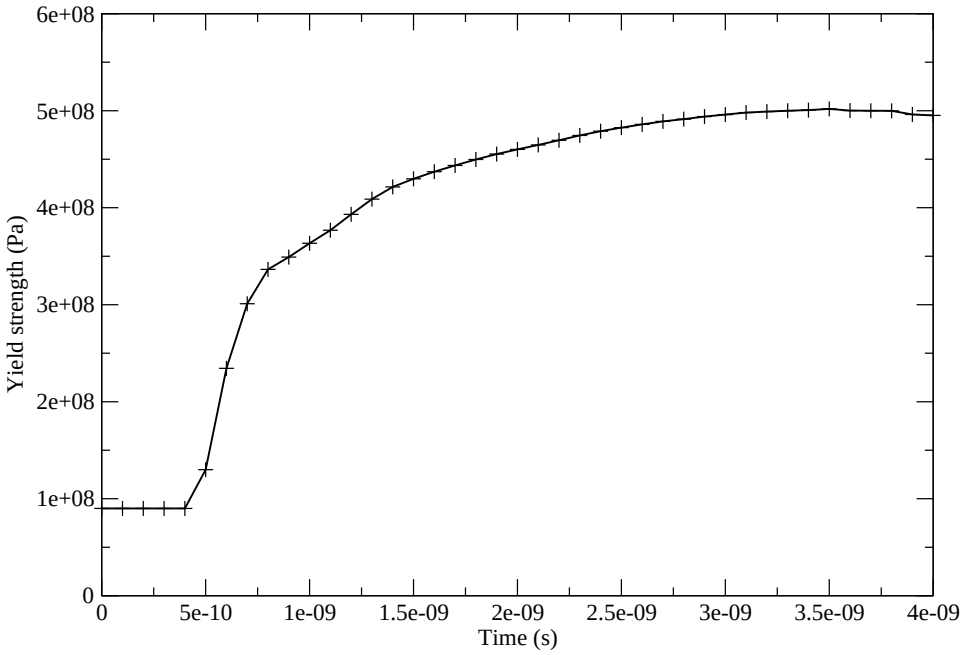

(a) Model K, yield strength evolution in high EPS material jet region.

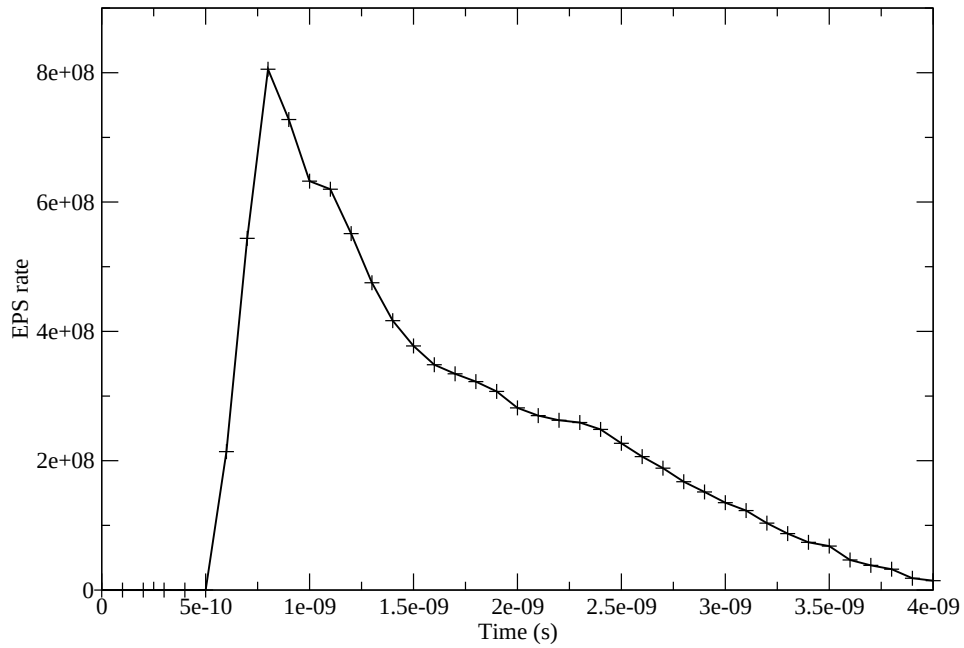

(b) Model K, EPS rate evolution in high EPS material jet region.

Figure B.80: Model K, evolution of yield strength and EPS rate in material jet.

B.4.2 Model L

The impact of a 2μm diameter heat conductive copper feedstock with initial velocity and temperature of 600 m/s and 593 K, respectively, is considered onto a heat conductive copper substrate with initial temperature of 298 K. The evolution of flattening ratio and height of feedstock centre is shown in Figure B.81. The flattening ratio reaches a steady state at 4.1 ns when its time dependant variation drops below 1%; at this time the variation in splat centre height is negligible indicating the initial impact velocity has been expended. The final value of flattening ratio, splat centre height and P^* is given in Table B.11. This flattening can be seen in Figure B.82 where the splat morphology at $1, 2$ and 4.1 ns are shown; additionally a lip of material can be seen at the edges of the feedstock.

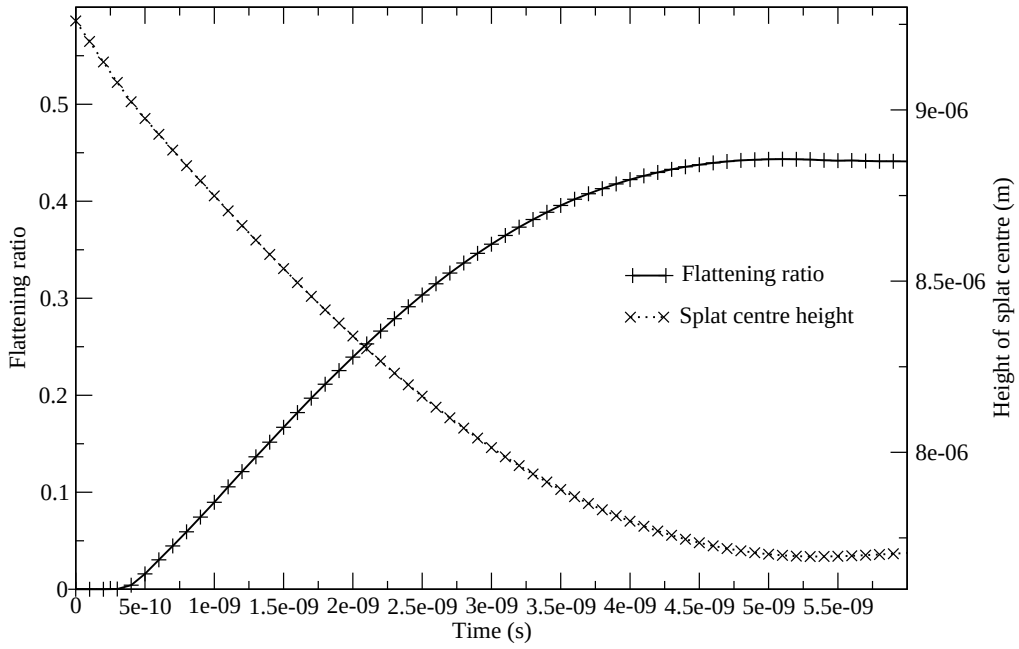

Figure B.81: Flattening ratio plot for a 2μm diameter conductive feedstock at 593 K and 600 m/s.

The temperature contours in Figure B.83 show peak temperature occurring early on in the impact at the leading edge of the forming lip feature, where heat conduction from

Flattening ratio	0.426
Splat centre height (μm)	7.784
P^*	0.738

Table B.11: Model L flattening ratio, P^* and splat centre height data at 4.1 ns.

the hot feedstock into the cold substrate acts to damp these temperature peaks resulting in more even heating of the feedstock before the formation of a colder layer of material at the feedstock/substrate interface. The yield strength contours (see Figure B.84) show that the whole splat has work hardened during the impact with the peak hardening found at the flanks of the interface between the feedstock and substrate. Peak rates of EPS occur at the leading edge of the forming lip feature in the the early stages of the impact with zones of elevated EPS rate radiating into the splat body (see Figure B.85). The EPS contours shown in Figure B.86 demonstrate the whole feedstock has undergone plastic strains with peak values found at the flanks of the feedstock/substrate interface where the shear stresses are at their highest.

The evolution of temperature, EPS, EPS rate and yield strength in these high EPS regions has been monitored and the results are shown in Figures B.87 and B.88. Significant heating occurs at 0.5 ns (see Figure B.87a) with peak temperatures reached at 0.9 ns and is followed by a period of cooling, where temperatures drop below the initial feedstock temperature due to conduction into the colder substrate. The period of peak heating coincides with that of peak EPS rate (see Figure B.88b), and there is no sign of the expected thermal softening that would indicate a shear band instability forming however (see Figure B.88a). Despite the elevated initial feedstock temperature, it appears that the experienced strain rates are high enough to prevent thermal softening becoming dominant and therefore has prevented material jetting from occurring; the lack of this feature indicates the feedstock has failed to bond to the substrate.

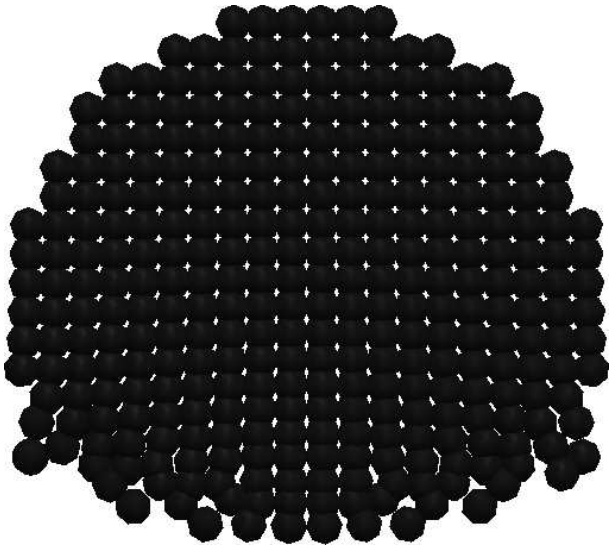

(a) 1 ns.

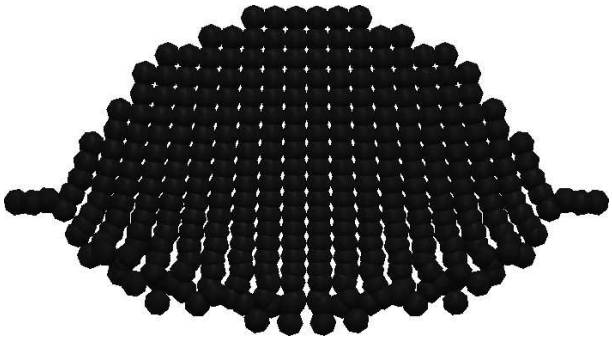

(b) 2 ns.

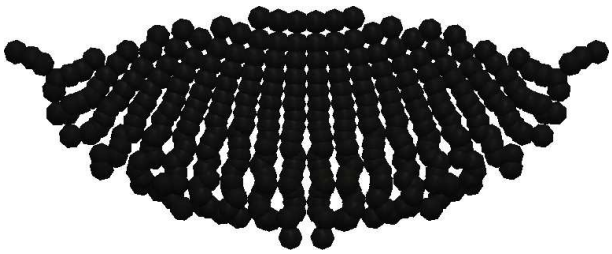

(c) 4.1 ns.

Figure B.82: Model L, cross section through centre of 3-D splat morphology.

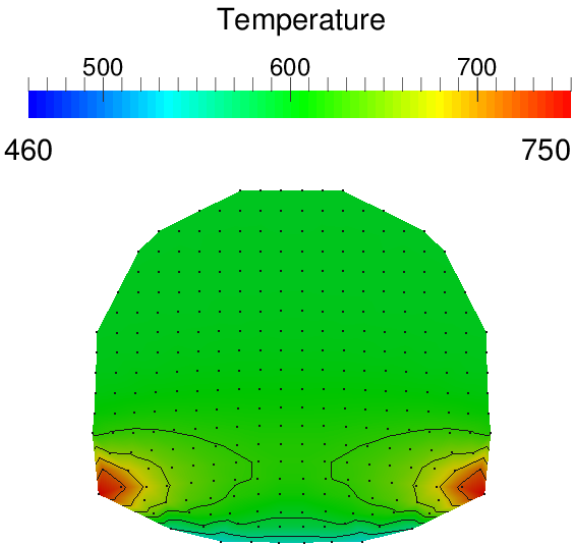

(a) 1 ns.

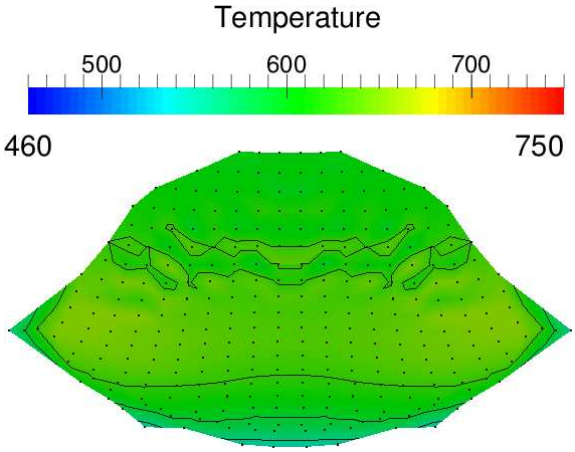

(b) 2 ns.

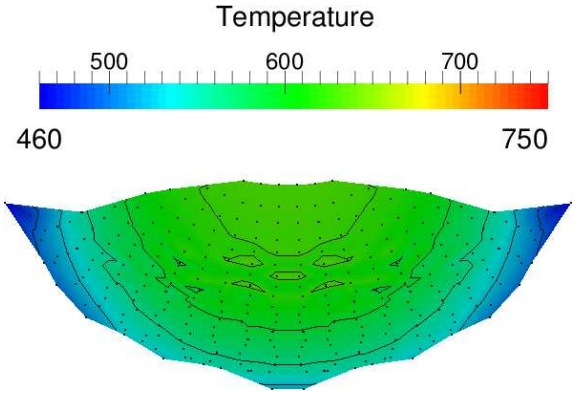

(c) 4.1 ns.

Figure B.83: Model L, temperature cross section through centre of 3-D splat morphology.

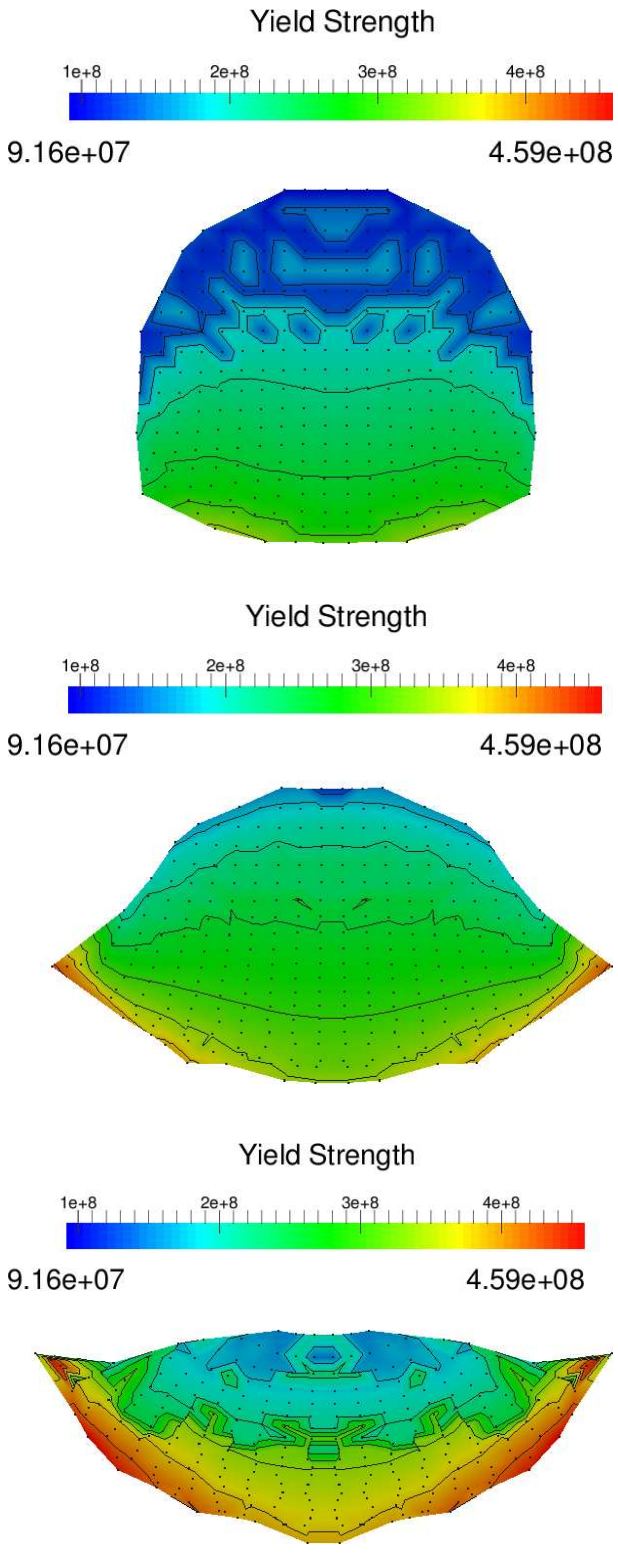

Figure B.84: Model L, yield strength cross section through centre of 3-D splat morphology.

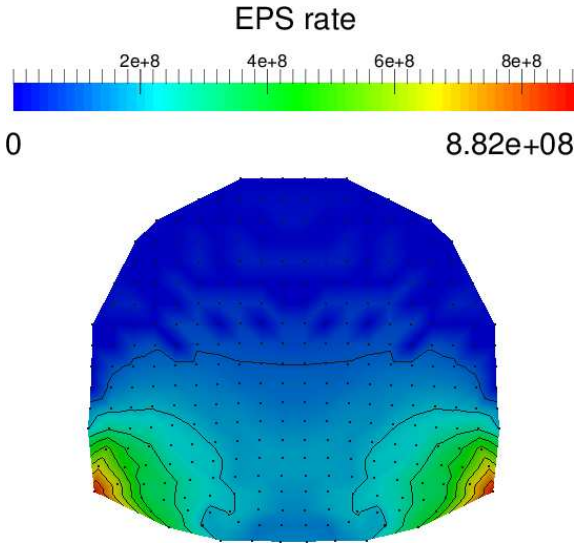

(a) 1 ns.

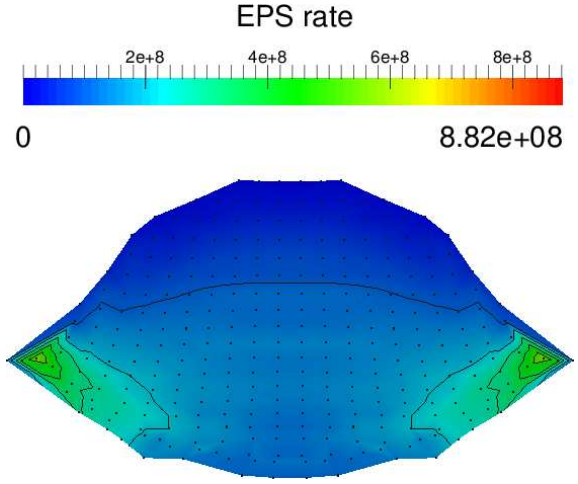

(b) 2 ns.

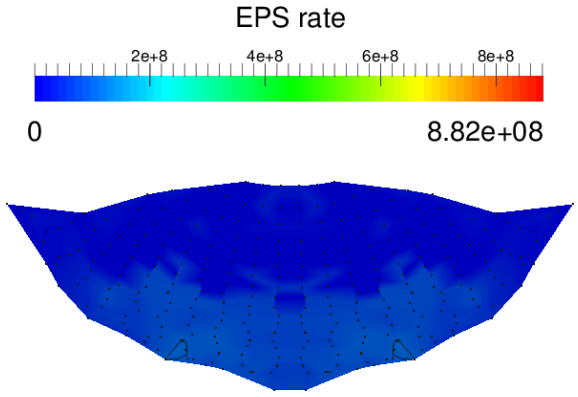

(c) 4.1 ns.

Figure B.85: Model L, EPS rate cross section through centre of 3-D splat morphology.

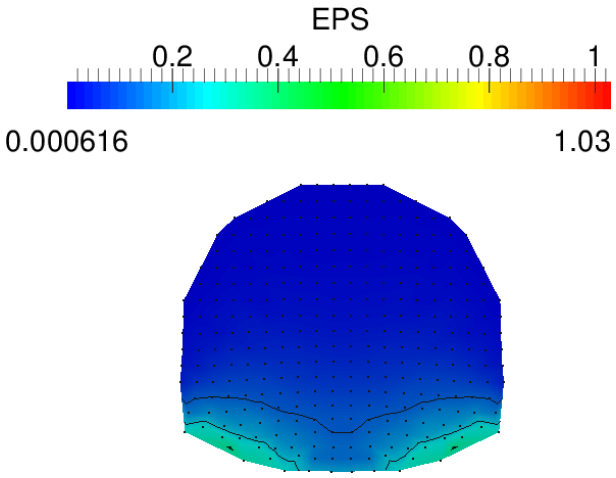

(a) 1 ns.

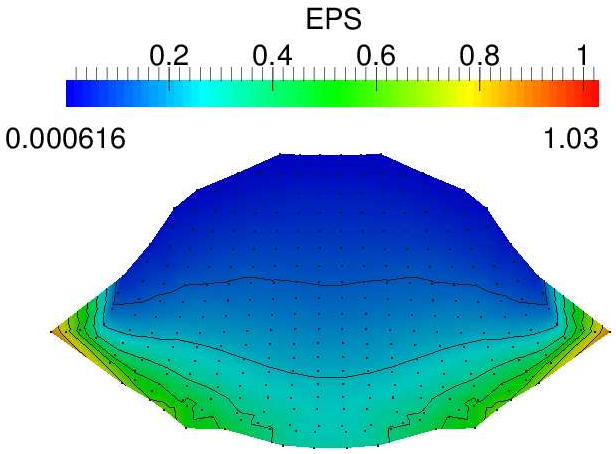

(b) 2 ns.

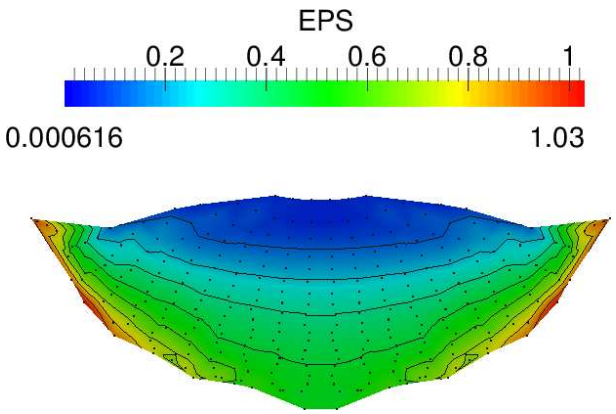

(c) 4.1 ns.

Figure B.86: Model L, EPS cross section through centre of 3-D splat morphology.

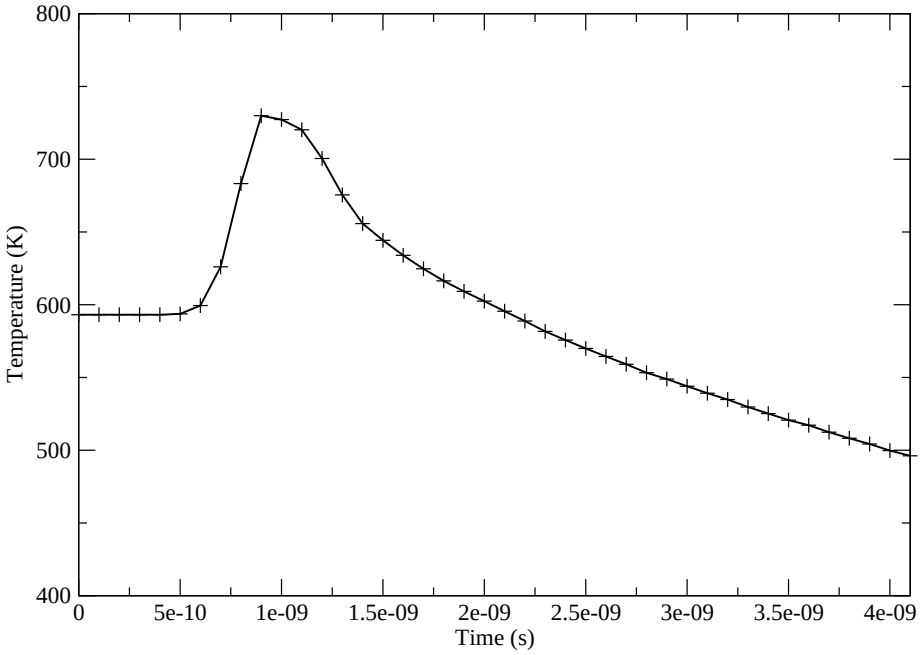

(a) Model L, temperature evolution in high EPS material jet region.

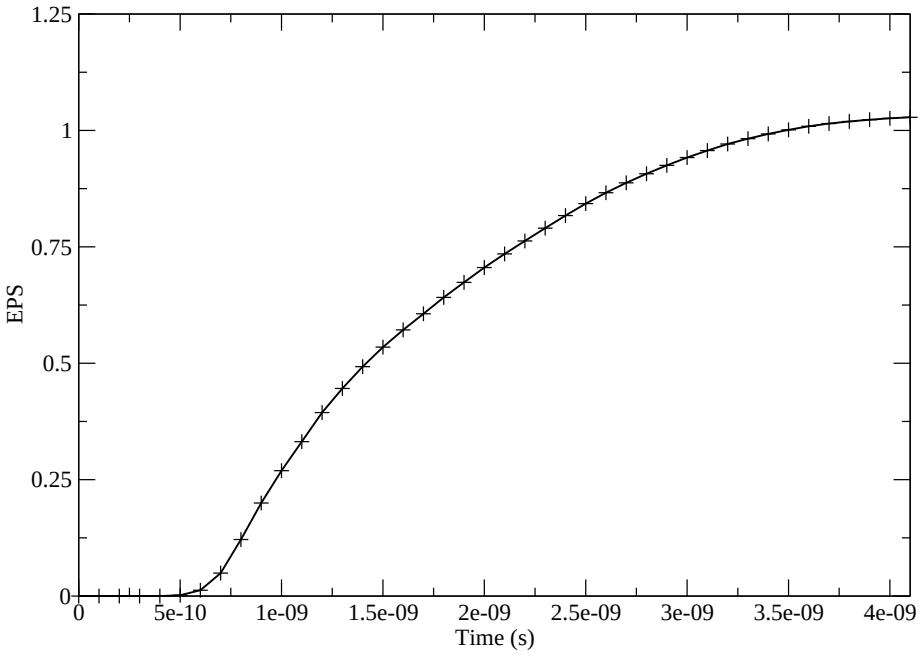

(b) Model L, EPS evolution in high EPS material jet region.

Figure B.87: Model L, evolution of temperature and EPS in material jet.

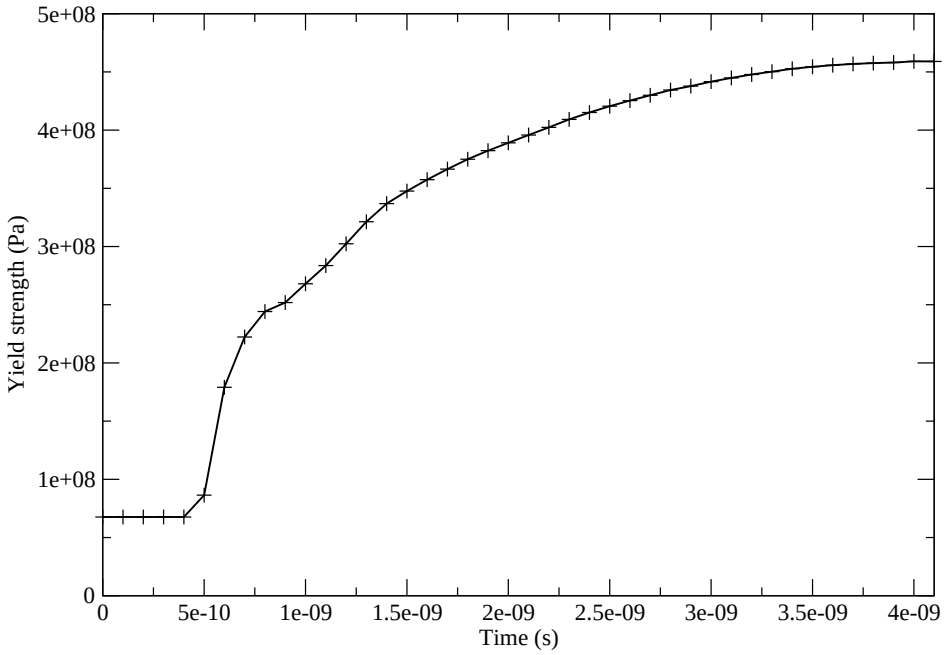

(a) Model L, yield strength evolution in high EPS material jet region.

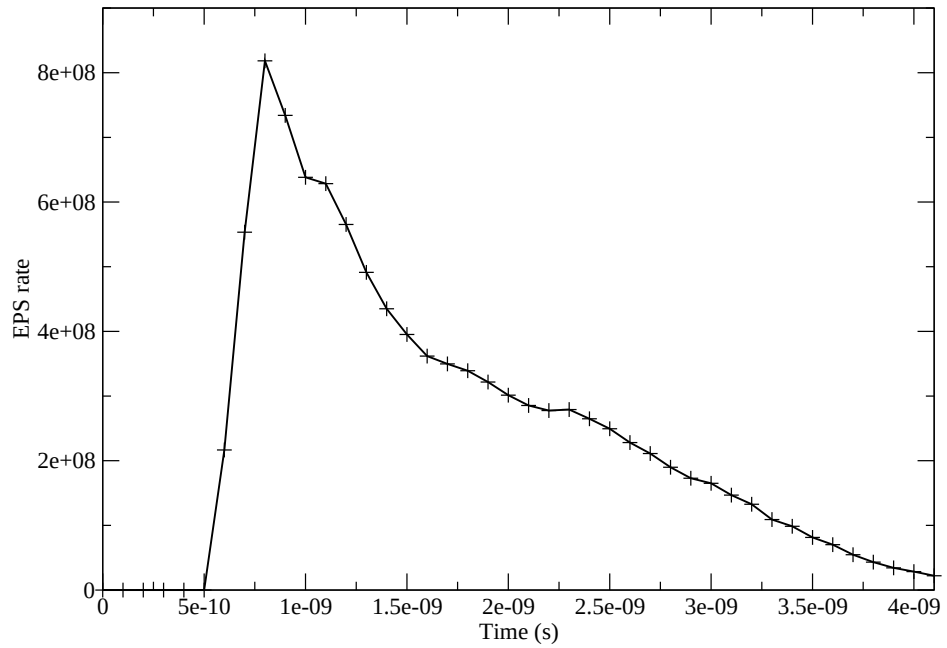

(b) Model L, EPS rate evolution in high EPS material jet region.

Figure B.88: Model L, evolution of yield strength and EPS rate in material jet.

Bibliography

[1] J. R Davis. *Handbook of Thermal Spray Technology.* ASM International, 2004.

[2] M. Dorfman. Thermal spray basics. *Adv. Mater. Process*, 15(3):47–50, 2002.

[3] Hamid Assadi, Frank Grtner, Thorsten Stoltenhoff, and Heinrich Kreye. Bonding mechanism in cold gas spraying. *Acta Materialia*, 51(15):4379–4394, September 2003.

[4] A. P. Alkhimov, V. F. Kosarev, and A. N. Papyrin. A method of Cold gas dynamic deposition. *Dokl. Akad. Nauk*, 318:1062–1065, 1990.

[5] T. Stoltenhoff, H. Kreye, and H. J. Richter. An analysis of the cold spray process and its coatings. *Journal of Thermal Spray Technology*, 11(4):542550, 2002.

[6] C. Borchers, F. Gartner, T. Stoltenhoff, H. Assadi, and H. Kreye. Microstructural and macroscopic properties of cold sprayed copper coatings. *Journal of Applied Physics*, 93(12):10064, 2003.

[7] Jongho Lee, Sumin Shin, HyungJun Kim, and Changhee Lee. Effect of gas temperature on critical velocity and deposition characteristics in kinetic spraying. *Applied Surface Science*, 253(7):3512–3520, January 2007.

[8] T. Van Steenkiste and D.W. Gorkiewicz. Analysis of tantalum coatings produced by the kinetic spray process. *Journal of Thermal Spray Technology*, 13(2):265–273, June 2004.

[9] Xian-Jin Ning, Jae-Hoon Jang, and Hyung-Jun Kim. The effects of powder properties on in-flight particle velocity and deposition process during low pressure cold spray process. *Applied Surface Science*, 253(18):7449–7455, July 2007.

[10] Tobias Schmidt, Frank Grtner, Hamid Assadi, and Heinrich Kreye. Development of a generalized parameter window for cold spray deposition. *Acta Materialia*, 54(3):729–742, February 2006.

[11] A. P. Alkhimov, A. N. Papyrin, V. F. Kosarev, N. I. Nesterovich, and M. M. Shushpanov. Gas-dynamic spray method for applying a coating, April 1994.

[12] Jon Affi, Hiroki Okazaki, Motohiro Yamada, and Masahiro Fukumoto. Fabrication of aluminum coating onto CFRP substrate by cold spray. *Materials Transactions*, 52(9):17591763, 2011.

[13] Jamil Assaad, Antoine Corbeil, Patrick F. Richer, and Bertrand Jodoin. Novel stacked wire mesh compact heat exchangers produced using cold spray. *Journal of Thermal Spray Technology*, 20(6):1192–1200, June 2011.

[14] Yannick Cormier, Philippe Dupuis, Bertrand Jodoin, and Antoine Corbeil. Net shape fins for compact heat exchanger produced by cold spray. *Journal of Thermal Spray Technology*, 22(7):1210–1221, July 2013.

[15] Ramesh Subramanian, Gregg P Wagner, and Brij B Seth. Thermal barrier coating applied with cold spray technique. (6,444,259), September 2002.

[16] A. Bacciochini, M.I. Radulescu, M. Yandouzi, G. Maines, J.J. Lee, and B. Jodoin. Reactive structural materials consolidated by cold spray: AlCuO thermite. *Surface and Coatings Technology*, 226:60–67, July 2013.

[17] Niraj Bala, Harpreet Singh, Satya Prakash, and J. Karthikeyan. Investigations on the behavior of HVOF and cold sprayed ni-20Cr coating on t22 boiler steel in actual boiler environment. *Journal of Thermal Spray Technology*, 21(1):144–158, November 2011.

[18] D. Dzhurinskiy, E. Maeva, Ev. Leshchinsky, and R. Gr. Maev. Corrosion protection of light alloys using low pressure cold spray. *Journal of Thermal Spray Technology*, 21(2):304–313, January 2012.

[19] R. C. Dykhuizen, M. F. Smith, D. L. Gilmore, R. A. Neiser, X. Jiang, and S. Sampath. Impact of high velocity cold spray particles. *Journal of Thermal Spray Technology*, 8(4):559564, 1999.

[20] L. Venkatesh, Naveen M. Chavan, and G. Sundararajan. The influence of powder particle velocity and microstructure on the properties of cold sprayed copper coatings. *Journal of Thermal Spray Technology*, 20(5):1009–1021, February 2011.

[21] H. Assadi, T. Schmidt, H. Richter, J.-O. Kliemann, K. Binder, F. Grtner, T. Klassen, and H. Kreye. On parameter selection in cold spraying. *Journal of Thermal Spray Technology*, 20(6):1161–1176, June 2011.

[22] Dina Goldbaum, J. Michael Shockley, Richard R. Chromik, Ahmad Rezaeian, Stephen Yue, Jean-Gabriel Legoux, and Eric Irissou. The effect of deposition conditions on adhesion strength of ti and Ti6Al4V cold spray splats. *Journal of Thermal Spray Technology*, 21(2):288–303, March 2012.

[23] P.C. King, S.H. Zahiri, and M. Jahedi. Focused ion beam micro-dissection of cold-sprayed particles. *Acta Materialia*, 56(19):5617–5626, November 2008.

[24] T. Hussain, D. G. McCartney, P. H. Shipway, and D. Zhang. Bonding mechanisms in cold spraying: The contributions of metallurgical and mechanical components. *Journal of Thermal Spray Technology*, 18(3):364–379, February 2009.

[25] C.-J. Li, H.-T. Wang, Q. Zhang, G.-J. Yang, W.-Y. Li, and H. L. Liao. Influence of spray materials and their surface oxidation on the critical velocity in cold spraying. *Journal of Thermal Spray Technology*, 19(1-2):95–101, January 2010.

[26] KeeHyun Kim, Makoto Watanabe, and Seiji Kuroda. Bonding mechanisms of thermally softened metallic powder particles and substrates impacted at high velocity. *Surface and Coatings Technology*, 204(14):2175–2180, April 2010.

[27] R. Morgan, P. Fox, J. Pattison, C. Sutcliffe, and W. O'Neill. Analysis of cold gas dynamically sprayed aluminium deposits. *Materials Letters*, 58(7-8):1317–1320, March 2004.

[28] T. Novoselova, P. Fox, R. Morgan, and W. O'Neill. Experimental study of titanium/aluminium deposits produced by cold gas dynamic spray. *Surface and Coatings Technology*, 200(8):2775–2783, January 2006.

[29] Shuo Yin, Xiaofang Wang, Wenya Li, Hanlin Liao, and Hongen Jie. Deformation behavior of the oxide film on the surface of cold sprayed powder particle. *Applied Surface Science*, 259:294–300, October 2012.

[30] Yuming Xiong, Gyuyeol Bae, Xiang Xiong, and Changhee Lee. The effects of successive impacts and cold welds on the deposition onset of cold spray coatings. *Journal of Thermal Spray Technology*, 19(3):575–585, 2010.

[31] T.H. Van Steenkiste, J.R. Smith, and R.E. Teets. Aluminum coatings via kinetic spray with relatively large powder particles. *Surface and Coatings Technology*, (154):237252, 2002.

[32] P. Richer, A. Ziga, M. Yandouzi, and B. Jodoin. CoNiCrAlY microstructural changes induced during cold gas dynamic spraying. *Surface and Coatings Technology*, 203(3-4):364–371, November 2008.

[33] Hong-Tao Wang, Chang-Jiu Li, Guan-Jun Yang, and Cheng-Xing Li. Cold spraying of Fe/Al powder mixture: Coating characteristics and influence of heat treatment on the phase structure. *Applied Surface Science*, 255(5):2538–2544, December 2008.

[34] Ha Yong Lee, Young Ho Yu, Young Cheol Lee, Young Pyo Hong, and Kyung Hyun Ko. Interfacial studies between cold-sprayed WO3, Y2O3 films and si substrate. *Applied Surface Science*, 227(1-4):244–249, April 2004.

[35] Victor K. Champagne, Dennis Helfritch, Phillip Leyman, Scott Grendahl, and Brad Klotz. Interface material mixing formed by the deposition of copper on aluminum by means of the cold spray process. *Journal of Thermal Spray Technology*, 14(3):330–334, September 2005.

[36] M. Grujicic, J.R. Saylor, D.E. Beasley, W.S. DeRosset, and D. Helfritch. Computational analysis of the interfacial bonding between feed-powder particles and the substrate in the cold-gas dynamic-spray process. *Applied Surface Science*, 219(3-4):211–227, December 2003.

[37] Hiromi Nakano, Motohiro Yamada, Masahiro Fukumoto, and Eiji Yamaguchi. Microstructure of interfacial region between cold-sprayed copper coating and AlN substrate coated with sputtered titanium and copper. *Journal of Thermal Spray Technology*, 20(3):407–411, March 2011.

[38] Peter C. King, Gyuyeol Bae, Saden H. Zahiri, Mahnaz Jahedi, and Changhee Lee. An experimental and finite element study of cold spray copper impact onto two aluminum substrates. *Journal of Thermal Spray Technology*, 19(3):620–634, 2010.

[39] S. Barradas, R. Molins, M. Jeandin, M. Arrigoni, M. Boustie, C. Bolis, L. Berthe, and M. Ducos. Application of laser shock adhesion testing to the study of the interlamellar strength and coatingsubstrate adhesion in cold-sprayed copper coating of aluminum. *Surface and Coatings Technology*, 197(1):18–27, July 2005.

[40] Yuming Xiong, Xiang Xiong, Sanghoon Yoon, Gyuyeol Bae, and Changhee Lee. Dependence of bonding mechanisms of cold sprayed coatings on strain-rate-induced non-equilibrium phase transformation. *Journal of Thermal Spray Technology*, 20(4):860–865, March 2011.

[41] K.-R. Ernst, J. Braeutigam, F. Gaertner, and T. Klassen. Effect of substrate temperature on cold-gas-sprayed coatings on ceramic substrates. *Journal of Thermal Spray Technology*, 22(2-3):422–432, March 2013.

[42] M. Perton, S. Costil, W. Wong, D. Poirier, E. Irissou, J.-G. Legoux, A. Blouin, and S. Yue. Effect of pulsed laser ablation and continuous laser heating on the adhesion and cohesion of cold sprayed ti-6Al-4V coatings. *Journal of Thermal Spray Technology*, 21(6):1322–1333, December 2012.

[43] Eric Irissou, Jean-Gabriel Legoux, Bernard Arsenault, and Christian Moreau. Investigation of al-Al2O3 cold spray coating formation and properties. *Journal of Thermal Spray Technology*, 16(5-6):661–668, October 2007.

[44] K. Ogawa, K. Ito, K. Ichimura, Y. Ichikawa, S. Ohno, and N. Onda. Characterization of low-pressure cold-sprayed aluminum coatings. *Journal of Thermal Spray Technology*, 17(5-6):728–735, November 2008.

[45] A. Shkodkin, A. Kashirin, O. Klyuev, and T. Buzdygar. Metal particle deposition stimulation by surface abrasive treatment in gas dynamic spraying. *Journal of Thermal Spray Technology*, 15(3):382–386, September 2006.

[46] Shuo Yin, Xinkun Suo, Jiaqing Su, Zhiwei Guo, Hanlin Liao, and Xiaofang Wang. Effects of substrate hardness and spray angle on the deposition behavior of cold-sprayed ti particles. *Journal of Thermal Spray Technology*, 23(1-2):76–83, January 2014.

[47] K. Taylor, B. Jodoin, and J. Karov. Particle loading effect in cold spray. *Journal of Thermal Spray Technology*, 15(2):273–279, June 2006.

[48] T. Novoselova, S. Celotto, R. Morgan, P. Fox, and W. ONeill. Formation of TiAl intermetallics by heat treatment of cold-sprayed precursor deposits. *Journal of Alloys and Compounds*, 436(1-2):69–77, June 2007.

[49] P. Sudharshan Phani, D. Srinivasa Rao, S.V. Joshi, and G. Sundararajan. Effect of process parameters and heat treatments on properties of cold sprayed copper coatings. *Journal of Thermal Spray Technology*, 16(3):425–434, June 2007.

[50] Dina Goldbaum, Richard R. Chromik, Stephen Yue, Eric Irissou, and Jean-Gabriel Legoux. Mechanical property mapping of cold sprayed ti splats and coatings. *Journal of Thermal Spray Technology*, 20(3):486–496, March 2011.

[51] Hengyong Bu, Mohammed Yandouzi, Chen Lu, and Bertrand Jodoin. Effect of heat treatment on the intermetallic layer of cold sprayed aluminum coatings on magnesium alloy. *Surface and Coatings Technology*, 205(19):4665–4671, June 2011.

[52] K. Spencer, V. Luzin, N. Matthews, and M.-X. Zhang. Residual stresses in cold spray al coatings: The effect of alloying and of process parameters. *Surface and Coatings Technology*, 206(19-20):4249–4255, May 2012.

[53] T.S. Price, P.H. Shipway, and D.G. McCartney. Effect of cold spray deposition of a titanium coating on fatigue behavior of a titanium alloy. *Journal of Thermal Spray Technology*, 15(4):507–512, December 2006.

[54] B. AL-Mangour, R. Dallala, F. Zhim, R. Mongrain, and S. Yue. Fatigue behavior of annealed cold-sprayed 316L stainless steel coating for biomedical applications. *Materials Letters*, 91:352–355, January 2013.

[55] Jan Cizek, Ondrej Kovarik, Jan Siegl, Khiam Aik Khor, and Ivo Dlouhy. Influence of plasma and cold spray deposited ti layers on high-cycle fatigue properties of Ti6Al4V substrates. *Surface and Coatings Technology*, 217:23–33, February 2013.

[56] T. Schmidt, F. Gaertner, and H. Kreye. New developments in cold spray based on higher gas and particle temperatures. *Journal of Thermal Spray Technology*, 15(4):488–494, December 2006.

[57] T. Hussain, D. G. McCartney, P. H. Shipway, and T. Marrocco. Corrosion behavior of cold sprayed titanium coatings and free standing deposits. *Journal of Thermal Spray Technology*, 20(1-2):260–274, January 2011.

[58] Saden H. Zahiri, Darren Fraser, Stefan Gulizia, and Mahnaz Jahedi. Effect of processing conditions on porosity formation in cold gas dynamic spraying of copper. *Journal of Thermal Spray Technology*, 15(3):422–430, September 2006.

[59] Sumin Shin, Sanghoon Yoon, Youngdo Kim, and Changhee Lee. Effect of particle parameters on the deposition characteristics of a hard/soft-particles composite in kinetic spraying. *Surface and Coatings Technology*, 201(6):3457–3461, December 2006.

[60] Gyuyeol Bae, Jae-il Jang, and Changhee Lee. Correlation of particle impact conditions with bonding, nanocrystal formation and mechanical properties in kinetic sprayed nickel. *Acta Materialia*, 60(8):3524–3535, May 2012.

[61] Chang-Jiu Li and Wen-Ya Li. Deposition characteristics of titanium coating in cold spraying. *Surface and Coatings Technology*, 167(2-3):278–283, April 2003.

[62] Heli Koivuluoto and Petri Vuoristo. Structural analysis of cold-sprayed nickel-based metallic and metallic-ceramic coatings. *Journal of Thermal Spray Technology*, 19(5):975–989, February 2010.

[63] Heli Koivuluoto, Andrew Coleman, Keith Murray, Martin Kearns, and Petri Vuoristo. High pressure cold sprayed (HPCS) and low pressure cold sprayed (LPCS) coatings prepared from OFHC cu feedstock: Overview from powder characteristics to coating properties. *Journal of Thermal Spray Technology*, 21(5):1065–1075, May 2012.

[64] Hengyong Bu, Mohammed Yandouzi, Chen Lu, Daniel MacDonald, and Bertrand Jodoin. Cold spray blended Al+Mg17Al12 coating for corrosion protection of AZ91D magnesium alloy. *Surface and Coatings Technology*, 207:155–162, August 2012.

[65] Yongshan Tao, Tianying Xiong, Chao Sun, Huazi Jin, Hao Du, and Tiefan Li. Effect of -Al2O3 on the properties of cold sprayed al/-Al2O3 composite coatings on AZ91D magnesium alloy. *Applied Surface Science*, 256(1):261–266, October 2009.

[66] Qiang Wang, Kevin Spencer, Nick Birbilis, and Ming-Xing Zhang. The influence of ceramic particles on bond strength of cold spray composite coatings on AZ91 alloy substrate. *Surface and Coatings Technology*, 205(1):50–56, September 2010.

[67] S. V. Klinkov, V. F. Kosarev, A. A. Sova, and I. Smurov. Calculation of particle parameters for cold spraying of metal-ceramic mixtures. *Journal of Thermal Spray Technology*, 18(5-6):944–956, June 2009.

[68] R. S. Lima, J. Karthikeyan, C. M. Kay, J. Lindemann, and C. C. Berndt. Microstructural characteristics of cold-sprayed nanostructured WCCo coatings. *Thin Solid Films*, 416(1):129135, 2002.

[69] Xueping Guo, Ga Zhang, Wen-Ya Li, Lucas Dembinski, Yang Gao, Hanlin Liao, and Christian Coddet. Microstructure, microhardness and dry friction behavior of cold-sprayed tin bronze coatings. *Applied Surface Science*, 254(5):1482–1488, December 2007.

[70] M. Fukumoto, H. Wada, K. Tanabe, M. Yamada, E. Yamaguchi, A. Niwa, M. Sugimoto, and M. Izawa. Effect of substrate temperature on deposition behavior of

copper particles on substrate surfaces in the cold spray process. *Journal of Thermal Spray Technology*, 16(5-6):643–650, October 2007.

[71] Jihane Ajaja, Dina Goldbaum, and Richard R. Chromik. Characterization of ti cold spray coatings by indentation methods. *Acta Astronautica*, 69(11-12):923–928, December 2011.

[72] Hengyong Bu, Mohammed Yandouzi, Chen Lu, and Bertrand Jodoin. Post-heat treatment effects on cold-sprayed aluminum coatings on AZ91D magnesium substrates. *Journal of Thermal Spray Technology*, 21(3-4):731–739, April 2012.

[73] N. Cinca and J.M. Guilemany. Structural and properties characterization of stellite coatings obtained by cold gas spraying. *Surface and Coatings Technology*, 220:90–97, April 2013.

[74] W. Wong, P. Vo, E. Irissou, A. N. Ryabinin, J.-G. Legoux, and S. Yue. Effect of particle morphology and size distribution on cold-sprayed pure titanium coatings. *Journal of Thermal Spray Technology*, June 2013.

[75] K. Spencer, D.M. Fabijanic, and M.-X. Zhang. The use of AlAl2O3 cold spray coatings to improve the surface properties of magnesium alloys. *Surface and Coatings Technology*, 204(3):336–344, October 2009.

[76] R. C. Dykhuizen and M. F. Smith. Gas dynamic principles of cold spray. *Journal of Thermal Spray Technology*, 7(2):205212, 1998.

[77] Taeyoung Han, Zhibo Zhao, Bryan A. Gillispie, and John R. Smith. Effects of spray conditions on coating formation by the kinetic spray process. *Journal of Thermal Spray Technology*, 14(3):373–383, September 2005.

[78] Hiroshi Katanoda, Minoru Fukuhara, and Naoko Iino. Numerical simulation on impact velocity of ceramic particles propelled by supersonic nitrogen gas flow in vacuum chamber. *Materials transactions*, 48(6):14631468, 2007.

[79] Sudharshan Phani Pardhasaradhi, Vishnukanthan Venkatachalapathy, Shrikant V Joshi, and Sundararajan Govindan. Optical diagnostics study of gas particle trans-

port phenomena in cold gas dynamic spraying and comparison with model predictions. *Journal of Thermal Spray Technology*, 17(4):551–563, October 2008.

[80] Wen-Ya Li, Chang-Jiu Li, Hong-Tao Wang, Cheng-Xin Li, and Hee-Seon Bang. Measurement and numerical simulation of particle velocity in cold spraying. *Journal of Thermal Spray Technology*, 15(4):559–562, December 2006.

[81] B. Samareh and A. Dolatabadi. A three-dimensional analysis of the cold spray process: The effects of substrate location and shape. *Journal of Thermal Spray Technology*, 16(5-6):634–642, October 2007.

[82] Shuo Yin, Yan Sun, Xiaofang Wang, Zhiwei Guo, and Hanlin Liao. Effect of spray angle on temperature distribution within the metallic substrate in cold spraying. *Journal of Thermal Spray Technology*, 22(6):983–991, May 2013.

[83] A. G. McDonald, A. N. Ryabinin, E. Irissou, and J.-G. Legoux. Gas-substrate heat exchange during cold-gas dynamic spraying. *Journal of Thermal Spray Technology*, 22(2-3):391–397, March 2013.

[84] Kensuke Yokoyama, Makoto Watanabe, Seiji Kuroda, Yoshihiko Gotoh, Tobias Schmidt, and Frank Gartner. Simulation of solid particle impact behavior for spray processes. *Materials transactions*, 47(7):1697, 2006.

[85] F. F. Wang, W. Y. Li, M. Yu, and H. L. Liao. Prediction of critical velocity during cold spraying based on a coupled thermomechanical eulerian model. *Journal of Thermal Spray Technology*, 23(1-2):60–67, January 2014.

[86] Z. Arabgol, H. Assadi, T. Schmidt, F. Grtner, and T. Klassen. Analysis of thermal history and residual stress in cold-sprayed coatings. *Journal of Thermal Spray Technology*, 23(1-2):84–90, January 2014.

[87] Shuo Yin, Xiaofang Wang, Bao-peng Xu, and Wenya Li. Examination on the calculation method for modelling the multi-particle impact process in cold spraying. *Journal of Thermal Spray Technology*, 19:1032–1041, 2010.

[88] R. A Gingold and J. J. Monaghan. Smoothed particle hydrodynamics: Theory and application to non-spherical stars. *Monthly Notes of the Royal Astronomy Society*, 181:375 – 389, 1977.

[89] L. B. Lucy. A numerical approach to tthe testing of the fission hypothesis. *The Astronomical Journal*, 82(12):1013 – 1024, 1977.

[90] J. J. Monaghan. Smoothed particle hydrodynamics. *Ann. Rev. Astron. Astrophys*, 30:543–74, 1992.

[91] J. J. Monaghan and J. C. Lattanzio. A refined particle method for astrophysical problems. *Astronomy and Astrophysics*, (149):135–143, 1985.

[92] Lars Hernquist and Neal Katz. Treesph: A unification of SPH with the hierarchical tree method. *The Astrophysical Journal Supplement Series*, 70:419–446, 1989.

[93] O Flebbe, S Munzel, H Herold, H Riffert, and H Ruder. Smoothed particle hydrodynamics: Physical viscosity and the simulation of accretion disks. *The Astrophysical Journal*, 431:754 – 760, 1994.

[94] S.J Watkins, A.S Bhattal, N Francis, J.A Turner, and A.P Whitworth. A new prescription for viscosity in smoothed particle hydrodynamics. *Astronomy & Astropyhsics Supplement Series*, 119:177 – 187, 1996.

[95] L. Brookshaw. A method of calculating radiative heat diffusion in particle simulations. *Proc. Astron. Soc. Aust*, 6:207, 1985.

[96] Paul. W CLeary. Modelling confined multi-material heat and mass flows using SPH. *Applied Mathematical Modelling*, 22:981 – 993, 1998.

[97] Paul. W Cleary and J. J. Monagahan. Conduction modelling using smoothed particle hydrodynamics. *Journal of Computational Physics*, 148:227–264, 1999.

[98] Joseph. P Morris, Patrick. J Fox, and Yi Zhu. Modeling low reynolds number incompressible flows using SPH. *Journal of Computational Physics*, 136:214 – 226, 1997.

[99] Pep Espaol and Mariano Revenga. Smoothed dissipative particle dynamics. *Physical Review E*, 67(2), February 2003.

[100] Damien Violeau. *Fluid mechanics and the SPH method: theory and applications*. Oxford University Press, Oxford, 2012.

[101] David A. Fulk. A numerical analysis of smoothed particle hydrodynamics. Technical report, DTIC Document, 1994.

[102] Holger Wendland. Piecewise polynomial, positive definite and compactly supported radial functions of minimal degree. *Advances in Computational Mathematics*, 4(1):389–396, 1995.

[103] J J Monaghan. Smoothed particle hydrodynamics. *Reports on Progress in Physics*, 68(8):1703–1759, August 2005.

[104] Gordon R. Johnson and Stephen R. Bissel. Normalized smoothing functions for SPH impact calculations. *International Journal For Neumerical Methods in Engineering*, 39:2725–2741, 1996.

[105] J.J Monaghan and R.A Gingold. Shock simulation by the particle method {SPH}. *Journal of Computational Physics*, 52(2):374 – 389, 1983.

[106] P.W. Randles and L.D Libersky. Smoothed particle hydrodynamics: Some recent improvements and applications. *Computer Methods in Applied Mechanics and Engineering*, 139:375–408, 1996.

[107] J. Bonet and T. S.L Lok. Variational and momentum preservation aspects of smooth particle hydrodynamic formulations. *Computer Methods in Applied Mechanics and Engineering*, 180:97–115, 1999.

[108] Wing Kim Liu, Shaofan Li, and Ted Belytschko. Moving least square reproducing kernel methods i methodology and convergence. *Computer Methods in Applied Mechanics and Engineering*, 1996.

[109] J.K. Chen and J.E Beraun. A generalized smoothed particle hydrodynamics method for nonlinear dynamic problems. *Computer Methods in Applied Mechanics and Engineering*, 190:225–239, 2000.

[110] M. B. Liu, G. R. Liu, and K. Y. Lam. A one-dimensional meshfree particle formulation for simulating shock waves. *Shock Waves*, 13(3):201–211, November 2003.

[111] J. J. Monaghan. Simulating free surface flows with SPH. *Journal of Computational Physics*, (110):399–406, 1994.

[112] J. J. Monaghan and A. Kos. Solitary waves on a cretan beach. *Journal of Waterway, Port, Coastal, and Ocean Engineering*, 125(3):145155, 1999.

[113] J.J. Monaghan and J.B. Kajtar. SPH particle boundary forces for arbitrary boundaries. *Computer Physics Communications*, 180(10):1811–1820, October 2009.

[114] Larry D. Libersky, Albert G. Petschek, Theodore C. Carney, Jim R. Hipp, and Firooz A. Allahdadi. High strain lagrangian hydrodynamics. *Journal of Computational Physics*, (109):67–75, 1993.

[115] M.B. Liu, G.R. Liu, and K.Y. Lam. Investigations into water mitigation using a meshless particle method. *Shock Waves*, 12(3):181–195, November 2002.

[116] G. R Liu and M. B Liu. *Smoothed particle hydrodynamics a meshfree particle method*. World Scientific, Singapore; London, 2003.

[117] Emily M. Ryan, Alexandre M. Tartakovsky, and Cristina Amon. A novel method for modeling neumann and robin boundary conditions in smoothed particle hydrodynamics. *Computer Physics Communications*, 181(12):2008–2023, December 2010.

[118] Larry D. Libersky and Albert G. Petschek. Smoothed particle hydrodynamics with strength of materials. *Proceedings of The Next Free Lagrange Conference*, pages 248–257, 1991.

[119] J. W. Swegle, D. L. Hicks, and S. W. Attaway. Smoothed particle hydrodynamics stability analysis. *Journal of Computational Physics*, (116):123–134, 1995.

[120] D.E. Grady and M.E. Kipp. Continuum modelling of explosive fracture in oil shale. *International Journal of Rock Mechanics and Mining Sciences Geomechanics Abstracts*, 17(3):147 – 157, 1980.

[121] W. Benz and E. Asphaug. Impact simulations with fracture. i. method and tests. *Icarus*, (107):98–116, 1994.

[122] Larry D. Libersky, Phil W. Randles, Ted C. Carney, and David L. Dickinson. Recent improvements in SPH modeling of hypervelocity impact. *International Journal of Impact Engineering*, 20(6):525532, 1997.

[123] Wm. Hoover, Carol Hoover, and Elizabeth Merritt. Smooth-particle applied mechanics: Conservation of angular momentum with tensile stability and velocity averaging. *Physical Review E*, 69(1), January 2004.

[124] J. J. Monaghan. On the problem of penetration in particle methods. *Journal of Computational Physics*, 82(1):1–15, 1989.

[125] P.W. Cleary, M. Prakash, and J. Ha. Novel applications of smoothed particle hydrodynamics (SPH) in metal forming. *Journal of Materials Processing Technology*, 177(1-3):41–48, July 2006.

[126] M. B. Liu, G. R. Liu, and K. Y. Lam. Adaptive smoothed particle hydrodynamics for high strain hydrodynamics with material strength. *Shock Waves*, 15(1):21–29, January 2006.

[127] Michael S. Fulbright, Willy Benz, and Melvyn B. Davies. A Method of smooth particle hydrodynamics using spheroidal kernels. *Astrophys.J.*, 440:254, 1995.

[128] Paul W. Cleary. Elastoplastic deformation during projectilewall collision. *Applied Mathematical Modelling*, 34(2):266–283, February 2010.

[129] Zhiyi Chen, Zili Dai, Yu Huang, and Guoqiang Bian. Numerical simulation of large deformation in shear panel dampers using smoothed particle hydrodynamics. *Engineering Structures*, 48:245–254, March 2013.

[130] G.J. Phillips and J. J. Monaghan. A numerical method for three-dimensional simulations of collapsing, isothermal, magnetic gas clouds. *Monthly Notes of the Royal Astronomy Society*, (216):883–895, 1985.

[131] Joseph Peter Morris. *Analysis of smoothed particle hydrodynamics with applications*. Monash University Australia, 1996.

[132] Y. Wen, D. L. Hicks, and J. W. Swegle. Stabilizing S.P.H with conservative smoothing, 1994.

[133] J.J. Monaghan. SPH without a tensile instability. *Journal of Computational Physics*, 159(2):290–311, April 2000.

[134] J. P. Gray, J. J. Monagahan, and R. P. Swift. SPH elastic dynamics. *Computer Methods in Applied Mechanics and Engineering*, (190):6641–6662, 2001.

[135] Wen-Ya Li, Shuo Yin, and Xiao-Fang Wang. Numerical investigations of the effect of oblique impact on particle deformation in cold spraying by the SPH method. *Applied Surface Science*, 256(12):3725–3734, April 2010.

[136] A. Manap, T. Okabe, and K. Ogawa. Computer simulation of cold sprayed deposition using smoothed particle hydrodynamics. *Procedia Engineering*, 10:1145–1150, January 2011.

[137] A. Manap, K. Ogawa, and O. Tomonaga. Numerical analysis of interfacial bonding of al-si particle and mild steel substrate by cold spray technique using the SPH method. *Journal of Solid Mechanics and Materials Engineering*, 6(3):241–250, 2012.

[138] Mark. L Wilkins. Calculation of elastic-plastic FLow. 1963.

[139] Gordon R. Johnson and William H. Cook. A constitutive model and data for metals. *Proceedings of the 7th International Symposium on Ballistics*, pages 541–547, 1983.

[140] A. J. C. Crespo, M. Gmez-Gesteira, and Robert A. Dalrymple. Boundary conditions generated by dynamic particles in SPH methods. *CMC-TECH SCIENCE PRESS-*, 5(3):173, 2007.

[141] M. B. Liu and G. R. Liu. Smoothed particle hydrodynamics (SPH): an overview and recent developments. *Archives of Computational Methods in Engineering*, 17(1):25–76, February 2010.

[142] H. S. Carlsaw and J. C. Jaeger. *Conduction of Heat in Solids*. Oxford University Press, London, 2 edition, 1965.

[143] Gordon R. Johnson and Tim J. Holmquist. Evaluation of cylinder-impact test data for constitutive model constants. *Journal of Applied Physics*, 64(8):3901, 1988.

[144] Saeed Rahmati and Abbas Ghaei. The use of particle/substrate material models in simulation of cold-gas dynamic-spray process. *Journal of Thermal Spray Technology*, 23(3):530–540, February 2014.